Ductile fracture at intermediate stress triaxialities: Experimental investigations and micro-mechanical modeling

by

Matthieu Dunand

Ingénieur de l'Ecole Polytechnique (2008)
M.S., Massachusetts Institute of Technology (2010)

Submitted to the Department of Mechanical Engineering
in Partial Fulfillment of the Requirements for the Degree of

Doctor of Science in Mechanical Engineering

at the

MASSACHUSETTS INSTITUTE OF TECHNOLOGY

June 2013

Author:_____
Department of Mechanical Engineering
May 17th, 2013

Certified by:_____
Dirk Mohr
CNRS Associate Professor
Thesis Supervisor

Certified by:_____
Tomasz Wierzbicki
Professor of Applied Mechanics
Thesis Supervisor

Accepted by:_____
David E. Hardt
Professor of Mechanical Engineering
Chairman, Committee on Graduate Students

Ductile fracture at intermediate stress triaxialities: Experimental investigations and micro-mechanical modeling

Matthieu Dunand

Submitted to the Department of Mechanical Engineering
in June 2013, in partial fulfillment of the requirements for the degree of
Doctor of Science in Mechanical Engineering

Abstract

Accurate predictions of the onset of ductile fracture play an increasingly important role in the design of lightweight sheet metal structures. With the development of virtual prototyping practices, most transportation vehicles are now computer-engineered in great detail before launching their mass production, thereby requiring reliable models for plasticity and fracture. This thesis reports on a comprehensive investigation into the effect of stress state on the onset of ductile fracture of an Advanced High Strength Steel (AHSS), covering development of new experimental procedures, material characterization and phenomenological as well as micro-mechanical modeling of the onset of fracture. Based on an extensive multi-axial experimental program, the anisotropic plasticity of the present material is described by a non-associated quadratic anisotropic model. Comparison of model predictions to experimental results reveals that the proposed model provides better predictions than associated isotropic or anisotropic quadratic models. Moreover, a structural validation is presented that demonstrates the higher prediction accuracy of the non-associated plasticity model. A hybrid experimental-numerical approach is proposed to investigate the dependence of the onset of fracture to stress state. The experimental program covers the complete range of positive stress triaxialities, from pure shear to equi-biaxial tension. It includes different full thickness specimens as well as multi-axial fracture experiments where combinations of tension and shear loadings are applied to a newly developed butterfly-shaped specimen. Loading paths to fracture are determined for each experiment in terms of stress triaxiality, Lode angle parameter and equivalent plastic strain and show a non-monotonic and strong dependence of ductility to stress state. The extensive fracture characterization is used to evaluate the predictive capabilities of two phenomenological and physics-inspired fracture models (the Modified Mohr-Coulomb and a shear-modified Gurson model) that take the effect of the first and third stress tensor invariants into account in predicting the onset of fracture. Finally, a micro-mechanical model relating the onset of fracture to plastic localization into a narrow band at the micro-scale is developed. The effect of stress state on localization is investigated numerically by means of a 3D void-containing unit cell submitted to well-controlled and proportional loadings in the macroscopic stress state. Based on simulation results, an analytical localization criterion is proposed which defines an open convex envelope in terms of the shear and normal stresses acting on the plane of localization and correlates well with experimental results.

Thesis supervisor: Tomasz Wierzbicki
Title: Professor of Applied Mechanics

Thesis supervisor: Dirk Mohr
Title: CNRS Associate Professor, Ecole Polytechnique

Acknowledgements

I deeply thank my two advisors, Pr. Tomasz Wierzbicki and Pr. Dirk Mohr, for their guidance and support throughout my stay at MIT in the Impact and Crashworthiness Laboratory. I highly appreciate the trust they granted me and the opportunities they gave me to carry out this thesis work. Their insightful suggestions and valuable feedbacks have had a critical influence on my research.

I am grateful to Professors Lallit Anand and David Parks for their willingness to serve on my thesis committee and to discuss my research, and for their high quality teaching in the area of solid mechanics that provided my with the theoretical background on which is built this work. In addition I would like to thank Dr. Lars Greve from Volkswagen for numerous fruitful discussions.

It has been a pleasure for me to work with the former and current members of the ICL, who created a great and motivating working environment: Dr. Carey Walters, Dr. JongMin Shim, Dr. Allison Beese, Dr. Meng Luo, Dr. Kirki Kofiani, Dr. Elham Sahraei Esfahani, Mr. Stéphane Marcadet, Mr. Kai Wang, Mr. Keunhwan Pack and Mr. Xiaowei Zhang. Special thanks go to Sheila McNary and Barbara Smith who made my life so much easier.

The financial support of my work by the Joint MIT/Industry AHSS Consortium and the Industrial Fracture Consortium is gratefully acknowledged.

Contents

List of figures

List of Tables

Chapter 1

General introduction

Contents

The accurate prediction of ductile fracture plays an important role in the design of lightweight thin-walled metal structures. Most transportation vehicles made from sheet materials are computer engineered in great detail before launching their mass production. In the specific example of automotive structures, both the engineering of the production process and of the final product require reliable models for plasticity and fracture. During the last decade, there has been a growing interest in fracture models that can be used in both sheet metal forming simulations as well as subsequent crash simulations.

1.1 Ductile fracture

Within this thesis, ductile fracture is considered as being the appearance of macroscopic cracks in an initially uncracked material after a significant amount of inelastic deformation. Ductile fracture is the result of a progressive material deterioration occurring during plastic deformation.

1.1.1 Experimental characterization

Numerous experimental investigations have been carried out to characterize ductile fracture. For practical reasons, investigated stress states are often limited to axisymmetric stress states or plane stress states.

Clausing (1970, [39]) performed an experimental study on axisymmetric and plane strain tensile fracture specimens of several materials and found a lower ductility for plane strain loading. Hancock and MacKenzie (1976, [70]) investigated the relationship between the ductility and the stress triaxiality for three different steels. They used smooth and U-notched axisymmetric tensile specimens and concluded that for all studied materials, the ductility is decreasing with stress triaxiality; the same authors also found good agreement between their experimental results and the predictions by Rice and Tracey's (1969, [128]) fracture model. Hancock and Brown (1983, [69]) compared experimental results from notched axisymmetric specimens and flat grooved plane strain specimens and concluded that the ductility was determined by the stress state, and not the strain state. Using split Hopkinson bars, Johnson and Cook (1985, [76]) performed dynamic torsion and notched tensile tests at different strain rates and temperatures. They concluded that the effect of stress triaxiality on the ductility of their tested metals was more significant than that of strain rate and temperature.

Bao (2003, [8]) carried out an extensive experimental program on aluminum 2024-T351 covering stress triaxialities ranging from compression to multi-axial tension, based on a mix of axisymmetric tensions, axisymmetric compression and plane stress condition. Considering stress triaxiality as the only relevant stress state parameter, Bao's results

suggested a transition region between shear and uniaxial tension, where ductility increases with stress triaxiality. Mohr and Henn (2007, [105]) proposed a butterfly-shaped flat specimen to study the onset of fracture over a wide range of stress triaxialities under plane stress condition. When using this specimen in conjunction with a dual actuator system (Mohr and Oswald, 2008, [109]), virtually any loading condition between pure shear and transverse plane strain tension can be imposed.

Reliable experimental results on ductile fracture at low and intermediate stress triaxialities are still difficult to obtain because of significant experimental challenges associated with the proper introduction of loading, the inherent localization deformation at the macroscopic level (necking), and the detection of the onset of fracture (e.g. Bao and Wierzbicki, 2004, [9]; Mohr and Henn, 2007, [105]; Barsoum and Faleskog, 2007, [14]; Brunig et al, 2008, [29]; Fagerholt et al, 2010, [54]; Gao et al, 2011, [58]; Haltom et al, 2013, [68]).

1.1.2 Ductile fracture models

1.1.2.1 Void growth models

Mechanisms responsible for ductile fracture are generally identified as the nucleation and growth of micro-voids that ultimately link to form cracks. The early investigations of McClintock (1968, [101]) and Rice and Tracey (1969, [128]) on the evolution of cylindrical and spherical holes in ductile matrices have set the foundation for numerous studies on the micromechanics associated with void growth. The most prominent is that of Gurson (1977, [66]), who proposed a porous plasticity model based on the micromechanical analysis of a thick spherical shell subject to hydrostatic pressure. The model describes the growth of voids and its influence on the material's stress carrying capacity at large mean stresses (but becomes less accurate for shear loads). The original Gurson model has been repeatedly modified to account for additional processes responsible for the material deterioration and subsequent ductile fracture: void nucleation (e.g. Chu and Needleman, 1980, [38]), loss of load-carrying capacity associated with void coalescence (e.g. Tvergaard and Needleman,

1984, [148]), enhanced strain hardening models (e.g. Leblond et al., 1995, [85]), void shape effects (e.g. Gologanu et al., 1993, [60]; Gologanu et al., 1994, [61]; Garajeu et al., 2000, [59]; Pardoen and Hutchinson, 2000, [123]) and plastic anisotropy (e.g. Benzerga et al., 2004, [20]). The reader is referred to Lassance et al. (2007, [82]) and Benzerga and Leblond (2010, [21]) for a comprehensive review of successive improvements of the Gurson model. Gurson type of models are not only used to describe macroscopic plastic behavior of materials with small void volume fractions, but also to predict ductile fracture assuming that fracture occurs as the void volume fraction reaches a critical value. As a result, "traditional" Gurson models are unable to predict fracture under shear-dominated loading conditions, where the void growth mechanism is inactive. Numerical investigations of an initially spherical void contained in a cubic unit cell submitted to various tri-axial loadings (e.g. Zhang et al., 2001, [157]; Gao and Kim, 2006, [56]) showed that the third stress invariant (or Lode parameter) has a strong influence on void shape evolution and on coalescence. The influence of the third stress invariant on the ductility of metals is also shown experimentally (e.g. Barsoum and Faleskog, 2007, [14]). This particular shortcoming of Gurson models has been addressed by the recent models of Xue (2008, [155]) and Nahshon and Hutchinson (2008, [112]). The latter consider the void volume fraction as damage parameter, and introduce a dependency of the damage evolution on the third stress invariant. This empirical modification has been introduced in an ad-hoc manner to deal with the material deterioration due to void distortion and inter-void linking under shearing. As a result, the Nahshon-Hutchinson model can predict failure under shear-dominated loading, such as during the cutting of sheet metal (Nahshon and Xue, 2009, [113]). However, Nielsen and Tvergaard (2009, [117]) found that this modification is inadequate in the case of high stress triaxialities, compromising the predictive capabilities of the original Gurson model for loading conditions where void growth is the main damage mechanism. Consequently, Nielsen and Tvergaard (2010, [118]) proposed a slight modification of the Nahshon-Hutchinson model, making the damage accumulation under shear-dominated stress states active only for low stress triaxialities. It is noted that these two recent shear-modified Gurson models do not account for the effect of void distortion at large shear strains. Micromechanical models that are able to deal with general ellipsoidal void shape evolution

are still at an early stage of development and require further validation (e.g. Leblond-Gologanu, 2008, [84]).

1.1.2.2 Uncoupled models

As an alternative to Gurson type of models, uncoupled fracture models have been developed for metals where standard incompressible plasticity models are used in conjunction with a separate fracture model (e.g. Fischer et al., 1995, [55]). Unlike in Gurson models, it is assumed that the evolution of damage has no effect on the effective stress-strain response of the material before fracture occurs. Within this framework, damage is measured through the scalar variable D, and its increase $dD \geq 0$ is defined though the increment of the equivalent plastic strain $\bar{\varepsilon}^p$ with respect to a stress-state dependent reference failure strain $\hat{\epsilon}$,

$$\mathrm{dD} = \frac{d\bar{\varepsilon}^p}{\hat{\varepsilon}(\boldsymbol{\sigma})} \tag{1-1}$$

Assuming an initial value of $D = 0$ for the material in its undeformed configuration, it is postulated that fracture initiates as $D = 1$. The reference failure strain may be interpreted as a weighting function and corresponds to the strain to fracture for monotonic proportional loading. It is either chosen empirically or inspired by micromechanical results. A comparative study of various weighting functions (including models based on the work of McClintock (1968, [101]), Rice and Tracey (1969, [128]), LeRoy et al. (1981, [92]), Cockcroft and Latham (1968, [41]), Oh et al. (1979, [119]), Brozzo et al. (1972, [27]), and Clift et al. (1990, [40])) showed that none of them can accurately describe the fracture behavior of a aluminum 2024 over a large range of stress triaxialities (Bao and Wierzbicki, 2004, [9]). Wilkins et al. (1980, [154]) proposed a weighting function depending on the asymmetry of the deviatoric principal stresses in addition to hydrostatic pressure. It was assumed that the effect of hydrostatic pressure and stress asymmetry on ductility were separable. Attempts to define a more general fracture criterion have led to the introduction of the third invariant of the stress tensor in the weighting function (e.g. Wierzbicki and Xue, 2005, [153]). Recently, Bai and Wierzbicki (2010, [5]) transposed the classical Mohr

Coulomb fracture criterion into the space of stress triaxiality, Lode angle and equivalent plastic strain, defining the so-called Modified Mohr-Coulomb (MMC) fracture criterion.

1.1.2.3 Damage mechanics and FLCs

There exist two more widely-used alternatives to the above two modeling approaches: Continuum Damage Mechanics (CDM) and Forming Limit Curves (FLC). In the framework of Continuum Damage Mechanics, material degradation is modeled through an internal damage variable while the constitutive equations are derived from the first and second principles of thermodynamics for continuous media (e.g. Lemaitre, 1985, [91]; Chaboche, 1988, [34, 35]). Most sheet metal forming processes are still designed against failure based on the concept of FLCs. The FLC is typically constructed in the space of the principal in-plane strains based on the experimental results for uniaxial tension and a series of Nakazima tests (e.g. Banabic et al., 2000, [6]). It is then assumed that failure (either necking or fracture) occurs as the strain path in a sheet metal forming operation crosses the FLC. In this approach, it is assumed that the FLC is independent of the loading path. Both the CDM and FLC approach are not considered in the present work and the detailed review of the associated literature is therefore omitted.

1.2 Ductile failure by plastic localization

The localization of plastic deformation within a narrow band is often an important precursor to ductile fracture (e.g. Dunand et al., 2013, [49]). Following the works of Marciniak and Kuczynski (1964, [100]) and Rice (1977, [127]), it is common practice to predict the onset of localization based on macroscopic constitutive theories through infinite band localization analysis (e.g. Mear and Hutchinson, 1985, [102], Duszek and Perzyna, 1991, [52]). As noted by Rice (1977, [127]), the identified onset of localization corresponds to the loss of ellipticity of the governing equilibrium equations. Consequently, onset of localization maps can also be directly computed by assessing the existence of non-positive

eigenvalues of the acoustic tensor (Michel et al., 2007, [103]; Danas and Ponte Castaneda, 2012, [45]).

For most metals, the strains at the onset of localization are very large. As a consequence, the effect of voids on the elasto-plastic moduli, even for very low porosities, needs to be taken into account when computing the instant of the onset of localization. This requires advanced constitutive theories such as the Gurson model (Gurson, 1977, [66]) and its extensions accounting for void nucleation (e.g. Chu and Needleman, 1980, [38]), for the loss of load-carrying capacity associated with void coalescence (e.g. Tvergaard and Needleman, 1984, [148]), for void shape effects (e.g., Gologanu et al., 1993, 1994, [60, 61]; Garajeu et al., 2000, [59]; Pardoen and Hutchinson, 2000, [123]) and for plastic anisotropy (e.g., Benzerga et al., 2004, [20]). As shown by Nahshon and Hutchinson (2008, [112]), additional modifications representing shear softening are necessary to obtain reasonable predictions of strain localization at low stress triaxialities.

Unit cell models provide a computationally-expensive alternative to macroscopic constitutive theories to describe the large deformation response of metals of low porosity. The early analysis with unit cell models was mostly limited to two-dimensional models, e.g. axisymmetric mechanical systems with spheroidal voids (e.g. Koplik and Needleman, 1988, [78]; Brocks et al, 1995, [24]; Pardoen and Hutchinson, 2000, [123]) or plane strain models with cylindrical voids (e.g. Tvergaard, 1981, [144]). Fully three-dimensional models have only been employed rather recently for plane strain conditions (e.g. Scheyvaerts et al., 2011, [131]; Nielsen et al., 2012, [116]; Rahman et al, 2012, [125]) and selected three-dimensional stress states (e.g. Barsoum and Faleskog, 2007, 2011, [13, 15]; Tekoglu, 2012, [141]). Aside from the macroscopic response, unit cell models provide valuable insight in the local deformation fields and allow for the detailed analysis of the void growth and coalescence process (e.g. Scheyvaerts et al., 2011, [131]). As discussed by Pardoen and Hutchinson (2000, [123]), it is useful to define *void growth* as the phase prior to the localization of deformation inside the intervoid ligament, while *void coalescence* describes the deformation process thereafter. Normal localization may be seen as diffuse necking of the ligament, while shear localization is characterized by the development of a shear band at the microscale. Due to the inherent periodicity of microstructures defined through unit cell

models, the *onset of coalescence* corresponds to the *onset of normal and/or shear localization* of plastic flow within a narrow band at the scale of the void.

Substantial efforts have been devoted to the development of micromechanics-based coalescence criteria. The first generation of coalescence criteria (Brown and Embury, 1973, [26]; Thomason, 1985, [142]; Benzerga 2002, [18]) is primarily concerned with the prediction of internal necking as a function of the void shape, relative spacing and the applied maximum normal stress. The effect of shear in addition to normal loads on the coalescence has been addressed recently by Tekoglu et al. (2012, [141]). They demonstrate that the introduction of non-linear parameter functions into the Benzerga model leads to an excellent agreement with their unit cell simulations for combined shear and tension. Furthermore, Tekoglu et al. (2012, [141]) present a micromechanical analysis to come up with an analytical coalescence model for general loading conditions.

Reliable experimental results on ductile fracture at low stress triaxialities are still difficult to obtain because of significant experimental challenges associated with the proper introduction of loading, the inherent localization deformation at the macroscopic level (necking), and the detection of the onset of fracture (e.g. Bao and Wierzbicki, 2004, [9]; Mohr and Henn, 2007, [105]; Brunig et al, 2008, [29]; Fagerholt et al, 2010, [54]; Gao et al, 2011, [58]; Haltom et al, 2013, [68]). Numerical results on localization are therefore of particular value for the development of ductile fracture modes at low stress triaxialities. Tvergaard (2008, 2009, [145, 146]) analyzed the behavior of a row of circular cylindrical holes under shear loading. He reports the formation of rotating micro-cracks as the result of void closure at low stress triaxialities. Furthermore, he points out that a maximum in the macroscopic shear stress accompanies the onset of localization of plastic flow. Nielsen et al. (2012, [116]) confirmed these observations using a three-dimensional unit cell model. In his most recent work, Tvergaard (2012, [147]) considered a square unit cell with a cylindrical void and fully periodic boundary conditions. By varying the normal stress during shearing, he found that increasing the stress triaxiality facilitates failure through shear localization.

Barsoum and Faleskog (2007, [13]) performed a micromechanical analysis on three-dimensional unit cells with spherical voids for combined tension and shear loading. Their model represents a layer of preexisting voids in a Levy-von Mises material; it features a

height to width ratio of 2:1 along with periodic boundary conditions on all three pairs of parallel boundaries. Using a kinematic condition comparing the deformation gradient rate inside and outside a band of localization (as proposed by Needleman and Tvergaard, 1992, [115]), they define the onset of shear localization and report the corresponding macroscopic von Mises equivalent strain as strain to failure (due to localization). Their simulation results for a constant stress triaxiality of 1.0 elucidate the effect of the Lode parameter on shear localization for stress states between generalized shear and axisymmetric tension. Their computational results also agree well with the observations from experiments where coalescence occurred by internal necking (triaxiality above 0.7). However, for low stress triaxialities and stress states closer to generalized shear, the macroscopic strains to failure predicted by the unit cell model are significantly higher than those found experimentally.

Gao et al. (2010, [57]) applied macroscopic normal stresses along the symmetry axes of a cubic unit cell with a spherical void and boundaries that remain flat and perpendicular throughout deformation. Assuming that void coalescence occurs when the macroscopic strain state shifts to a uniaxial strain state, they computed the corresponding macroscopic effective strain as a function of the stress triaxiality (ranging from 0.33 to 2) and of the Lode angle. Their results indicate that the macroscopic strain to coalescence increases monotonically as a function of the Lode angle from axisymmetric tension to axisymmetric compression. Furthermore, their simulations indicate that this Lode angle effect on coalescence becomes more pronounced at low stress triaxialities. They also show that the effective strain to coalescence decreases when assuming a Gurson instead of a Levy-von Mises matrix.

More recently, Barsoum and Faleskog (2011, [15]) made use of their unit cell model to investigate the localization of deformation into a narrow planar band different from the plane of normal stress axisymmetry and for a wider range of stress states. Irrespective of the stress state, they observe the lowest macroscopic effective strain to localization for bands oriented at an angle of about 45° with respect to the direction of the minimum principal macroscopic stress. The computed localization loci for stress triaxialities ranging from 0.75 to 2 show the lowest strains to localization for generalized shear. The loci are approximately

symmetric with respect to the Lode parameter, showing slightly higher localization strains for axisymmetric compression than axisymmetric tension.

1.3 Thesis outline and objectives

This thesis is a comprehensive investigation on the onset of ductile failure in initially uncracked Advanced High Strength Steel (AHSS) sheets. The two main objectives of this work consist in characterizing and modeling the effect of stress state on the onset of ductile fracture of a representative AHSS under positive stress triaxialities. Investigations are limited to room temperature and low strain rate loading conditions. A possible anisotropy of the fracture properties is disregarded.

Experimental procedures are developed to investigate fracture of sheet materials for stress states ranging from pure shear to equi-biaxial tension. A hybrid experimental-numerical method is used to evaluate the evolution of strains and stresses within the specimen during loading and the material state at the onset of fracture. This approach permits to account for complex specimen geometries and through-the-thickness localization of deformation that occurs before failure in most ductile fracture experiments on sheet specimens. A key component of this hybrid experimental-numerical approach is the constitutive model. The proposed plasticity model, built upon a non-associated flow rule, is validated over a wide range of loading conditions and large strains. The extensive experimental work is used to perform a critical evaluation the predictive capabilities of two state-of-the-art ductile fracture models: the shear-modified Gurson model (Nielsen and Tvergaard, 2010, [118]) and the Modified Mohr-Coulomb (MMC) fracture model (Bai and Wierzbicki, 2010, [5]). Finally, and considering that plastic localization at the micro-scale is an important precursor to ductile fracture, a numerical model based on three-dimensional unit cell is built to investigate the effect of stress state on the onset of plastic localization into a narrow planar band in a void-containing material. An analytical criterion is proposed to relate the onset of plastic localization to the normal and shear stresses acting on the plane of localization.

The Thesis is decomposed in seven chapters. Each chapter, apart from Chapter 1 and Chapter 7, addresses one specific topic and corresponds to a peer-reviewed publication. A list of publications related to the present thesis is given in Appendix A.

Chapter 2 is focused on the experimental characterization and phenomenological modeling of the plasticity of AHSS sheets under multi-axial monotonic loading conditions. The accuracy of quadratic plane stress plasticity models is evaluated for a dual phase and a TRIP-assisted steel. Both sheet materials exhibit a considerable direction-dependence of the r-ratio while the uniaxial stress-strain curves are approximately the same irrespective of the specimen direction. Isotropic and anisotropic associated as well as non-associated quadratic plasticity models are considered to describe this behavior. Using a newly-developed dual-actuator system, combinations of normal and tangential loads are applied to a flat specimen in order to characterize the sheet material response under more than 20 distinct multi-axial loading states. The comparison of the experimental results with the plasticity model predictions reveals that both the associated and non-associated quadratic formulations provide good estimates of the stress-strain response under multi-axial loading. However, the non-associated model is recommended when an accurate description of the thinning behavior is important. Moreover, a structural validation example is presented that demonstrates the higher prediction accuracy of the non-associated plasticity model.

In Chapter 3, a basic ductile fracture testing program is carried out on specimens extracted from TRIP780 steel sheets including tensile specimens with a central hole and circular notches. In addition, equi-biaxial punch tests are performed. The surface strain fields are measured using two- and three-dimensional digital image correlation. Due to the localization of plastic deformation during the testing of the tensile specimens, finite element simulations are performed of each test to obtain the stress and strain histories at the material point where fracture initiates. Error estimates are made based on the differences between the predicted and measured local strains. The results from the testing of tensile specimens with a central hole as well as from punch tests show that equivalent strains of more than 0.8 can be achieved at approximately constant stress triaxialities to fracture of about 0.3 and 0.66, respectively. The error analysis demonstrates that both the equivalent plastic strain and the stress triaxiality are very sensitive to uncertainties in the experimental measurements and the

numerical model assumptions. The results from computations with very fine solid element meshes agree well with the experiments when the strain hardening is identified from experiments up to very large strains.

Chapter 4 is concerned with multi-axial ductile fracture experiments on sheet metals. Different stress-states are achieved within a flat specimen by applying different combinations of normal and transverse loads to the specimen boundaries. The specimen geometry is optimized such that fracture initiates remote from the free specimen boundaries. Fracture experiments are carried out on TRIP780 steel for four different loading conditions, varying from pure shear to transverse plane strain tension. Hybrid experimental-numerical analyses are performed to determine the stress and strain fields within the specimen gage section. The results show that strain localization cannot be avoided prior to the onset of fracture. Through-thickness necking prevails under tension-dominated loading while the deformation localizes along a band crossing the entire gage section under shear-dominated loading. Both experimental and simulation results demonstrate that the proposed fracture testing method is very sensitive to imperfections in the specimen machining. The loading paths to fracture are determined in terms of stress triaxiality, Lode angle parameter and equivalent plastic strain. The experimental data indicates that the relationship between the stress triaxiality and the equivalent plastic strain at the onset of ductile fracture is not unique.

In Chapter 5, the predictive capabilities of the shear-modified Gurson model (Nielsen and Tvergaard, 2010, [118]) and the Modified Mohr-Coulomb (MMC) fracture model (Bai and Wierzbicki, 2010, [5]) are evaluated. Both phenomenological fracture models are physics-inspired and take the effect of the first and third stress tensor invariants into account in predicting the onset of ductile fracture. The MMC model is based on the assumption that the initiation of fracture is determined by a critical stress state, while the shear-modified Gurson model assumes void growth as the governing mechanism. Fracture experiments on TRIP-assisted steel sheets covering a wide range of stress states (from shear to equibiaxial tension) are used to calibrate and validate these models. The model accuracy is quantified based on the predictions of the displacement to fracture for experiments which have not been used for calibration. It is found that the MMC model predictions agree well with all experiments (less than 4% error), while less accurate predictions are observed for the shear-

modified Gurson model. A comparison of plots of the strain to fracture as a function of the stress triaxiality and the normalized third invariant reveals significant differences between the two models except within the vicinity of stress states that have been used for calibration.

In Chapter 6, the effect of the stress state on the localization of plastic flow in a Levy-von Mises material is investigated numerically. A unit cell model is built with a spherical central void that acts as a defect triggering the onset of flow localization along a narrow band. Periodic boundary conditions are defined along all boundaries of the unit cell. Shear and normal loading is applied such that the macroscopic stress triaxiality and Lode parameter remain constant throughout the entire loading history. Due to the initially orthogonal symmetry of the unit cell model the deformation-induced anisotropy associated with void shape changes, both co-rotational and radial loading paths are considered. The simulation results demonstrate that the macroscopic equivalent plastic strain at the onset of localization decreases in stress triaxiality and is a convex, non-symmetric function of the Lode parameter. In addition to predicting the onset of localization through unit cell analysis, an analytical criterion is proposed which defines an open convex envelope in terms of the shear and normal stresses acting on the plane of localization.

1.4 Material

1.4.1 TRIP780 steel

All the experimental work presented in this manuscript is performed on specimens extracted from 1.4mm thick TRIP780 steel sheets provided by POSCO (Korea). The chemical composition of the present TRIP780 material as measured by energy-dispersive X-ray analysis is given in Table 1-1. Micrographs (Fig. 1-1) reveal a fine grain structure with a maximum grain size of about $10\mu m$ and show that martensite and austenite grains (in blue/brown in Fig. 1-1) tend to segregate in bands parallel to the sheet rolling direction.

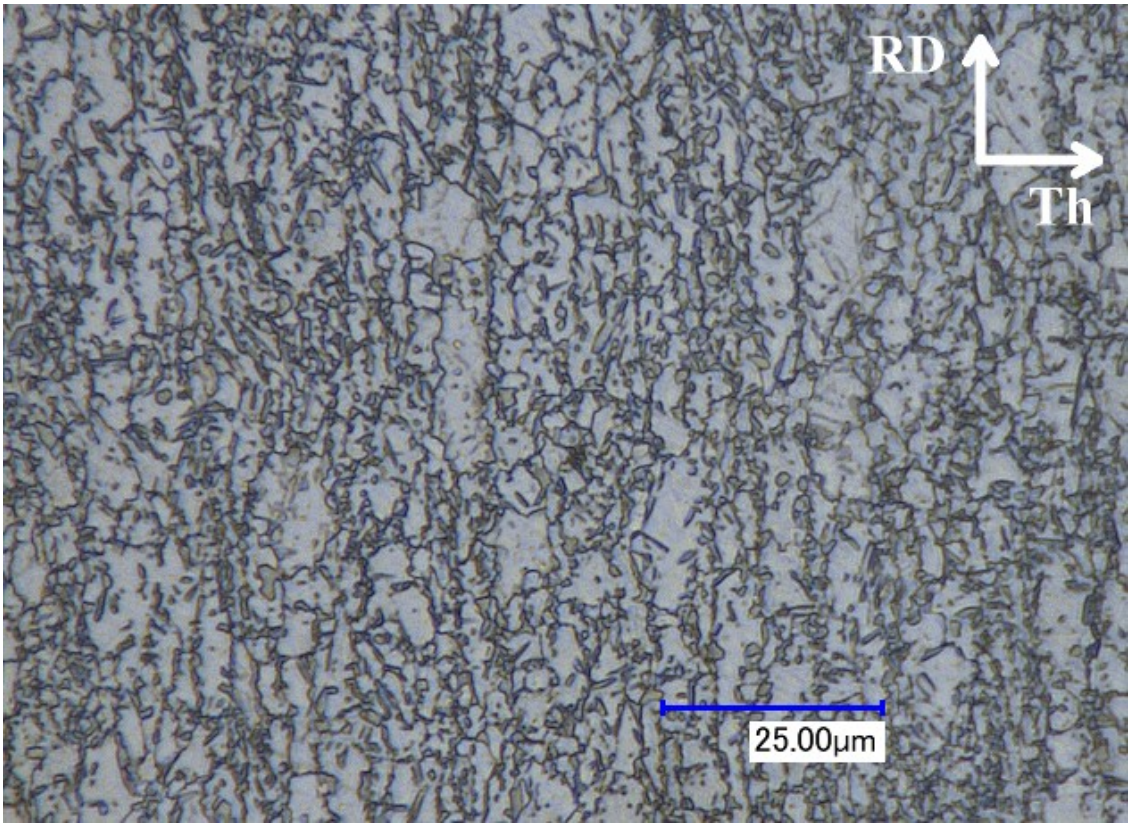

Figure 1-1: Optical micrograph of the undeformed TRIP material. The *RD* and *Th* orientations correspond to the sheet rolling and through-the-thickness directions, respectively.

TRansformation Induced Plasticity (TRIP) steels present complex multi-phase microstructures consisting of a ferritic matrix and a dispersion of multiphase grains of bainite, martensite and metastable retained austenite (Jacques et al., 2001, [75]). The austenitic phase transforms to martensite when subject to mechanical or thermal loading (e.g. Angel, 1954, [2]; Lecroisey and Pineau, 1972, [86]; Olsen and Cohen, 1975, [120]; Stringfellow et al., 1992, [137]). The austenite-to-martensite formation is displacive which gives rise to internal stresses that may cause the yielding of the surrounding austenite matrix (e.g. Greenwood and Johnson, 1965, [65]). The active formation of martensite substantially increases the macroscopic work-hardening rate while the associated transformation strain contributes to the ductility of TRIP steels.

Table 1-1: Chemical composition of the TRIP780 material in wt-%

C	Al	Mn	Si	Mo
1.70	0.47	2.50	0.59	0.08

1.4.2 Plasticity of AHSS

From a mechanical point of view, TRIP-assisted and DP steels may be considered as composite material at the micro-scale. Papatriantafillou et al. (2006, [122]) made use of homogenization techniques for nonlinear composites (e.g. Ponte Castaneda, 1992, [124]) to estimate the effective properties of TRIP-assisted steels. Based on the work by Stringfellow et al. (1992, [137]) for fully austenitic TRIP steels, Papatriantafillou et al. (2006, [122]) formulated the computational procedure for a four phase metallic composite with evolving phase volume fractions and isotropic viscoplastic phase behavior. Turteltaub and Suiker (2005, [143]) presented a more detailed multi-scale model for TRIP-assisted steels which includes anisotropic features associated with the phase crystal orientations and the martensite twinning. A mean-field model which describes DP steels as a composite of isotropic elasto-plastic phases with spherical inclusions has been proposed by Delannay et al. (2007, [47]). This model has been enhanced further to TRIP-assisted steels (Delannay et al., 2008, [48]) using the assumption that spherical austenite inclusions transform instantaneously into spherical martensite inclusions. Based on the intermediate strain rate tensile testing of TRIP600 and DP600 steels, Huh et al. (2008, [74]) conclude that both the flow and ultimate tensile strength increase as the level of pre-strain increases.

Most AHSS exhibit a pronounced Bauschinger effect. Banu et al. (2006, [7]) adopted an isotropic Swift law combined with saturated kinematic hardening of the Amstrong-Frederick type to model a series of Bauschinger simple shear tests on a DP600 steel. The accurate modeling of the cyclic behavior of AHSS is important in drawing operations where the sheet material is both bent and unbent. Using a stack of laminated dogbone specimens

along with an anti-buckling device, Yoshida et al. (2002, [156]) measured the response of a DP590 steel under cyclic uniaxial tension-compression loading at large strains. Their study shows that the combination of isotropic, non-linear kinematic and linear kinematic hardening provides a satisfactory model for the observed transient and permanent softening in the dual phase steel. As Yoshida et al. (2002, [156]), Lee et al. (2005, [89]) emphasize the importance of an accurate description of the Bauschinger and transient behavior in view of springback computations. Based on the comparison of uniaxial experiments on a DP steel and simulations, Lee et al. (2005, [89]) concluded that a modified Chaboche type combined isotropic-kinematic hardening law provides a good representation of the Bauschinger and transient behavior. However, a recent study by Tarigopula et al. (2008, [140]) on a DP800 steel demonstrated that the modeling of transient anisotropy in plastic flow induced by strain-path changes cannot be represented correctly when using a non-linear combined isotropic-kinematic hardening model. Broggiato et al. (2008, [25]) performed 3-point-bending tests on two DP600 and a TRIP700 steel. Their results show that the cyclic hardening behavior of both steel grades is very similar and can be modeled using a non-linear combined isotropic-kinematic hardening model. Using a double-wedge device, Cao et al. (2008, [32]) performed uni-axial tension-compression tests on 1.6mm thick DP600 steel. They modeled their experiments using using a modified Chaboche type combined isotropic-kinematic hardening law (with permanent softening and non-symmetric reloading) as well as the two-surface model by Lee et al. (2007, [88]).

The dynamic testing of TRIP steels is of particular interest because of the temperature sensitivity of the austenite-to-martensite transformation. Extrapolating from the results on temperature-dependence of fully austenitic stainless steels (e.g. Olsen and Cohen, 1975, [120]), it may be expected that phase transformation in TRIP-assisted steels will cease as the temperature rises due to adiabatic heating. However, despite the smaller amount of martensite being formed at high strain rates, the experiments by Wei et al. (2007, [152]) on a cold-rolled TRIP steel suggest an increase of both the initial yield and tensile strength with increasing strain rate. The observation is also supported by the high strain rate experiments of Durrenberger et al. (2007, 2008, [50, 51]) on TRIP700 and TRIP800 steels. Furthermore, Durrenberger et al. (2007, [50]) proposed a single internal parameter model to describe the

BCC-like strain rate history effect in a DP600 and TRIP700 steel and the FCC-like effect in a TRIP800 steel. Rusinek and Kelpaczko (2008, [130]) investigated the effect of heating during the mechanical testing and reported that the stored energy in TRIP steels is affected by phase transformation.

1.5 Characterization of the stress state

1.5.1 Stress invariants

Throughout our discussion, a clear description of the stress state is important. The frame invariant part of the stress is described through the first invariant of the Cauchy stress tensor $\boldsymbol{\sigma}$, and the second and third invariants of the corresponding deviatoric stress tensor, $\boldsymbol{s} = \boldsymbol{\sigma} - (\mathrm{tr}\boldsymbol{\sigma}/3)\mathbf{1}$,

$$I_1 = \mathrm{tr}(\boldsymbol{\sigma}) \tag{1-2}$$

$$J_2 = \sqrt{\frac{1}{2}\boldsymbol{s}:\boldsymbol{s}} \tag{1-3}$$

and

$$J_3 = \det(\boldsymbol{s}) \tag{1-4}$$

Note that the hydrostatic stress σ_m and the von Mises equivalent stress $\bar{\sigma}$ are respectively proportional to the first and second invariants,

$$\sigma_m = \frac{1}{3} I_1 \tag{1-5}$$

$$\bar{\sigma} = \sqrt{3}\, J_2 \tag{1-6}$$

The stress state may be characterized through two dimensionless functions of the above invariants. We define the stress triaxiality η as the ratio of the mean stress and equivalent von Mises stress,

$$\eta = \frac{\sigma_m}{\sigma_{VM}} = \frac{\mathrm{I}_1}{3\sqrt{3J_2}} \tag{1-7}$$

with $-\infty \leq \eta \leq \infty$. The normalized third invariant ξ is written as

$$\xi = \frac{27}{2}\frac{J_3}{{\sigma_{VM}}^3} = \frac{3\sqrt{3}}{2}\frac{J_3}{{J_2}^{\frac{3}{2}}} \tag{1-8}$$

and lies in the range $-1 \leq \xi \leq 1$; it characterizes the position of the second principal stress σ_{II} with respect to the maximum and minimum principal stresses σ_I and σ_{III}.

Alternatively the third invariant can be described in terms of the so-called Lode angle parameter

$$\bar{\theta} = 1 - \frac{2}{\pi}\arccos(\xi) \tag{1-9}$$

According to the definition above, the Lode angle parameter approximates the negative Lode number μ (Lode, 1925, [95]),

$$\mu = 2\frac{\sigma_{II} - \sigma_{III}}{\sigma_I - \sigma_{III}} - 1 \cong -\bar{\theta} \tag{1-10}$$

As compared to the original Lode number, it has the advantage of being independent of I_1 and thus being perpendicular to the coordinate η.

Note that the principal stresses Σ_I, Σ_{II} and Σ_{III} are got back using

$$\sigma_I = \bar{\sigma}[\eta + f_I(\bar{\theta})] \tag{1-11}$$

$$\sigma_{II} = \bar{\sigma}[\eta + f_{II}(\bar{\theta})] \tag{1-12}$$

$$\sigma_{III} = \bar{\sigma}[\eta + f_{III}(\bar{\theta})] \tag{1-13}$$

with the deviator dependent functions

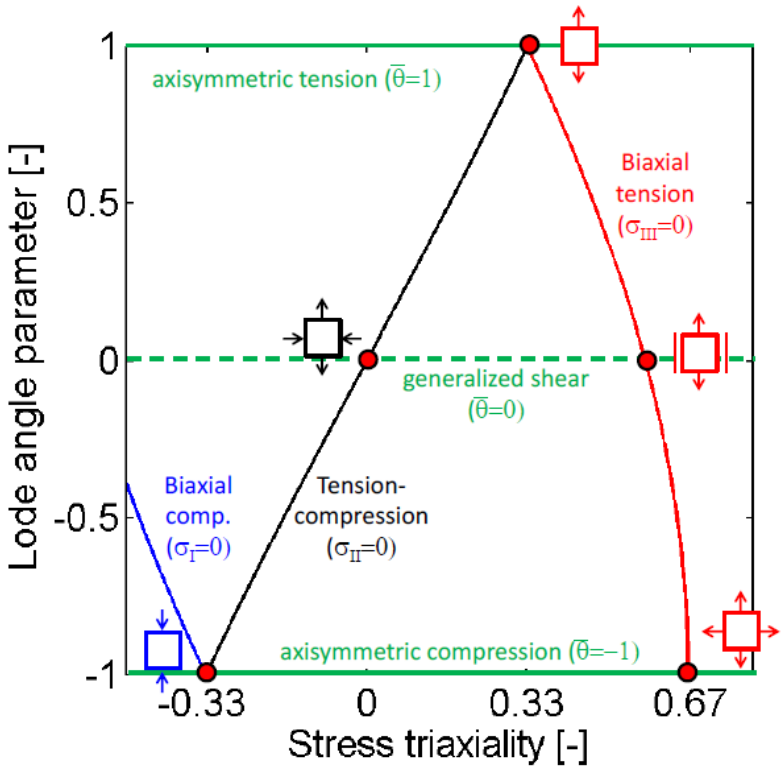

Figure 1-2: Characterization of the stress states in terms of stress triaxiality and Lode angle parameter. The blue, black and red lines highlight the plane stress states as described by Eq. (1-18).

$$f_I(\bar{\theta}) = \frac{2}{3}\cos\left(\frac{\pi}{6}(1-\bar{\theta})\right) \tag{1-14}$$

$$f_{II}(\bar{\theta}) = \frac{2}{3}\cos\left(\frac{\pi}{6}(3+\bar{\theta})\right) \tag{1-15}$$

$$f_{III}(\bar{\theta}) = -\frac{2}{3}\cos\left(\frac{\pi}{6}(1+\bar{\theta})\right) \tag{1-16}$$

Throughout this manuscript, the term stress state is employed to make reference to the pair of parameters $(\eta, \bar{\theta})$. Well-known stress states that we will refer to frequently are:

- Uniaxial tension $(\eta = 0.33, \bar{\theta} = 1)$

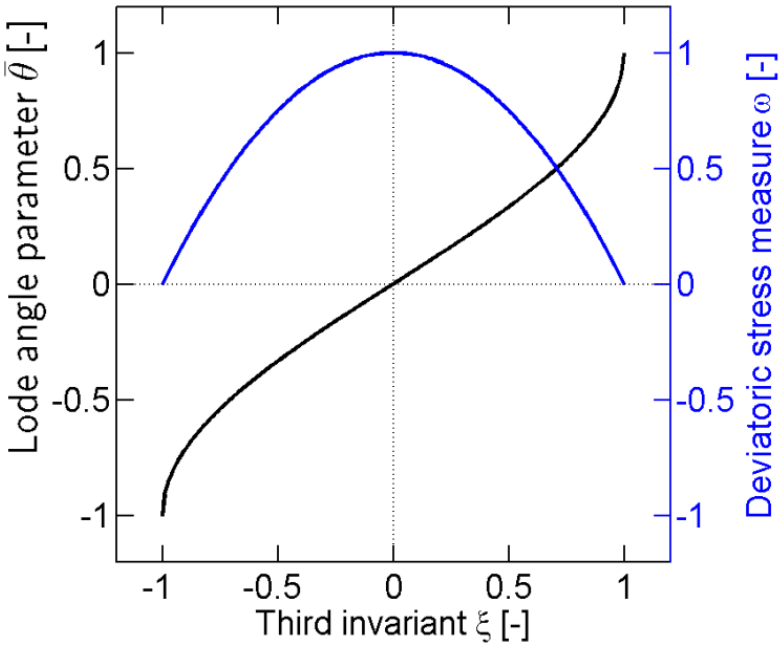

Figure 1-3: Relation between the normalized third stress invariant ξ, the Lode angle parameter $\bar{\theta}$ and the deviatoric stress measure ω.

- Pure shear ($\eta = 0., \bar{\theta} = 0$)
- Generalized shear ($\bar{\theta} = 0$)
- Axisymmetric tension ($\bar{\theta} = 1$)
- Axisymmetric compression ($\bar{\theta} = -1$)

A representation of the $(\eta, \bar{\theta})$ stress state space is depicted in Fig. 1-2.

Note that the shear-modeified Gurson model (Chapter 5) is not formulated in terms of the normalized third invariant or Lode angle parameter but makes use of a non-dimensional metric ω,

$$\omega = 1 - \xi^2 \tag{1-17}$$

with $0 \leq \omega \leq 1$. The relation between the normalized third invariant ξ, the Lode angle parameter $\bar{\theta}$ and ω is depicted in Fig. 1-3. Note that ω is an even function of ξ and therefore

does not differentiate between stress states with opposite third invariants. For example, axisymmetric stress states with two equal minor principal stresses (e.g. uniaxial tension) and two equal major principal stresses (e.g. equibiaxial tension) both feature $\omega = 0$.

1.5.2 Plane stress condition

In sheet materials, the plane stress condition often prevails: one of the principal stress direction is parallel to the sheet thickness direction and the corresponding principal stress is equal to zero.

In case of plane stress, the stress triaxiality η and the normalized third invariant ξ are uniquely related according to the relationship

$$\xi = -\frac{27}{2}\eta\left(\eta^2 - \frac{1}{3}\right) \quad \text{for} \quad -\frac{2}{3} \leq \eta \leq \frac{2}{3} \tag{1-18}$$

In this investigation we focus more specifically on stress states in the vicinity of biaxial tension, i.e. plane stress states between uniaxial tension and equi-biaxial tension. In this case the stress triaxiality varies between 1/3 (uniaxial tension) and 2/3 (equi-biaxial tension). At the same time, the third invariant decreases from 1 (uniaxial tension) to -1 (equi-biaxial tension).

Chapter 2

Non-associated plasticity model for AHSS

Contents

[1] This Chapter is reproduced from: Mohr, D., M. Dunand, and K.H. Kim (2010). "Evaluation of associated and non-associated quadratic plasticity models for advanced high strength steel sheets under multi-axial loading". International Journal of Plasticity **26**(7): p. 939-956.

2.1 Introduction

In this Chapter, we investigate the large deformation behavior of a DP590 and TRIP780 steel under monotonic multi-axial loading. The key purpose of this study is to evaluate existing phenomenological plasticity models for sheet materials. The reader is referred to Chaboche (2008, [36]) for a recent review of macroscopic plasticity theories. Different yield surfaces have been used in the past to model advanced high strength steels: von Mises yield surface (e.g. Yoshida et al., 2002, [156]; Durrenberger et al., 2007, [50]), quadratic anisotropic Hill (1948, [73]) yield function (e.g. Banu et al., 2006, [7]; Padmanabhan et al., 2007, [121]; Broggiato et al., 2007, [25]; Chen and Koc, 2007, [37]), high exponent isotropic Hershey (1954, [72]) yield function (Tarigopula et al., 2008, [140]), non-quadratic anisotropic Barlat (2003, [10]) yield function (Lee et al., 2005, 2008, [89, 90]). Here, we focus on simple quadratic yield functions and evaluate their predictive capabilities for multi-axial loading conditions. Moreover, following the work by Stoughton (2002, [134]), we include both associated and non-associated quadratic flow rules. The discussion of non-associated formulations in metal plasticity has been partially initiated by the experimental observations of Spitzig and Richmond (1984, [133]). Non-associated plasticity models for metals have been considered by Casey and Sullivan (1985, [33]), Brünig and Obrecht (1998, [30]), Brünig (1999, [28]), Lademo et al. (1999, [81]), Stoughton (2002, [134]), Stoughton and Yoon (2004, 2008, [42, 135, 136]) and Cvitanic et al. (2008).

Kuwabara (2007, [79]) provides a comprehensive review of experimental techniques measuring the anisotropic behavior of sheet materials. As an alternative to the testing of cruciform specimens (e.g. Makinde et al., 1992, [98]; Boehler et al., 1994, [23]; Lin and Ding, 1995, [93]; Müller and Pöhlandt, 1996, [111]; Kuwabara et al., 1998, [80]), we make use of a newly-developed combined tension and shear technique (Mohr and Oswald, 2008, [109]). Similar to the experimental work reported in Wang et al. (2008, [151]), the technique of Oswald and Mohr (2008, [109]) achieves multi-axial stress-states through the application of normal and tangential loads to a rectangular sheet specimen. The DP590 and TRIP780 sheet materials are each loaded monotonically along more than 20 different multi-axial loading paths. The comparison of the simulation and experimental results suggests that the

use of Hill's (1948, [73]) quadratic anisotropic yield surface along with a non-associated flow rule provides satisfactory results from a phenomenological point of view.

2.2 Experiments

2.2.1 Material

In addition, to the TRIP780 steel described in Section 1.5, experiments described thereafter have also been performed on a 2.3mm thick DP590 provided by POSCO (Korea). This Dual-Phase steel is composed of a ferrite matrix with martensite inclusions (Fig. 2-1). The chemical composition of the DP steel is given in Table 2-1.

Table 2-1: Chemical composition of the DP590 material in wt-%

C	Mn	Si	Mo
~ 0.08	~ 1.5	~ 0.8	~ 0.08

2.2.2 Uniaxial experiments

Dogbone-shaped tensile specimens are cut from the sheet materials using a waterjet. In accordance with ASTM E8 [3], the specimens featured a 12.7mm wide and 50mm long gage section. The specimens have been placed into an electro-mechanical universal testing machine with wedge grips (Model G45, MTS, Eden-Prarie). All experiments have been carried out at a cross-head loading velocity of less than 1mm/min. Both the axial and width strain are continuously measured using a digital image correlation system (VIC2D, Correlated Solution, SC). For this, a random speckle pattern with an average speckle size of about 10μm has been applied to the specimen gage section.

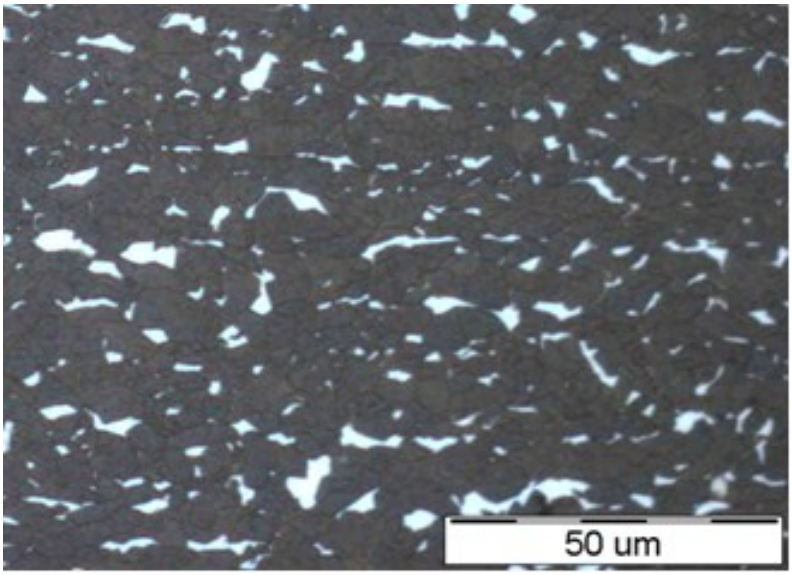

Figure 2-1: Micrographs showing the different phases in the undeformed microstructures of the DP590 steel (white=martensite, dark=ferrite).

In the case of the DP590 steel, tensile specimens are cut from three different directions: $\alpha = 0°$ (rolling direction), $\alpha = 45°$ and $\alpha = 90°$ (transverse direction). The corresponding uniaxial engineering stress-strain curves are plotted in Fig. 2-2a up to their respective stress maximum. The results show that except for a short plateau at the beginning of the experiment along the rolling direction, all stress-strain curves lie almost on top of each other. The maximum engineering stress is 630MPa for $\alpha = 0°$ and 620MPa for the other directions. Tensile specimens are cut every 15° from the TRIP780 sheet. The second group of curves in Fig. 2-2a shows only the results for $\alpha = 0°$, $\alpha = 45°$ and $\alpha = 90°$ since nearly the same stress-strain response is measured irrespective of the specimen orientation. The maximum differences in the stress level of up to 5% are observed at the very beginning of plastic deformation. The engineering stress at necking is about 850MPa for the TRIP780 steel specimens.

Using a Young's modulus of $E = 185GPa$ $(190GPa)$ and an elastic Poisson's ratio of $\nu = 0.3$, we calculated the logarithmic plastic axial and width strains from the measured TRIP (DP590) stress-strain curves. Assuming plastic incompressibility, the plastic thickness

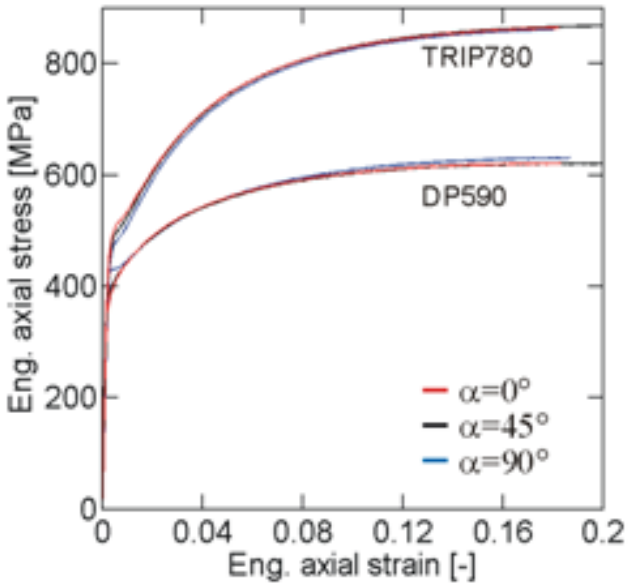

(a)

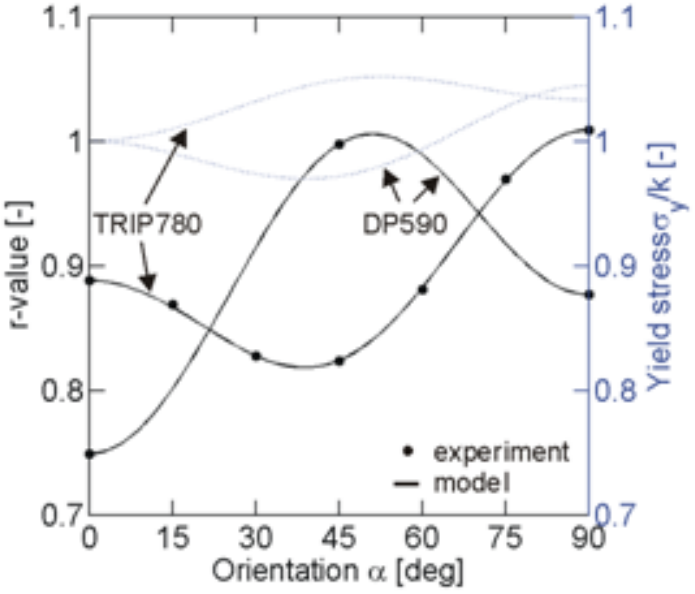

(b)

Figure 2-2: Results from uniaxial tensile testing of the DP590 and TRIP780 : (a) engineering stress-strain curves; (b) calculated and measured r-ratio variations (black curves and solid dots, respectively) and calculated yield stress variations (dotted blue curves).

strain is determined from the measured axial and width strain. The r-values are then determined from the slopes of the corresponding linear approximation of the logarithmic plastic width strain versus logarithmic plastic thickness strain curves ($r = d\varepsilon_w^p / d\varepsilon_{th}^p$). The solid dots in Fig. 2-2b show the identified r-values as a function of the specimen orientation angle α. The average r-value, $\bar{r}$, defined as

$$\bar{r} = \frac{1}{4}(r_0 + 2r_{45} + r_{90}) \tag{2-1}$$

is 0.91 for the DP590 and 0.89 for the TRIP780 steel.

2.2.3 Biaxial experiments

2.2.3.1 Biaxial testing technique

A series of biaxial experiments is performed using a newly-developed dual actuator system. The reader is refereed to Mohr and Oswald (2008, [109]) for details on the multi-axial testing procedure. The dual actuator system applies tangential and normal loads to the boundaries of a flat specimen. The horizontal actuator applies the tangential force to the lower specimen boundary. As shown in Fig. 2-3, the lower specimen clamp is mounted onto a low friction sliding table. A load cell positioned between the horizontal actuator and the lower specimen clamp measures the tangential force. The normal force is applied through the vertical actuator in the upper cross-head. Two additional load cells have been integrated into the lower sliding table to measure the total vertical force. For all tests, the hydraulic dual actuator system is run in the force-controlled mode.

Figure 2-4 shows the exact shape and dimensions of the specimen. It features a $h = 4.5mm$ high and $w = 50mm$ wide gage section. The thickness of the gage section has been symmetrically reduced to about $t = 0.5mm$ using a conventional milling process. The displacements are measured directly on the specimen surface using a digital image correlation system (VIC2D, Correlated Solutions Inc, SC). More than 200 photographs are

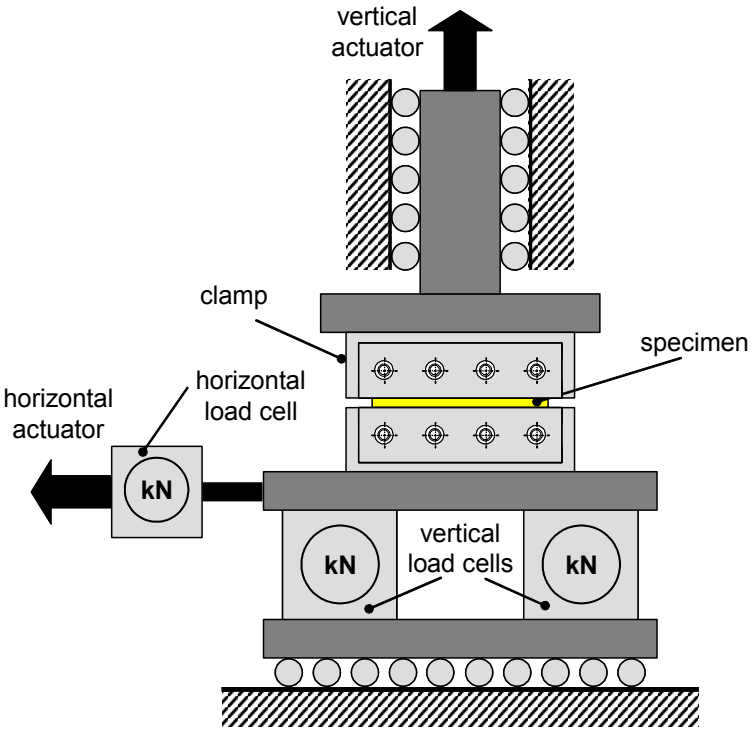

Figure 2-3: Schematic of the dual actuator system

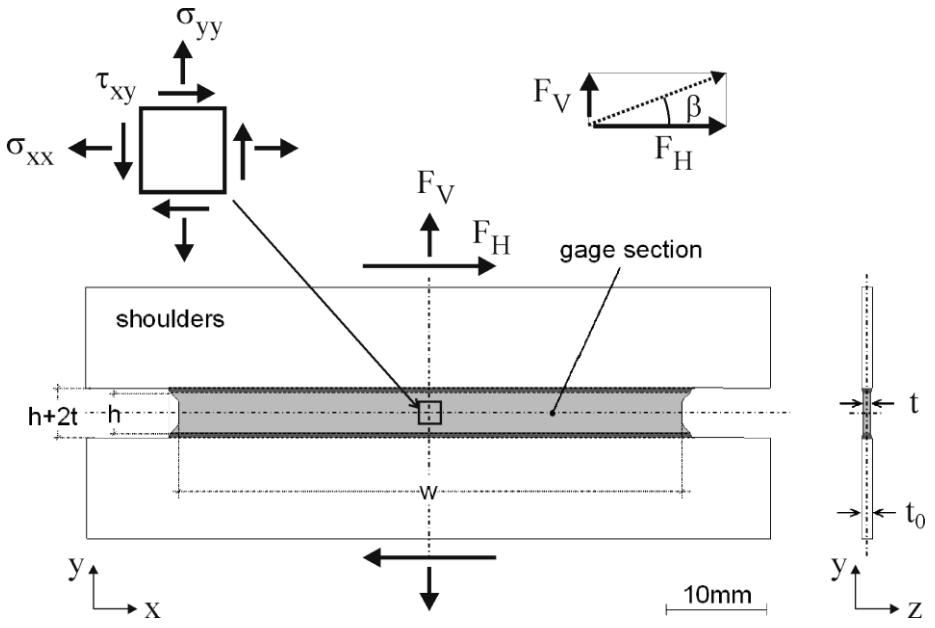

Figure 2-4: Specimen geometry and the definition of the biaxial loading angle β

taken throughout each monotonic experiment. The data is acquired using the software packages FastTrack DAX (Instron, Canton, MA) and VicSnap (Correlated Solution, SC).

The experimental technique allows for the testing of the sheet material for different combinations of normal and shear loading. As illustrated in Fig. 2-4, we define the so-called *biaxial loading angle* β, $0° \leq \beta \leq 90°$, to quantify the ratio of normal to shear loads,

$$\tan\beta \equiv \frac{F_V}{F_H} \tag{2-2}$$

The limiting cases of $\beta = 0°$ and $\beta = 90°$ correspond to pure shear and transverse plane strain tension, respectively. In the case of orthotropic sheet materials, we introduce the *specimen orientation angle* α to report the orientation of the sheet rolling direction with respect to the vertical axis of the dual actuator system. We refer to the horizontal and vertical axis as the x- and y-direction, respectively.

As demonstrated by Mohr and Oswald (2008, [109]), the specimen is designed such that the engineering stress along the y-direction, Σ_y, may be approximated by

$$\Sigma_y \cong \frac{F_V}{A_0} \tag{2-3}$$

with the initial cross-sectional area of $A_0 = wt$. Equation (2-3) implies that the variations of the stress Σ_y are negligible along the x-direction. Similarly, due to the large width-to-height ratio, we may assume that the shear stress variations along the x-direction are small. Hence, the engineering shear stress Σ_{xy} associated with the horizontal force measurement F_H reads

$$\Sigma_{xy} \cong \frac{F_H}{A_0} \tag{2-4}$$

The corresponding engineering normal strain E_y and engineering shear strain E_{xy} are determined from DIC. The state of stress in the specimen gage section is plane stress, while the state of deformation in this specimen is transverse plane strain. In other words, the strain along the x-direction is approximately zero, $E_{xx} \cong 0$. In order to study distinct features of the material's constitutive response, it may be useful to map the measured stresses and

strains into a coordinate system which is attached to the material's orthotropy axes (see Mohr and Jacquemin, 2008, [106]). However, the present work focuses on the validation of existing constitutive models which may be readily performed in the machine coordinate system.

2.2.3.2 Biaxial testing program

Biaxial tests are performed over a wide range of loading conditions by varying the biaxial loading angle β as well as by cutting the specimens at different angles α relative to the rolling direction. Three different batches of specimen have been extracted along three

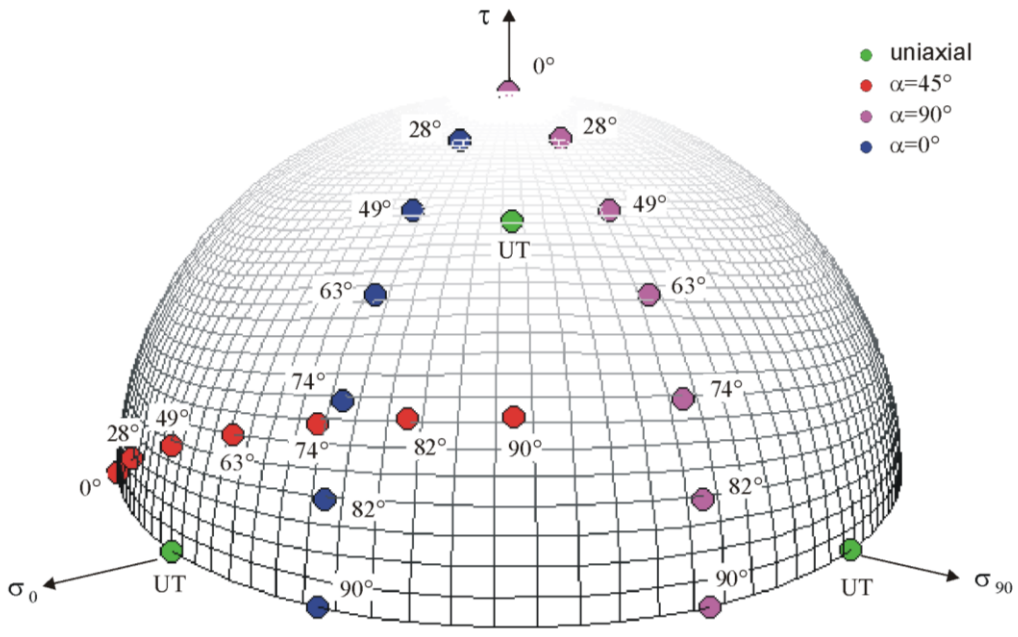

Figure 2-5: Visualization of the loading states in the 3-dimensional stress-space. The solid dots represent the intersection of the linear stress paths with a quadratic yield surface. The labels next to the data points denote the biaxial loading angle β while the point color corresponds to the specimen orientation α (see legend). The green dots correspond to uniaxial tension (UT).

different sheet directions ($\alpha = 0°$, $\alpha = 45°$,$\alpha = 90°$) and subsequently tested at the following biaxial loading angles: $\beta = 0°$, $\beta = 28°$, $\beta = 49°$, $\beta = 63°$, $\beta = 74°$, $\beta = 82°$ and $\beta = 90°$. Note that the limiting cases $\beta = 0°$ and $\beta = 90°$ correspond to pure shear and transverse plane strain loading, respectively. Figure 2-5 shows a graph which illustrates the different loading states on a generic von Mises yield surface in the plane stress subspace $(\sigma_0, \sigma_{90}, \tau)$, where σ_0 is the normal stress in the rolling direction, σ_{90} is the normal stress in the cross-rolling direction, and τ is the corresponding shear stress component. From each experiment, we obtain a normal stress versus normal strain curve as well as a shear stress versus shear strain curve. All measured normal and shear stress-strain curves are depicted in Figures 2-8 and 2-11. The results will be discussed in detail throughout our comparison of the experimental results with the numerical simulations in Section 2.4.

2.3 Quadratic plane stress plasticity models

In the case of aluminum alloys, direct measurements of distinct points on the yield surface (e.g. Green et al., 2004, [64]) have shown that non-quadratic functions are needed to describe the boundary of the elastic domain with satisfactory accuracy. To the best knowledge of the authors, no such yield surface measurements have been published in the open literature for dual phase or TRIP-assisted steel sheets. The use of non-quadratic yield envelopes for steels is usually justified through the upper bound calculations by Logan and Hosford (1980, [96]) or by r-value measurements. In the latter case, the assumption of associated plastic flow is imposed and the shape of the yield surface is adjusted such that the r-values are predicted accurately. However, as pointed out by Stoughton (2002, [134]), Bishop and Hill's (1951, [22]) proof of the associated flow rule is only valid if slip according to Schmid'a law is the dominant deformation mechanism at the crystal level.

Similar to the results by Padmanabhan et al. (2007, [121]) on a DP600, the present uniaxial experiments indicated a pronounced direction dependency of the r-value (Fig. 2-2b), while nearly the same stress-strain curve has been measured for all specimen directions. In other words, the r-value measurements suggest planar anisotropy while the material's

response is planar isotropic as far as the stress level is concerned. It is straightforward to show that a standard associated plasticity model with a quadratic yield surface cannot replicate this behavior. As an alternative to the formulation of non-quadratic associated plasticity models (e.g. Barlat, 2003, [10, 11]), we loosen the constraint of associated plastic flow. As suggested by Stoughton (2002, [134]), we make use of a quadratic yield surface in conjunction with a non-associated quadratic plastic flow potential. Thus, the computational efficiency of quadratic plasticity models is maintained while providing a model structure that can describe the present uniaxial experiments accurately. The reader is referred to Stoughton (2002, [134]) for the proof of the uniqueness of the states of stress and strain as well as the proof of stability of plastic flow.

2.3.1 Plane stress yield surface

As discussed above, we limit our attention to the quadratic yield function proposed by Hill (1948, [73]). It may be written in the form

$$f(\boldsymbol{\sigma}, k) = \bar{\sigma} - k = 0 \tag{2-5}$$

where $\bar{\sigma}$ is the equivalent stress,

$$\bar{\sigma} = \sqrt{(\boldsymbol{P}\boldsymbol{\sigma}) \cdot \boldsymbol{\sigma}} \tag{2-6}$$

$\boldsymbol{\sigma}$ denotes the Cauchy stress vector in material coordinates

$$\boldsymbol{\sigma} = [\sigma_0 \quad \sigma_{90} \quad \tau]^T \tag{2-7}$$

with the true stress components σ_0 along the rolling direction, σ_{90} along the cross-rolling direction and the corresponding shear stress τ. $\boldsymbol{P}$ is a symmetric positive-definite matrix defined through the three independent parameters P_{12}, P_{22} and P_{33}:

$$\boldsymbol{P} = \begin{bmatrix} 1 & P_{12} & 0 \\ P_{12} & P_{22} & 0 \\ 0 & 0 & P_{33} \end{bmatrix} \tag{2-8}$$

2.3.2 Flow rule

The flow rule describes the incremental evolution of the plastic strain vector

$$d\boldsymbol{\varepsilon^p} = \begin{bmatrix} d\varepsilon_0^p & d\varepsilon_{90}^p & d\gamma^p \end{bmatrix}^T \tag{2-9}$$

ε_0^p and ε_{90}^p denote the plastic strain components along the rolling and cross-rolling direction, while γ^p denotes the plastic engineering shear strain (which is twice the mathematical shear strain). The direction of plastic flow is assumed to be aligned to the stress derivative of the flow potential function $g(\boldsymbol{\sigma})$,

$$d\boldsymbol{\varepsilon^p} = d\lambda \frac{\partial g}{\partial \boldsymbol{\sigma}} \tag{2-10}$$

where $d\lambda \geq 0$ is a scalar plastic multiplier. In close analogy with the yield function, the potential function $g(\boldsymbol{\sigma})$ is defined as a quadratic function in stress space,

$$g(\boldsymbol{\sigma}) = \sqrt{(\boldsymbol{G\sigma}) \cdot \boldsymbol{\sigma}} \tag{2-11}$$

with the positive definite coefficient matrix

$$\boldsymbol{G} = \begin{bmatrix} 1 & G_{12} & 0 \\ G_{12} & G_{22} & 0 \\ 0 & 0 & G_{33} \end{bmatrix} \tag{2-12}$$

Note that in the special case of $\boldsymbol{P} = \boldsymbol{G}$, we recover the associated flow rule.

2.3.3 Isotropic hardening

The distinction between isotropic and kinematic hardening is omitted since the present evaluation is limited to monotonic loading conditions. Isotropic strain hardening is described through the relationship between the deformation resistance k and the equivalent plastic strain. Formally, we introduce the hardening modulus $h = h(\bar{\varepsilon}^p)$ and the evolution equation

$$dk = h(\bar{\varepsilon}^p) d\bar{\varepsilon}^p \quad \text{with} \quad k(\bar{\varepsilon}^p = 0) = k_0 \tag{2-13}$$

The equivalent plastic strain $\bar{\varepsilon}^p$ is defined as incrementally work-conjugate to the equivalent stress, i.e.

$$\boldsymbol{\sigma} \cdot d\boldsymbol{\varepsilon^p} = \bar{\sigma} d\bar{\varepsilon}^p \tag{2-14}$$

Upon evaluation of this relationship for non-associated plastic flow, we obtain the following relationship between the equivalent plastic strain and the plastic multiplier,

$$d\bar{\varepsilon}^p = \frac{g(\boldsymbol{\sigma})}{\bar{\sigma}} d\lambda \tag{2-15}$$

as well as the relationship between the equivalent plastic strain and the plastic strain tensor,

$$d\bar{\varepsilon}^p = \left(\frac{g}{\bar{\sigma}}\right)^2 \sqrt{[\boldsymbol{P}\boldsymbol{G}^{-1}(d\boldsymbol{\varepsilon^p})] \cdot \boldsymbol{G}^{-1}(d\boldsymbol{\varepsilon^p})} \tag{2-16}$$

The evaluation of the present experimental data for the TRIP780 and DP590 steel revealed that the Swift (1952, [139]) law provides a good approximation of the relationship between the equivalents stress and the equivalent plastic strain. In the case of monotonic loading, the Swift law reads

$$\bar{\sigma} = A(\bar{\varepsilon}^p + \varepsilon_0)^n \tag{2-17}$$

with the model parameters A, ε_0 and n. Consequently, we chose the following special function to define the hardening modulus as a function of the equivalent plastic strain:

$$h(\bar{\varepsilon}^p) = nA(\bar{\varepsilon}^p + \varepsilon_0)^{n-1} \tag{2-18}$$

In the case of the structural validation simulations (see Section 2.5), the modified Swift law approximation is employed for an equivalent plastic strain of up to 0.2. Thereafter, we use a piecewise-linear extrapolation curve which has been determined from biaxial punch experiments (see Section 3.4.4). In the context of non-associated plastic flow, it may be computationally convenient to consider the option of defining the hardening as a function of the plastic multiplier integral λ with

$$\lambda = \int_0^t d\lambda \tag{2-19}$$

In this special case, the hardening law (2-18) is rewritten as

$$h(\lambda) = nA(\lambda + \varepsilon_0)^{n-1} \tag{2-20}$$

Stoughton (2002, [134]) proposed the second option while Cvitanic et al. (2008, [42]) chose the work-conjugate hardening law formulation in their non AFR model. It is noted that both approaches are identical in the case of associated plastic flow.

2.3.4 Model calibration

It is common practice to calibrate anisotropic plasticity models based on Lankford's r-values. According to our flow rule, the dependence of the r-value on the loading direction is

$$r(\alpha) = \frac{(G_{33} + 2G_{12} - G_{22} - 1)\sin^2\alpha\cos^2\alpha - G_{12}}{(1 - G_{22})\cos^2\alpha + G_{12} + G_{22}} \tag{2-21}$$

where α denotes the angle between the material rolling direction and the loading axis. In the present comparative study, we consider four special parameter settings of the general non-associated quadratic plasticity model. For historic reasons, we refer to these special cases as different models:

- Model #1: Isotropic yield surface with associated plastic flow. By setting $P_{11} = P_{22} = 1.0$, $P_{12} = -0.5$ and $P_{33} = 3.0$, we recover the isotropic von Mises yield surface. Furthermore, we assume $\boldsymbol{G} = \boldsymbol{P}$ which corresponds to associated plastic flow.
- Model #2: Orthotropic yield surface with associated plastic flow. By imposing associated plastic flow, $\boldsymbol{G} = \boldsymbol{P}$, we may use the r-value measurements to calibrate both coefficient matrices. The relationships among the r-values r_0, r_{45} and r_{90} and the coefficients read:

$$G_{12} = -\frac{r_0}{1+r_0}, \quad G_{22} = \frac{r_0}{r_{90}}\frac{1+r_{90}}{1+r_0} \quad \text{and} \quad G_{33} = \frac{1+2r_{45}}{r_{90}}\frac{r_0+r_{90}}{1+r_0} \tag{2-22}$$

- Model #3: Planar isotropic (normal anisotropic) yield surface with associated plastic flow. In this case, we still have $\boldsymbol{G} = \boldsymbol{P}$, while both matrices are calibrated based on the average r-value:

$$G_{12} = -\frac{\bar{r}}{1+\bar{r}}, \quad G_{22} = 1 \quad \text{and} \quad G_{33} = 2\frac{1+2\bar{r}}{1+\bar{r}} \tag{2-23}$$

- Model #4: Isotropic yield surface with non-associated orthotropic plastic flow potential. As in model #1, we set $P_{11} = P_{22} = 1.0$, $P_{12} = -0.5$ and $P_{33} = 3.0$. At the same time, we make use of the coefficients determined for model #2 to predict the direction of plastic flow.

- Model #5: Planar isotropic yield surface with non-associated orthotropic plastic flow potential. The same $\boldsymbol{G}$ matrix as for model #2 is used to define the flow rule. The yield surface is defined through the Hill parameters for planar isotropy (see Eq. 2-23). However, instead of using the measured average r-value, a suitable $\bar{r}$ may be identified from calibrating the model with respect to the transverse plane strain tension tests ($\beta = 90°$). The analytical expressions for the yield stresses under transverse plane strain conditions read

$$\sigma_y^{TPS-0} = \frac{k}{\sqrt{1 - 2P_{12}\left(\frac{G_{12}}{G_{22}}\right) + P_{22}\left(\frac{G_{12}}{G_{22}}\right)^2}} \tag{2-24}$$

for loading along the rolling direction and

$$\sigma_y^{TPS-0} = \frac{k}{\sqrt{G_{12}^2 - 2P_{12}G_{12} + P_{22}}} \tag{2-25}$$

for loading along the cross-rolling direction. In the present case, $\bar{r} = 0.91$ yielded the best result which incidentally corresponds to the real average of the measured r-values.

- Model #6: The same yield surface and flow rule as for model #5, but with hardening defined through the plastic multiplier integral (Stoughton approach) instead of the work-conjugate equivalent plastic strain.

Tables 2-2 and 2-3 summarize the corresponding parameter settings for the DP590 and TRIP780 steel, respectively.

Table 2-2: Swift hardening law parameters for the TRIP780 and DP590 sheets

	$K\ [MPa]$	$n\ [-]$	$\varepsilon_0\ [-]$
TRIP780	1460	0.204	1.63×10^{-3}
DP590	1017	0.182	3.23×10^{-3}

	r_0	r_{45}	r_{90}	P_{12}	P_{22}	P_{33}	G_{12}	G_{22}	G_{33}
TRIP780									
isotropic	1.00	1.00	1.00	-0.50	1.00	3.00	-0.50	1.00	3.00
orthotropic	0.89	0.82	1.01	-0.47	0.94	2.64	-0.47	0.94	2.64
planar isotropic	0.89	0.89	0.89	-0.47	1.00	2.94	-0.47	1.00	2.94
non associated	0.89	0.82	1.01	-0.50	1.00	3.00	-0.47	0.94	2.64
DP590									
isotropic	1.00	1.00	1.00	-0.50	1.00	3.00	-0.50	1.00	3.00
orthotropic	0.75	1.00	0.87	-0.43	0.92	3.19	-0.43	0.92	3.19
planar isotropic	0.91	0.91	0.91	-0.48	1.00	2.95	-0.48	1.00	2.95
non associated	0.75	1.00	0.87	-0.50	1.00	3.00	-0.43	0.92	3.19

Table 2-3: Plasticity model parameters for the TRIP780 and DP590 sheets

2.4 Results and comparison

A standard return-mapping algorithm is used to implement the constitutive model(s) into a commercial finite element program (user subroutine for ABAQUS/explicit [1]). Using the different sets of parameters (Table 2-3), finite element simulations are performed to investigate the predicative capabilities of all six plasticity models. The finite element model of the biaxial experiment comprises a single reduced integration plane stress element (Abaqus element CPS4R) that is subject to different radial engineering stress paths as specified by the biaxial loading angle β. The transverse plane strain condition is imposed by imposing kinematic constraints on displacement boundary conditions. The outcomes of each single-element simulation are two engineering stress-strain curves (normal and shear) which are the compared to the experimental results.

2.4.1 Uniaxial stress-strain curve and r-ratios

Figure 2-6 and 2-7 compare all experimental and simulation results for uniaxial loading. Models #1, #3, #4, #5 and #6 all predict the same uniaxial stress-strain curves irrespective of the loading direction. Note that the curves labeled isotropic, planar isotropic and non-associated are all lying on top of each other in Figures 2-6a and 2-7a. Model #2 is the only one using a fully-orthotropic yield surface and consequently the stress-level can only be predicted with high accuracy for the specimens loaded along the rolling direction, while the stress level is respectively under- and overestimated for 45° and 90° loading.

The orthotropic Hill model with associated flow rule (model #2) can describe the direction dependency of the r-values. The solid black lines in Fig. 2-2b show the r-value variations that are predicted after calibrating the Hill model. Observe the good agreement of the model with the experimental data points (solid dots) for the TRIP780 steel. However, since the flow rule and the yield surface are associated in the standard Hill model, the r-value direction dependency translates into a direction-dependency of the stress-strain curves. The direction-dependent yield stress which is given by

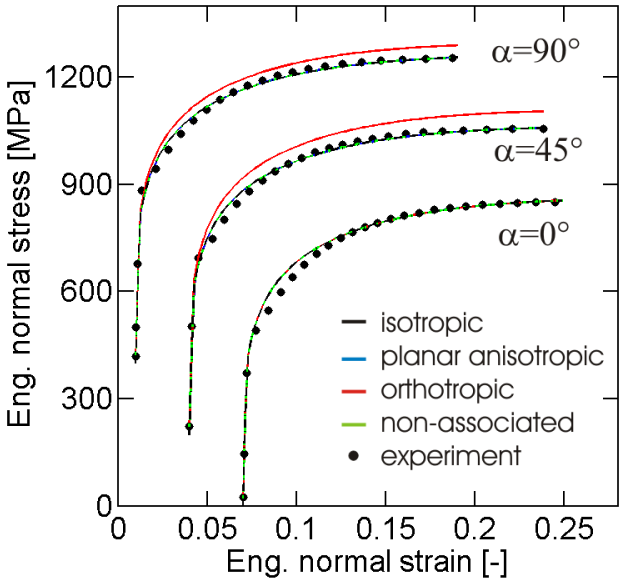

(a)

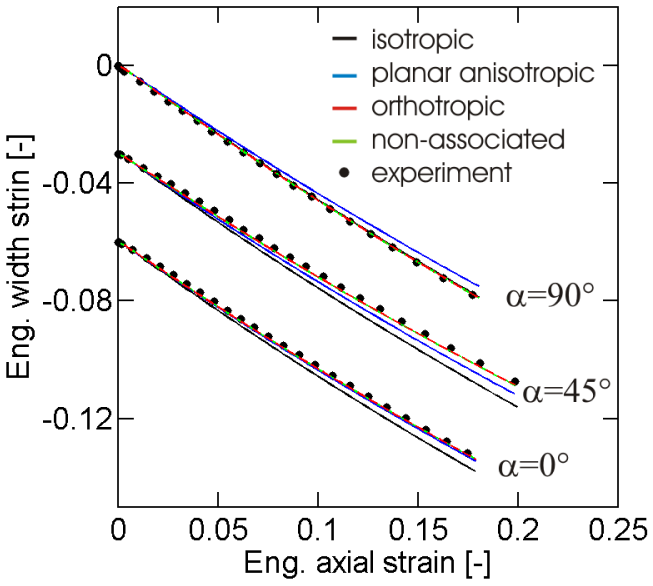

(b)

Figure 2-6: Model predictions for uniaxial loading of TRIP780. (a) engineering stress-curves; (b) strain along the width direction as a function of the axial engineering strain. The experimental results are shown by dots, while the solid lines correspond to the model predictions.

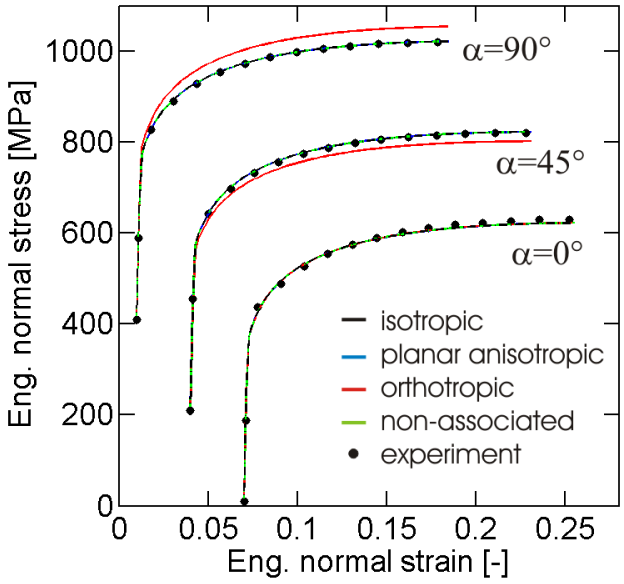

(a)

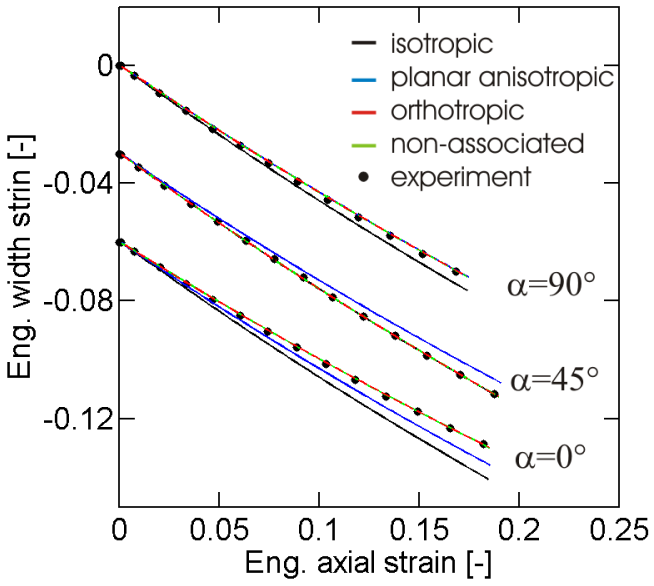

(b)

Figure 2-7: Model predictions for uniaxial loading of DP590. (a) engineering stress-curves; (b) strain along the width direction as a function of the axial engineering strain. The experimental results are shown by dots, while the solid lines correspond to the model predictions.

$$\sigma_y(\alpha) = \frac{k}{\sqrt{\cos^4\alpha + \sin^2\alpha\cos^2\alpha\,(2P_{12} + P_{33}) + \sin^4\alpha\,P_{22}}} \tag{2-26}$$

is plotted as dotted blue lines in Fig. 2-2b. The ratio of the maximum and minimum yield stress is 1.05 for the TRIP780 and 1.08 for the DP590. Due to this direction-dependency of the yield stress, the standard Hill model (model #2) cannot predict the uniaxial stress-strain curves to a great degree of accuracy for all specimen orientations (see red curves in Figs. 2-6a and 2-7a. Model #4 makes use of a von Mises yield surface and a Hill flow rule. As a result, both the r-ratio variations and the uniaxial stress-strain curves are modeled accurately for all specimen orientations. The same accuracy with respect to the uniaxial experiments may be achieved by using a planar isotropic (i.e. normal anisotropic) yield surface along with the Hill flow rule (models #5 and #6).

2.4.2 Multi-axial experiments

Each multi-axial experiment is simulated using the plasticity models. Subsequently, we extracted one normal stress-strain curve and one shear stress-strain curve from each simulation and compared the computational and experimental results. Figure 2-8 summarizes the stress-strain curves for the TRIP780 material. The solid curves represent the simulation results for the isotropic von Mises model; the experimental results are shown by dashed lines. The model and the experiments show a remarkably good overall agreement. Note that the transverse plane strain stress-strain response ($\beta = 90°$) is predicted accurately for all three specimen orientations ($\alpha = 0°$, 45° and 90°). The same holds true for the shear stress-strain curves where the relative error in the estimated stress level is less than 5% irrespective of the specimen orientation α and the biaxial loading angle β. The simulation results for the other models are more or less identical (within 1% as far as the stress level is concerned). Even though the other models predict different r-ratios than the isotropic von Mises model, this anisotropic feature played only a minor role as far as the predictions under multi-axial loading are concerned. The only noteworthy exception is the prediction of the

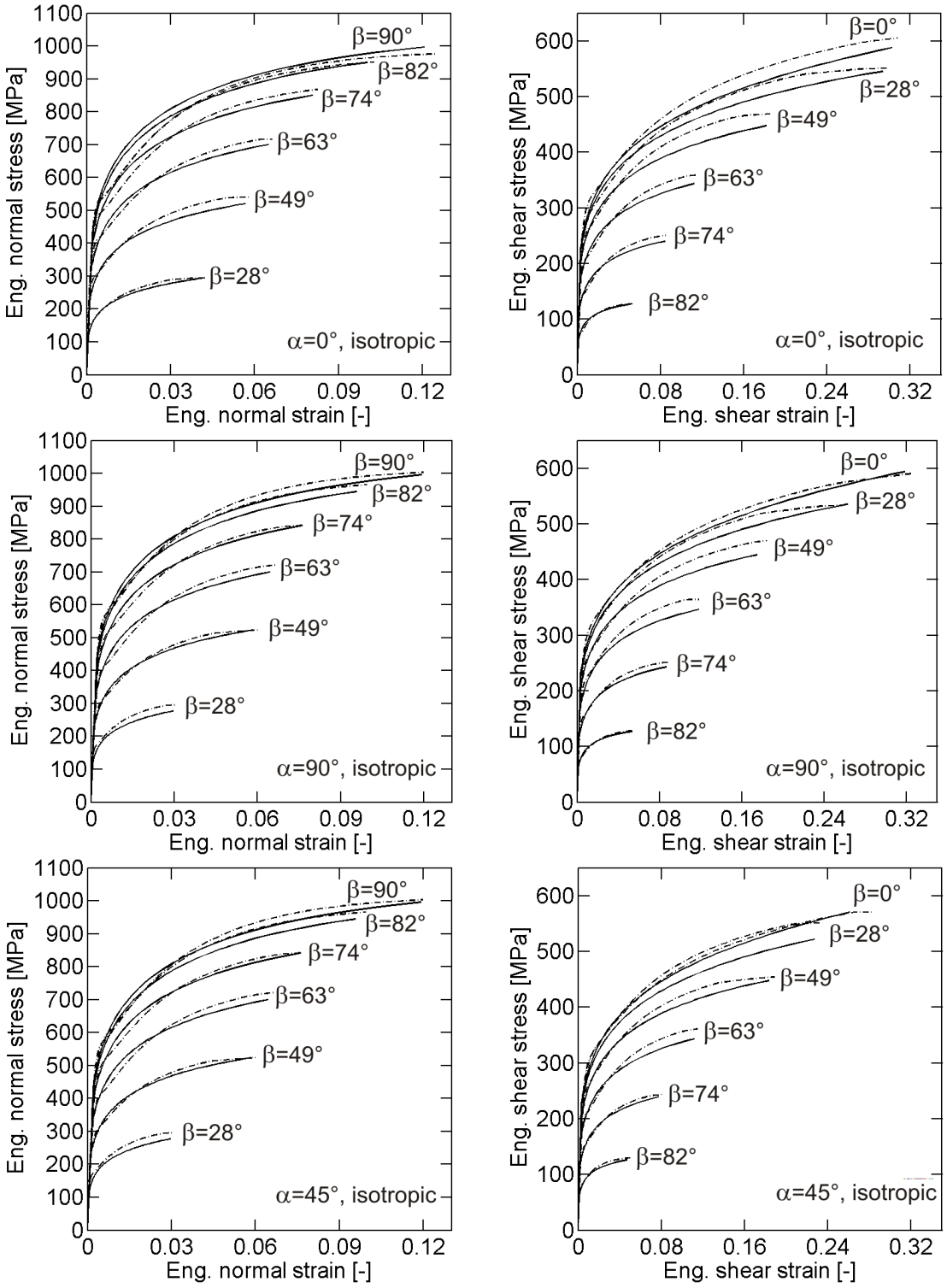

Figure 2-8: TRIP780 results : Normal stress-strain curves (left column) and shear stress-strain curves (right column) for different specimen orientations and biaxial loading angles The experimental results are shown by dashed curves while the solid lines depict the prediction of the associated isotropic von Mises model.

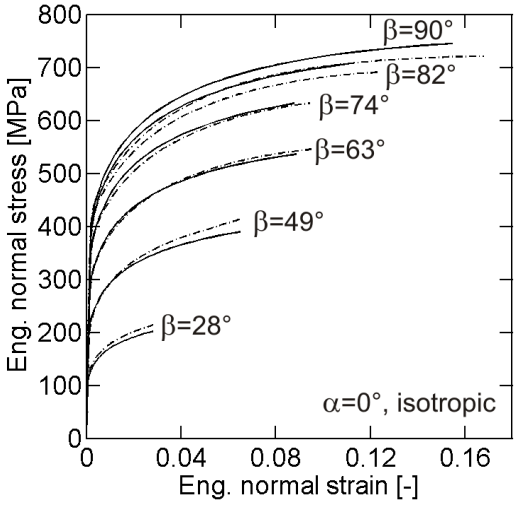
Eng. normal stress [MPa]
Eng. normal strain [-]
β=90°
β=82°
β=74°
β=63°
β=49°
β=28°
α=0°, isotropic

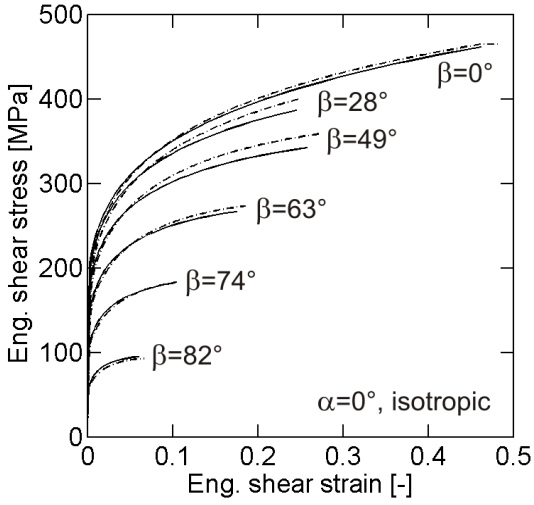
Eng. shear stress [MPa]
Eng. shear strain [-]
β=0°
β=28°
β=49°
β=63°
β=74°
β=82°
α=0°, isotropic

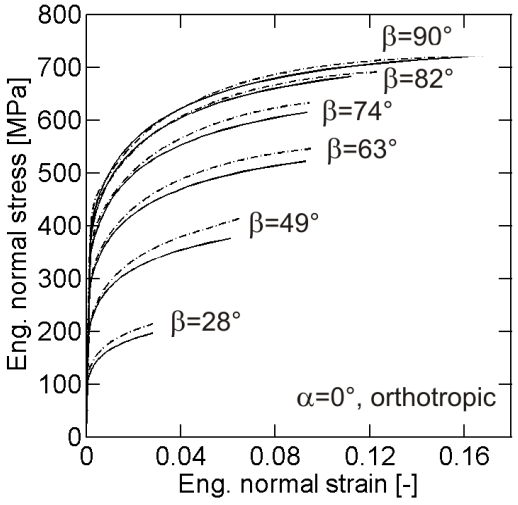
Eng. normal stress [MPa]
Eng. normal strain [-]
β=90°
β=82°
β=74°
β=63°
β=49°
β=28°
α=0°, orthotropic

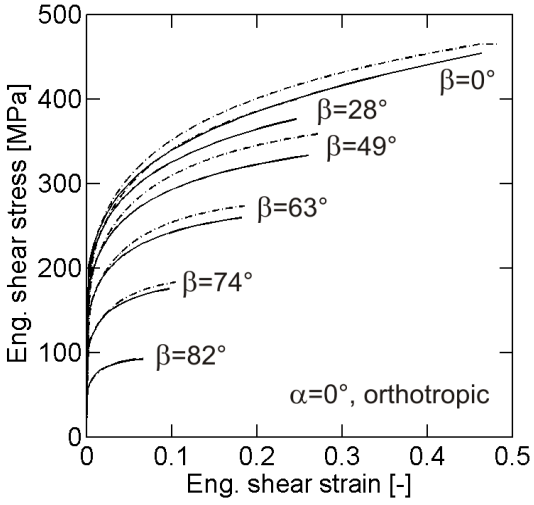
Eng. shear stress [MPa]
Eng. shear strain [-]
β=0°
β=28°
β=49°
β=63°
β=74°
β=82°
α=0°, orthotropic

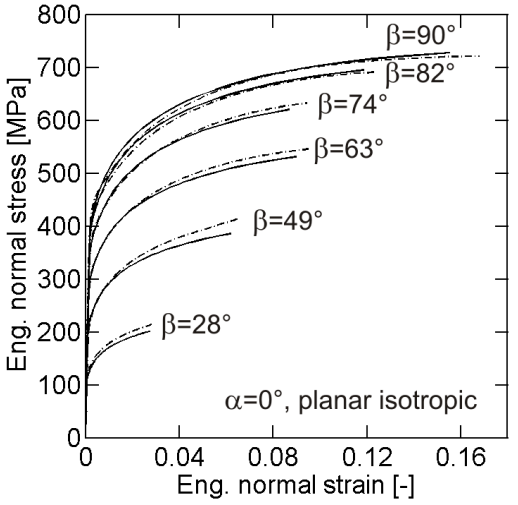
Eng. normal stress [MPa]
Eng. normal strain [-]
β=90°
β=82°
β=74°
β=63°
β=49°
β=28°
α=0°, planar isotropic

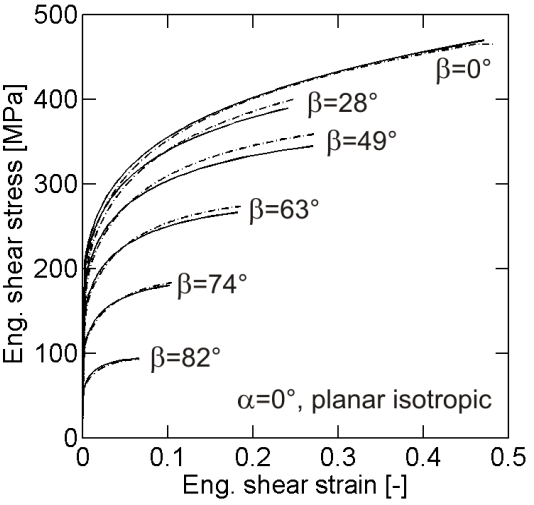
Eng. shear stress [MPa]
Eng. shear strain [-]
β=0°
β=28°
β=49°
β=63°
β=74°
β=82°
α=0°, planar isotropic

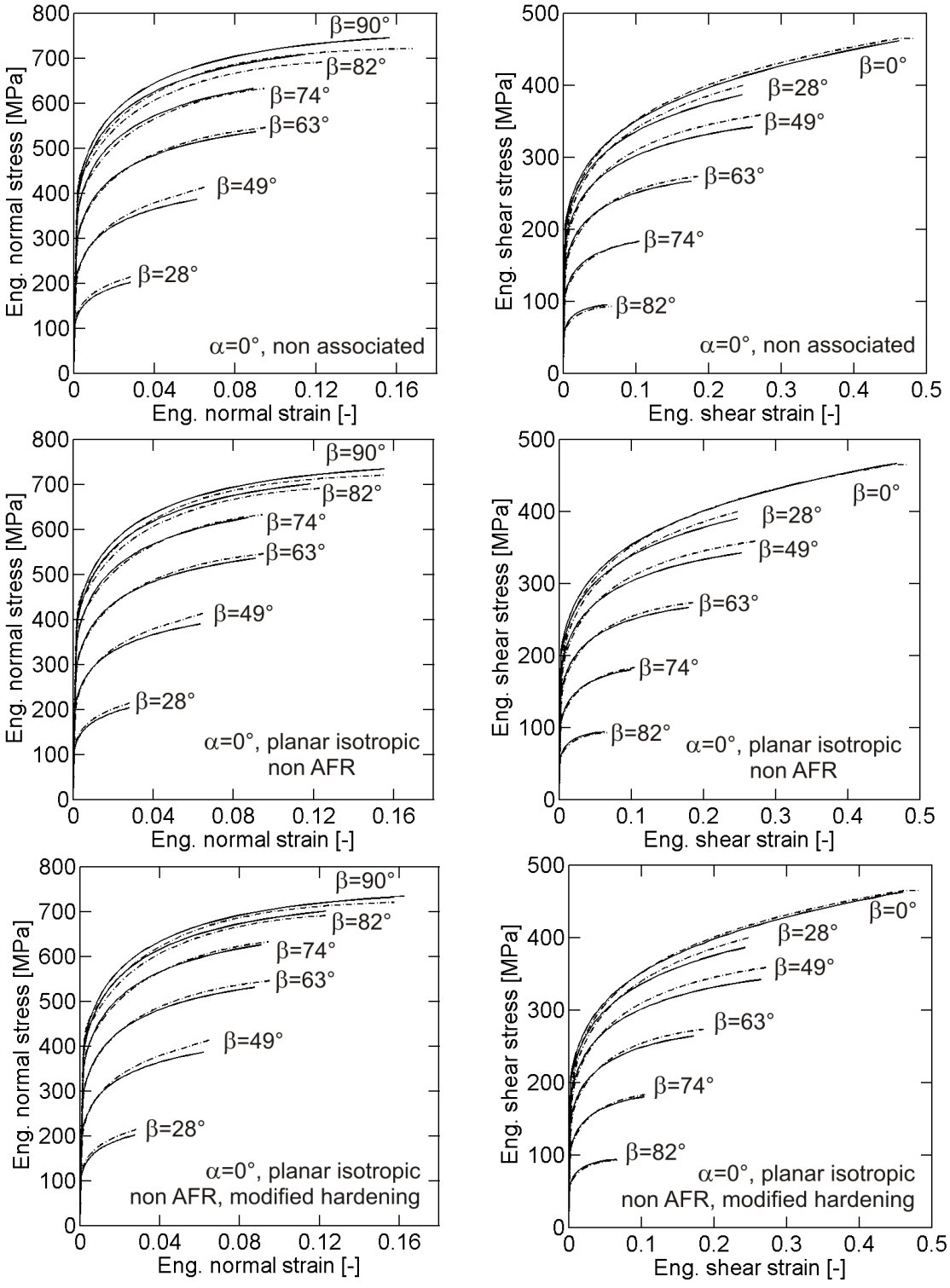

Figure 2-9: DP 590 results for a specimen orientation of $\alpha = 0°$. Each row of figures corresponds to a different simulation model (dashed lines = experiment, solid lines=simulation).

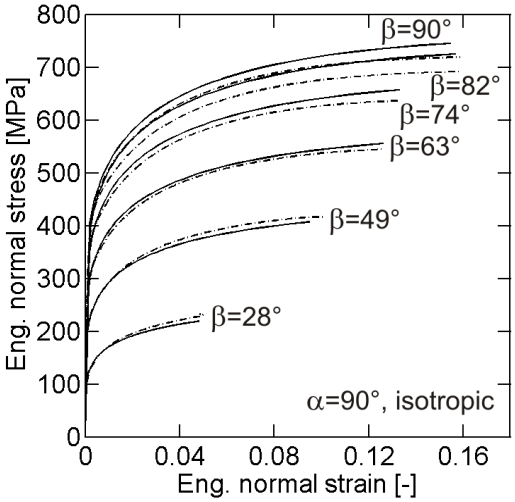
Eng. normal stress [MPa]
Eng. normal strain [-]
β=90°
β=82°
β=74°
β=63°
β=49°
β=28°
α=90°, isotropic

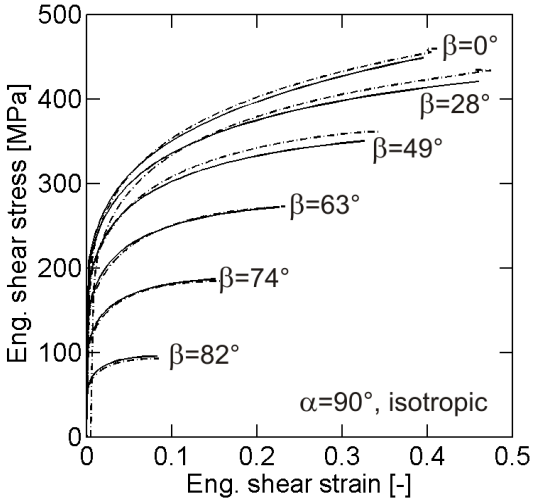
Eng. shear stress [MPa]
Eng. shear strain [-]
β=0°
β=28°
β=49°
β=63°
β=74°
β=82°
α=90°, isotropic

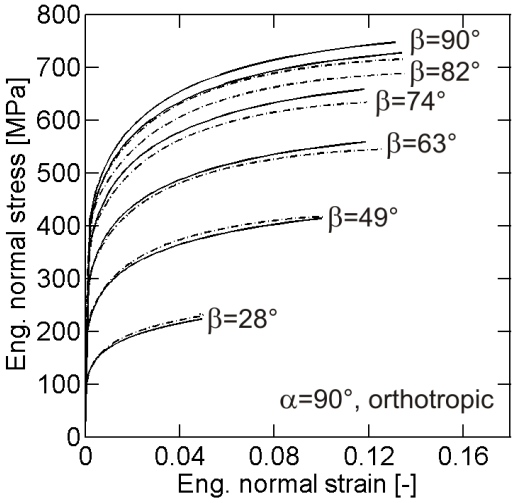
Eng. normal stress [MPa]
Eng. normal strain [-]
β=90°
β=82°
β=74°
β=63°
β=49°
β=28°
α=90°, orthotropic

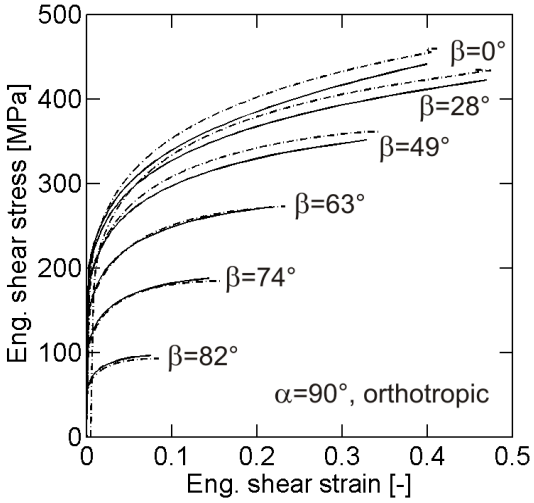
Eng. shear stress [MPa]
Eng. shear strain [-]
β=0°
β=28°
β=49°
β=63°
β=74°
β=82°
α=90°, orthotropic

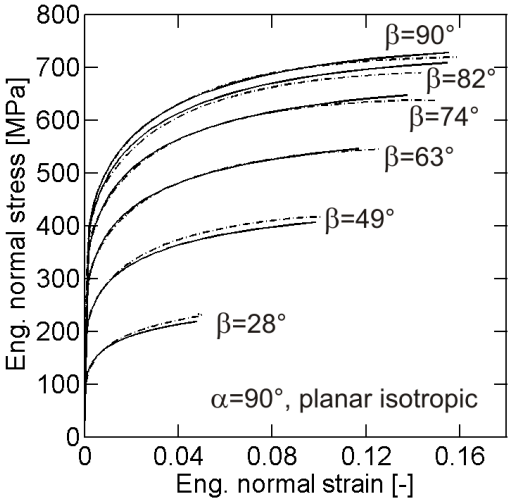
Eng. normal stress [MPa]
Eng. normal strain [-]
β=90°
β=82°
β=74°
β=63°
β=49°
β=28°
α=90°, planar isotropic

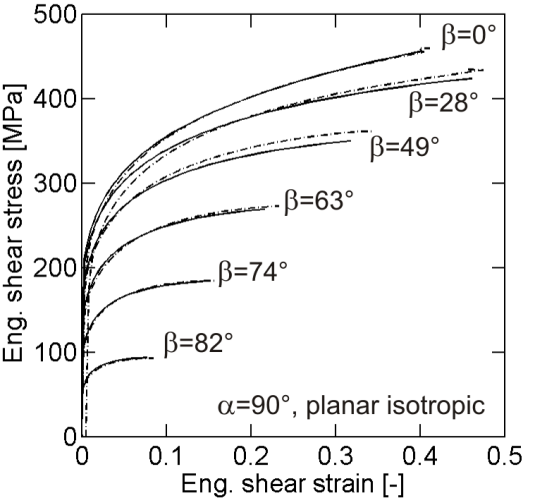
Eng. shear stress [MPa]
Eng. shear strain [-]
β=0°
β=28°
β=49°
β=63°
β=74°
β=82°
α=90°, planar isotropic

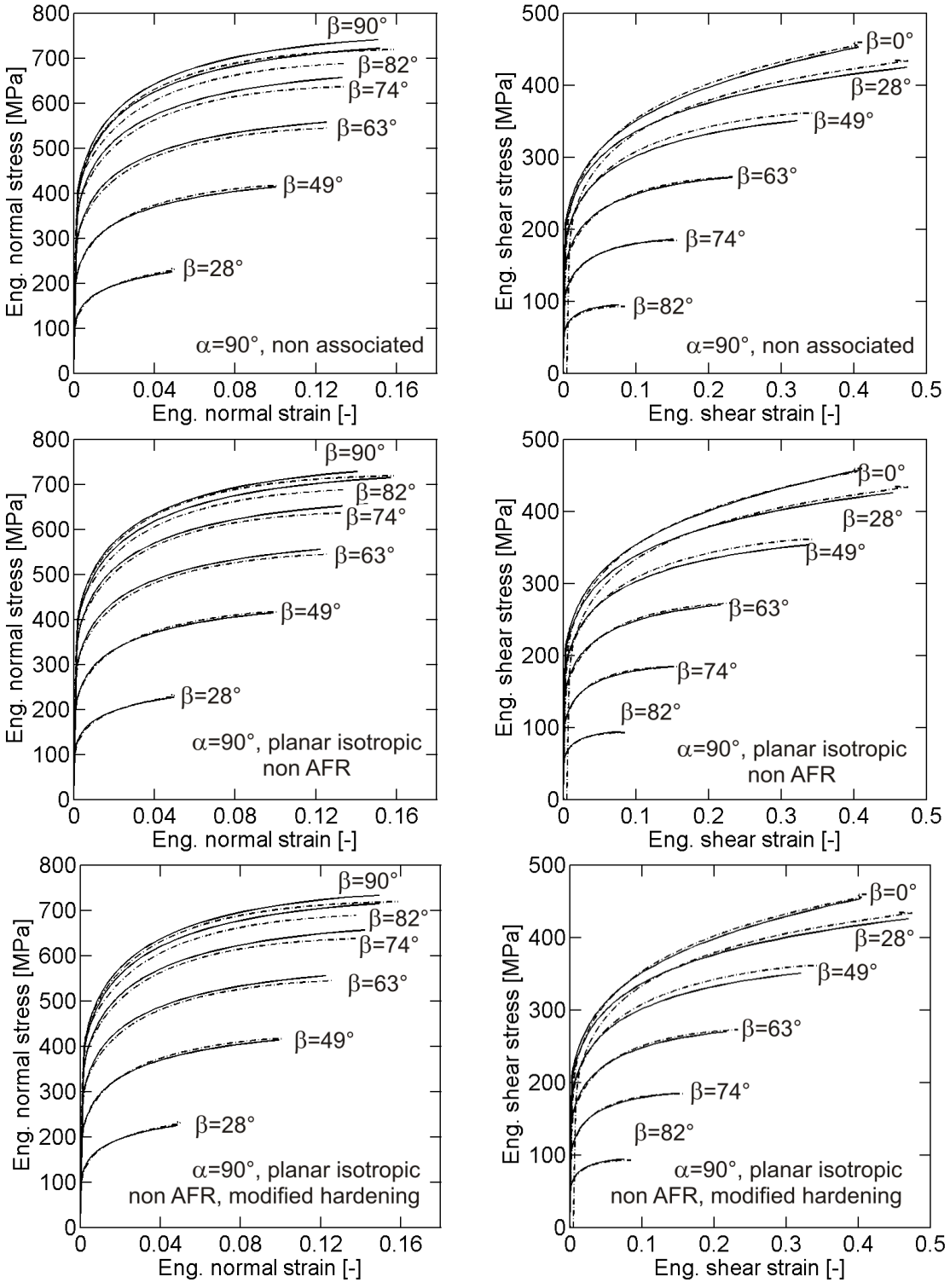

Figure 2-10: DP 590 results for a specimen orientation of $\alpha = 90°$. Each row of figures corresponds to a different simulation model (dashed lines = experiment, solid lines=simulation).

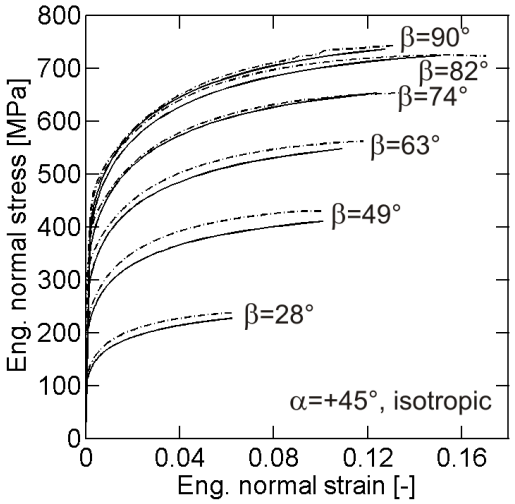
Eng. normal stress [MPa]
Eng. normal strain [-]
β=90°
β=82°
β=74°
β=63°
β=49°
β=28°
α=+45°, isotropic

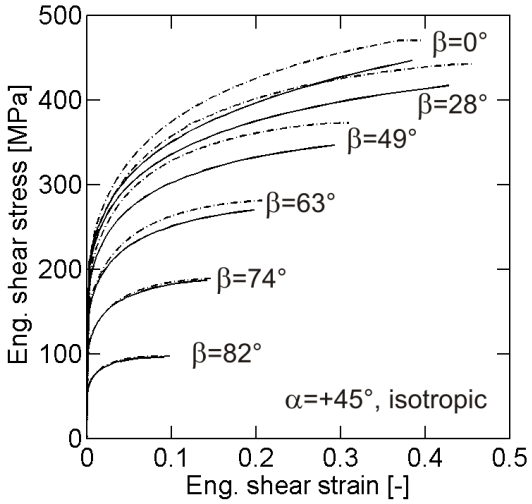
Eng. shear stress [MPa]
Eng. shear strain [-]
β=0°
β=28°
β=49°
β=63°
β=74°
β=82°
α=+45°, isotropic

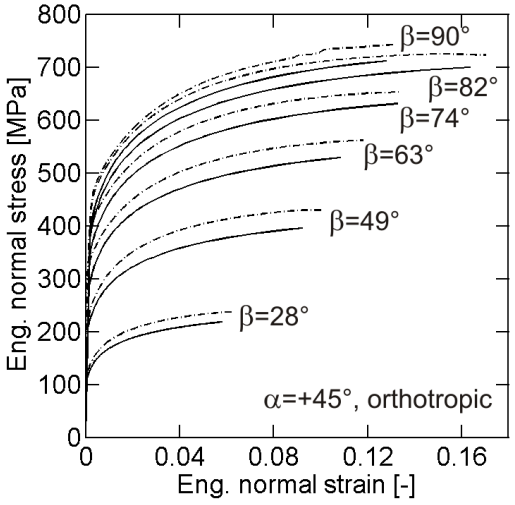
Eng. normal stress [MPa]
Eng. normal strain [-]
β=90°
β=82°
β=74°
β=63°
β=49°
β=28°
α=+45°, orthotropic

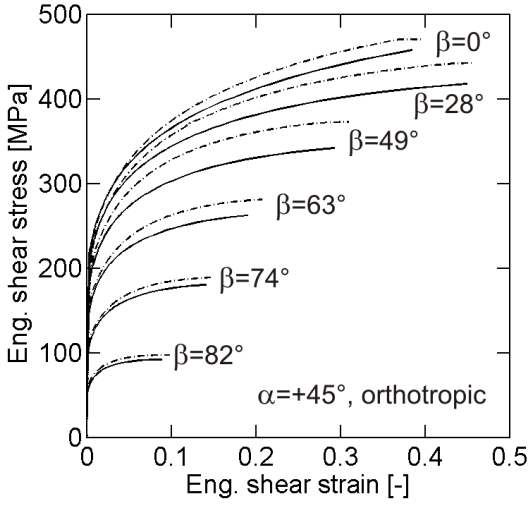
Eng. shear stress [MPa]
Eng. shear strain [-]
β=0°
β=28°
β=49°
β=63°
β=74°
β=82°
α=+45°, orthotropic

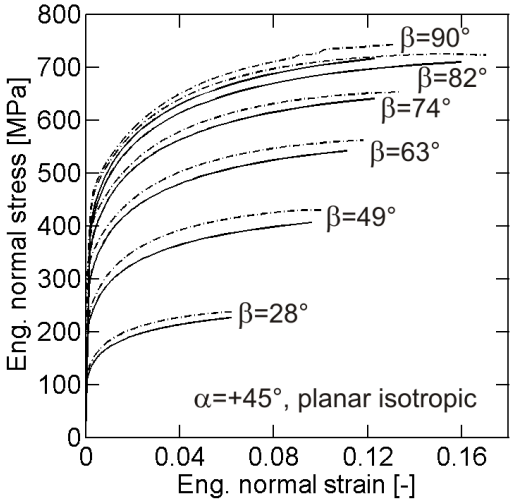
Eng. normal stress [MPa]
Eng. normal strain [-]
β=90°
β=82°
β=74°
β=63°
β=49°
β=28°
α=+45°, planar isotropic

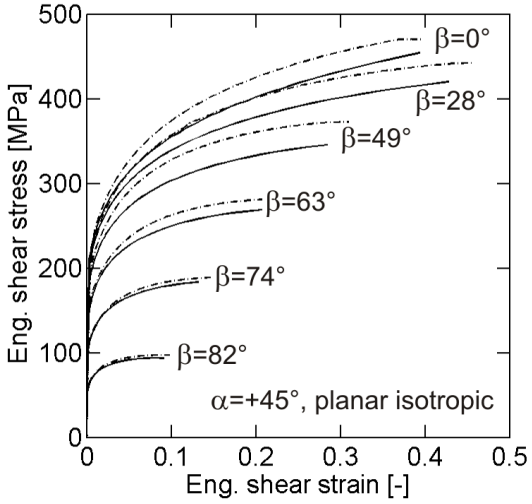
Eng. shear stress [MPa]
Eng. shear strain [-]
β=0°
β=28°
β=49°
β=63°
β=74°
β=82°
α=+45°, planar isotropic

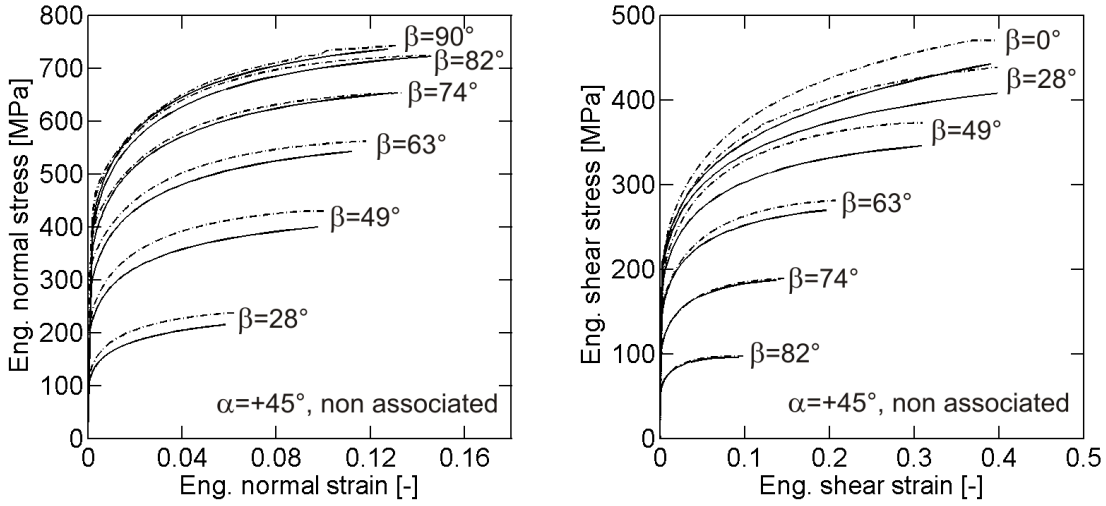

Figure 2-11: DP 590 results for a specimen orientation of $\alpha = 45°$. Each row of figures corresponds to a different simulation model (dashed lines = experiment, solid lines=simulation).

pure shear stress-strain curve for the associated Hill model (model #2). Here, the Hill model overestimates the shear stress by about 5%. This is due to the low value of the parameter P_{33}. Note that the yield stress τ_y for pure shear loading is $\tau_y = k/\sqrt{P_{33}}$.

The differences among the plasticity models become more apparent when simulating the multi-axial experiments on the DP590. Note that the anisotropy described by the measured r-ratio variations is relatively weak in the case of the TRIP780 steel, but more pronounced for the DP590 (Fig. 2-2b). Figures 2-9 to 2-11 show the comparison of all experiments with the simulation results for different models and specimen orientations. As for the TRIP780, we observe a good overall agreement for all curves. Despite small differences between the predicted stress-strain curves of the isotropic von Mises and orthotropic Hill models, there is no visible difference between the associated and non-associated isotropic models (models #1 and #4). This suggests that the multi-axial stress-strain curve predictions are more sensitive to the yield surface than to the flow rule. The yield strength under transverse plane strain tension is overestimated by models #1 and #4, while the transversely isotropic model #3 provides a better approximation. Note that the

even though both models #1 and #3 are isotropic with respect to rotations in the sheet plane, the yield envelopes for $\tau = 0$ are not identical; we have $P_{12} = -0.467$ in the case of model #3 and hence its yield surface lies inside the von Mises envelope of model #1 (where $P_{12} = -0.5$).

The orthotropic model #2 underestimates the pure shear strength ($\beta = 0°$) of the DP590 for $\alpha = 0°/90°$. As for the TRIP780, this is due to the value of P_{33} which is larger than 3 in the present case. All simulations are less accurate for $\alpha = 45°$ than for $\alpha = 0°/90°$. In particular the shear stress-strain curves show more pronounced differences between the simulations and experiments. This appears to be the case irrespective of the choice of the plasticity model. In terms of normal stresses along the material axes, shear loading for $\alpha = 45°$ may be considered as the combination of tension along the rolling direction and compression along the transverse direction. In other words, unlike for $\alpha = 0°$ and $\alpha = 90°$, the experiments on $\alpha = 45°$ specimens involve compressive loading along one material axis. Therefore, an initial back stress in the cold-rolled DP590 material may be partially responsible for the increased discrepancy between the simulations and experiments for $\alpha = 45°$. Cyclic experiments or in-plane compression tests would be needed to quantify this effect.

The use of the planar isotropic yield surface in combination with an orthotropic flow rule (model #5) may be seen as the most accurate model. It provides an accurate description of all uniaxial data while its prediction accuracy for multi-axial loading is similar to that of model #3. The differences between Cvitanic's and Stoughton's formulation of the isotropic hardening law (models #5 and #6) do not become apparent for the present set of data and loading condition (the label "modified hardening" is used in Figs. 2-9 to 2-11 to indicate the use of the Stoughton's approach).

2.5 Structural validation

The analysis of the biaxial plasticity experiments does not provide a clear answer as to whether the direction of plastic flow is associated or non-associated with the yield surface.

In this section, a structural experiment is presented to elucidate the difference between these two modeling approaches. In the previous material experiments, the stress and strain fields are approximately uniform throughout the entire specimen. In a structural experiment, the fields are usually non-uniform and a wider range of stress states is covered by a single experiment. Even though it is difficult to deduce material properties from a structural experiment, the comparison of numerical simulations with the experimental results can be used to validate the underlying material model. Here, we perform a structural experiment on a butterfly-shaped specimen. Subsequently, a finite element analysis is performed to assess the influence of the flow rule assumption on the simulation results.

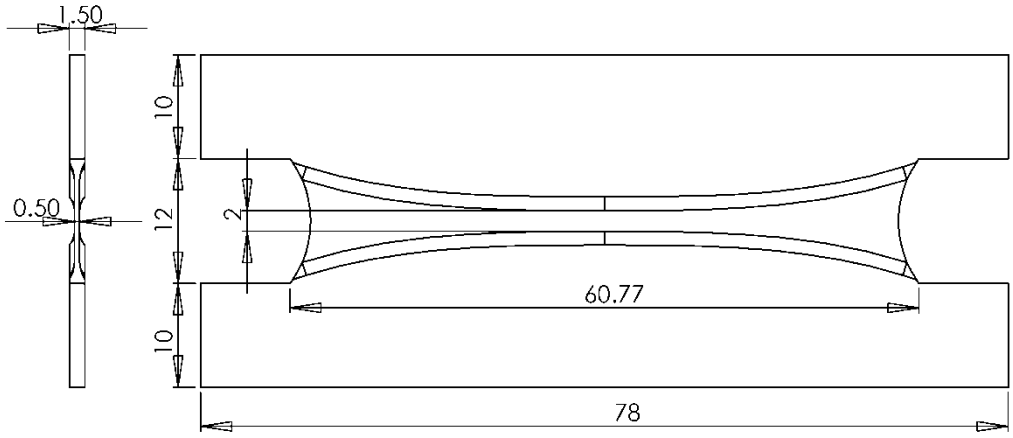

Figure 2-12: Schematic of the butterfly-shaped specimen. The clamping pressure is applied over an area of 10mm x 78mm on the top and bottom of the specimen.

2.5.1 Experiment

Figure 2-12 shows the geometry of the butterfly-shaped specimen. It has been developed for fracture testing (see Chapter 4), but in the present context we are only interested in its elasto-plastic response. The specimen is extracted from a 1.4*mm* thick TRIP780 sheet using CNC machining. The material rolling direction is aligned with the vertical direction of the testing machine (corresponds also to vertical direction of Fig. 2-12). After verifying the dimensions of the machined specimens, we make use of the same dual-actuator system as for biaxial plasticity testing to subject the specimen to a combination of

horizontal (tangential) and vertical (normal) loads ($\beta = 63°$ until the maximum force is reached). The displacements of the specimen boundaries are measured using digital image correlation. The measured vertical and horizontal force-displacement curves are shown as solid dots in Fig. 2-13.

2.5.2 Finite elements model

The specimen geometry is discretized using first-order reduced integration solid elements (element C3D8R of the Abaqus element library). Due to the symmetry of the mechanical problem only one half of the specimen is meshed with at least five elements along the thickness direction. A total of 80,000 elements is used to mesh the entire specimen geometry. The DIC measured displacements and rotations (almost zero) are applied to the boundaries of the virtual specimen assuming that the boundary surfaces remain plane throughout testing. The simulations are performed using Abaqus/explicit with double precision. The material density and loading velocity are scaled such that more than 500,000 explicit time steps are required to compute the quasi-static solution of the boundary value problem.

A user subroutine of the associated and non-associated plasticity model is programmed for solid elements. In the three-dimensional case, the Cauchy stress vector $\boldsymbol{\sigma}$ is written as

$$\boldsymbol{\sigma} = [\sigma_0 \quad \sigma_{90} \quad \sigma_n \quad \tau \quad \tau_{0n} \quad \tau_{90n}]^T \tag{2-27}$$

where we introduced the through-thickness normal stress σ_n and the out-of-plane shear stress components τ_{0n} and τ_{90n}. The corresponding $\boldsymbol{P}$-matrix defining the quadratic yield function reads:

$$\boldsymbol{P} = \begin{bmatrix} 1 & P_{12} & -(1+P_{12}) & 0 & 0 & 0 \\ P_{12} & P_{22} & -(P_{22}+P_{12}) & 0 & 0 & 0 \\ -(1+P_{12}) & -(P_{22}+P_{12}) & 1+2P_{12}+P_{22} & 0 & 0 & 0 \\ 0 & 0 & 0 & P_{33} & 0 & 0 \\ 0 & 0 & 0 & 0 & 3 & 0 \\ 0 & 0 & 0 & 0 & 0 & 3 \end{bmatrix} \tag{2-28}$$

Analogously, the $\boldsymbol{G}$-matrix is extended from the two- to the three-dimensional case.

2.5.3 Results

The numerical simulations are performed for material model #1 (isotropic yield with AFR), model #2 (orthotropic yield with AFR) and model #5 (planar isotropic yield with non-AFR). Figure 2-13 shows the predicted vertical and horizontal force-displacement curves. It is interesting to observe that the isotropic model overestimates the vertical force (Fig. 2-13a) while it underestimates the horizontal force (Fig. 2-13b). The simulation with the associated orthotropic model (red curves) provides an accurate prediction of the vertical force up to a displacement of about 0.3mm, but overestimates the vertical force level thereafter. The same model overestimates the horizontal force up to its maximum. Beyond this point, the horizontal force decreases much faster in the simulation than in the experiments. The non-associated planar isotropic model (blue curves) provides the best overall predictions. It slightly underestimates the vertical force level at the beginning of the experiments, but provides very accurate predictions of the tangential force-displacement curve including its decreasing branch.

The advantages of the non-associated model become also apparent when comparing the fields of deformation. Figure 2-14a shows the DIC measured field of deformation towards the end of the experiment. A band of deformation localization is clearly visible at that point. The corresponding numerical predictions (Figs. 2-14b and 2-14c) reveal that the predictions of both the associated isotropic and the associated orthotropic models are noticeably different from the experimental result. The orientation of the band of localization is almost opposite to that observed in the experiment. However, the predicted orientation of

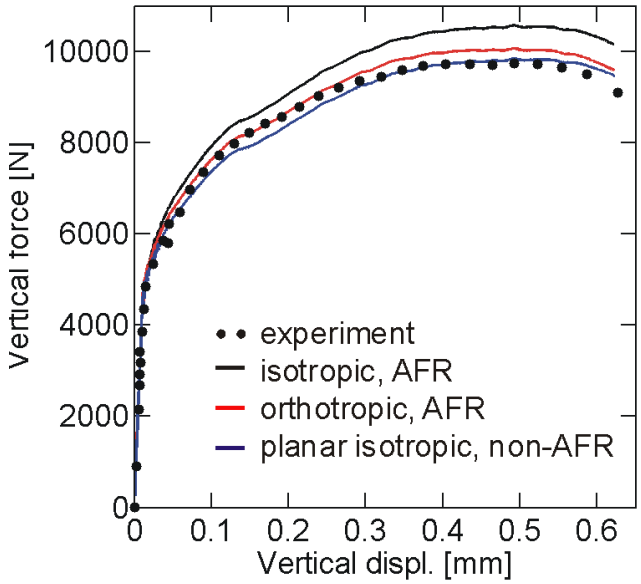

(a)

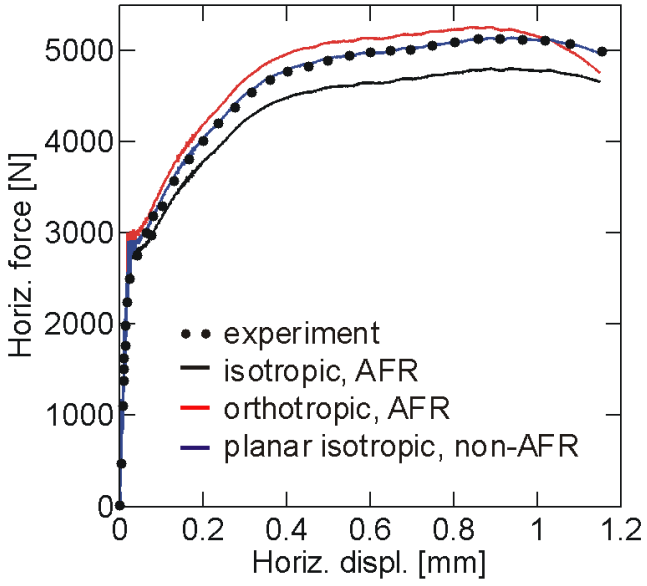

(b)

Figure 2-13: Results for butterfly specimen : (a) vertical force-displacement curve, (b) horizontal force-displacement curve.

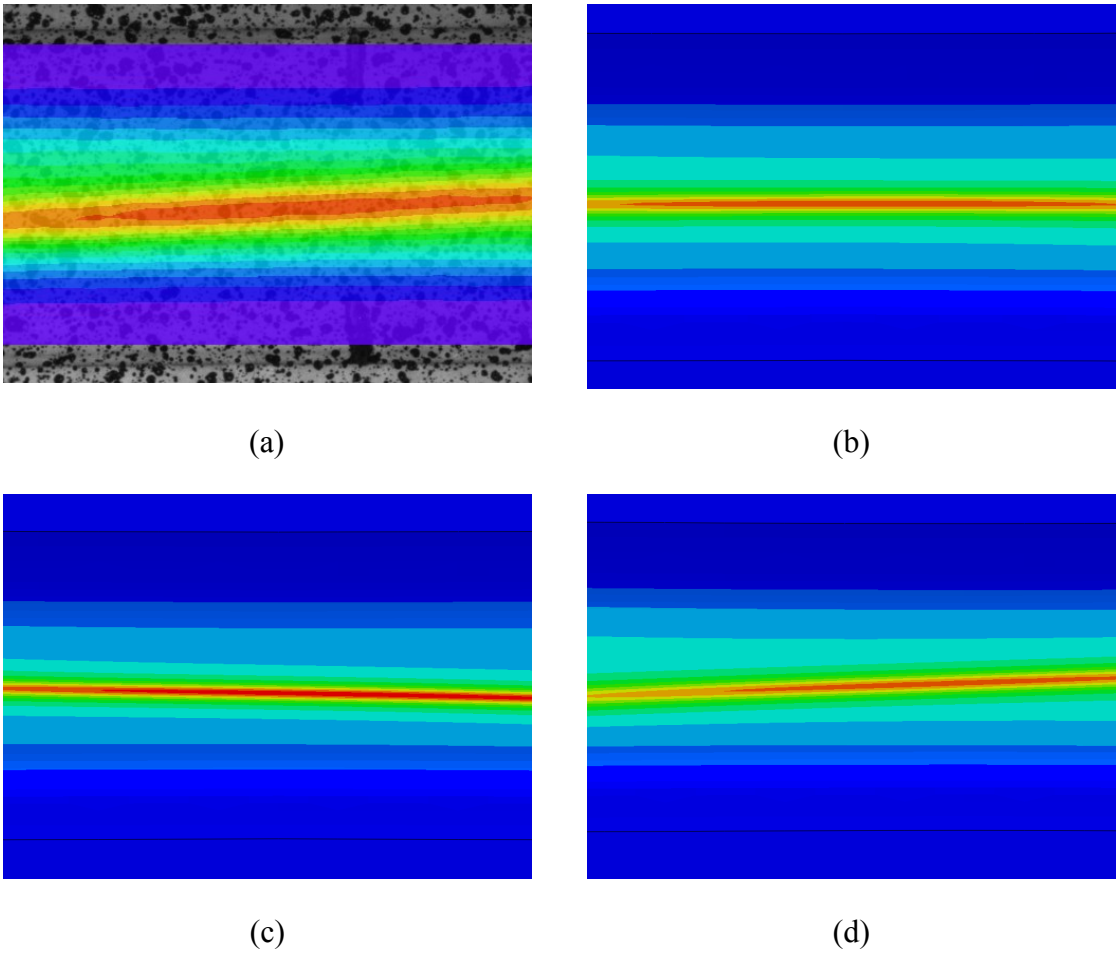

Figure 2-14: Contour plot of the maximum principal strain fields before the onset of fracture : (a) experiment, (b) isotropic model with AFR, (c) orthotropic model with AFR, (d) planar isotropic model with AFR. The Lagrangian strain ranging from 0 to 0.8 is shown for the experiment, while the logarithmic strain ranging from 0 to 0.95 is depicted for the simulations. In all four cases, the strain fields are plotted on the undeformed configuration of the butterfly specimen.

the simulations with non-associated flow rule (Fig. 2-14d) agrees well with the experimental observation (Fig. 2-14a).

2.6 Discussion

The results for uniaxial tension clearly indicate that the anisotropy of the material needs to be taken into account in order to obtain satisfactory predictions of the direction-dependent thickness reduction. Thus, different anisotropic models have been considered for the multi-axial simulations in addition to the isotropic Levy-von Mises model. The comparison of the simulation and experimental results shows that all models provide overall good estimates of the stress-strain curves for a wide range of multi-axial loading conditions. Both associated and non-associated plasticity models have been considered. The present comparison of the respective model predictions with the results from biaxial plasticity tests does not provide a clear answer to the question as to whether the plasticity of the DP and TRIP steels is associated or non-associated. However, the example of a butterfly-shaped specimen shows strong evidence that the plasticity of the TRIP steel is non-associated.

Both the associated and non-associated model types appear to perform well under the tested multi-axial loading conditions. Highly accurate measurements and repeatable material properties would be needed to shed more light on this issue. Here, the accuracy of the experimentally-measured stresses is only about $\pm 2\%$ for the multi-axial experiments (Mohr and Oswald, 2008, [109]). The uniaxial tensile experiments have shown that almost the same stress-strain curve is obtained while the r-ratio varies for different specimen orientations. Therefore, a non-associated plasticity model with a planar isotropic yield surface and a non-associated anisotropic flow potential is proposed to model the uniaxial experiments.

Most of the present biaxial plasticity experiments have been performed under force control. The material has been loaded along radial loading paths in stress space. Thus, the choice of the yield surface had a stronger effect on the measured stress-strain curves for multi-axial loading than the flow rule. Note that the multi-axial simulation results for model #1 (isotropic yield surface and isotropic flow rule) and model #4 (isotropic yield and orthotropic flow rule) are almost identical for loading angles and specimen orientations. Similarly, all multi-axial predictions for model #3 (planar isotropic yield surface and associated flow) and model #5 (planar isotropic yield surface and non-associated flow) were

almost identical. The differences between the isotropic von Mises surface and the orthotropic Hill'48 surface are small for the tested DP590 material. A future study on a sheet material with a higher degree of anisotropy may allow for a better differentiation between the prediction accuracy of associated and non-associated plasticity models. Furthermore, it is recommended to include equi-biaxial tensile tests in the experimental program to validate the assumption of a quadratic yield function.

2.7 Concluding remarks

The isotropic Levy-von Mises model and the associated orthotropic Hill (1948, [73]) plasticity models are considered in this study to describe the large deformation response of advanced high strength steel sheets. The uniaxial tensile experiments on a dual phase and TRIP-assisted steel reveal a pronounced in-plane direction-dependence of the r-ratios while the measured stress-strain curves appeared to be direction-independent. Here, Stoughton's (2002, [134]) non-associated quadratic flow rule is employed as an alternative to non-quadratic associated plasticity models. Using a newly-developed testing technique for sheet materials (Mohr and Oswald, 2008, [109]), a series of multi-axial experiments has been performed on the dual phase steel DP590 and the TRIP-assisted steel TRIP780. The comparison of the biaxial experiments with the simulation results shows that both the associated and non-associated quadratic plasticity model provide a satisfactory description of the mechanical response under multi-axial loading. However, the non-associated model is recommended for the DP590 and TRIP780 materials when the thinning of the sheets needs to be predicted with a high degree of accuracy. Moreover, a structural validation example is presented that elucidates substantial differences between the simulations with associated and non-associated flow rule. In the case of the non-associated flow rule the force-displacement curves as well as the position of the strain localization band are predicted accurately.

The present results for the TRIP780 also show that - unlike in fully austenitic steels (see Mohr and Jacquemin, 2008, [106]) - the presence of martensitic phase transformation in TRIP-assisted steel does not require a modification of the associated hardening model.

Chapter 3

Hybrid experimental-numerical analysis of basic fracture experiments

Contents

3.1 Introduction

In most fracture experiments on sheet materials, the localization of plastic deformation through necking cannot be avoided. After necking, the stress fields within the specimen gage section become non-uniform and of three-dimensional nature (stresses in the thickness direction develop). Consequently, the stress history prior to fracture can no longer be

[2] This Chapter is reproduced from: Dunand, M. and D. Mohr (2010). "Hybrid experimental-numerical analysis of basic ductile fracture experiments for sheet metals". International Journal of Solids and Structures **47**(9): p. 1130-1143.

estimated from the force history measurements using simple analytical formulas. Unless reliable in-situ neutron diffraction stress measurements (e.g. Lee et al., 2003, [87]) and three-dimensional tomography based digital image correlation measurements (e.g. Baranger et al., 2009, [12]) are available, the stress and strain histories prior to fracture need to be determined in a hybrid experimental-numerical approach. In other words, a detailed finite element analysis of each experiment is required to identify the stress and strain fields. This forced marriage of experimental and computational mechanics involves the risk of adding up the errors from both the experiment and the numerical simulation.

In this Chapter, we limit our attention to the determination of the stress triaxiality and the equivalent plastic strain history to fracture. In an attempt to identify the intrinsic material behavior, we analyze the local stress and strain fields after necking. A series of three different types of fracture experiments is carried out on TRIP assisted steel: notched tensile tests, punch tests and tensile test on specimens with a central hole. The common feature of these three types of fracture experiments is their simplicity: (1) the specimens can be easily extracted from sheet material, and (2) all experiments can be performed on a universal testing machine. For each type of specimen, the accuracy of the hybrid experimental-numerical loading history identification is evaluated from the comparison of local digital image correlation measurements with FE predictions. It is found that the shell element meshes are not suitable for post-necking analysis of local strain fields. Conversely, solid element simulations provide accurate estimates of the measured local strain fields when the plasticity model is identified for large strains. The results demonstrate the stress triaxiality in specimens with a central hole is close to 0.3 all the way to fracture. Furthermore, it is noted that this type of experiment is also suitable for the identification of the stress-strain curve for very large strains.

3.2 Methodology

The goal of this Chapter is to obtain reliable time histories of the stress triaxiality and the equivalent plastic strain at the point of the onset of fracture. In particular, we focus on

three fracture tests that may be easily performed on full-thickness specimens: (1) notched tensile specimens, (2) a tensile specimen with central hole, and (3) a disc specimen for punch testing. It is noted that the first two types of specimens can develop diffuse necking (localization through the width of the gage section) prior to the onset of localized necking (through the thickness localization) while the punch test cannot develop diffuse necking because of its geometry. Here, we make use of a hybrid experimental-numerical approach to determine the loading histories. As a result, the determination of the strain to fracture is not affected by these different necking behaviors. In this section, we discuss the methodology to assess the error of the hybrid experimental-numerical approach.

3.2.1 Determination of the onset of fracture

The displacement fields on the specimen surface are measured using either two-dimensional or three-dimensional Digital Image Correlation (DIC). Based on the DIC measurements, we define the *instant of onset of fracture* (not the location) by the first detectable discontinuity in the measured displacement field at the specimen surface. Subsequently, a finite element simulation is performed of each experiment. Post-processing of those simulations gives then access to the evolution of the stress triaxiality and the equivalent plastic strain. For the three types of experiments performed within this study, it is assumed that the *location of the onset of fracture* coincides with the location of the highest equivalent plastic strain within the specimen at the instant of onset of fracture. The corresponding equivalent plastic strain is referred to as *fracture strain* $\bar{\varepsilon}_f$.

3.2.2 Sources of error

3.2.2.1 Experimental error

Among all experimental uncertainties, we consider the error in the optical displacement field measurement as critically important for the determination of the fracture strain and triaxiality. Possible errors in the initial specimen geometry including thickness

can be easily eliminated through dimensional verification prior to each experiment. The accuracy of the DIC procedure used to measure the fracture displacement depends mainly on the quality of the speckle pattern applied on the specimen and on the interpolation function used during the correlation. In order to get the least error, the pattern has been applied following the recommendations of Sutton et al. (2009, [138]) in terms of speckle size and density. Based on correlations performed on computer-generated sinusoidal waves, Sutton et al. (2009, [138]) concluded that for an appropriate speckle pattern, cubic B-spline displacement field interpolation functions produce an interpolation bias of about 1/40 pixel.

3.2.2.2 Computational error

The solution obtained from finite element analysis usually differs from the exact solution of the corresponding physical problem. In addition to shortcomings of the material model, the FEA is affected by different sources of errors (e.g. Bathe, 1996, [16]). In particular, errors associated with the spatial and time discretization as well as the constitutive model are monitored in this study:

- Spatial discretization errors are minimized by increasing the number of elements. To find a suitable mesh, we start with a coarse mesh that is successively refined by dividing the elements' characteristic dimensions by two until the result converges. It is considered that convergence is achieved when an additional element division does not change the final plastic strain by more than 0.5%.
- Time discretization errors are minimized by increasing the number of implicit time steps. It is considered that convergence is achieved when adding 50% more time increments does not change the final plastic strain by more than 0.5%.

Furthermore, round-off errors are minimized by using the double precision floating point format in our computations with explicit time integration.

3.2.3 Error estimation

Due to the redundancy of measurements, we compare the logarithmic strain history obtained from DIC with that computed by FEA at the point on the surface where the first displacement field discontinuity appears. For every time step in the finite element simulation, there is a difference between the computed strain increment $d\varepsilon_{FEA}$ at the surface of the specimen and the actual strain increment $d\varepsilon_{DIC}$ measured by DIC. The error affecting the determined plastic strain increment at the location of the onset of fracture, $\delta(d\bar{\varepsilon}^p)$, is then estimated based on the strain increment difference on the specimen surface,

$$\delta(d\bar{\varepsilon}^p) \cong \frac{d\bar{\varepsilon}^p}{|d\varepsilon_{DIC}|}|d\varepsilon_{DIC} - d\varepsilon_{FEA}| \tag{3-1}$$

Furthermore, we estimate the error in the accumulated equivalent plastic strain as

$$\delta\bar{\varepsilon}^p \cong \int_0^{\bar{\varepsilon}_f} \frac{|d\varepsilon_{DIC} - d\varepsilon_{FEA}|}{|d\varepsilon_{DIC}|} d\bar{\varepsilon}^p \tag{3-2}$$

It is noted that the above error estimate represents both computational and experimental uncertainties. Using the definition of the stress triaxiality,

$$\eta = \frac{\sigma_m}{\bar{\sigma}_{VM}} \quad \text{with} \quad \sigma_m = \frac{\mathrm{tr}\,\boldsymbol{\sigma}}{3} \tag{3-3}$$

the error in the stress triaxiality is related to the error in the hydrostatic stress $\boldsymbol{\sigma_m}$ and that in the von Mises stress,

$$\delta\eta = \frac{1}{\bar{\sigma}_{VM}}[\delta\sigma_m + \eta\,\delta\bar{\sigma}_{VM}] \tag{3-4}$$

It is assumed that all the components of the stress tensor are computed with the same relative error,

$$\frac{\delta\sigma_m}{|\sigma_m|} = \frac{\delta\bar{\sigma}_{VM}}{\bar{\sigma}_{VM}} = \frac{\delta\bar{\sigma}}{\bar{\sigma}} \tag{3-5}$$

and thus

$$\delta\eta = 2\frac{\eta}{\bar{\sigma}_{VM}}\delta\bar{\sigma} \tag{3-6}$$

Using the hardening law, the first order estimate of the error in stress triaxiality may be written as

$$\delta\eta = 2\frac{\eta}{\bar{\sigma}_{VM}}H(\bar{\varepsilon}^p)\delta\bar{\varepsilon}^p \tag{3-7}$$

3.3 Notched tensile tests

The first type of specimen considered in this study is a flat tensile specimen with circular cutouts (Figs. 3-1a to 3-1c). The stress triaxiality within the specimen is a function of the notch radius. For very large notch radii the stress state near the specimen center (prior to necking) corresponds to uniaxial tension, while the plane strain condition (along the width direction) is achieved for very small notch radii. In the case of isotropic materials, this variation of stress state corresponds to a range of triaxialities from 0.33 to 0.58.

3.3.1 Experimental procedure

Specimens are extracted from the sheet material using water-jet cutting. The specimen loading axis is always oriented along the rolling direction. All specimens are 20mm wide and feature a b=10mm wide notched gage section. Three different notch radii are considered: R=20mm, R=10mm and R=6.67mm. The specimens are tested on a hydraulic testing machine (Instron Model 8080) with custom-made high pressure clamps. All experiments are carried out under displacement control at a constant crosshead velocity of 0.5mm/min.

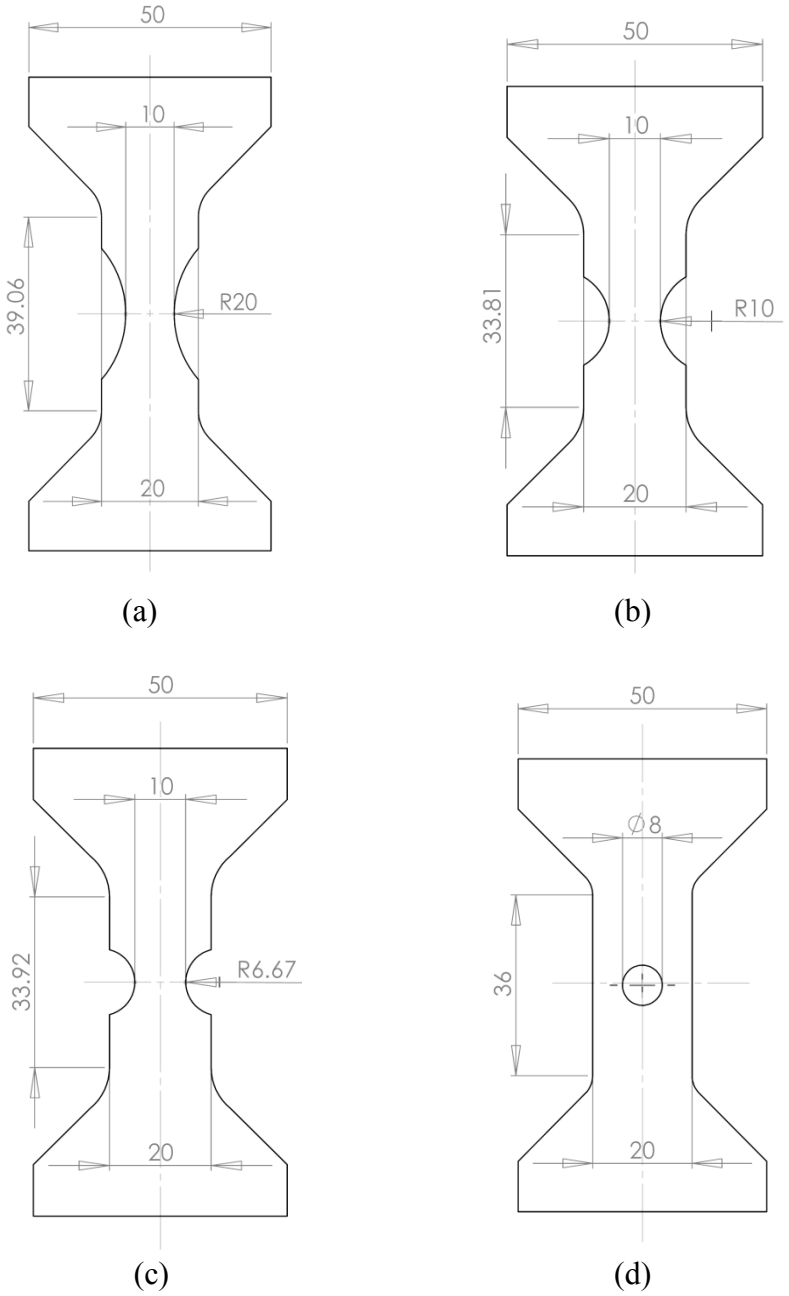

Figure 3-1: (a)-(c) Tensile specimens with different notch radii, (d) tensile specimen with central hole. The special shape of specimen shoulders is due to the geometry of our high pressure grips; the total clamping force is applied to an area of 50 x 10 mm at the top of the shoulders.

During the tests, two digital cameras (QImaging Retiga 1300i with 105mm Nikon Nikkor lenses) take about 300 pictures (resolution 1300x1300 pixels) of the speckle-painted front and back surface of the specimens. The pictures of the front surface are used to determine the displacements of the specimen boundaries. The front camera is positioned at a distance of 1.25m to take pictures of the entire specimen (square pixel edge length of 51μm). The photographs of the back face are used to perform accurate DIC measurements of the displacement field at the center of the specimen gage section. For that purpose, the second camera is positioned at a distance of 0.25m which reduces the square pixel edge length to 9.5μm. The average speckle size is about 70μm on both faces. The displacement field is calculated by DIC (VIC2D, Correlated Solutions) based on the assumption of an affine transformation of the 21x21 pixel neighborhood of each point of interest. The logarithmic axial strain at the center of the specimen is computed from the relative vertical displacement Δv of two points located at the center of the specimen,

$$\varepsilon = \ln\left(1 + \frac{\Delta v}{\Delta_y}\right) \tag{3-8}$$

Both points are located on the vertical axis of symmetry at an initial distance of $\Delta y = 20$ pixels (190μm). For each specimen geometry, we also performed an interrupted test: the monotonic displacement loading has been interrupted at a crosshead displacement of approximately 98% of the measured displacement to fracture. Subsequently, two 12 mm long samples have been extracted from the deformed specimen gage section; the small samples are embedded in an epoxy matrix for polishing; low magnification pictures are then taken to determine the thickness profile along the specimen's planes of symmetry.

3.3.2 Experimental results

The force-displacement curves for the three different notched geometries (black solid dots in Fig. 3-2) are shown all the way to fracture. All feature a force maximum before fracture occurs. The displacement to fracture presents small variations for different tests carried out on a given geometry (less than 3%). The measured fracture displacements and

the corresponding experimental uncertainty are summarized in Table 3-1. DIC analysis of the strain fields shows significant strain localization near the center of the specimens. The evolution of the logarithmic axial strain with respect to displacement is shown as solid blue dots in Fig. 3-2. Irrespective of the notch radius, two consecutive increases of the local strain rate become apparent. The first corresponds to the development of diffuse necking, while the second indicates the onset of localized necking. The localized necking provokes a severe thickness reduction at the center of the specimens. The measured thickness variations along the axial plane of symmetry of the samples obtained from interrupted tests are depicted in Fig. 3-3. Observe the severe thickness reduction for all three geometries.

3.3.3 Finite element model

Implicit finite element simulations are performed of each experiment using Abaqus/standard. Reduced integration eight-node 3D solid elements (type C3D8R of the Abaqus element library) are used to mesh the specimens. Exploiting the symmetry of the specimen geometry, material properties and loading conditions, only one eighth of the specimen is modeled: the mesh represents the upper right quarter of the specimen, with half its thickness (Fig. 3-4). A constant velocity is uniformly imposed to the upper boundary. A zero normal displacement condition is imposed to the three boundaries that correspond to symmetry planes.

The effect of mesh density and time discretization on the computational predictions is studied for the R=10mm notch specimen geometry. Four meshes are considered (Fig. 3-4):

(i) coarse mesh with an element edge length of $l_e = 400\mu m$ at the specimen center and $n_t = 2$ elements in thickness direction (half thickness),

(ii) medium mesh with $l_e = 200\mu m$ and $n_t = 4$;

(iii) fine mesh with $l_e = 100\mu m$ and $n_t = 8$;

(iv) very fine mesh with $l_e = 50\mu m$ and $n_t = 16$;

The meshes are designed such that the elements near the specimen center feature the same dimension in the in-plane directions. In addition to solid element simulations, we make use

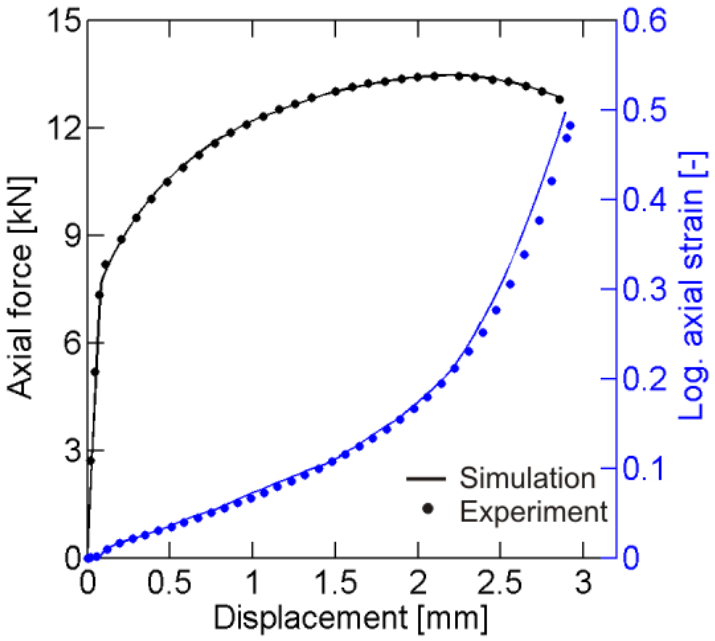

(a) $R = 20mm$

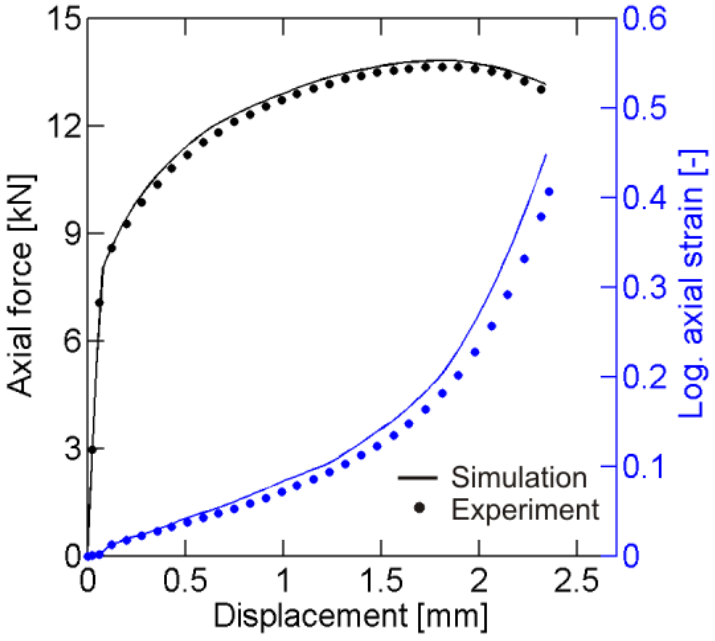

(b) $R = 10mm$

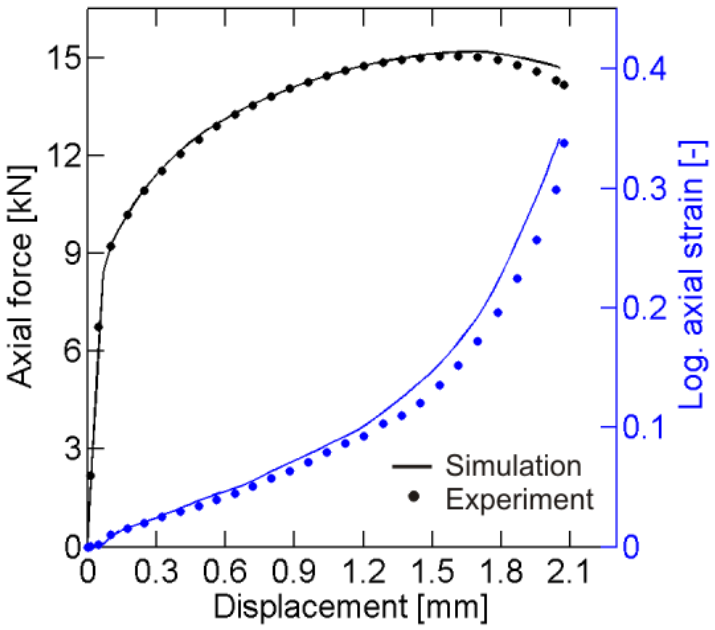

(c) $R = 6.67mm$

Figure 3-2: Experimental (points) and simulation (solid curves) results for tensile specimen with circular cutouts. Force displacement curves are in black and central logarithmic axial strain versus displacement curves in blue.

Table 3-1: Experimental results and fracture predictions for the tensile specimens with circular cutouts

Notch radius [mm]	Fracture displacement		Fracture plastic strain		Stress triaxiality at fracture	
	Value [mm]	Variation [%]	Value [-]	Variation [%]	Value [-]	Variation [%]
6.67	2.048	1.28	0.422	5.09	0.626	1.90
10	2.336	1.21	0.552	5.22	0.653	1.97
20	2.887	1.22	0.585	5.38	0.614	2.43

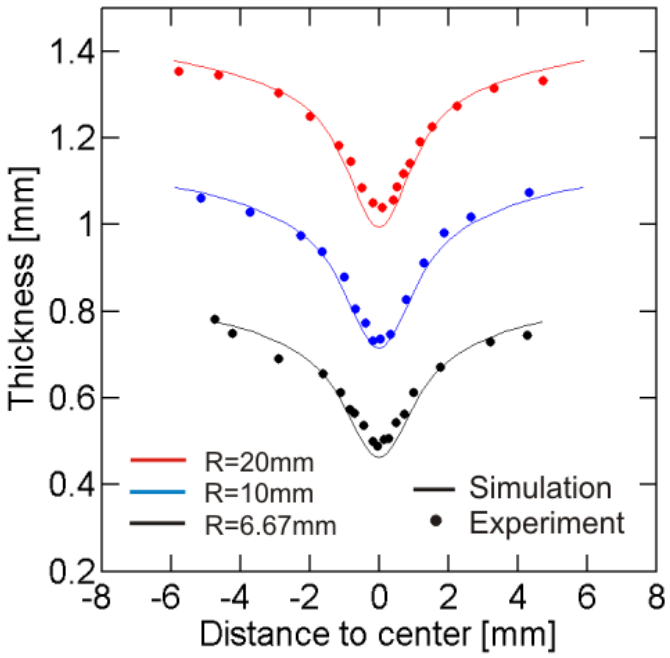

Figure 3-3: Thickness profile along the axial plane of symmetry for the 3 geometries. The curves corresponding to the 10mm and 6.67mm notched geometries are shifted by -0.3mm and -0.6mm respectively.

of first-order plane stress shell elements (S4R) with five integration points in the thickness direction. The simulations are run up to the fracture displacement. Forty equally spaced time increments are used. The corresponding force-displacement curves as well the evolution of the equivalent plastic strain at the center of the specimen with respect to displacement are plotted in Fig. 3-5a. The force-displacement curves lie on top of each other for all solid element meshes. However, the comparison with the results from shell element simulations shows that solid elements are required in order to provide meaningful predictions after the force maximum has been reached (after the onset of necking). Therefore, we limit our attention to the solid element simulations.

The predictions of force-displacement relationship are approximately mesh size independent, but the mesh density has a noticeable effect on the predicted strains at the specimen center. The final plastic strain computed with the coarse mesh is 7.3% lower than that for the very fine mesh. The relative error between the fine and very fine meshes being

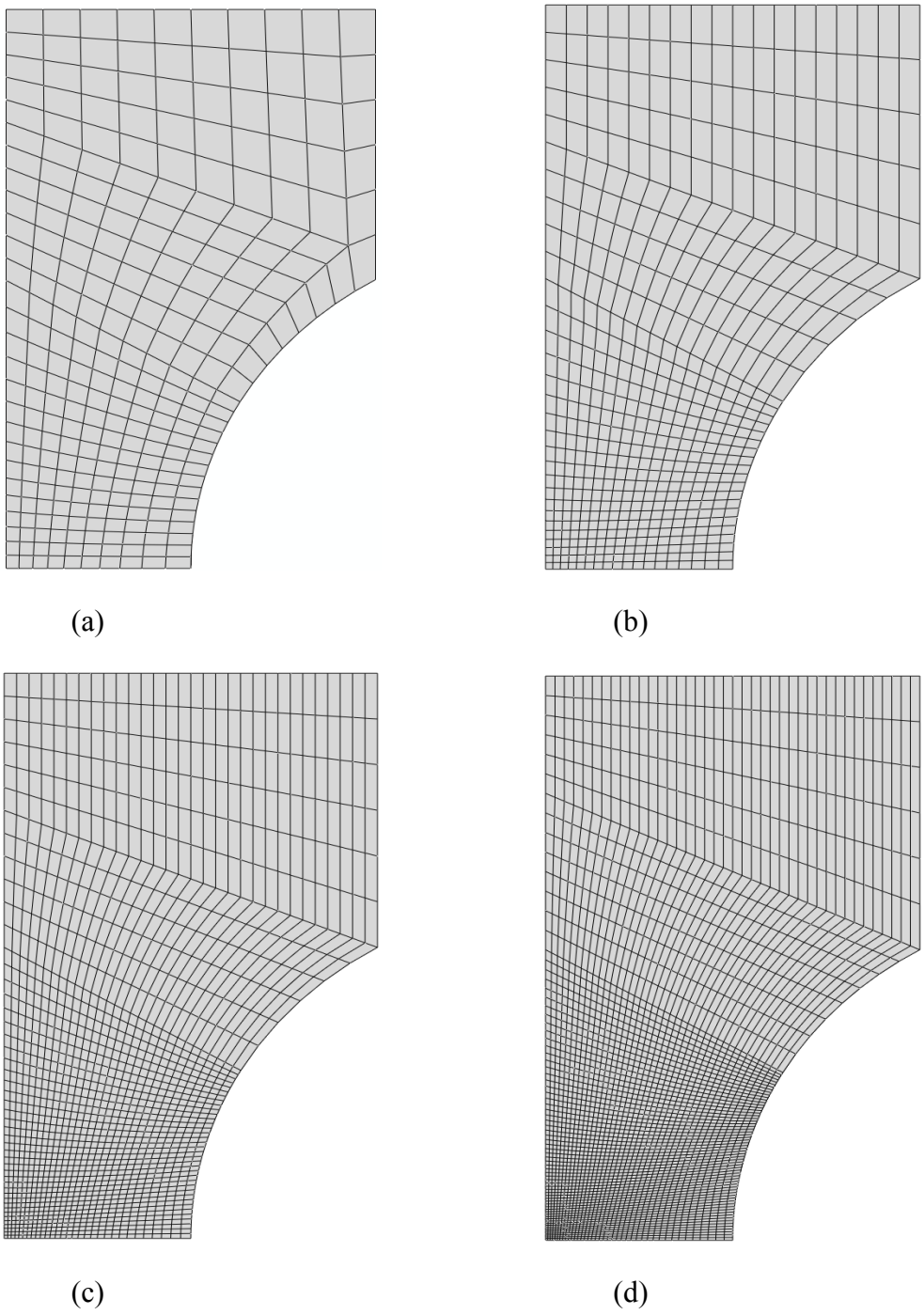

Figure 3-4: Meshes of the 10 *mm* notched radius specimen. (a) Coarse mesh with 2 elements through half the thickness, (b) medium mesh with 4 elements through half the thickness, (c) fine mesh with 8 elements through half the thickness, (d) very fine mesh, with 16 elements through half the thickness.

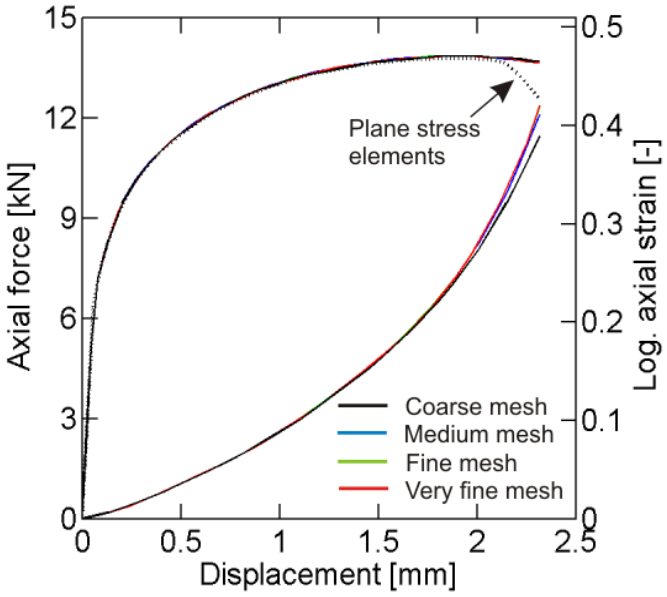

(a)

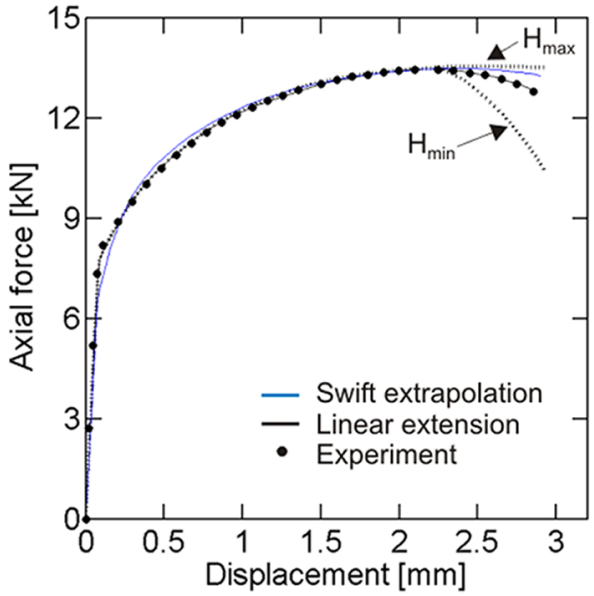

(b)

Figure 3-5: Modeling of notched tensile specimens. (a) Effects of spatial discretization on the predicted force and strain versus displacement curves for R=10*mm*. (b) Influence of the strain hardening extrapolation on the prediction of the force-displacement curve for R= 20*mm*.

only 0.2%. Errors due to time discretization are evaluated by running a simulation on the fine mesh with 40, 60 and 90 implicit time steps. The difference in the final plastic strain between 40 and 90 steps is 0.7%, while a difference of less than 0.2% is observed for 60 time steps. In the following, all simulations of notched tensile tests are performed using at least 8 solid elements through the half-thickness and at least 60 equally spaced implicit time increments.

3.3.4 Extrapolation of the stress-strain curve

The Swift strain hardening curve has been validated for equivalent plastic strains of up to 0.2 (point of necking under uniaxial tension). However, in notched tensile specimens, the plastic strains at the specimen center are much higher than 0.2. The comparison of the experimentally-measured force-displacement curve for R=20mm (black solid dots in Fig. 3-5b) with the simulation results shows that the Swift model assumption overestimates the force level (blue solid line). The assumption of a tangent modulus of $H_{min} = 0$ for strains greater than 0.2 yields an underestimation of the force level. To obtain a better extrapolation of the measured stress-strain curve, we defined two segments of constant slope H_1 and H_2; here, H_1 corresponds to the range of intermediate plastic strains (from 0.2 to 0.35), H_2 to the range of high plastic strains ($\bar{\varepsilon}^p$ higher than 0.35). The two strain hardening rate moduli are calibrated such that the simulation provides a good prediction of the experimentally-measured force-displacement curve (Fig. 3-5b).

3.3.5 Comparison of simulations and experiments

In Fig. 3-2, we show the simulated force-displacement curves (solid black lines) all the way to fracture. The agreement with the experimental results (depicted with black dots) is very good for the 20mm (Fig. 3-2a) and 10mm (Fig. 3-2b) notch geometries. The force difference between simulation and experimental results is less than 1% in both cases. For the 6.67mm notch geometry (Fig. 3-2c), the peak of force, corresponding to the onset of localized necking, is delayed in the simulation by relative displacement of about 5%. As a result, the FEA predicted force drop is too small: the axial force at the onset of fracture is

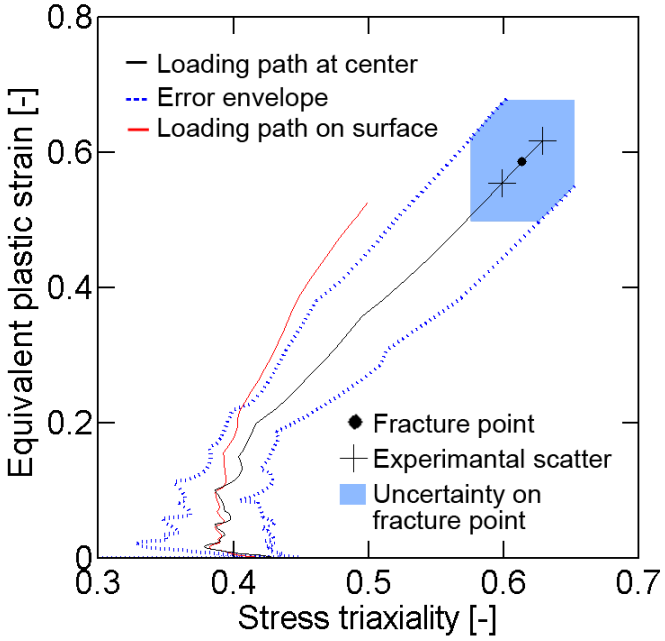

(a) $R = 20mm$

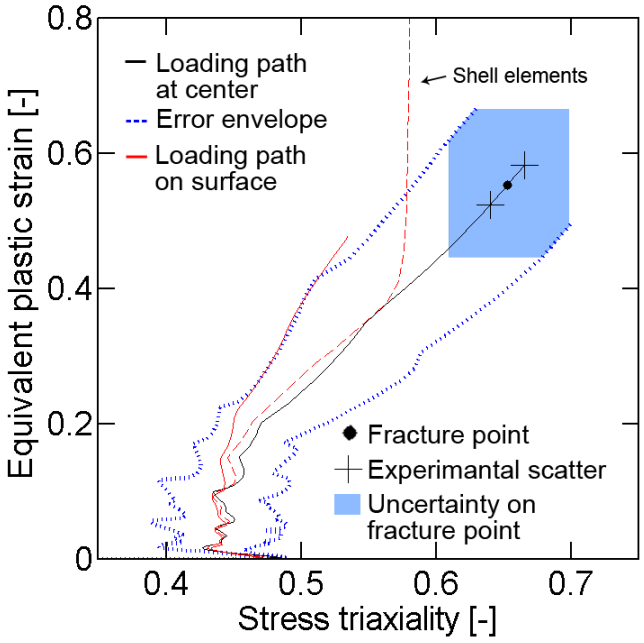

(b) $R = 10mm$

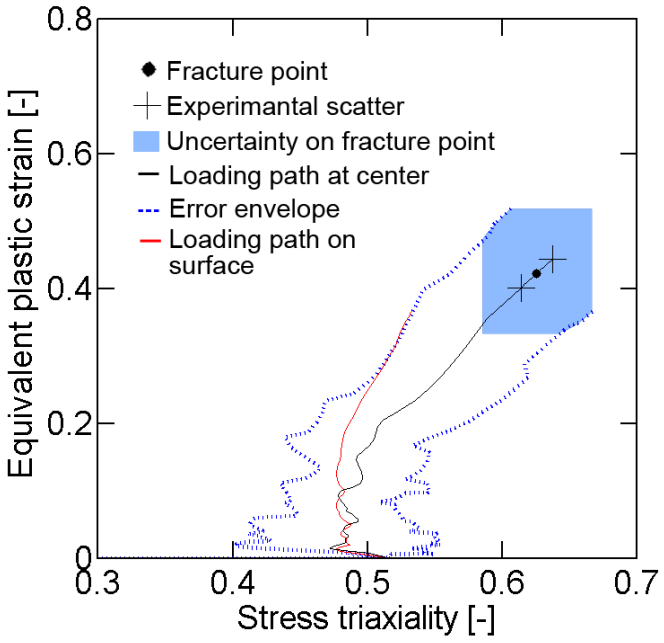

(c) $R = 6.67mm$

Figure 3-6: Loading paths at the center of the specimen. The red solid line depicts the loading path at the surface, the black solid line at the mid-plane; black dots and the crosses highlight the onset of fracture including experimental scatter (min/max). The dashed blue lines show the error envelopes.

3.7% higher in the simulation than in the experiment. The comparison of the evolution of the logarithmic axial strain at the center of the gage section with respect to the displacement (depicted in blue in Fig. 3-2) also shows a good agreement. Irrespective of the notch radius, the simulations are able to describe the characteristic increases in strain rates that have been observed in the experiments. Relative differences between simulation and DIC strains in case of the 20mm notch geometry are about 3% (Fig. 3-2a). For the 10mm notch geometry (Fig. 3-2b), the computed strain is of up to 10% higher than the DIC measurement. As far as the 6.67mm notch geometry is concerned (Fig. 3-2c), the first increase of strain rate is too large in the simulation, while the predicted strain rate increase after the onset of localized necking appears to be smaller than that given by DIC. As a result, differences between

simulated and measured strains tend to decrease at the end of the simulation, to be almost zero at fracture. Figure 3-3 depicts the thickness profile along the axial plane of symmetry of the specimens (20mm in red, 10mm in blue, 6.67mm in black). Note that both the amplitude of thickness variation and the size of the area of localization are very well predicted by the simulations.

3.3.6 Stress triaxiality and equivalent plastic strain evolution

Figures 3-6a to 3-6c show the evolution of the equivalent plastic strain as a function of the stress triaxiality η at the center of the gage area. The red solid lines depict the evolution on the specimen surface, while the black solid lines show the evolution at the very center of the specimen (intersection point of all three symmetry planes). The large solid dot marks the onset of fracture that is obtained when using the average fracture displacement from three experiments. The crosses indicate the corresponding simulation results for the measured minimum and maximum displacement to fracture (see also Table 3-1). The comparison of the red and black curves clearly shows that the stress and strain state at the specimen surface is significantly different from that at the specimen mid-plane. In other words, there is a strong gradient along the thickness direction within the central zone of strain localization. The equivalent plastic strains to fracture inside the specimen are 11.5% (20mm notch) and 15.8% (10mm notch) higher inside the specimen than on the surface (see Fig. 3-7). Localized necking also leads to the development of out-of-plane stress components in the middle of the specimen (while the surface deforms under plane stress), which increases the stress triaxiality. Furthermore, the strains measured at the specimen surface are not representative for the strain to fracture of the material (red line in Fig. 3-6). It is also noted that the stress triaxiality exhibits very strong variations during loading. For instance, for R=20mm it increases from $\eta = 0.40$ before the onset of localized necking to $\eta = 0.61$ at the onset of fracture.

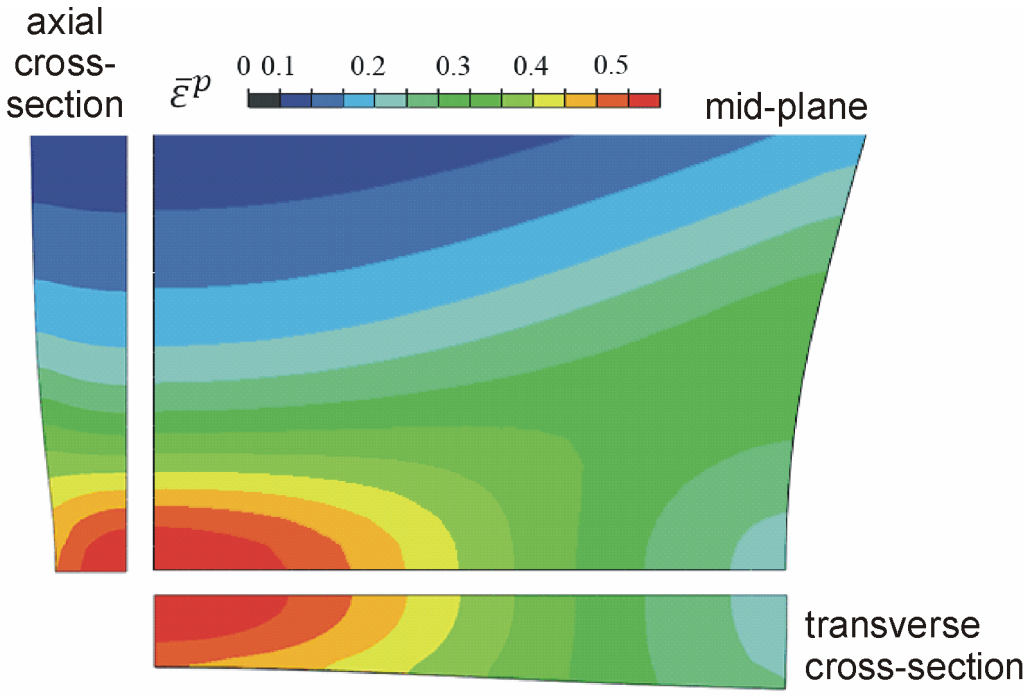

Figure 3-7: Contour plot of the equivalent plastic strain at the instant of the onset of fracture in a notched specimen with R=10mm.

3.3.7 Uncertainty analysis

Three different types of errors affecting both the plastic strain and the stress triaxiality at the onset of fracture are summarized in Table 3-2. Considering DIC accuracy and camera resolution, the relative displacement of the specimen boundaries is measured in all experiments with an accuracy of 2.5μm. Due to the strain localization at the center of the specimen, the errors in the fracture displacement translate to even larger errors in the fracture strain. This small uncertainty in the measured fracture displacement (relative error of about 0.1%) leads to an error of about 0.004 on the fracture strain and 0.002 on the stress triaxiality at the onset of fracture.

Table 3-2: Errors in the evaluation of the plastic strain and stress triaxiality at the onset of fracture

Notch radius [mm]	Fracture plastic strain			Stress triaxiality at fracture		
	Displacement error [-]	Modeling error [-]	Total error [-]	Displacement error [-]	Modeling error [-]	Total error [-]
6.67	$0.34\ 10^{-2}$	$7.31\ 10^{-2}$	$7.65\ 10^{-2}$	$0.14\ 10^{-2}$	$3.16\ 10^{-2}$	$3.30\ 10^{-2}$
10	$0.43\ 10^{-2}$	$8.34\ 10^{-2}$	$8.77\ 10^{-2}$	$0.17\ 10^{-2}$	$3.57\ 10^{-2}$	$3.74\ 10^{-2}$
20	$0.46\ 10^{-2}$	$6.34\ 10^{-2}$	$6.80\ 10^{-2}$	$0.17\ 10^{-2}$	$2.55\ 10^{-2}$	$2.72\ 10^{-2}$

Errors due to the inaccuracy of the constitutive model are computed according to Eq. 3-2. For all three specimen geometries, the estimated error $\delta(\bar{\varepsilon}^p)$ on the plastic strain is less than 0.03 at the onset of localized necking and reaches 0.063 at the point of fracture for the 20mm notch geometry (0.083 and 0.073 for the 10mm and 6.67mm geometries, respectively). This emphasizes the difficulty of modeling the post necking behavior of the specimen with great accuracy. According to Eq. 3-7, this corresponds to errors on the stress triaxiality at the onset of fracture of 0.025 for the 20mm geometry, 0.036 for R=10mm and 0.032 for R=6.67mm. The errors affecting the plastic strain versus stress triaxiality curves are depicted in Figs. 3-6a to 3-6c by dashed blue lines. Those lines can be seen as the upper and lower boundaries on the evolution of the actual material state in the stress triaxiality/plastic strain space at the fracture locus. Colored areas surrounding fracture points depict the uncertainty on the actual fracture point due to both errors (plus experimental scatter). Those areas represent the precision achievable when determining the material state at the onset of fracture using tensile specimens with circular cutouts. Note that errors affecting stress triaxiality are very important for small strains, even if strain errors are then very small. According to Eq. 3-7, $\delta\eta$ is proportional to the current strain hardening modulus $H(\bar{\varepsilon}^p)$; the latter is very high for small strains, but decreases monotonically as the strain increases (e.g. $H = 8100MPa$ for $\bar{\varepsilon}^p = 0.01$ and $H = 40MPa$ for $\bar{\varepsilon}^p = 0.5$).

To illustrate the large error associated with the use of shell elements, we added a red dashed line to Fig. 3-6b which shows the predicted loading path evolution from a shell element simulation. The loading path agrees well with the solid element simulation prior to

necking, whereas the predicted strain increases to unrealistically high values after the onset of necking.

3.4 Circular punch test

The circular punch test is a standard sheet metal forming test that characterizes the formability of sheet materials under stress states that are close to equi-biaxial tension. Analogously to our analysis of the notched tensile test, we assess the accuracy of the circular punch test.

3.4.1 Experimental procedure

The circular sheet specimen is clamped on a circular die and subsequently loaded through a hemispherical punch. The punch and die have a diameter of 44.5mm and 100mm, respectively. The clamping pressure is applied through eight M10-12.9 screws. The experiment is carried out in a universal testing machine (MTS, Model G45) at a constant punch velocity of 5mm/min. In order to limit the effects of friction, a stack of six oil-lubricated 90μm thick Teflon layers is put between the specimen and the punch during each test.

Three-dimensional Digital Image Correlation (Vic3D, Correlated Solutions) is used to measure the out-of-plane deformation of the specimen. In our vertical experimental set-up, the clamping die is fixed on a special metal frame (Walters, 2009, [150]). A leaning mirror is integrated into that frame to record pictures of the speckle-painted bottom surface of the specimen with two digital cameras. The cameras see the specimen at a distance of 2.5m at an angle of 20° from the punching direction. Each camera records about 300 pictures during the test; the edge length of a square pixel is about 100μm. The displacement field is calculated by DIC for the entire free surface of the specimen assuming an affine transformation of the 21x21pixels neighborhood of each point. The interpolation of the gray values is performed with a 6-tap filter. The logarithmic strain field is then calculated by averaging the displacement gradient over an area of 11x11 pixels.

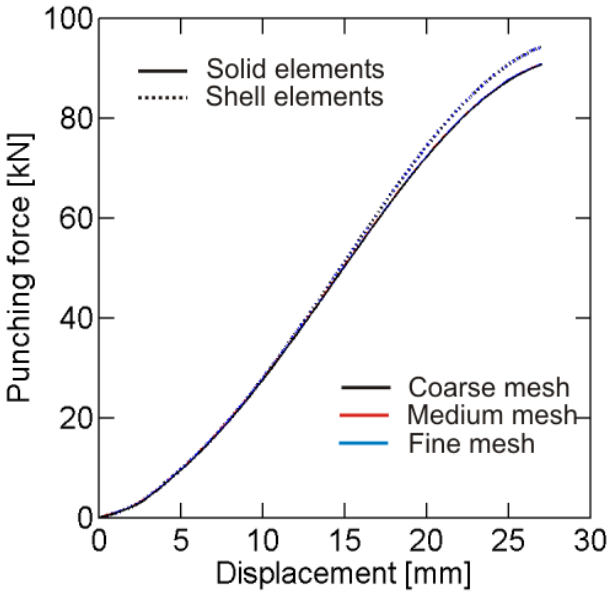

(a)

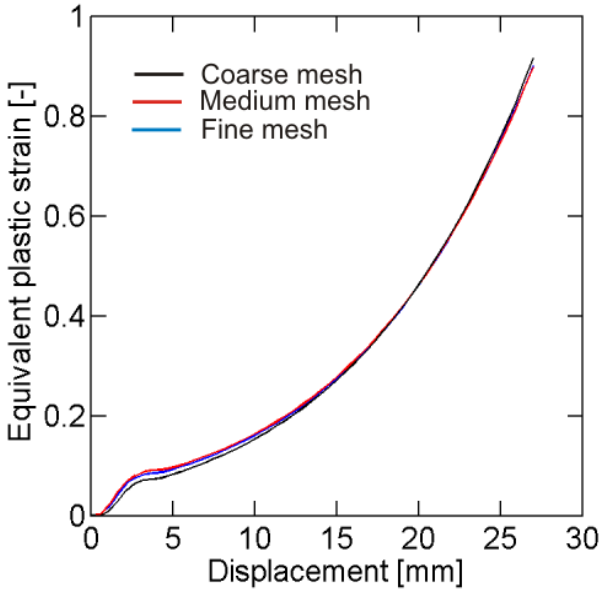

(b)

Figure 3-8: Punch test analysis. Influence of the mesh density on (a) the force-displacement curve, and (b) the equivalent plastic strain versus displacement curve. Results for solid and shell elements are depicted with solid and dashed lines, respectively;

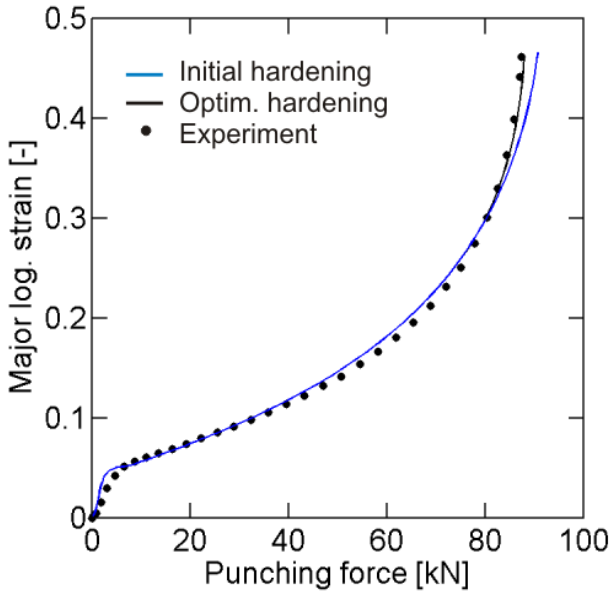

(c)

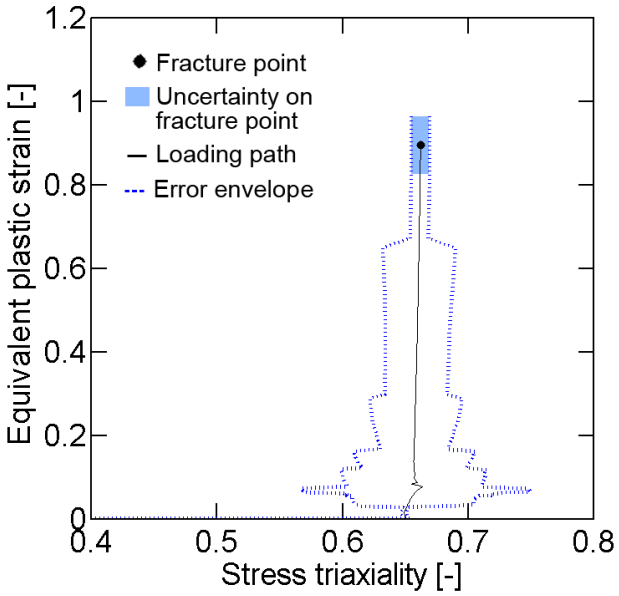

(d)

(c) Evolution of the major logarithmic strain on the specimen surface as a function of the punch force; (d) Loading paths in the $(\eta, \bar{\varepsilon}^p)$ space on the specimen's outer surface at the center of the specimen. The black dot indicates the onset of fracture, the dashed blue lines shows the error envelope.

3.4.2 Experimental Results

The measured force-displacement curve increases monotonically until a sharp drop in force level is observed at the instant of onset of fracture. The recorded cross-head displacement includes the deformation of the clamping fixture as well as the deformation of the punch and the testing frame in addition to the effective punch displacement. Since the punch behaves like a non-linear spring (because of the increasing contact area between the punch and the specimen) it is difficult to extract the displacement associated with permanent deformation of the specimen from these measurements. Moreover, we observed that most of the Teflon layers are torn apart during the punching which may be considered as permanent deformation of the testing device. The initial thickness of the Teflon stack is 0.55*mm*, but we measure a final thickness of 0.12*mm* after the experiment. In order to eliminate these experimental uncertainties in the punch displacement measurements, we present most experimental results as a function of the punch force instead of the punch displacement.

Figure 3-8c depicts the evolution of the maximum principal true strain on top of the dome measured by DIC. Observe that the applied force reaches a plateau in this displacement controlled experiment. Fracture initiates on top of the dome which indicates that friction was close to zero in this experiment. After fracture initiation, cracks propagate along the rolling direction of the sheet. Both measured principal strains at the apex of the deformed specimen exceed 0.4 at the onset of fracture. Post-mortem analysis revealed that the sheet thickness is reduced by almost 60%, from 1.43*mm* (initial) to 0.58*mm* (final).

In addition to measuring the strain at the specimen apex, the DIC measurements are used to verify two important features of this experiment. Firstly, the DIC measurements demonstrate that the radial displacements are negligibly small along the interface between the specimen and the clamping ring (less than 0.05mm). Secondly, the DIC measurements demonstrate that the strain maximum prior to fracture is located at the specimen center which re-confirms that friction effects have been successfully eliminated by the lubricated Teflon layers (Burford et al., 1991, [31])

3.4.3 Numerical modeling

A quarter of the mechanical system is modeled because of the symmetry of the punch experiment and the orthotropic material behavior. Eight-node reduced-integration solid element meshes are employed in conjunction with the implicit solver of Abaqus. In addition, we make use of a shell element mesh along with the explicit solver of Abaqus because of the high computational efficiency of the shell contact formulation. In all FE models, the punch and the die are modeled as rigid bodies. The portion of the specimen that is clamped in the die is limited to 5*mm* in the simulation (i.e. the diameter of the circular specimen in the FE model is 110mm). The displacements of all nodes located on the outer edge of the specimen are set to zero. A condition of zero-normal displacement is imposed along the two edges that correspond to planes of symmetry. For shell meshes, no rotation around the edge direction is allowed on those two boundaries. A frictionless node-to-surface contact is defined between the punch and the specimen. In the case of shell elements, contact is defined for the sheet surface while thickness variations are taken into account. A constant velocity is applied to the punch, while the die is fixed in space.

The predicted force-displacement curves from an implicit simulation with 100 time steps using a coarse mesh (60/3 reduced-integration solid elements along the radial/thickness direction), an intermediate mesh (120/6) and a fine mesh (240/12) all lie on top of each other (Fig. 3-8a). Similarly, the results from quasi-static explicit simulations with reduced-integratioon shell elements (using the same number of integration points through-the-thickness as solid elements along that direction) are all identical. However, there is a noticeable difference between shell and solid element simulations for large punch displacements. This difference may be attributed to the errors associated with the assumption of plane stress and zero plastic out-of-plane shear strains in the shell element formulation. Analysis of the solid element simulations reveals that the out-of–plane compression stress reaches 90*MPa* on the contact surface with the punch; the maximal out-of-plane logarithmic shear strain is about 0.035. Unlike the results for the force-displacement curves, the solid element model predictions of the equivalent plastic strain feature a weak mesh size effect. At the center, the final equivalent plastic strain reaches 0.92

for a coarse mesh, whereas it is 0.90 for a fine mesh. Between a medium and fine mesh, the relative difference is almost zero. The results from implicit simulations with different numbers of time steps (65, 100, 150 and 200) revealed only small differences. The final maximal equivalent plastic strain reaches 0.92 when using 65 time steps and 0.90 for 200 steps.

Based on our brief analysis, the punch experiment will be analyzed using a finite element model with (i) 120 solid elements along the radial direction, (ii) 6 solid elements in thickness direction, (iii) 100 implicit time steps, and (iv) frictionless kinematic node-to-surface contact.

3.4.4 Identification of strain hardening response

When plotting the evolution of the major principal strain at the center of the specimen as a function of the punching force (Fig. 3-8c), it becomes apparent that the simulation model (blue curve) underestimates the strain in comparison with the experiment (solid black dots). Recall that the hardening curve used in the simulation has been calibrated based on the experimental results from uniaxial and notched tensile tests. However, since the maximum equivalent plastic strain reached in a punch test (about 0.9) is still much larger than that reached in a notched tensile test (about 0.6), we may improve the extrapolation of the stress-strain curve for large strains. Here, a third linear hardening segment is introduced for $\bar{\varepsilon}^p > 0.6$. The best correlation between simulation and the punch experiment is achieved when using a hardening modulus of $H_3 = 100MPa$ in this third segment. The corresponding simulation result is depicted as a black solid line in Fig. 3-8c. It is emphasized that this modification of the hardening curve does not affect the results from the previous section on notched tensile tests. Note that the hardening curve identification based on the biaxial experiments depends on the choice of the yield function (e.g. Banabic et al., 2000, [6]). Up to the strain of necking under uniaxial tension (about 0.2), we may interpret the good agreement of the simulations and the biaxial experiments as a partial validation of the plasticity model. Furthermore, the yield surface has been validated for the present material for a similar range of modest strains through multi-axial experiments (Chapter 2). However,

the assumption of a quadratic yield function may become inadequate for very large strains in the case of texture evolution.

Table 3-3: Stress strain curve beyond the onset of necking

Equivalent plastic strain [-]	0.2	0.35	0.6	
Equivalent stress [MPa]	1050	1140	1240	
Hardening modulus [MPa]	600	400		100

3.4.5 Simulation results and uncertainty analysis

The numerical simulation is performed up to the instance where the computed surface strain equals the measured surface strain at the onset of fracture ($\varepsilon = 0.461$). The simulated curve shows very good agreement with the experimental results (depicted with black dots). Furthermore, the predicted thickness reduction is in excellent agreement with the experiment. Figure 3-8d depicts the evolution of the equivalent plastic strain as a function of the stress triaxiality (black curve); here, it is assumed that fracture initiates on the free specimen surface. The loading state at the onset of fracture is depicted as a black dot. Fracture occurs at a computed stress triaxiality of $\eta = 0.66$ (equi-biaxial tension).

The modeling error affecting the computation of the equivalent plastic strain and the stress triaxiality is evaluated according to Eqs. (3-2) and (3-7); it is shown by blue dashed lines in Fig. 3-8d. Modeling errors at the onset of fracture are summarized in Table 3-4. A complete evaluation of the errors affecting the hybrid experimental-numerical result would require evaluating the precision of the 3D DIC method. However, the authors could not identify such an evaluation in the open literature. For the case of one-dimensional DIC, Sutton et al. (2009, [138]) reported that the 6-tap optimized filter interpolation function does not produce any significant error. Thus, we neglect this source of error in our analysis.

Table 3-4: Fracture point and error estimation for the circular punched specimen

Fracture plastic strain		Stress triaxiality at fracture	
Value [-]	Error [-]	Value [-]	Error [-]
0.896	$6.86\ 10^{-2}$	0.662	$0.73\ 10^{-2}$

3.5 Tensile specimen with central hole

Conventional uniaxial tensile specimens develop a pronounced neck at large strains which yields a change in stress state throughout the experiment from uniaxial tension to transverse plane strain. In an attempt to keep the stress triaxiality more constant throughout the experiment, we make use of tensile specimens with a central hole. The presence of a central hole creates a strain concentration which favors the fracture initiation at the intersection of the hole and the transverse axis of symmetry of the specimen.

3.5.1 Experimental procedure

The tensile specimens are 20*mm* wide and feature an 8*mm* diameter circular hole at the center (Fig. 3-1d). For the first set of specimens, the central hole is cut using a water-jet. In order to obtain a better edge finish, we prepared a second set of specimens with a 7mm diameter water jet cut hole that is subsequently enlarged to 8mm using CNC milling (with a 0.125" diameter end mill). The experimental procedure follows closely the program outlined for the notched specimens. To evaluate the error in the computed strains, we determined the axial logarithmic strain on the transverse symmetry axis at a distance of 40 pixels ($380\mu m$) from the hole. A measurement right at the edge of the hole is not possible as the DIC algorithm needs a continuous displacement field in the vicinity of the point of interest.

3.5.2 Experimental results

The measured force-displacement curves for the two sets of specimens are shown in Fig. 3-9a as crosses for the waterjet cut specimens and as solid dots for the CNC milled specimens. The waterjet-prepared specimens are extracted from a slightly thinner part of the sheet (1.46*mm* instead of 1.5*mm*), resulting in a lower force displacement curve. The measurements demonstrate that the machining technique has a strong influence on the fracture displacement. It is about 2.1*mm* for CNC-milled specimens and only 1.7*mm* for the waterjet cut specimens. The waterjet cuts the sheet by abrasion (abrasive jet), which leaves a non-smooth edge with numerous geometric defects. It is speculated that those defects along with some residual plastic strains are responsible for the premature failure of the water-jet cut specimens. Consequently, the results for water-jet cut specimens are discarded in the following analysis.

The force-displacement curve (Fig. 3-9a) exhibits a peak before fracture occurs. An important width reduction (diffuse necking) is observed within both specimen ligaments (Fig. 3-10a), which appears to intensify as the force reaches its maximum. The displacement to fracture varies among the CNC-milled specimens (Table 3-5). Observe from Fig. 3-10c that axial strain field features steep gradients around the transverse axis of symmetry of the specimen. The evolution of the surface strain (blue curve in Fig. 3-9a) shows that the surface strain reaches values of up to 0.7 prior to fracture.

Table 3-5: Experimental results and fracture predictions for the tensile specimen with central hole

Fracture displacement		Fracture plastic strain		Stress triaxiality at fracture	
Value [mm]	Variation [%]	Value [-]	Variation [%]	Value [-]	Variation [%]
2.089	2.24	0.834	6.67	0.282	1.45

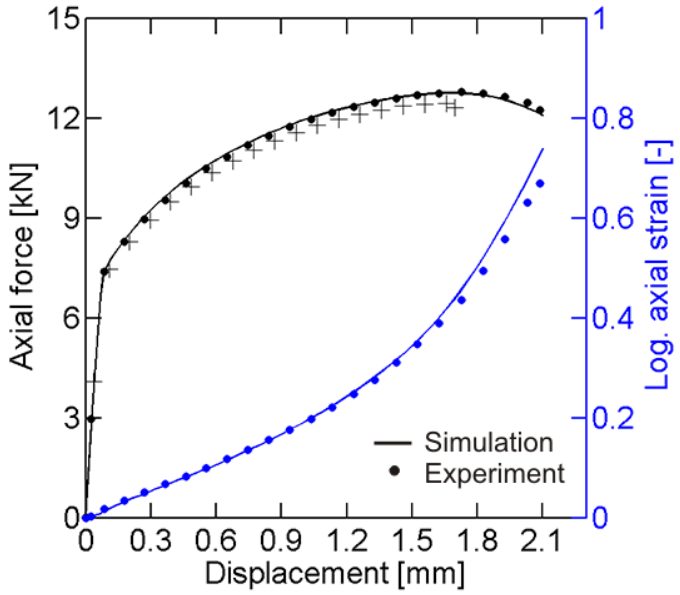

(a)

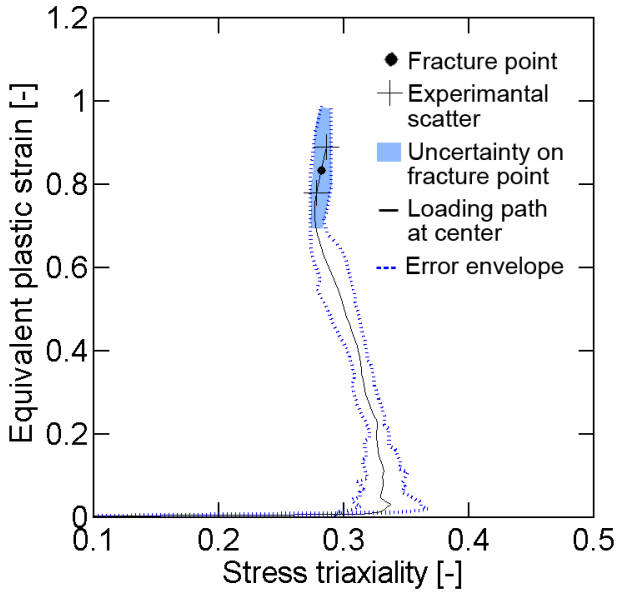

(b)

Figure 3-9: Analysis of a tensile test with a central hole. (a) Force-displacement curves and logarithmic strain versus displacement curves from experiments (dots = CNC-machined, crosses = waterjet cut) and simulation (solid lines); (b) Loading path at the center of the specimen (black solid line); the black dot and the crosses highlight the onset of fracture including experimental scatter (min/max). The dashed blue lines show the error envelopes.

3.5.3 Numerical modeling

Based on the results from Section 3.3, eight-node solid elements (with reduced integration) are used to mesh one eighth of the specimen (Fig 3-10b). A constant velocity is applied to the upper boundary. A zero normal displacement condition is imposed to the three boundaries corresponding to symmetry planes. Since the experimental results indicate that through-the-thickness localization is less important with this specimen design than for notched tensile specimens, we assume that 8 elements through the half thickness are enough to describe the stress and strain variations along the thickness direction. However, we use a biased mesh with the smallest elements at the intersection of the hole with the transverse plane of symmetry (Fig. 3-10b). In this vicinity, the elements have also the same length in the axial and transverse directions. Implicit simulations are performed using a coarse mesh (smallest in-plane element edge length is $120\mu m$), a medium mesh ($60\mu m$) and a fine mesh ($30\mu m$). As for the notched tensile tests, we find the same force-displacement curves for all mesh sizes. The effect of mesh size on the equivalent plastic strain is also weak for the element located at the hole boundary (on the specimen mid-plane). The final equivalent plastic strain computed with the coarse mesh is 0.83 compared to 0.86 when using the fine mesh. Errors due to time discretization are also evaluated by running simulations with 50, 75, 100 and 150 time increments. The difference in final plastic strain is already negligible (0.004) when comparing the results for 75 and 100 time increments. Thus, we make use of the implicit analysis with 75 time steps and a medium mesh to determine the loading history to fracture.

3.5.4 Numerical results and error estimation

The simulated force-displacement curve is depicted as a black solid line in Fig. 9a. It is in excellent agreement with the experimental data (solid dots). The maximum difference between the experimentally-measured and numerically-predicted force level is smaller than 2%. This good correlation is seen as a validation of the strain hardening curve that has been determined from the notched tension and punch tests. The FEA predicted evolution of the surface strain (blue line in Fig. 3-9a) is also close to the DIC measurements (blue dots).

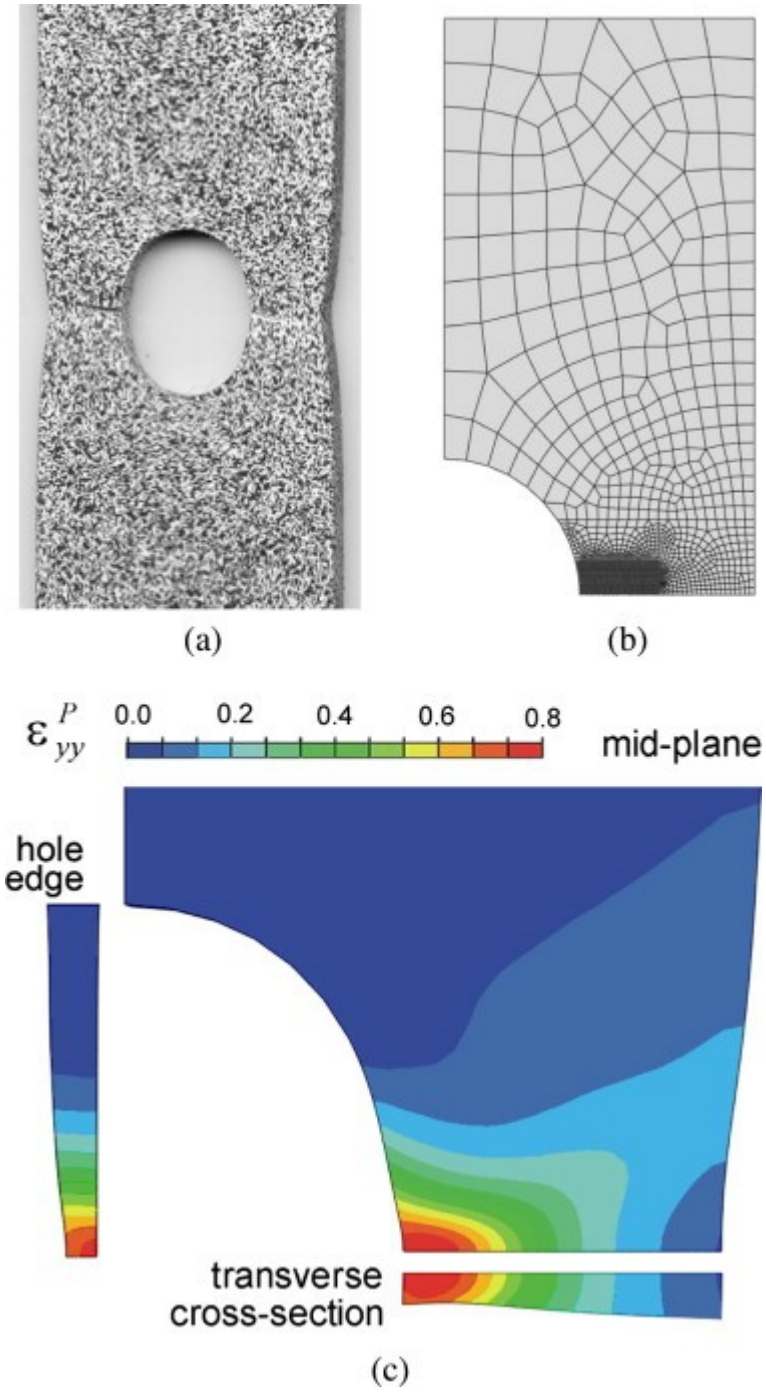

Figure 3-10: Specimen with a central hole. (a) Specimen after crack initiation, (b) medium FE mesh, (c) Logarithmic axial strain computed on specimen surface at the instant of the onset of fracture.

Table 3-6: Errors in the evaluation of the plastic strain and stress triaxiality at the onset of fracture

Fracture plastic strain			Stress triaxiality at fracture		
Displacement error [-]	Modeling error [-]	Total error[-]	Displacement error [-]	Modeling error [-]	Total error [-]
$0.22\ 10^{-2}$	$9.49\ 10^{-2}$	$9.71\ 10^{-2}$	$0.03\ 10^{-2}$	$0.43\ 10^{-2}$	$0.46\ 10^{-2}$

Similar to the results for notched tensile tests, the strains computed by FEA are higher than the DIC measurements. Here, the final computed strain is overestimated by about 10%.

The evolution of the equivalent plastic strain as a function of the stress triaxiality is shown in Fig. 3-9b. The black solid dot highlights the instant of onset of fracture. The differences due to scatter in the measured fracture displacement is represented with solid crosses. The identified fracture strain as well as the stress triaxiality at the onset of fracture are summarized in Table 3-5 along with the corresponding error estimates (Table 3-6).

As compared to the results for notched tensile specimens, the stress triaxiality variations in the tensile specimen with a central hole are small. It varies between 0.277 and 0.338. At the onset of fracture, the stress triaxiality is $\eta = 0.282$ which is close to uniaxial tension ($\eta = 0.33$). The estimated equivalent plastic strain to fracture is 0.83. The relative displacements of the specimen boundaries are computed with a precision of $2.5\mu m$ which translates into an uncertainty of 0.002 for the fracture strain and of less than is 0.001 for the stress triaxiality. The modeling errors according to Eqs. 3-2 and 3-7 are 0.095 for the fracture strain and 0.004 for the stress triaxiality.

3.6 Discussion and recommendations

3.6.1 Identification of the strain hardening response

The proper identification of the strain hardening model for very large strains is critically important for the reliable determination of the fracture strains. It is emphasized that conventional extrapolation formulas such as the modified Swift model seem to provide a poor approximation of the strain hardening behavior of advanced high strength steels at large strains. The present study shows that the Swift assumption leads to substantial errors in the simulation results after the onset of necking which is consistent with earlier results on martensitic steel (Mohr and Ebnoether, 2009, [104]). When hydraulic bulge testing devices are not available or a bulge test is impossible to realize (because of the very large specimen size), we propose the following procedure to identify the strain hardening function $H(\bar{\varepsilon}^p)$:

(i) Uniaxial tensile testing of dogbone specimens up to the strain of necking (ASTM E8, 2004, [3]);

(ii) Uniaxial testing of a tensile specimen with a central hole; the stress-strain curve can then be identified through inverse calibration;

One may also model the post-necking behavior of uniaxial tensile test and determine the stress-strain curve from inverse analysis (e.g. Mohr and Ebnoether, 2009, [104]). However, since the stress state in the neck of a uniaxial tension specimen is close to transverse plane strain, the maximum equivalent plastic strain achieved using a uniaxial tensile specimen with a central hole is expected to be larger. Furthermore, the stress gradients through the sheet thickness are smaller for the later type of specimen. From an experimental point of view, we note that the location of the zone of localization is a priori known when using a specimen with a central hole. This allows for the proper positioning of the DIC system before the experiment. Note that in a uniaxial tensile test, the position of the emerging neck is unknown before the experiment and may thus occur outside the field of vision of the camera system.

3.6.2 Numerical modeling

Shell element simulations provide accurate predictions of the large deformation behavior of sheet metal structures before the onset of through-the-thickness necking. However, the strain and stress state predictions of shell element simulations after the onset of through-the-thickness necking are not reliable as out-of-plane stresses become important. The same limitation becomes apparent under the presence of high surface pressures (e.g. final phase of the punch test). Thus, we strongly recommend using solid element meshes to determine the stress and strain histories all the way to fracture. When evaluating the effect of mesh density on the simulation results, it is important to monitor the strain evolution within the zone of localization. The global force-displacement curves are usually not mesh size sensitive since the material within the zone of localization contributes only little to the "internal energy" (elastic strain energy plus plastic dissipation) of the entire structure. As a rule of thumb, we recommend sixteen first-order solid elements through the full thickness of the sheet.

3.6.3 Summary of the loading paths to fracture

Figure 3-11a summarizes the results from all simulations in a single graph of equivalent plastic strain versus stress triaxiality. Recall that the critical element (integration point) is positioned on the sheet mid-plane for the notched tensile specimens and the specimen with a central hole, while it is located on the specimen surface for the punch experiment. We observe the high ductility for stress states close to uniaxial tension and those close to equi-biaxial tension. The strain path for the notched tensile specimen features stress states close to transverse plane strain which exhibit the lowest ductility. As an alternative to showing the results in the $(\eta, \bar{\varepsilon}^p)$-plane, we also computed the loading paths to fracture in terms of the principal plastic strains in the plane of the sheet. The minor and major strains shown in Fig. 3-11b are calculated from the in-plane components of the plastic strain tensor. Note that these strains are different from the eigenvalues of the plastic strain tensor (unless the out-of-plane shear strain components are zero).

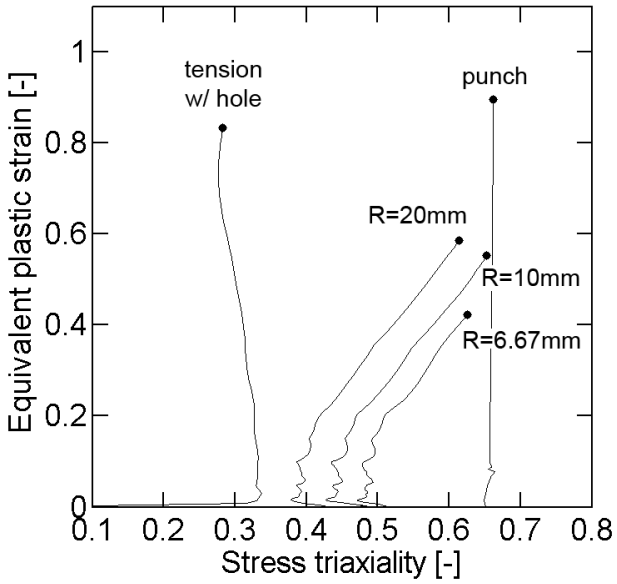

(a)

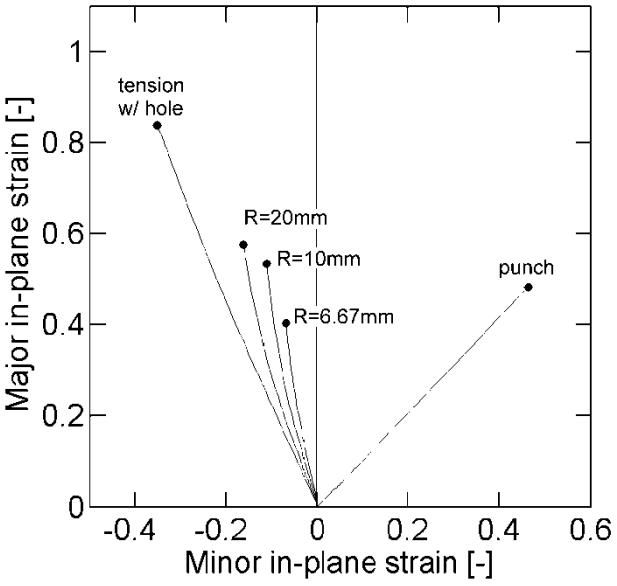

(b)

Figure 3-11: Stress and strain histories for the 5 geometries in the stress triaxiality versus equivalent plastic strain space (a) and in the in-plane major strain versus in-plane minor strain space (b).

3.6.4 Effect of porosity

All numerical results presented in this paper are obtained under the simplifying assumption that the effect of (micro-)porosity evolution on the effective plastic behavior can be neglected. There is strong theoretical evidence that the evolution of porosity changes the predicted stress triaxialities (e.g. Danas and Ponte Castaneda, 2009, [46]). However, it is difficult to quantify the effect of porosity on the plastic behavior of the TRIP780 steel based on our macroscopic measurements (surface displacement fields and total force). At the same time, the numerical predictions of the non-porous plasticity model employed in this study agree well with all macroscopic measurements for various loading conditions.

The evolution of porosity clearly plays an important role as far as the onset of fracture is concerned. The initial microstructure is void free, but micrographs of highly deformed specimens indicate that voids initiate and grow throughout loading. Figure 3-12 shows micrographs of the axial plane of symmetry at the center of the notched specimens prior to fracture (after applying about 97% of the displacement to fracture). Voids and microcracks are clearly visible at this stage of deformation. Observe that the microcracks are aligned with the loading direction. This observation may be explained using the anisotropic porous plasticity model of Danas and Ponte Castaneda (2009, [44]). Their homogenization-based computations show that the severe elongation of initially spherical voids under transverse plane strain loading causes the loss of ellipticity of the effective porous medium. In other words, the axial microcracks may be considered as the result of the coalescence of highly elongated voids. However, in the present case, the onset of fracture is also affected by material heterogeneities at the microstructural level. Energy dispersive X-ray analysis revealed that the locations of the microcracks seen in Fig. 3-12 coincide with the position of Mn and Mo segregation bands.

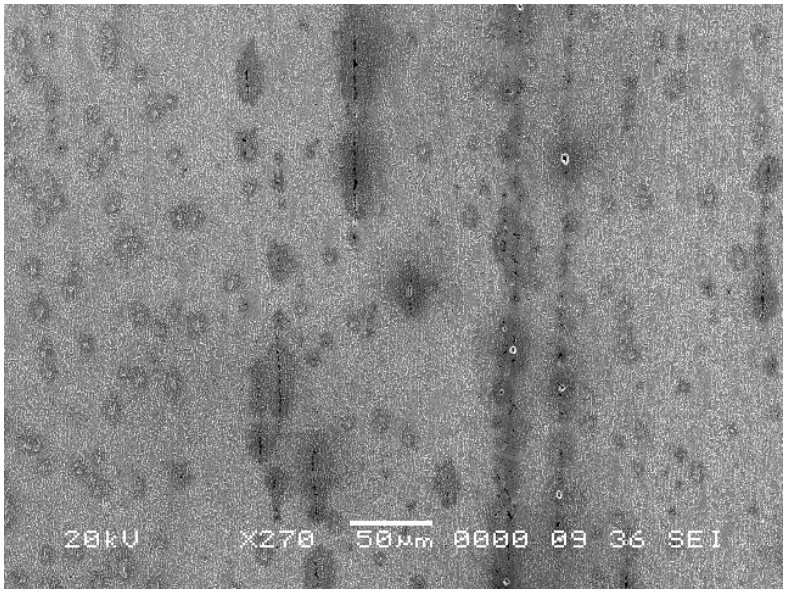

(a)

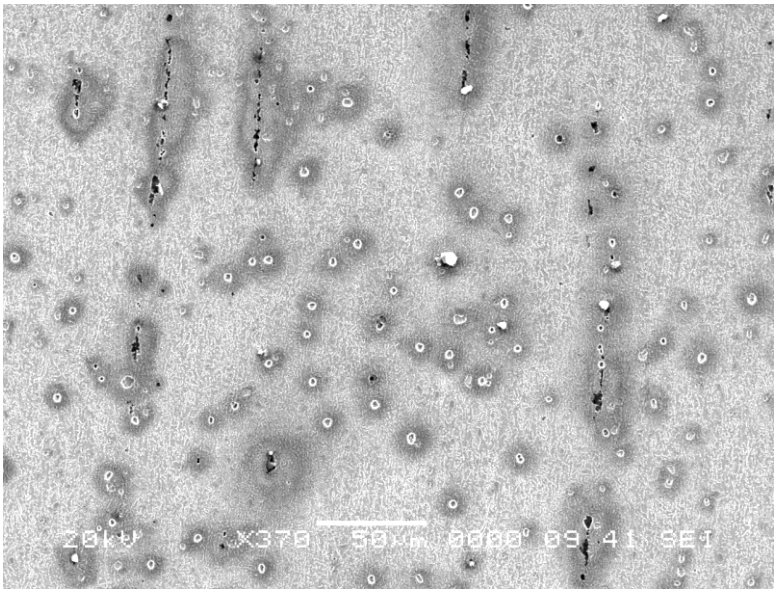

(b)

Figure 3-12: Micrographs of the axial plane of symmetry of deformed notched tensile specimens : (a) R=20*mm* notch specimen strained to 98.3% of the fracture displacement, (b) R=6.67 *mm* notch specimen strained to 96.8% of the fracture displacement. The vertical and horizontal directions of the pictures correspond to the axial and thickness directions of specimen, respectively.

3.7 Concluding remarks

Five different fracture tests have been performed on specimens extracted from TRIP780 sheets and analyzed in great detail to obtain reliable estimates of the loading path to fracture for stress triaxialities ranging from uniaxial tension to equi-biaxial tension. The main conclusions are:

(1) Shell element simulations are not suitable for the evaluation of the local loading path after the onset of through-the-thickness necking.

(2) Solid element simulations can provide accurate predictions. Both coarse and fine meshes predict usually the same overall force-displacement response, but it is important to evaluate the accuracy of an FE simulation through the comparison of the predicted strains within the neck with DIC surface strain measurements. For the present material and loading conditions, sixteen first order solid elements along the thickness direction provided sufficiently accurate results for the local fields.

(3) It is important to identify the strain hardening curve for large strains from experiments. The analytical extrapolation (e.g. Swift law) based on data for uniaxial tension prior to necking is not sufficiently accurate. When data from hydraulic bulge tests is not available, we recommend the inverse identification of the stress-strain curve using the results from the testing of uniaxial tensile specimen with a large central hole.

(4) The stress-triaxiality is approximately constant all the way to fracture for a tensile specimen with a central hole and during a punch test; it increases monotonically throughout notched tensile tests.

Chapter 4

Fracture experiments under combined normal and shear loading

Contents

[3] This Chapter is reproduced from: Dunand, M. and D. Mohr (2011). "Optimized butterfly specimen for the fracture testing of sheet materials under combined normal and shear loading". *Engineering Fracture Mechanics* **78**(17): p. 2919-2934.

4.1 Introduction

In sheet metal forming, the failure of the sheet metal is typically predicted using Forming Limit Diagrams (FLDs), e.g. Keeler et al. (1964, [77]). The FLD defines the onset of necking as failure while the so-called Fracture Forming Limit Diagram (FFLD) concept has been introduced to predict the fracture after necking (Embury et al., 1977, [53]). Most experimental techniques for determining FLDs and FFLDs comprise a plurality of specimens that are inserted into a testing system of only one degree of motion. For instance, the Hasek (1978, [71]) test makes use of a family of circular disc specimens with round cut-outs of different radius that are inserted into a punch/die system. The axial motion of the punch is the only degree of freedom of the testing system. The Nakazima (1971, [114]) test relies on a similar punch/die system to load strips of different width all the way to fracture. In the hydraulic bulge test, only one type of specimen is used while different states of loading are achieved by varying the elliptical geometry of the die (e.g. Rees, 1995, [126]). The common feature of these testing techniques is a single degree of freedom loading system. This degree of freedom is used to vary the intensity of loading along a proportional loading path which is preset by the specific combination of specimen and testing system. It cannot by changed throughout the experiment. It is also worth noting that none of the aforementioned testing techniques allows for the reversal of the loading direction. In other words, the described experimental techniques for FLD and FFLD determination are limited to monotonic proportional loading paths.

Due to this limitation, the effect of non-linear and/or non-monotonic loading paths can only be studied when the specimens are cut from pre-deformed sheets. Laukonis and Ghosh (1978, [83]) studied the failure under uniaxial tension of equibiaxialy pre-strained aluminum killed steel and 2036-T4 Aluminum specimens. Llod and Sang (1979, [94]) performed uniaxial tensile pre-straining followed by uniaxial tension in the orthogonal direction on 2036-T4 and 5182-0 Aluminum sheets. Graf and Hosford (1994, [62]) characterized the influence of strain path changes on the FLD of 6111-T4 aluminum sheets by pre-straining their specimens under either uniaxial, transverse plane strain or equibiaxial tension. All experimental studies reported a significant dependence of failure on strain-path changes.

Mohr and Henn (2007, [105]) proposed an experimental technique that makes use of a universal biaxial loading device to test a butterfly-shaped specimen under different states of loading. This technique is fundamentally different from the established FLD tests in the sense that the state of loading is varied by changing the displacement boundary conditions rather than the shape of the specimen. In conjunction with a dual actuator system (Mohr and Oswald, 2008, [109]), this experimental technique can be employed to perform fracture tests along non-linear and non-monotonic loading paths, for stress states ranging from pure shear to transverse plane strain tension. However, it is not suitable to the calibration of conventional FLDs, as it does not cover stress states ranging from transverse plane strain to equi-biaxial tension. The original specimen by Mohr and Henn (2007, [105]) features a flat gage section of uniform thickness that is designed such that cracks are most likely to initiate within the specimen center. Bai (2008, [4]) modified this geometry by including a second curvature, resulting in a specimen with a non-flat gage section. Irrespective of the specific specimen geometry, a hybrid experimental-numerical approach is required to determine the stress and strain states at the onset of fracture.

As part of this Thesis, the original specimen design by Mohr and Henn (2007, [105]) is revisited to come up with a reliable experimental technique to investigate the effect of combined loading histories on the onset of fracture. This involves the design of a new specimen and the presentation of a hybrid experimental-numerical technique to determine the loading path prior to the onset of fracture. The effect of the boundary curvatures on the stress and strain fields is investigated numerically. Subsequently, specimens with the apparently “optimal” geometry are extracted from TRIP780 steel sheets and tested over a wide range of multi-axial loading conditions. The analysis of the experiments reveals that the validity of the proposed hybrid experimental-numerical technique is very sensitive to imperfections in the initial specimen geometry. Furthermore, it is shown that the local stress and strain fields within the specimen gage section cannot be computed with high accuracy after the localization of deformation under shear-dominated loading conditions. The results for tension-dominated loading indicate that the equivalent plastic strain at the onset of fracture cannot be expressed as a monotonic function of the stress triaxiality only.

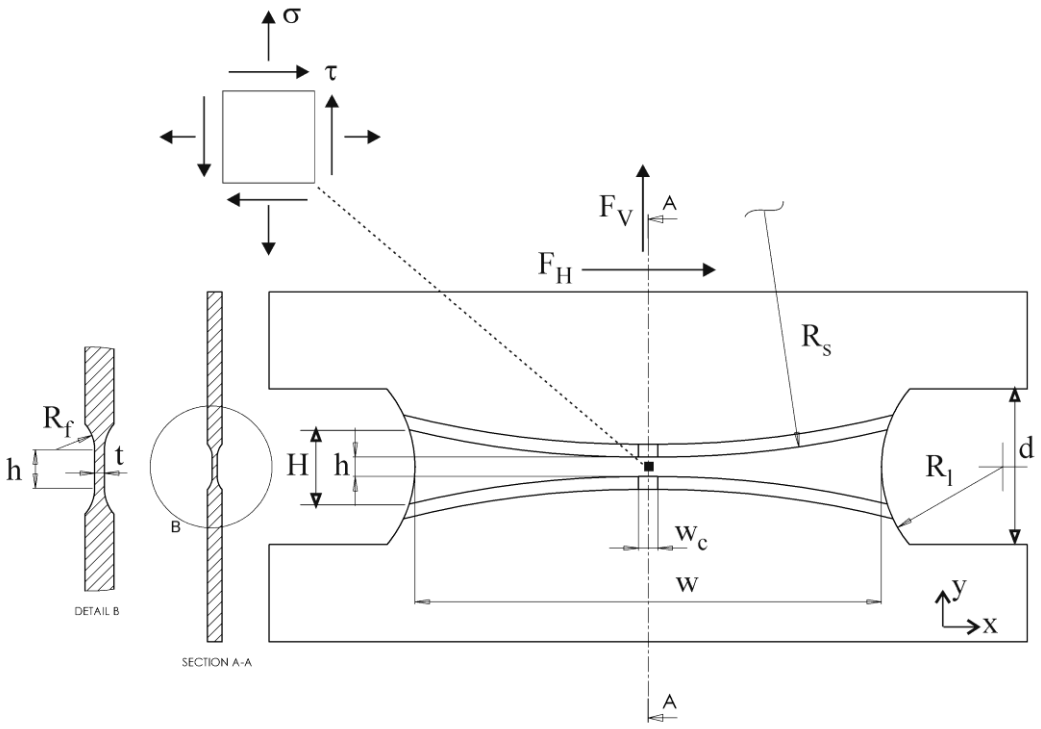

Figure 4-1: Schematic of the specimen.

4.2 Specimen design

Figure 4-1 shows a schematic of the proposed fracture specimen. The specimen features an abrupt change in thickness between the gage section of thickness t and the specimen shoulders. Different states of stress and strain may be achieved within the specimen gage section by applying different combinations of normal loading F_V and tangential loading F_H to the top and bottom specimen boundaries. An attempt is made to optimize the specimen geometry such that the cracks initiate within the flat $h \times w_c$ large central area of the gage section.

In a plane stress specimen, the stress state is always uniaxial tension along the free boundaries, irrespective of the state of stress at the specimen center. This can pose a challenge when characterizing the onset of fracture at low stress triaxialities since early

cracks may initiate along the specimen boundaries rather than at the specimen center. The boundaries of the proposed specimen are curved to avoid the crack initiation at the gage section boundaries. A short parametric study is presented in subsection 4.2.2 to gain further insight into the effect of the boundary curvatures on the stress and strain distributions within the gage section.

4.2.1 Theoretical range of loading states

Prior to necking, the state of stress near the specimen center is plane stress in the (x,y)-plane with the superposed transverse plane strain constraint in the x-direction (see Fig. 4-1 for coordinate frame definition). The transverse plane strain condition implies that the strain along the specimen width direction (corresponds to x-direction in Fig. 4-1) is zero, $\varepsilon_{xx} \simeq 0$. For an isotropic rigid-plastic Levy-von Mises solid, the corresponding stress tensor may be written as

$$\boldsymbol{\sigma} = \begin{bmatrix} 0.5\sigma & \tau & 0 \\ \tau & \sigma & 0 \\ 0 & 0 & 0 \end{bmatrix} \tag{4-1}$$

Throughout our discussion, we use the stress triaxiality η and the Lode angle parameter $\bar{\theta}$ to characterize the stress state (despite the small anisotropy of the material). The stress triaxiality is defined by the negative ratio of hydrostatic pressure $p = -\operatorname{tr}\boldsymbol{\sigma}/3$ and the von Mises equivalent stress, $\bar{\sigma}_{VM}$,

$$\eta = -\frac{p}{\bar{\sigma}_{VM}} = \frac{\operatorname{sign}\sigma}{\sqrt{3 + 12\left(\frac{\tau}{\sigma}\right)^2}} \tag{4-2}$$

The stress triaxiality is zero for shear-dominated loading ($\sigma/\tau \to 0$) while it approaches asymptotically its maximum value of $\eta = 1/\sqrt{3} \simeq 0.58$ as the normal stress becomes dominant ($\sigma/\tau \to \infty$).

The Lode angle parameter $\bar{\theta}$ is related to the normalized third invariant ξ of the stress tensor. We have

$$\bar{\theta} = 1 - \frac{2}{\pi}\mathrm{acos}\,\xi \tag{4-3}$$

where ξ is defined as

$$\xi = \frac{27}{2}\frac{\det(\boldsymbol{\sigma} + p\mathbf{I})}{\bar{\sigma}_{VM}^3} = \frac{\frac{27}{4}\frac{\sigma}{|\tau|}}{\left[\frac{3}{4}\left(\frac{\sigma}{\tau}\right)^2 + 3\right]^{\frac{3}{2}}} \tag{4-4}$$

Unlike the stress triaxiality, the Lode angle parameter is not a monotonically increasing function in σ/τ. We have $\bar{\theta} = 0$ for both $\sigma/\tau \to 0$ (pure shear) and $\sigma/\tau \to \infty$ (transverse plane strain tension), while it reaches its maximum of $\bar{\theta} = 1$ for $\sigma/\tau \simeq 1.38$, which corresponds to uniaxial tension. The theoretical relationship between the Lode angle parameter and the stress triaxiality for the present type of experiment is shown in Fig. 4-2. In addition, the biaxial loading angle, β, defined as

$$\tan\beta = \frac{F_V}{F_H} \simeq \frac{\sigma}{\tau} \tag{4-5}$$

is depicted as curve parameter in Fig. 4-2. In this notation, $\beta = 0°$ corresponds to pure shear, while $\beta = 90°$ corresponds to transverse plane strain tension.

4.2.2 Parametric study on specimen geometry

The geometry of the proposed fracture specimen is described by three geometric parameters (Fig. 4-1): the shoulder radius R_s, the lateral radius R_l and the fillet radius R_f. The gage section thickness t and height h are not considered as model parameters. From a theoretical point of view, the thickness does not affect the stress distribution in a plane stress specimen. The width is important and should be as large as possible for stress field uniformity. In view of the force limitations of real testing systems, it is usually advantageous to increase the specimen width at the expense of thickness. Here, a gage section thickness of $t = 0.5mm$ is chosen. This corresponds to a lower limit for thicknesses that can still be

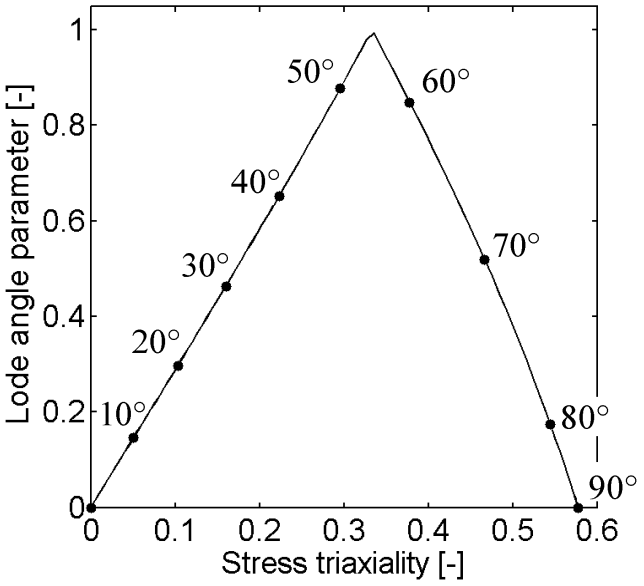

Figure 4-2: Plot of the Lode angle parameter as a function of the stress triaxiality for plane stress conditions. The labels next to the solid dots indicate the corresponding biaxial loading angle.

machined within reasonable dimensional tolerances (e.g. thickness variations of less than 5%). In order to produce transverse plane strain conditions near the specimen center, the distance h between the top and bottom shoulders needs to be small. Furthermore, the risk of buckling under shear loading may be lowered by choosing a small gage section height. In the present design, a thickness of $h = 2mm$ is chosen to provide a sufficiently large flat area for two-dimensional DIC measurements.

The finite element program Abaqus/explict [1] is used to compute the stress and strain fields within specimens of different geometry. The linear plane stress elements CPS4R and CPS3 are used in two-dimensional models while the solid elements C3D8R and C3D6 are employed to discretize three-dimensional geometries. It will be shown in Section 4.3 that very fine meshes are needed to provide an accurate estimation of all local stress and strain fields. Within the framework of this subsection, rather coarse finite element meshes are employed; however, these are chosen such that the effect of various geometric features can still be studied with satisfactory accuracy.

4.2.2.1 Effect of the shoulder curvature

The main reason for introducing the shoulder radius R_s is to reduce the amount of plastic deformation towards the free specimen boundaries, thereby avoiding premature fracture away from the specimen center. Since this problem is expected to be most critical for pure shear loadings, we performed all simulations for this loading condition using plane stress elements. Furthermore, we neglect the deformation of the specimen shoulders and model the gage section only (see meshes shown in Fig. 4-3 to 4-5). Three different radii are considered to demonstrate the effect of the shoulder curvature: $R_s = 50mm$, $R_s = 100mm$ and $R_s = 200mm$. Figure 4-3 to 4-5 includes plots of the variation of the equivalent plastic strain and stress triaxiality along the x-direction at an advanced stage of deformation. Each solid dot represents the result at one integration point of the plane stress mesh. The plot of the stress triaxiality shows a narrow zone at the specimen center with very small ($\eta = 0 \pm 0.01$) variations in stress triaxiality. The width of this zone in x-direction increases as the shoulder radius increases (compare Figs. 4-3 to 4-5). The corresponding equivalent plastic strain plots show more pronounced variations. For instance, for $R_s = 50mm$, the equivalent plastic strain varies from 0.135 to 0.15 within a central zone of $w_c = 2mm$. Note that the equivalent plastic strain reaches its maximum at the tangential point between the flat and curved boundary of the central gage section. The homogeneity of the strain distribution can be improved by increasing the shoulder radius (see Fig. 4-6). Since the small increase in the equivalent strain appears to be due to the change in curvature between the flat and round shoulder region, we considered a boundary of clothoidial shape where the curvature increases linearly with the distance from the specimen center. Figure 4-6 shows the smooth plastic strain profile which is obtained for the clothoidally-shaped boundary with the shape parameter $\sqrt{RL}$ (R is the radius of curvature and L is the length along the clothoidal boundary).

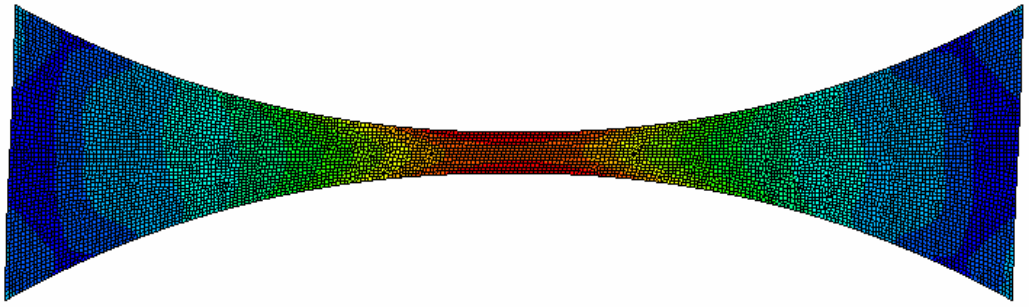

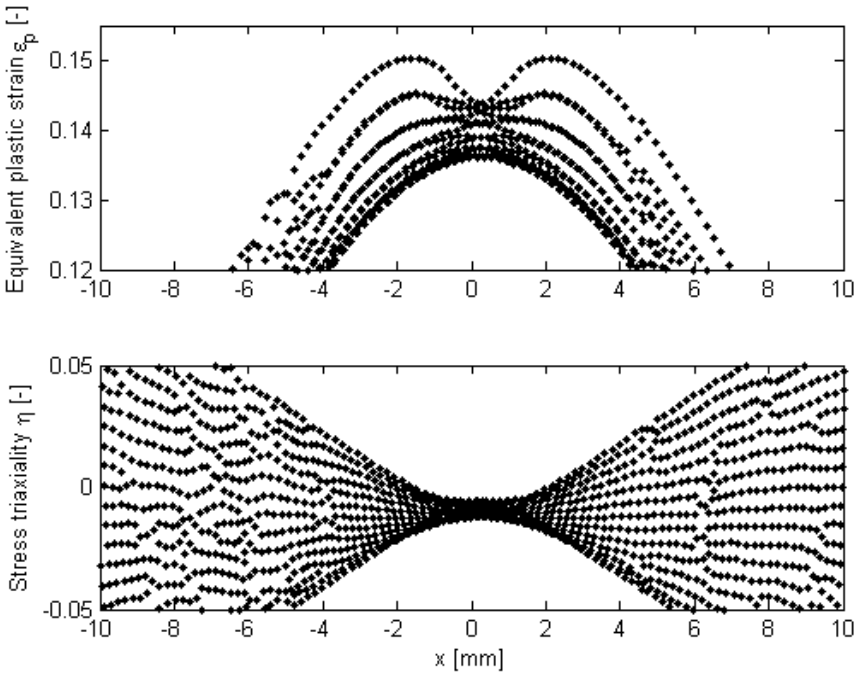

Figure 4-3: Equivalent plastic strain and stress triaxiality near the specimen center for $R_s = 50mm$

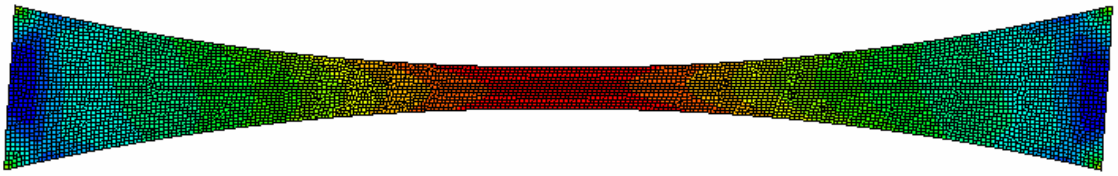

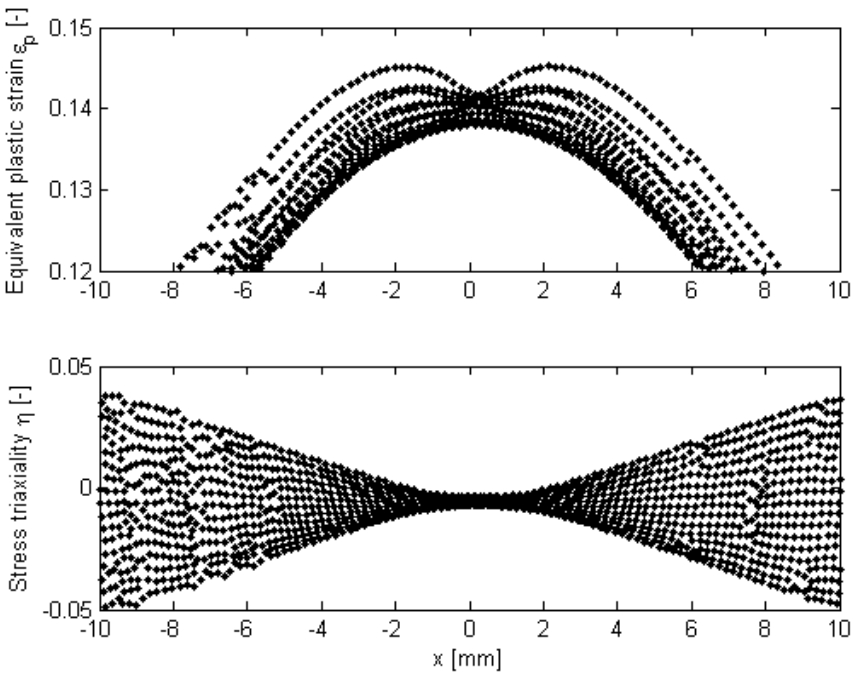

Figure 4-4: Equivalent plastic strain and stress triaxiality near the specimen center for $R_s = 100mm$

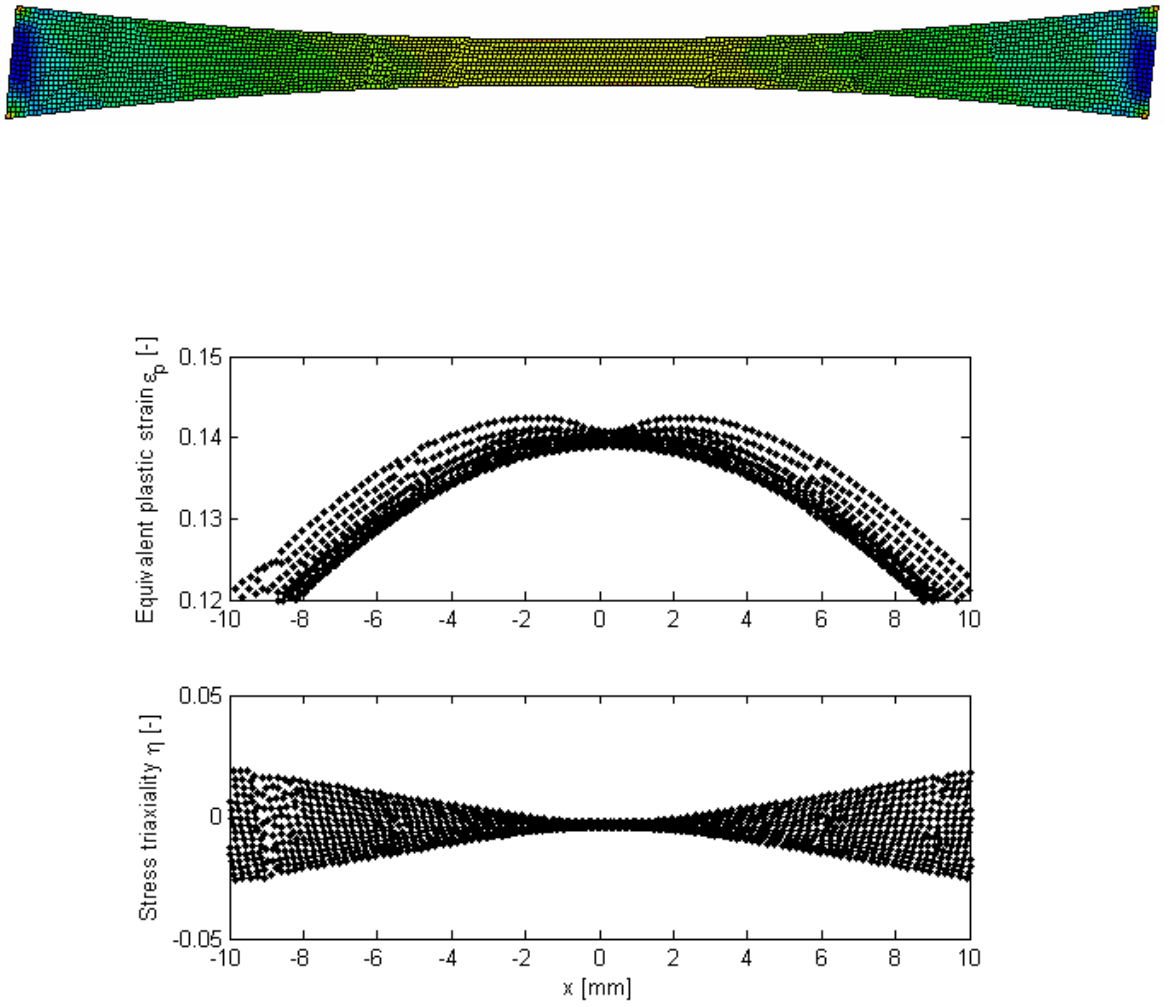

Figure 4-5: Equivalent plastic strain and stress triaxiality near the specimen center for $R_s = 200mm$

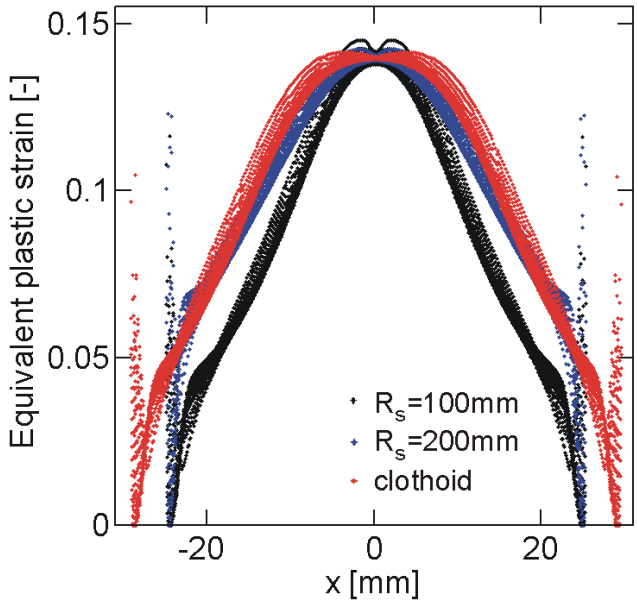

(a)

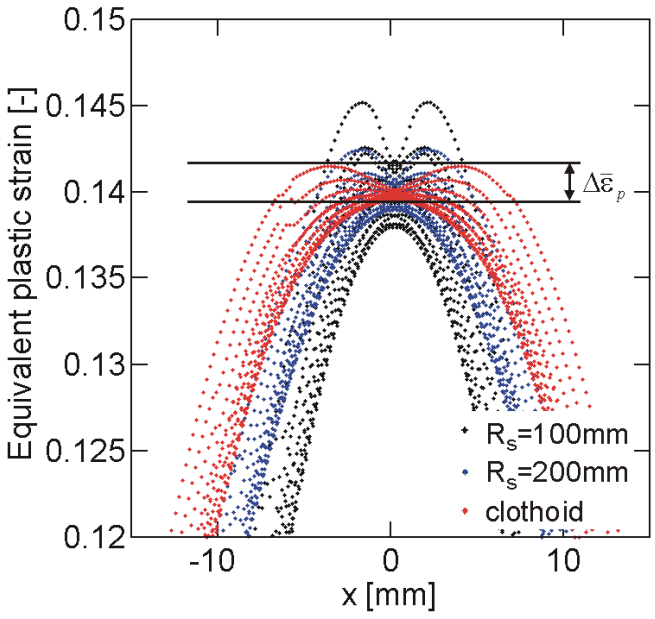

(b)

Figure 4-6: Influence of the shoulder curvature on the equivalent plastic strain : (a) Equivalent plastic strain at all integration points within the finite element mesh as a function of the corresponding x-coordinates; (b) magnified detail of (a).

4.2.2.2 Effect of the lateral boundary curvature

The effect of the lateral boundary curvature on the maximum equivalent strain is investigated for the clothoidal shoulder geometry. The curvature of the lateral boundary is described by the radius R_l in Fig. 4-1. The same intersection points of the lateral boundaries with the specimen shoulders are chosen for all plane stress simulations while the lateral boundary radius R_l is varied. Figure 4-7 depicts the variation of the equivalent plastic strain at that boundary along the vertical direction ($y = 0$ corresponds to the specimen center line) for macroscopic shear loading ($\beta = 0°$). The thick solid line shows the strain distribution for a straight boundary, i.e. $R_l = \infty$ (configuration "D"). The strain distribution is non-uniform and increases monotonically from 0.0 at the specimen center to values as high as 0.1 near the specimen shoulder. Increasing the lateral boundary radius decreases the strain near the specimen shoulder (Fig. 4-7). Observe from curves A, B and C that the location of maximum strain is no longer at the corner with the specimen shoulder. It appears that configuration B with a radius of $R_l = 10mm$ provides the lowest maximum value of the equivalent plastic strain along the lateral boundary. In Fig. 4-7, we also show the results for negative curvatures, i.e. configurations where the gage section features an outward notch as initially proposed by Mohr and Henn (2007, [105]). The simulation results clearly show that these configurations (E and F) lead to very high strain concentrations near the specimen shoulders and should thus be avoided.

4.2.2.3 Effect of the fillet radius

A 3D solid element model is used to investigate the effect of the fillet radius between the specimen gage section and the specimen shoulders for macroscopic tensile loading ($\beta = 90°$). Figure 4-8 shows the distribution of the stress triaxiality and the equivalent plastic strain in the central vertical cross-section (corresponds to section A-A in Fig. 4-1). The simulation results for $R_f = 0.5mm$, $R_f = 1mm$ and $R_f = 2mm$ demonstrate that the equivalent plastic strain decreases faster from the gage section to the shoulder area for smaller fillet radii. On the other hand, small fillet radii induce a peak in stress triaxiality within the radius area. For instance, in the case of $R_f = 0.5mm$, the stress triaxiality

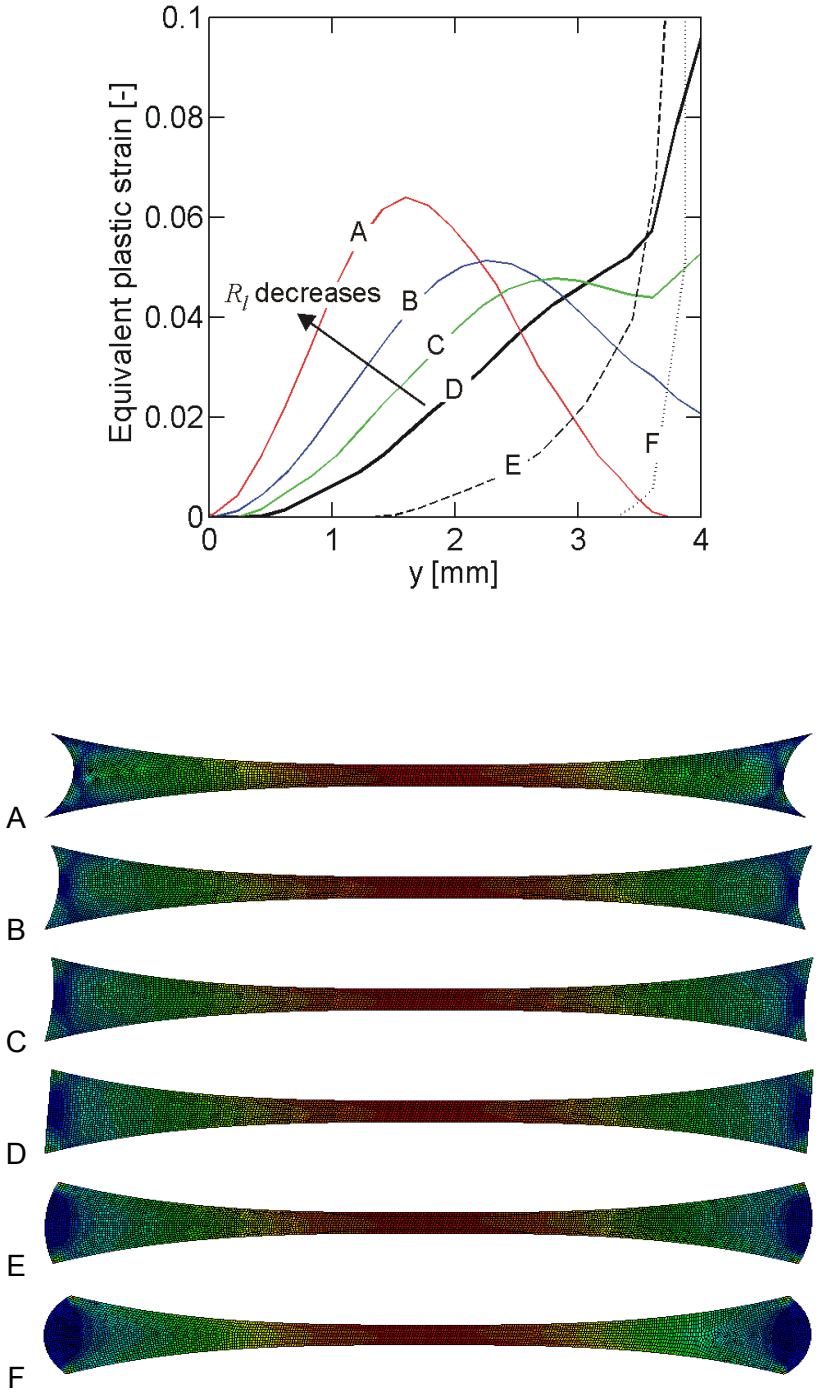

Figure 4-7: Variation of the lateral boundary curvature : (A) $R_L = 5mm$, (B) $R_L = 10mm$, (C) $R_L = 20mm$, (D) $R_L = \infty$, (E) $R_L = -10mm$ and (F). $R_L = -5mm$

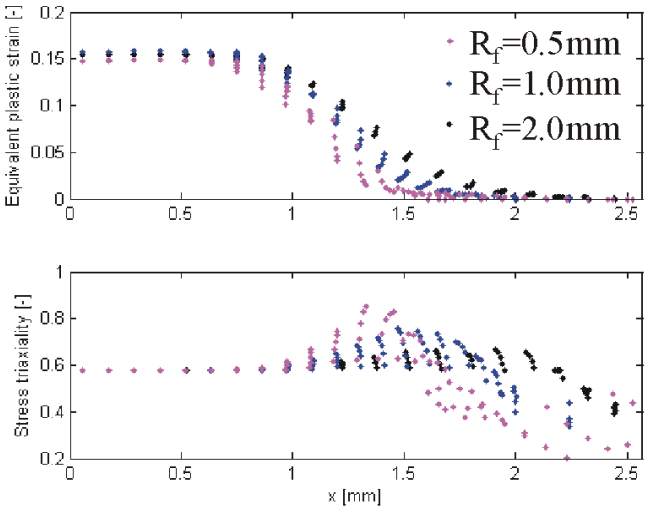

(a)

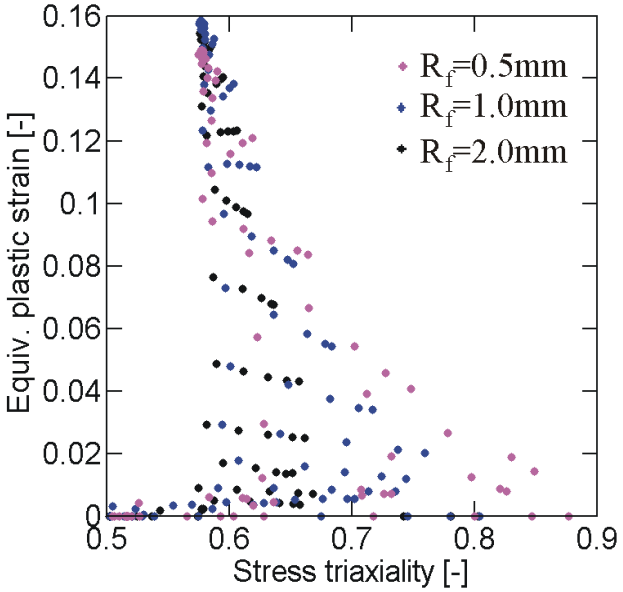

(b)

Figure 4-8: Influence of the fillet curvature on the stress triaxiality and equivalent plastic strain.

increase from 0.58 within the gage section to about 0.8 in the radius region. However, the plot of the equivalent plastic strain versus stress triaxiality reveals that the corresponding plastic strains at high stress triaxialities are very small. Thus, it is concluded that the choice of the fillet radius has only a little effect on the experimental results and should be made based on manufacturing constraints.

4.2.3 Final specimen geometry

The final specimen, sketched in Fig. 2-12 has the following dimensions: gage section thickness $t = 0.5mm$, minimum gage section height $h = 2mm$, maximum gage section height $H = 8mm$, gage section width $w = 57mm$, uniform gage section width $w_c = 0mm$, free distance between clamps $d = 12mm$, lateral boundary radius of $R_l = 10mm$ and fillet radius of $R_f = 0.5mm$. The shape of the clothoidal boundary (x_c, y_c) in the first quadrant is given by the Fresnel integrals

$$x_c(L) = \int_0^L \cos\left(\frac{l}{a}\right)^2 dl \tag{4-6}$$

$$y_c(L) = \frac{h}{2} + \int_0^L \sin\left(\frac{l}{a}\right)^2 dl \tag{4-7}$$

with the curve length L and the curvature parameter $a = 67mm$.

4.3 Hybrid experimental-numerical analysis procedure

Specimens of the final geometry are prepared and tested in a dual actuator system under four different loading configurations: $\beta = 0°, 25°, 63°$ and $90°$. In this section, the underlying hybrid experimental-numerical analysis procedure is presented. The corresponding experimental results are discussed in Section 4.4.

4.3.1 Specimen preparation

The specimens are extracted from the 1.5mm thick sheet material by waterjet cutting. The thickness reduction of the gage section is then performed by CNC-machining. The first set of specimens is machined using a ball end mill of hemispherical shape; the second set is machined using a corner radius end mill. Unlike the ball end mills, the corner radius end mill features a small flat area at the bottom of the end mill.

4.3.2 Dual actuator system

The tests are performed using a dual actuator system (Mohr and Oswald, 2008, [109]). The custom-made dual actuator system applies tangential and normal loads to the boundaries of the butterfly specimen, which is clamped using high pressure grips. The horizontal actuator applies the tangential force to the lower specimen boundary. As shown in Fig 2-3, the lower specimen clamp is mounted onto a low friction sliding table. A load cell positioned between the horizontal actuator and the lower specimen clamp measures the tangential force. The normal force is applied through the vertical actuator in the upper cross-head. Two additional load cells are integrated into the lower sliding table to measure the total vertical force. Combined tension-shear experiments are performed for biaxial loading angles β between 0° and 90°. In all experiments, we observe a sudden drop in force level which is considered as the instant of the onset of fracture.

4.3.3 Optical strain and displacement measurements

During the tests, Digital Image Correlation (DIC) is used to measure the surface displacement and strain fields. For that purpose, two digital cameras (QImaging Retiga 1300i with 105mm Nikon Nikkor lenses) take about 500 pictures (resolution 1300x1030 pixels) of the speckle painted front and back surfaces of the specimen. The pictures of the front camera are used to determine the displacements of the specimen boundaries (translations and rotation). The front camera is positioned at a distance of 1.25m to take pictures of the entire specimen (square pixel edge length of 50µm). The photographs of the

back face are used to perform accurate DIC measurements of the displacement field at the center of the specimen gage section. For that purpose, the second camera is positioned at a distance of 0.25m which reduces the square pixel edge length to 9µm. The average speckle size is about 70µm on both faces. The displacement field is calculated by DIC (VIC2D, Correlated Solutions) based on the assumption of a quadratic transformation of the 35x35 pixel neighborhood of each point of interest. The engineering axial and shear strains at the center of the specimen are computed from the relative horizontal and vertical displacements Δu and Δv of two points located at the center of the specimen:

$$E_y = \frac{\Delta v}{\Delta y} \tag{4-8}$$

$$E_{xy} = \frac{\Delta u}{\Delta y} \tag{4-9}$$

Both points are located on the vertical axis of symmetry at an initial distance of $\Delta y = 20 pixels$ (180µm).

4.3.4 Finite Element model

Simulations of each experiment are carried out using the explicit version of the finite element analysis software Abaqus [1]. The non-associated quadratic plasticity model (model #5 in Section 2.3) is implemented in a user material subroutine (VUMAT for Abaqus/Explicit). Reduced integration 3D solid elements (types C3D6R and C3D8R from the Abaqus element library) are used to mesh the specimen. Exploiting the symmetry of the specimen geometry, only half of its thickness is modeled. Note that the portion of the specimen shoulders between the clamps are not included in the mesh; DIC measurements have shown that the slip between the specimen and the high pressure clamp is negligibly small.

The translations and rotations of the straight boundary line between the clamps and the specimen shoulders are measured by DIC during each experiment. Subsequently, the measured translation and rotation histories are imposed on the boundaries of the computa-

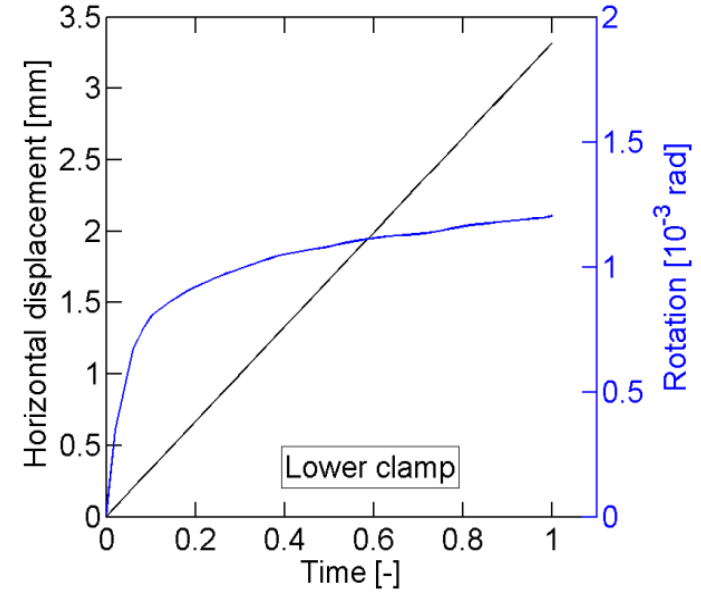

(a)

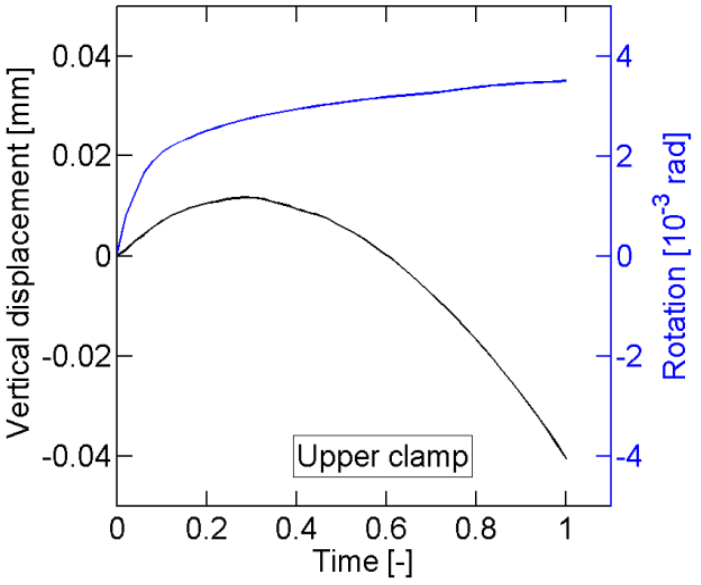

(b)

Figure 4-9: Boundary conditions during a pure transverse loading ($\beta = 0°$). Translation (black line) and rotation (blue line) of the lower clamp (a) and the upper clamp (b).

ional model. Figure 4-9 shows the corresponding time histories for pure transverse loading ($\beta = 0°$). Due to the high rigidity of the testing machine, the rotations are very small. Assuming zero rotations in the FEA model does not change the predicted force-displacement curves, but it has a significant effect on the fracture strain: in case of shear loading ($\beta = 0°$), the fracture strain is about 5% higher when imposing both translations and rotations.

Double precision simulations are run up to the experimentally measured instant of the onset of fracture. The loading velocity is artificially modified in order to complete the computational analysis after about 600,000 time increments. The mesh size is chosen such that dividing all element dimensions by two does not change the computed fracture strain by more than 0.5%. Spatial discretization errors are mostly significant in regions where strain gradients are steep; thus, different meshes are used for tension-dominated loadings ($\beta = 90°$ and $63°$) and for shear-dominated loadings ($\beta = 0°$ and $25°$). In tension-dominated experiments, strains localize through the thickness at the center of the gage section; consequently, the corresponding mesh features eight elements in the through-thickness direction. On the other hand, the meshes used to simulate shear-dominated experiments have only four elements through the thickness, while an increased mesh density along the width of the gage section is required. Both meshes consist of about 70,000 elements. Their main characteristics are summarized in Table 4-1. Note that both meshes are very fine with elements dimensions close to the actual grain size of the TRIP steel.

Table 4-1: Characteristics of meshes used in Finite Element Simulations

Loading	Number of elements in the gage section			Size of the critical element [μm]		
	Height	Width	Thickness	Height	Width	Thickness
Shear-dominated	60	210	4	36	215	65
Tension-dominated	80	54	8	26	788	32

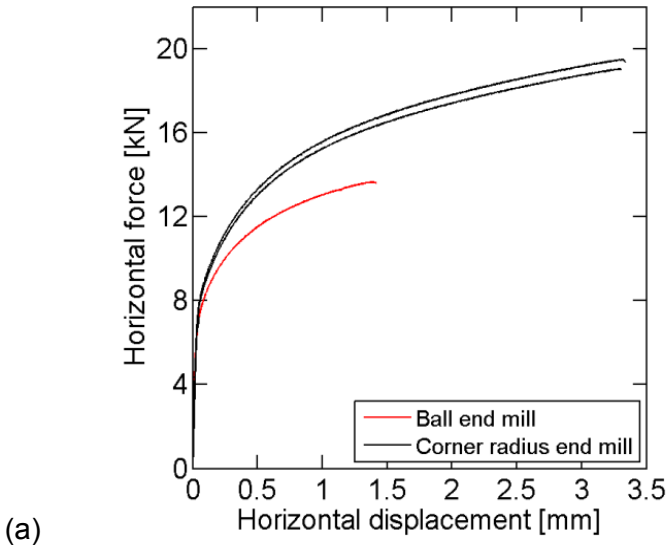

(a)

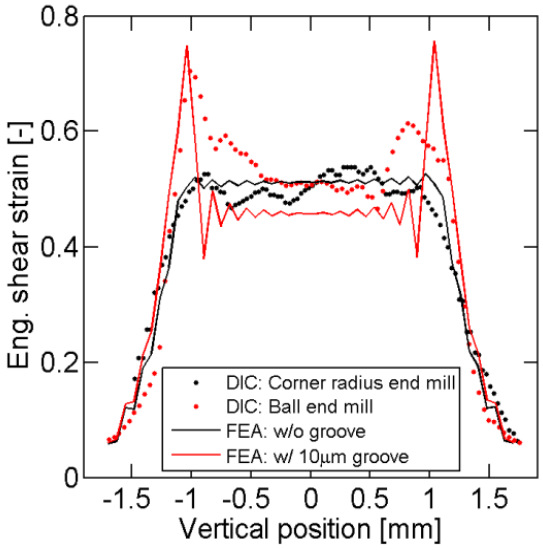

(b)

Figure 4-10: Influence of the specimen machining on a pure transverse loading experiment ($\beta = 0°$). (a) Schematic of a ball end mill. (b) Schematic of a corner radius end mill. (c) Force displacement curves for a specimen prepared with ball end mills (red line) and for two specimens prepared with corner radius end mills (black lines) submitted to a pure transverse loading: $\beta = 0°$. (d) Engineering shear strain along the vertical symmetry axis of the specimen as measured by DIC on the surface of the specimen prepared with ball end mills (red points) or prepared with corner radius end mills (black points), and as computed by FEA for a mesh with a flat gage section (black line) or with a 10µm groove along the fillets (red line). The position 0 corresponds to the horizontal axis of symmetry of the specimen.

4.4 Results

4.4.1 Effect of the milling procedure

The sensitivity of the experimental results with respect to the machining process is investigated for pure shear loading experiments ($\beta = 0°$). Figure 4-10a shows the measured force-displacement curves for specimens machined with ball and corner end mills, respectively. Observe that the horizontal displacement at which fracture occurs is about 55% lower for the specimen machined with ball end mills (red line in Fig. 4-10a). Figure 4-10b depicts the engineering shear strain at the surface for each type of specimen; it is plotted along the vertical axis of symmetry for a horizontal displacement of 1.5mm. In the specimen machined with the ball end mill (red dotted line in Fig. 4-10b), the strain remains constant along the vertical direction near the center of the gage section, but it exhibits pronounced peaks near the boundaries between the gage section and the specimen shoulders. The specimen machined with the corner radius end mill (black points in Fig. 4-10b) shows a more or less constant strain throughout the entire gage section. It is speculated that the use of a ball end mill has created a groove at the boundary of the clothoidally-shaped shoulder region. To shed more light on this issue, we introduced a $10\mu m$ deep groove into the finite element mesh and ran the simulation to the same horizontal displacement as in the experiment. The corresponding simulation results confirm the experimentally-observed localization of shear deformation (red solid line in Fig. 4-10b), while a uniform shear strain distribution is observed for a simulation without groove (black solid line in Fig. 4-10b). Based on these observations, all subsequent experimental results are reported for specimens that have been machined using a corner radius end mill.

4.4.2 Experimental results

Experiments are performed for four different loading conditions: $\beta = 0°, 25°, 63°$ and $90°$. Pure shear and pure tension experiments (at $\beta = 0°$ and $\beta = 90°$, respectively) are performed under displacement control, while both combined loading experiments ($\beta = 25°$

and 63°) are initially performed under force control, to guarantee proportional loading conditions. For $\beta = 25°$ and 63°, the control mode is switched to displacement control shortly before the onset of localization to track the decreasing load thereafter. From each experiment, we obtain (1) the tangential force versus horizontal displacement curve and (2) the axial force versus vertical displacement curve. In addition, the evolution of engineering shear and axial strains is recorded. The measured force-displacement curves are depicted with black solid dots (blue solid dots represent the measured strain evolution at the specimen center) in Fig. 4-11b ($\beta = 0°$), Fig. 4-11e-f ($\beta = 25°$), Fig. 4-11c-d ($\beta = 63°$) and Fig. 4-11a ($\beta = 90°$).

In experiments with tension-dominated loading ($\beta = 63°$ and $\beta = 90°$), the vertical force-displacement curves exhibit a peak prior to fracture (see Figs. 4-11a and 4-11c). This maximum seems to coincide with the onset of localized necking. Note that this force peak is also associated with a noticeable surface strain rate increase at the center of the gage section (see Figs. 4-11a and 4-11c-d). The deformation localizes at the center of the specimen which leads to a pronounced thickness reduction in the form of a neck and subsequent onset of fracture.

In the shear-dominated experiments ($\beta = 0°$ and $\beta = 25°$), the measured force-displacement curves increase monotonically until fracture (Figs. 4-11b and 4-11e-f). At the same time, the engineering surface strains at the specimen center increase almost linearly with respect to the displacement. However, full-field DIC shows that, for large deformations, the deformation localizes along the clothoidally-shaped shoulders, away from the vertical axis of symmetry of the specimen. Figure 11a shows a contour plot of the maximum principal Lagrangian surface strain as measured by DIC close to the instant of failure for $\beta = 25°$. Since similar observations are made for $\beta = 0°$, it is tentatively concluded that fracture initiates along the shoulder radius for shear-dominated loading conditions.

Regardless of the loading condition, the crack propagation is unstable, i.e. it is not possible to stop the experiment before the initiated crack has traveled through the entire

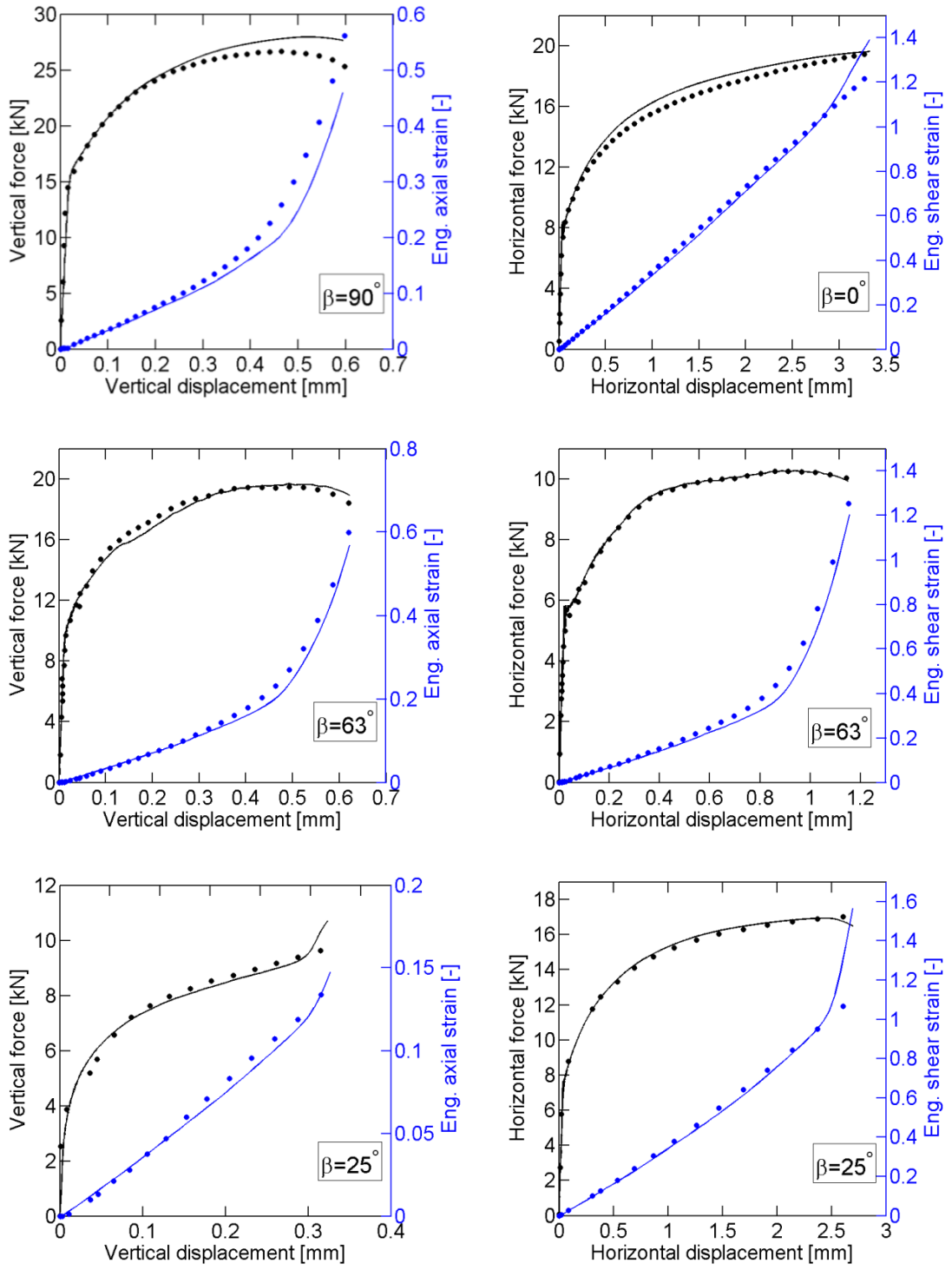

Figure 4-11: Experimental (dots) and simulation (lines) results. (a): $\beta = 90°$. (b): $\beta = 0°$. (c) and (d): $\beta = 63°$. (e) and (f): $\beta = 25°$. The force displacement curves are depicted in black, while engineering surface strains are plotted in blue.

gage section, breaking the specimen into two pieces (Fig. 4-13). It is therefore not possible to determine experimentally the location of fracture initiation.

4.4.3 Comparison of simulations and experiments

Figure 4-11 includes the simulation results for all four loading conditions. The simulated force-displacement curves are depicted with black solid lines, while the evolution of engineering axial and shear strains are plotted with blue solid lines. In case of pure tensile loading ($\beta = 90°$, in Fig. 4-11a), the correlation between simulation and experimental results is good for small displacements. However, the force level predicted by FEA is too high for displacements larger than $0.3mm$. At the onset of fracture, the computed vertical force is about 9% higher than the experimental measurement. Note also that the characteristic force peak, which is associated with the onset of through-thickness localization, occurs later in the simulation. As a result, the axial engineering surface strain at the onset of fracture is about 18% lower in the simulation than in the experiment which corresponds to an absolute difference in strain of 0.086.

The numerical results for $\beta = 63°$ (Fig. 4-11c-d) are in good agreement with experimental results. The simulation is able to predict accurately the vertical and horizontal force histories, including the drop in force level prior to fracture. Shear and axial strains are also predicted with great accuracy. The relative difference between strains computed by FEA and those measured by DIC is about 6%

The simulation results for shear-dominated experiments ($\beta = 0°$ in Fig. 4-11b and $\beta = 25°$ in Fig. 4-11.e-f) agree well with the experimental measurements up to about 85% of the displacement to fracture. Thereafter, the simulation results show an abrupt increase in strain rate while experimental shear and axial strains increase linearly all the way to fracture in both cases. As a result, at the instant of onset of fracture, surface strains obtained from FEA are much higher than the experimental measurements at the center of the gage section. For the loading at $\beta = 25°$, the computed engineering axial and shear strains at fracture are respectively 0.15 and 1.56, compared to 0.14 and 1.11 measured by DIC (note that the paint did not peel off despite these large strains). Also observe that this increase of strain rate cor-

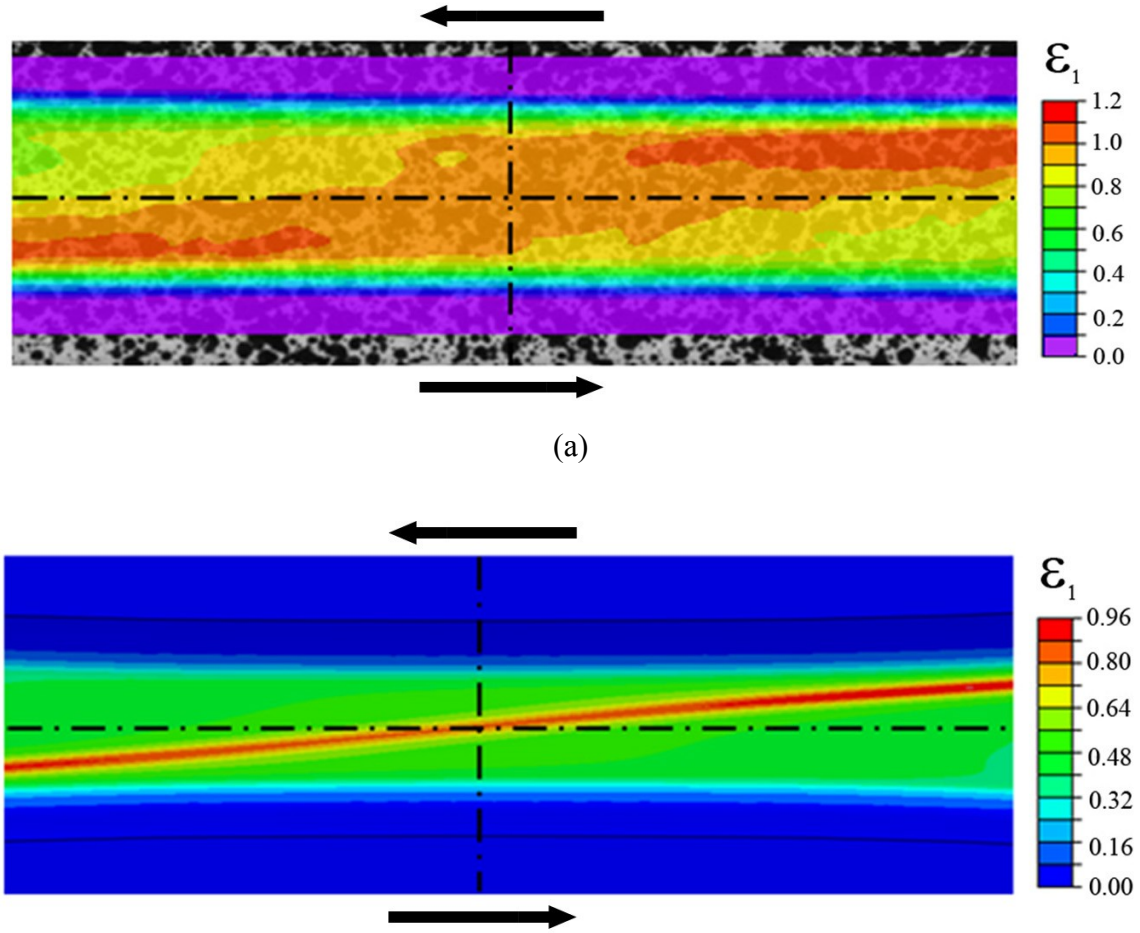

Figure 4-12: Principal strain at the surface of a specimen loaded with an angle $\beta = 25°$ just before failure, as measured by DIC (a) and as computed by FEA (b). Black dotted lines depict the axes of symmetry. Note that DIC measures Lagrangian strains while FEA computes logarithmic strains. Arrows show the orientation of the transverse loading.

relates with a drop of the predicted horizontal force (Fig. 4-11f) and a substantial increase of the predicted vertical force (Fig. 4-11e); both phenomena are not observed in the corresponding experiments. Further analysis of the simulation results reveals that those abrupt strain rate increases are associated with the development of a narrow band of strain localization. Figure 4-12b depicts the contour plot of the maximum principal strain on the surface of a specimen submitted to a loading angle of $\beta = 25°$, as computed by FEA at the

instant of fracture. The comparison with Fig. 4-12a shows that the localization of deformation is less severe in the experiment and does not extend from the specimen shoulders to the specimen center.

4.4.4 Local stress and strain histories

For each loading angle, we identify the location of the so-called 'critical element' where the equivalent plastic strain reaches its maximum at the instant of onset of fracture. Figure 4-14 shows the evolution of the equivalent plastic strain $\bar{\varepsilon}^p$ as a function of the stress triaxiality η (Fig. 13a) and the Lode angle parameter $\bar{\theta}$ (Fig. 4-14b) at the locations of the respective 'critical elements'. These four locations are represented by solid dots on the fractured specimens shown in Fig. 4-13. Diamond shaped dots in Fig. 4-14 indicate the points where the reliability of the simulations breaks down. Recall that the comparisons of the experimental and numerical results had shown that the finite element simulations of the shear-dominated experiments are no longer reliable after the appearance of a band of strain localization.

In tension-dominated experiments ($\beta = 90°$, in black in Fig. 4-14 and $\beta = 63°$, in red), the stress triaxiality is initially constant and then increases in a linear manner after the onset of through-thickness necking; a stress triaxiality of about 0.68 is reached at the onset of fracture in both experiments. Note that this increase is due to the development of a three-dimensional stress state inside the neck. For pure tensile loading, we observe a nearly constant Lode angle parameter of $\bar{\theta} = 0$. In shear-dominated experiments, both stress triaxiality and Lode angle are approximately constant throughout loading. Observe that the TRIP780 material exhibits a very large ductility: the determined strains are greater than 0.6 in both shear-dominated experiments, while a strain of 0.92 is reached for loading at $\beta = 63°$. Furthermore, it is worth noting that the apparent strain to fracture for $\beta = 63°$ is almost twice as high as that for $\beta = 90°$ even though the stress-triaxiality is the same at the instant of onset of fracture. This comparison clearly demonstrates that the strain to fracture does not depend on the stress triaxiality only. For example, the effect of loading history and/

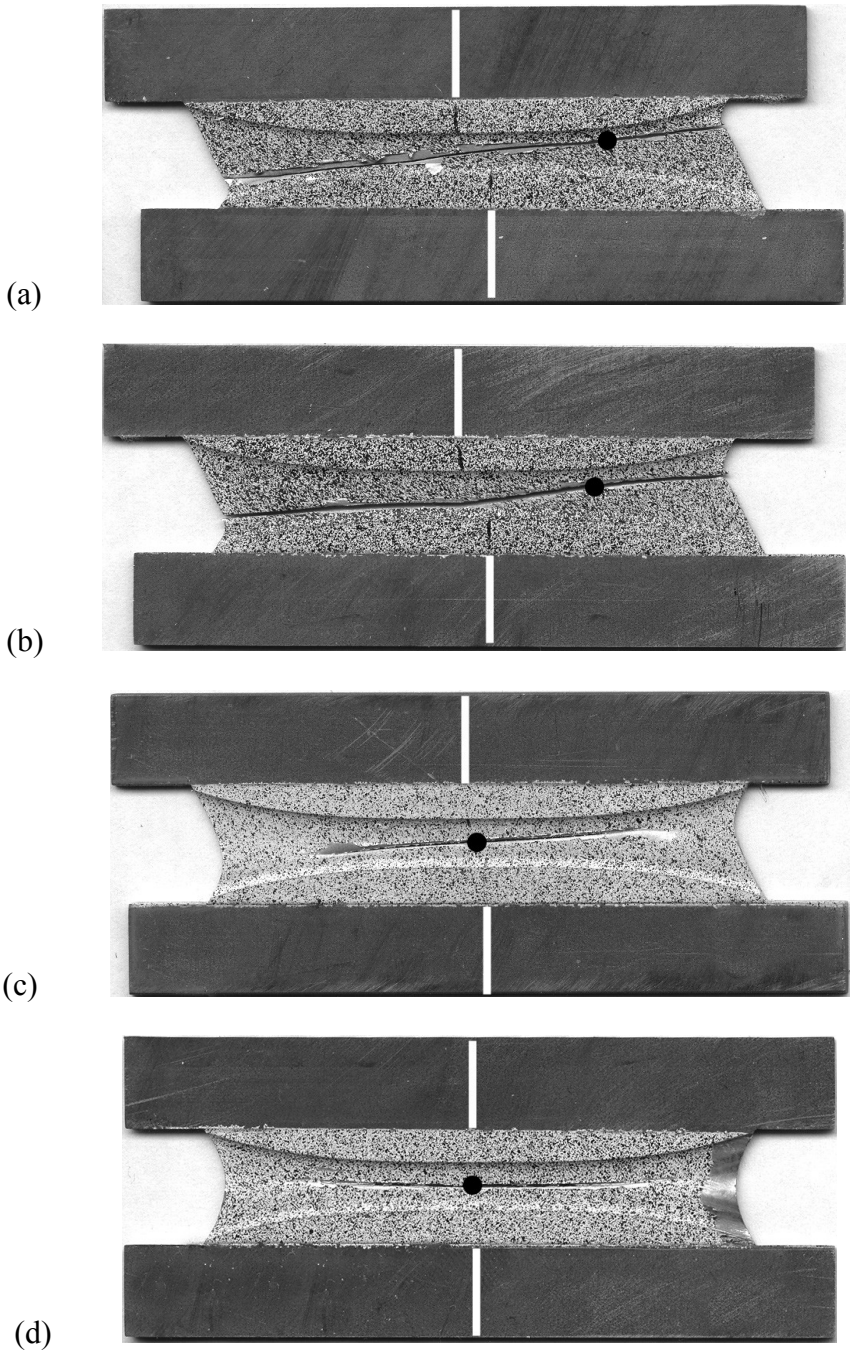

Figure 4-13: Fractured specimens for different loading cases : (a) $\beta = 0°$; (b) $\beta = 25°$; (c) $\beta = 63°$; (d) $\beta = 90°$. The vertical white lines indicate the position of the vertical axis of symmetry of the undeformed geometry. Black dots highlight the position where fracture is assumed to initiate according to the 'critical element' definition.

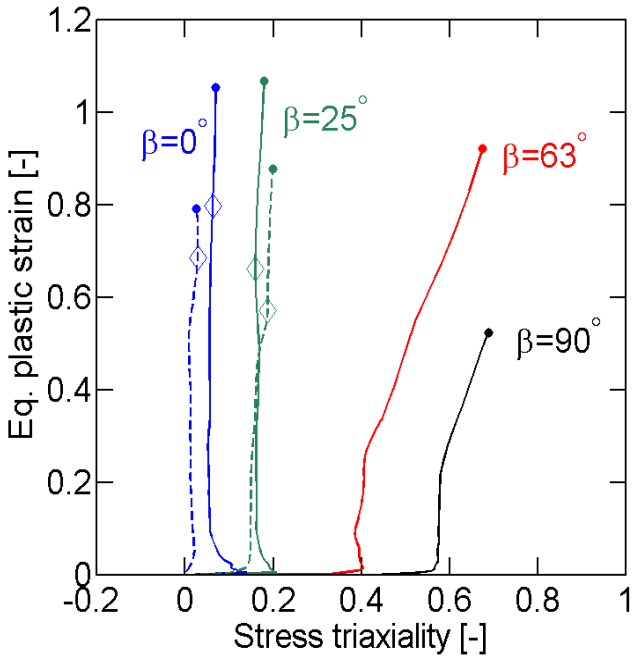

(a)

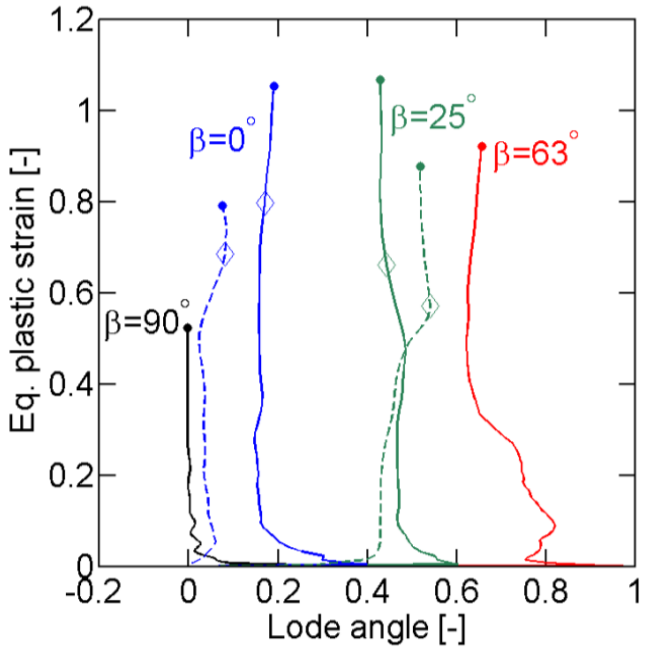

(b)

Figure 4-14: Loading paths for four loading conditions at the location of the corresponding 'critical element' (in solid lines) and at the center of the gage section (in dashed lines): Evolution of equivalent plastic strain as a function of (a) the stress triaxiality, and (b) the Lode angle parameter. Diamonds shaped dots indicate the instant when the reliability of the simulations of shear-dominated experiments breaks down.

or the effect of the Lode angle need to be taken into account in order to predict the onset of ductile fracture.

In shear-dominated experiments, the 'critical element' is located near the gage section boundary with the specimen shoulder (see Figs. 4-13a and 4-13b), while the highest equivalent strain is reached at the specimen center for the two tension-dominated loading cases. For reference, we also show the results at the specimen center for shear-dominated loading (dashed lines in Fig. 4-14). Observe that the equivalent plastic strain at the center of the gage section is about 20% lower than the strain inside the 'critical element'. Note that the stress triaxialities are approximately the same at the two locations in each specimen, while the Lode angle parameter is lower by almost 0.2 at the center of the gage section for $\beta = 0°$.

4.5 Discussion

4.5.1 Strain localization during loading

The localization of deformation within the specimen gage section occurs in all experiments. For tension-dominated loadings, we observe through-thickness necking which results in the development of three dimensional stress and strain states near the specimen center. It appears to be impossible to avoid this type of localization in experiments where the sheet mid-plane remains flat. In shear-dominated experiments, the deformation localizes along the gage section shoulders at very large strains. It is worth noting that the strain field is still approximately homogeneous at the gage section center for engineering shear strains of about 1.0. However, strain gradients of the order of $0.01\mu m^{-1}$ are present after the onset of strain localization (estimated based on the FE results shown in Fig 4-12). Clearly, very fine meshes are required to describe the strain localization under shear-dominated loading; coarse meshes would result in significant approximation errors especially for the fracture strain.

As far as the plasticity model is concerned, we note that our estimates of the local stress and strain fields are based on a simple phenomenological local plasticity model. The presence of large strain gradients may require the use of non-local material theories such as strain gradient plasticity models (e.g. Gurtin and Anand, 2005, [67]). Furthermore, the evolution of the mesostructure (void nucleation, growth and shape change) may need to be taken into account at very large strains (e.g. Danas and Ponte Castaneda, 2009, [46]).

4.5.2 Determination of the location of fracture initiation

In the present hybrid experimental-numerical procedure, the *location* of the onset of fracture cannot be determined experimentally. It is reemphasized that the loading histories shown in Fig. 4-14 have been identified based on the assumption that fracture initiates at the location of the maximum equivalent plastic strain. However, since the exact location of the onset of fracture is unknown, there is no experimental evidence that fracture initiates at a specific material point. The only conclusion that may be drawn is that the material remains intact when subject to the loading histories shown in Fig. 4-14. In other words, the end points of the trajectories shown in Fig. 4-14 should be interpreted as a lower bound rather than as the exact instant of onset of fracture for a particular loading history.

In order to discuss the possible uncertainty associated with the assumption of the critical element definition, we plotted the simulation results for all Gauss integration points within the gage section in the same $(\eta, \bar{\varepsilon}^p)$- and $(\bar{\theta}, \bar{\varepsilon}^p)$-diagrams (Fig. 4-15). The results for tension-dominated experiments (red and black in Fig. 4-15) are plotted for the instant of onset of fracture, while the results for shear-dominated experiments (blue and green in Fig 4-15) are extracted from the simulation results shortly before the reliability of the simulations breaks down due to the development of a localization band. For $\beta = 25°$ (green dots in Fig. 4-15), we observe that the equivalent strain reaches very high values at many integration points at the instant of onset of fracture. At the same time, the stress triaxiality varies significantly among these data points. For instance, the stress triaxiality (resp. Lode angle parameter) varies from 0.15 (resp. 0.44, for elements located on the surface of the specimen) to 0.25 (resp. 0.60, for elements located at mid-thickness) at the integration points

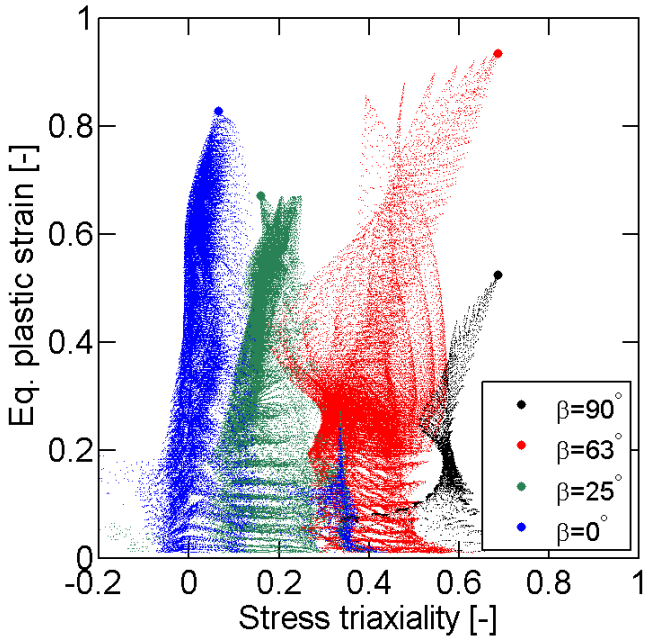

(a)

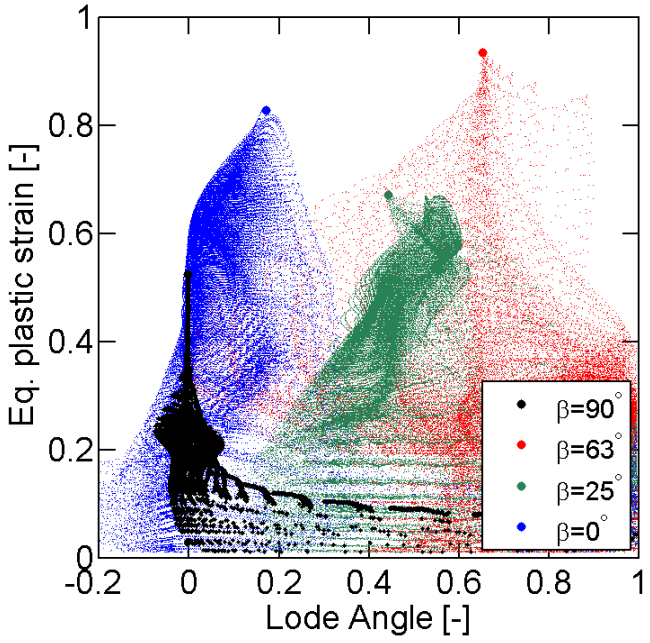

(b)

Figure 4-15: Stress and strain states for four loading conditions. (a) stress triaxiality versus equivalent plastic strain; (b) Lode angle versus equivalent plastic strain space. The dots represent the results at the Gauss points of the finite element mesh. The large dots correspond to the 'critical elements'. Results are plotted at the instant of onset of fracture for the tension dominated loadings (in red and black) and shortly before the formation of a deformation localization band for the shear-dominated loadings (in blue and green).

where the equivalent plastic strain exceeds 98% of the value of the 'critical element'. Thus, it is difficult to justify the specific choice of the 'critical element' without any experimental evidence on the location of the onset of fracture. This problem appears to be less significant for $\beta = 0°$ and $\beta = 90°$. For these loading conditions, the data clouds in Fig. 4-15 show a more pronounced strain peak within a narrow range of stress triaxialities.

4.6 Concluding remarks

The experimental technique by Mohr and Henn (2007, [105]) for the combined shear and tension fracture testing of metals has been revisited. The butterfly specimen design has been optimized further to increase the homogeneity of the stress and strain fields at the specimen center. Subsequently, a hybrid experimental-numerical analysis is performed for fracture experiments on TRIP780 steel specimens submitted to different combinations of loading ranging from pure shear to transverse plane strain tension. It is concluded that:

(1) The experimental results are very sensitive to inaccuracies in the initial specimen dimensions. It is important to verify the exact specimen geometry after machining to guarantee that local thickness variations do not exceed $10\mu m$.

(2) For shear-dominated loading, a band of localized deformation emerges as the engineering shear strains exceed 1.0. For tensile-dominated loading, through-thickness necking initiates at equivalent plastic strains of less than 0.3.

(3) Both the stress triaxiality and the Lode angle parameter remain more or less constant for shear-dominated loading conditions. In the case of tension-dominated loading, we observe a linear increase in stress triaxiality after the onset of through-thickness necking.

(4) The numerical simulations agree with the experimental results for tensile-dominated loading. However, numerical predictions for shear-

dominated loading become invalid with the development of a band of strain localization.

(5) The results indicate that the equivalent plastic strain at the onset of fracture cannot be expressed as a function of the stress triaxiality only. We observed significantly different strains to fracture for two specimens that had been subject to different loading histories, but which failed at the same stress triaxiality.

The loading paths have been determined in terms of equivalent plastic strain, stress triaxiality and Lode angle parameter for selected elements within the specimen gage section. It is recommended to interpret the determined strains to fracture as a lower bound for the respective loading histories since the exact location of the onset of fracture could not be determined experimentally.

Chapter 5

Predictive capabilities of two ductile fracture models

Contents

[4] This Chapter is reproduced from: Dunand, M. and D. Mohr (2011). "On the predictive capabilities of the shear modified Gurson and the modified Mohr–Coulomb fracture models over a wide range of stress triaxialities and Lode angles". *Journal of the Mechanics and Physics of Solids* **59**(7): p. 1374-1394.

5.1 Introduction

In this Chapter, the fracture prediction capabilities of the shear-modified Gurson model by Nielsen and Tvergaard (2010, [118]) and the Modified Mohr-Coulomb (MMC) fracture model (Bai and Wierzbicki, 2010, [5]) are investigated for a representative advanced high strength steel sheet material. Both phenomenological fracture models are physics-inspired and take the effect of the first and third stress tensor invariants into account in predicting the onset of ductile fracture. The MMC model is based on the assumption that the initiation of fracture is determined by a critical stress state, while the shear-modified Gurson model assumes void growth as the governing mechanism. The results from an extensive experimental program (Chapter 3 and Chapter 4) are used to calibrate and validate the fracture models. The program includes fracture experiments under nine different loading conditions thereby covering a wide range of stress triaxialities and Lode angles. After calibration of the model parameters using inverse methods, the models are evaluated based on their ability to predict the fracture displacements in experiments that have not been used for calibration. It is found that the MMC model predictions agree well with all experiments (less than 4% error), while less accurate predictions are observed for the shear-modified Gurson model. A comparison of plots of the strain to fracture as a function of the stress triaxiality and the normalized third invariant reveals significant differences between the two models except within the vicinity of stress states that have been used for calibration

5.2 Experimental results

Experimental results are used to identify the material model parameters and to assess the predictive capabilities of the fracture models. Nine distinct experiments have been performed to characterize the fracture response. We briefly recall the experimental procedures that have been detailed in Chapter 3 and Chapter 4.

5.2.1 Tensile experiments

Tensile experiments are performed on flat specimens with circular cutouts (Figs. 3-1a to 3-1c) and on a flat specimen with a central hole (Fig. 3-1d). The specimen loading axis is always oriented along the rolling direction. All notched specimens are 20mm wide and feature a b=10mm wide notched gage section. Specimens with three different notched radii are prepared: R=20mm, R=10mm and R=6.67mm. A forth type of specimen featuring an 8mm diameter circular hole at the center is also used. All experiments are carried out under displacement control at a constant crosshead velocity of 0.5mm/min. Digital Image Correlation (DIC) is used to measure the relative displacement of specimen boundaries and the displacement field at the center of the gage section. The measured force-displacement curves are depicted in Fig 5-1 with black dots. For all four geometries, a force maximum is reached before fracture occurs. It is associated with the onset of through-the-thickness necking at the specimen center for the notched geometries and in the two specimen ligaments for the central hole geometry.

The instant of the onset of fracture is defined through the first discontinuity in the measured surface displacement field. In all tests, the appearance of the first surface crack also corresponds to a sudden drop of the applied force. The corresponding relative displacement of the specimen boundaries is referred to as “displacement to fracture” or “fracture displacement”. Three specimens of each geometry are tested. The variations in the measured fracture displacement are less than 1.3% for each notched geometry, and about 2.2% for the specimen with a central hole.

5.2.2 Circular punch experiment

A sheet specimen is clamped on a circular die and subsequently loaded through a hemispherical punch. The punch and die have a diameter of 44.5mm and 100mm, respectively. The clamping pressure is applied through eight M10-12.9 screws. The experiment is carried out on a screw-driven universal testing machine (MTS, Model G45) at a constant punch velocity of 5mm/min. In order to limit the effects of friction, a stack of six

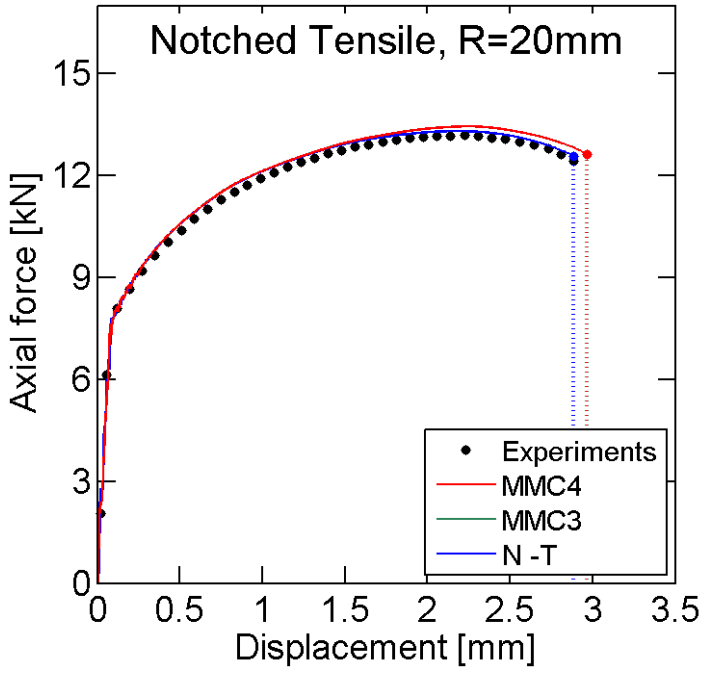

(a)

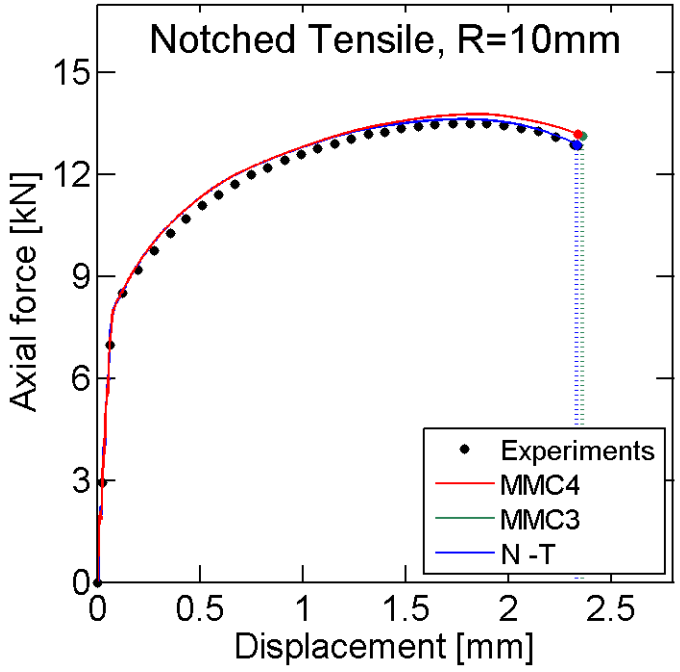

(b)

Figure 5-1: Force displacement curves for tensile specimens with (a) a 20mm notch, (b) a 10mm notch, (c) a 6.67mm notch and (d) a central hole. Experimental results are depicted

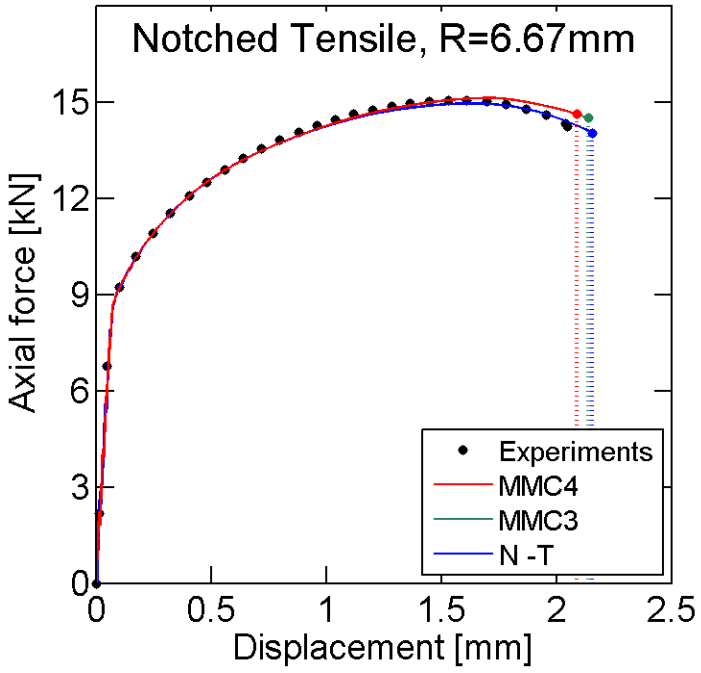

(c)

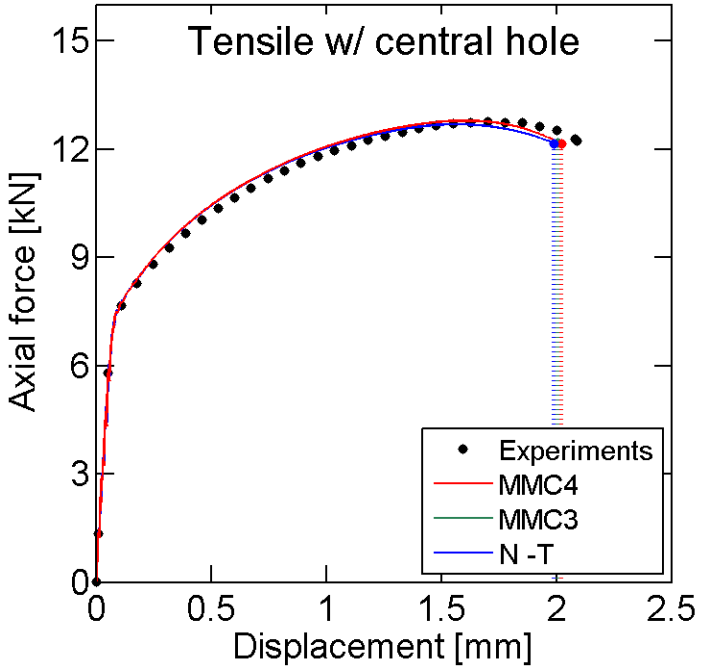

(d)

in black, numerical results using the 4-parameters MMC model in red, the 3-parameters MMC model in green and the Nieslsen-Tvergaard model in blue. Vertical dashed line show displacements to fracture.

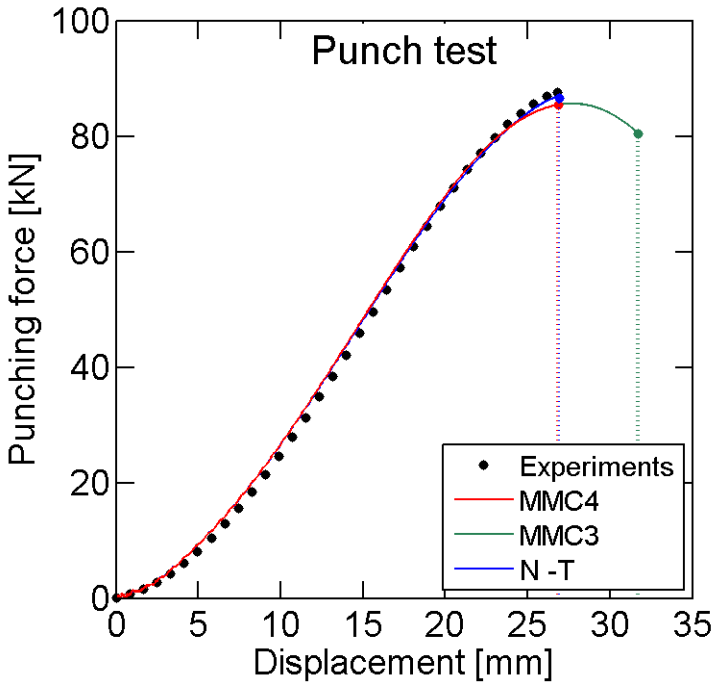

Figure 5-2: Force displacement curves for the punch experiment. Experimental results depicted in black, numerical results using the 4-parameters MMC model in red, the 3-parameters MMC model in green and the Nieslsen-Tvergaard model in blue. Vertical dashed line show displacements to fracture.

oil-lubricated 90µm thick Teflon layers is put between the specimen and the punch during each test. Three-dimensional Digital Image Correlation is used to measure the out-of-plane deformation of the specimen. The applied force versus punch displacement curve is depicted with black dots in Fig. 5-2; it increases monotonically until a sharp drop in the force level is observed at the instant of the onset of fracture.

5.2.3 Multi-axial fracture experiments

Bi-axial fracture experiments are carried out in a dual actuator system (Mohr and Oswald, 2008, [109]) that permits to apply a combination of normal and transverse loads to the boundaries of a butterfly-shaped specimen. The specimen geometry is sketched in Fig. 2-

12; it features a gage section of reduced thickness which is bounded by shoulders of clothoid shape. The butterfly specimen has been designed such that fracture initiates at the center of the gage section, remote from the lateral free edges. The ratio of the applied vertical force F_V and the horizontal force F_H, is characterized by the biaxial loading angle β:

$$\tan\beta = \frac{F_V}{F_H} \tag{5-1}$$

$\beta = 0°$ corresponds to pure shear while $\beta = 90°$ corresponds to transverse plane strain tension. Four different loading conditions are investigated: $\beta = 0°$ (pure shear), $\beta = 25°$ (shear-dominated), $\beta = 63°$ (tension dominated) and $\beta = 90°$ (transverse plane strain tension). All experiments are performed under force control to enforce a constant loading angle β. During the experiments for $\beta = 63°$ and $90°$, the control mode is switched to displacement control shortly before the onset of localized necking; the actuator velocities are chosen such that β remains approximately constant. Displacements of the specimen boundaries (both translations and possible rotations) are recorded by Digital Image Correlation (DIC) throughout the experiments.

For each experiment, we measure two force-displacement curves: (1) the tangential force versus horizontal displacement curve, and (2) the axial force versus vertical displacement curve (depicted with black dots in Fig. 5-3). In experiments for tension-dominated loading ($\beta = 63°$ and $\beta = 90°$), the vertical force-displacement curves exhibit a peak prior to fracture, which seems to coincide with the onset of localized necking. In the shear-dominated experiments ($\beta = 0°$ and $\beta = 25°$), the measured force-displacement curves increase monotonically until fracture. The fracture displacement is defined as the relative displacement (either horizontal or vertical) of the specimen boundaries at which a sudden drop of force occurs.

5.2.4 Stress and strain states

In almost all experiments described above, plastic deformation localizes within the gage section prior to fracture. A finite element simulation is performed of each experiment to obtain the stress and strain history at the location of fracture initiation. All specimens are

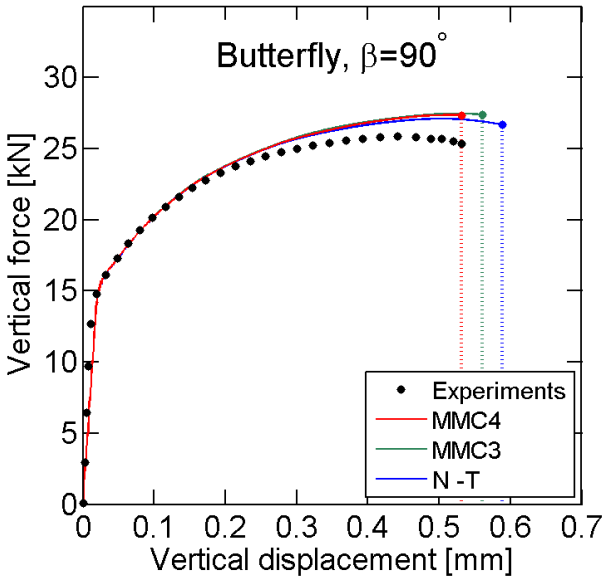
Butterfly, β=90°
Vertical force [kN]
Vertical displacement [mm]
Experiments
MMC4
MMC3
N -T

(a)

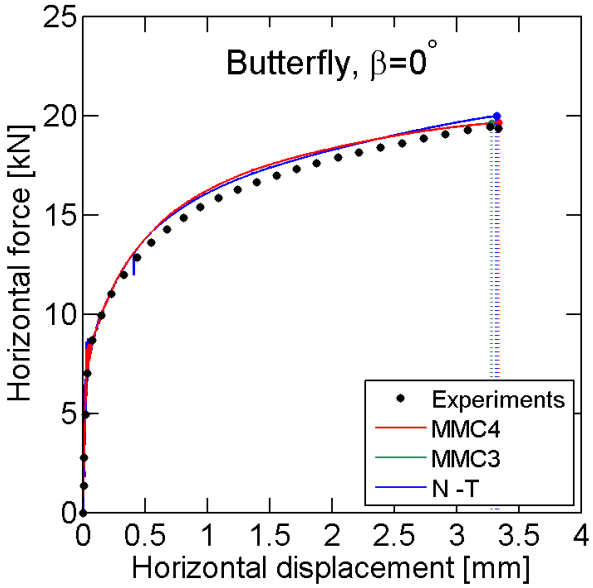
Butterfly, β=0°
Horizontal force [kN]
Horizontal displacement [mm]
Experiments
MMC4
MMC3
N -T

(b)

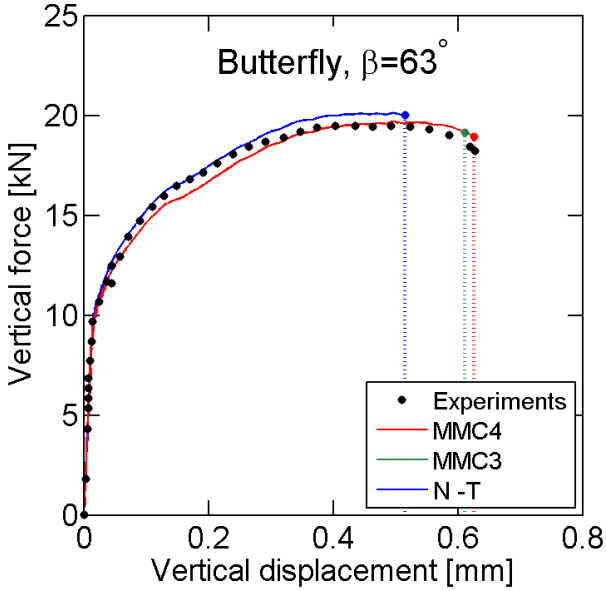
Butterfly, β=63°
Vertical force [kN]
Vertical displacement [mm]
Experiments
MMC4
MMC3
N -T

(c)

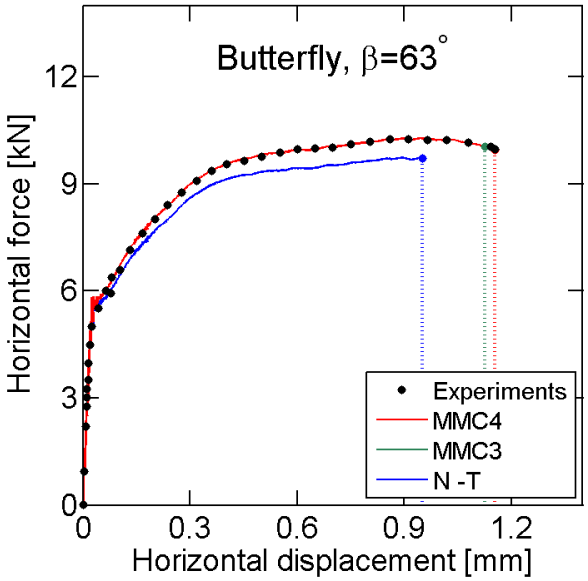
Butterfly, β=63°
Horizontal force [kN]
Horizontal displacement [mm]
Experiments
MMC4
MMC3
N -T

(d)

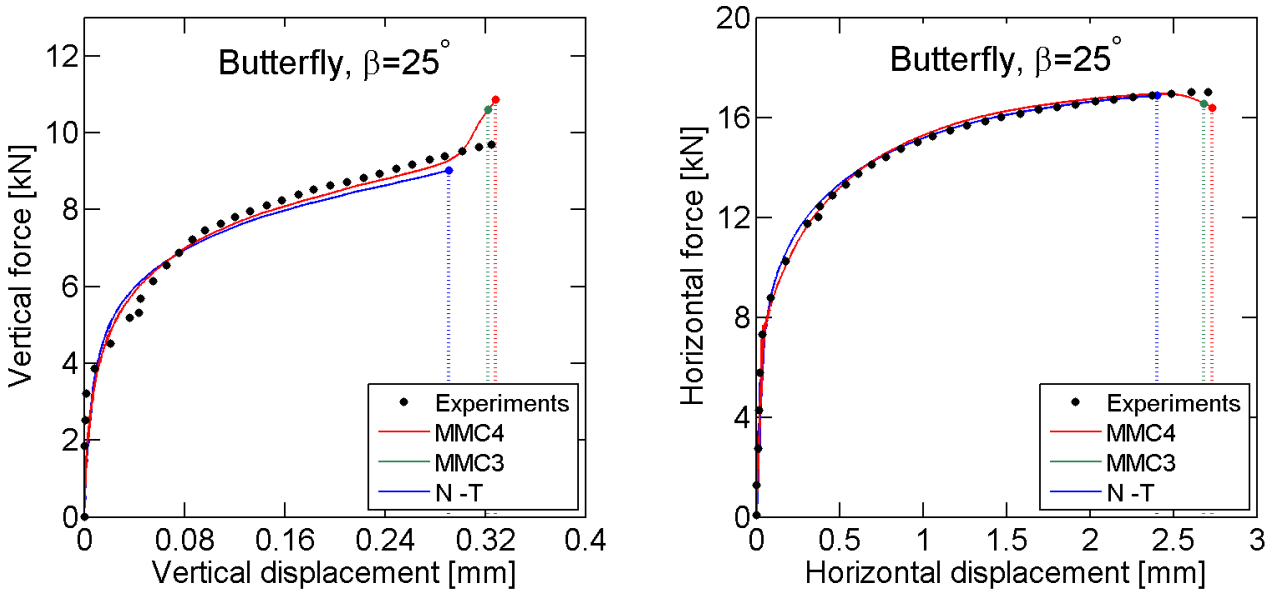

(e) (f)

Figure 5-3: Force displacement curves for the butterfly experiments. (a): $\beta = 90°$. (b): $\beta = 0°$. (c) and (d): $\beta = 63°$. (e) and (f): $\beta = 25°$. Experimental results depicted in black, numerical results using the 4-parameters MMC model in red, the 3-parameters MMC model in green and the Nieslsen-Tvergaard model in blue. Vertical dashed line show displacements to fracture.

meshed with reduced-integration eight-node 3D elements (type C3D8R of the Abaqus/Explicit library). Exploiting the symmetry of the specimen geometry, only half of the butterfly specimen, a quarter of the punch specimen and an eighth of tensile specimens are meshed. Details on the FE meshes and discretization errors are given in Chapter 3. The displacements measured by DIC are directly imposed as boundary conditions in the numerical model.

Table 5-1 provides an overview on the stress states and maximum strains reached in different specimens as obtained from hybrid experimental-numerical analysis. The final strain corresponds to the maximum equivalent plastic strain within the specimen gage

Table 5-1: Experimental program.

Experiment		Stress state: initial / average / final		Final strain [-]
Specimen	Characteristic	Triaxiality η [-]	Third invariant ξ [-]	
butterfly	$\beta = 0°$	0.06 / 0.09 / 0.12	0.24 / 0.31 / 0.35	1.04
butterfly	$\beta = 25°$	0.16 / 0.16 / 0.17	0.67 / 0.65 / 0.60	1.08
butterfly	$\beta = 63°$	0.39 / 0.51 / 0.68	0.94 / 0.87 / 0.85	0.93
butterfly	$\beta = 90°$	0.57 / 0.58 / 0.61	0.02 / 0.02 / 0.0	0.33
central hole		0.33 / 0.30 / 0.26	0.99 / 0.97 / 0.91	0.79
notched	R=6.67mm	0.47 / 0.53 / 0.62	0.68 / 0.54 / 0.30	0.42
notched	R=10mm	0.44 / 0.51 / 0.64	0.82 / 0.63 / 0.32	0.51
notched	R=20mm	0.38 / 0.47 / 0.64	0.96 / 0.77 / 0.42	0.59
punch		0.65 / 0.66 / 0.66	-1.00	0.90

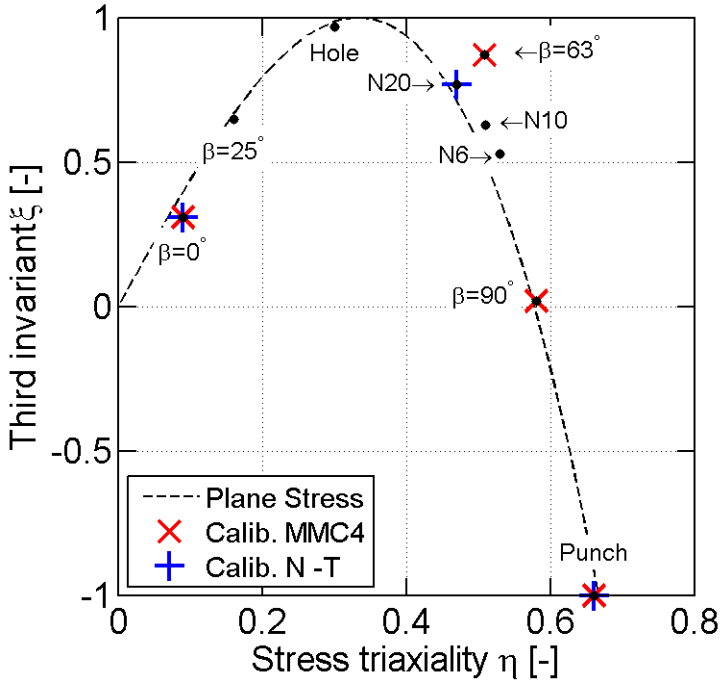

Figure 5-4: Average stress state in each experiment at the location where the highest equivalent plastic strain is reached. Experiments used to calibrate the 4-parameter MMC model are depicted with red stars, while experiments used to calibrate the Nielsen-Tvergaard model are depicted with blue crosses. The black dashed line show the relation between stress triaxiality and third stress invariant in case of plane stress condition.

section when the fracture displacement is reached. The average triaxiality and normalized third invariants, defined as

$$\eta_{av} = \frac{1}{\varepsilon_f}\int_0^{\varepsilon_f} \eta d\bar{\varepsilon}^p \quad \text{and} \quad \xi_{av} = \frac{1}{\varepsilon_f}\int_0^{\varepsilon_f} \xi d\bar{\varepsilon}^p \tag{5-2}$$

are reported for the integration point of the highest equivalent plastic strain. The experimental program for the TRIP steel covers the entire range of positive stress triaxialities accessible in sheet materials ($0 \leq \eta \leq 2/3$), and the full range of third stress invariants ($-1 \leq \xi \leq 1$), as illustrated in Fig. 5-4.

5.3 Phenomenological approach (uncoupled model)

We make use of a non-associated plasticity model which has been validated for a series of uniaxial and multi-axial plasticity experiments (Chapter 2). The damage accumulation will be modeled independently using the so-called Modified Mohr-Coulomb (MMC) model (Bai and Wierzbicki, 2010, [5]). This particular weighting function is considered as it includes parameters that can adjust the damage accumulation function for low and high stress triaxialities as well as the Lode angle parameter.

5.3.1 Plasticity Model

The plasticity model presented in Chapter 2 with calibration #5 is used. We make use of a planar isotropic quadratic yield function,

$$f(\boldsymbol{\sigma}, k) = \bar{\sigma} - k = 0 \quad , \quad \bar{\sigma} = \sqrt{(\boldsymbol{P\sigma}) \cdot \boldsymbol{\sigma}} \tag{5-3}$$

in conjunction with a non-associated flow rule

$$d\boldsymbol{\varepsilon_p} = d\lambda \frac{\partial g}{\partial \boldsymbol{\sigma}} \tag{5-4}$$

$d\lambda \geq 0$ denotes the plastic multiplier. The anisotropic quadratic flow potential reads

$$g = \sqrt{(\boldsymbol{G\sigma}) \cdot \boldsymbol{\sigma}} \tag{5-5}$$

P and **G** are symmetric positive-semidefinite matrices, with $\bar{\sigma} = 0$ and $g = 0$ if and only if $\boldsymbol{\sigma}$ is a hydrostatic stress state. The values for the non-zero components of **P** and **G** are given in Table 5-2. $\boldsymbol{\sigma}$ denotes the Cauchy stress vector in material coordinates,

$$\boldsymbol{\sigma} = [\sigma_0 \quad \sigma_{90} \quad \sigma_n \quad \tau \quad \tau_{0n} \quad \tau_{90n}]^T \tag{5-6}$$

The components σ_0, σ_{90} and σ_n represent the true normal stress in the rolling, transverse and out-of-plane directions; τ denotes the corresponding in-plane shear stress, while τ_{0n} and τ_{90n} represent the corresponding out-of-plane shear stresses. Isotropic strain hardening is described as

$$dk = h(\bar{\varepsilon}^p)d\bar{\varepsilon}^p \tag{5-7}$$

where $h = h(\bar{\varepsilon}^p)$ defines the strain hardening modulus. The strain hardening response of the material is modeled by a piecewise-linear stress-strain curve which has been determined from biaxial punch experiments and validated for multi-axial loading conditions, as detailed in Chapter 3 and Chapter 4.

Table 5-2: Plasticity model coefficients.

Yield function							Flow potential						
P_{11}	P_{12}	P_{13}	P_{22}	P_{23}	P_{33}	P_{44}	G_{11}	G_{12}	G_{13}	G_{22}	G_{23}	G_{33}	G_{44}
1.00	-0.47	-0.53	1.00	-0.53	1.06	2.94	1.00	-0.47	-0.53	0.94	-0.47	1.00	2.64

Table 5-3: Strain hardening parameters

K [MPa]	ε_0 [-]	n [-]
1460	1.63×10^{-3}	0.204

5.3.2 MMC fracture model

The original Mohr-Coulomb failure criterion (Mohr, 1900, [110]) is formulated in the stress space and assumes that failure occurs when the shear and normal stresses on any plane of normal vector $\boldsymbol{n}$ verify the condition

$$\max_{\mathbf{n}}(\tau + c_1\sigma_n) = c_\alpha \tag{5-8}$$

with the friction coefficient c_1 and the cohesion c_α. Bai and Wierzbicki (2010, [5]) transformed Eq. (5-8) into the space of stress triaxiality, Lode angle and equivalent plastic strain to fracture assuming proportional monotonic loading, a pressure and Lode angle dependent isotropic plasticity model, and isotropic strain hardening according to the power law. The resulting explicit expression for the fracture strain reads

$$\hat{\varepsilon}(\eta,\xi) = \left\{ c_2 \left[c_3 + \frac{\sqrt{3}}{2-\sqrt{3}}\left(c^{ax}(\xi) - c_3\right)\left(\sec\left(\frac{\bar{\theta}(\xi)\pi}{6}\right) - 1\right)\right] \cdot \left[\sqrt{\frac{1+c_1^2}{3}}\cos\left(\frac{\bar{\theta}(\xi)\pi}{6}\right) + c_1\left(\eta + \frac{1}{3}\sin\left(\frac{\bar{\theta}(\xi)\pi}{6}\right)\right)\right]\right\}^{-\frac{1}{n}} \tag{5-9}$$

with

$$c^{ax}(\xi) = \begin{cases} 1 & \text{for } \xi \geq 0 \\ c_{ax} & \text{for } \xi < 0 \end{cases} \tag{5-10}$$

The exponent n describes the strain hardening of the material. The coefficient c_2 is related to c_α in Eq. (5-8), while c_3 and c_{ax} characterize the dependence of the underlying plasticity model on the third stress invariant. c_3 controls the amount of Lode angle dependence of the fracture locus and $c^{ax}(\xi)$ controls the asymmetry of the fracture locus with respect to the plane $\xi = 0$. Despite the discontinuity of $c^{ax}(\xi)$, the fracture strain $\hat{\varepsilon}(\eta,\xi)$ is a continuous function of the stress invariants η and ξ. To apply the MMC fracture model for non-proportional loadings, Bai and Wierzbicki (2010, [5]) make use of Eq. (5-9) as reference strain in Eq. (1-1).

5.3.3 Calibration

Even though the expression for $\hat{\varepsilon}(\eta,\xi)$ is obtained from rigorous analytical derivations, the model parameters of the MMC model are identified through inverse calibration while their physical meaning is disregarded (Luo et al., 2010, [97]). This is due to the fact that the underlying plasticity model is not applicable to most engineering materials (e.g. the plastic behavior is pressure-independent). Furthermore, experimental evidence supporting the validity of the stress-based Mohr-Coulomb model is still scarce and the plasticity model parameters that control the pressure and Lode angle dependency are used (or abused) to obtain a good agreement of model predictions and experiments. Equation (5-9) is therefore considered as a physics-inspired function for the reference failure strain in an uncoupled damage model.

The power law exponent n is determined from the stress-strain curve for uniaxial tension while all other parameters: c_1, c_2, c_3 and c_{ax} are calibrated based on fracture experiments. We calibrate the four MMC model parameters using the three butterfly fracture experiments (at $\beta = 0°$, $\beta = 63°$ and $\beta = 90°$) and the punch test. These four experiments cover a wide range of positive stress triaxialities and the complete range of third stress invariants ($-1 \leq \xi \leq 1$). The calibration consists in finding a set of parameters $[c_1 \quad c_2 \quad c_3 \quad c_{ax}]$ such that the model describes correctly the onset of fracture in all calibration experiments. This is done by minimizing the least square error (LSE) function

$$\mathrm{LSE}(\mathrm{c}_1,\mathrm{c}_2,\mathrm{c}_3,\mathrm{c}_{\mathrm{ax}}) = \frac{1}{N}\sum_{N}\left(\left[D\left(\bar{\varepsilon}_f\right)\right]_{\exp} - 1\right)^2 = \frac{1}{N}\sum_{N}\left(\left[\int_0^{\bar{\varepsilon}_f}\frac{d\bar{\varepsilon}^p}{\hat{\varepsilon}(\eta,\xi)}\right]_{\exp} - 1\right)^2 \quad (5\text{-}11)$$

where N=4 is the number of calibration tests. $\eta(t), \xi(t)$ and $\bar{\varepsilon}^p(t)$ are the loading histories for the critical element where fracture is assumed to initiate. Recall that the constitutive equations are not coupled to damage evolution and hence the loading histories are independent from the fracture parameters $\mathrm{c}_1, \mathrm{c}_2, \mathrm{c}_3, \mathrm{c}_{\mathrm{ax}}$. An approximation of the minimum of Eq. (5-11) is determined through Monte Carlo sampling. A typical first guess for the critical element can be the integration point where the equivalent plastic strain is maximal when fracture displacement is reached. To validate the set of parameters obtained from

minimization of Eq. (5-11), it must be verified a posteriori that the chosen critical element is indeed the point where the damage indicator D is the highest at the instant of onset of fracture. The identified MMC model parameters are given in Table 5-4. They correspond to a least square error of $LSE < 10^{-4}$, showing that the MMC criterion is able to perfectly fit the results of all four calibration experiments.

As an alternative to the four parameter MMC model (referred to as MMC4), an attempt is made to calibrate a simplified three parameter version of the MMC model (MMC3) where $c_{ax} = 1$ is imposed prior to calibration (Beese et al., 2010, [17]). In this case, all nine tests are used for calibration. The least square error is $LSE = 5.4\ 10^{-2}$. Optimized parameters are given in Table 5-4.

Table 5-4: Parameters of the Modified Mohr-Coulomb fracture model.

Calibration	c_1 [-]	c_2 [-]	c_3 [-]	c_{ax} [-]	n [-]	LSE [-]
MMC4	0.3472	0.9098	1.7003	1.546	0.204	$< 10^{-4}$
MMC3	0.2416	1.2820	1.2741	1	0.204	$5.4\ 10^{-2}$

5.4 Shear-modified Gurson model

As outlined in the introduction, numerous modifications of the original Gurson model have been proposed to model ductile fracture. Here, we briefly recall the constitutive equations of a recent extension by Nielsen and Tvergaard (2010, [118]) which includes all features of the original Gurson model as well as the effect of the third invariant on the damage accumulation.

5.4.1 Constitutive equations of the coupled plasticity and fracture model

In the framework of the Gurson model (1977, [66]), the material state is described by the void volume fraction *f*, the macroscopic plastic strain tensor $\boldsymbol{\varepsilon^p}$, and the deformation resistance k of the (undamaged) matrix material. According to the GTN-model, the macroscopic yield surface is given by $\phi(\boldsymbol{\sigma}, k, f) = 0$, where

$$\phi(\boldsymbol{\sigma}, k, f) = \left(\frac{\bar{\sigma}}{k}\right)^2 + 2q_1 f^* \cosh\left(\frac{3}{2} q_2 \frac{\sigma_m}{k}\right) - (q_1 f^*)^2 - 1 \tag{5-12}$$

is a function of the equivalent stress $\bar{\sigma}$ and the mean stress σ_m at the macroscopic level. q_1 and q_2 are model parameters (Tvergaard, 1981, [144]), while the function $f^* = f^*(f)$ accounts for the loss of load carrying capacity before fracture (Tvergaard and Needleman, 1984, [148]):

$$f^* = \begin{cases} f & \text{for} \quad f \leq f_c \\ f_c + \dfrac{f - f_c}{f_f - f_c}(f_U^* - f_c) & \text{for} \quad f > f_c \end{cases} \quad \text{with} \quad f_U^* = \frac{1}{q_1} \tag{5-13}$$

The plastic anisotropy of the TRIP-assisted steel is introduced in the yield surface through the use of the Hill'48 equivalent stress $\bar{\sigma}$. This technique is widely used in the literature (e.g. Grange et al., 2000, [63]; Benzarga & Besson, 2001, [19]) to apply Gurson type models to orthotropic materials.

An associated flow rule is adopted

$$\dot{\boldsymbol{\varepsilon}}^{\boldsymbol{p}} = \dot{\lambda}\left(\frac{k}{2}\right)\left(\frac{\partial \phi}{\partial \boldsymbol{\sigma}}\right) \tag{5-14}$$

where $\dot{\lambda}$ is the plastic multiplier. The use of a non-associated flow rule is omitted in the case of the shear-modified Gurson model, since Stoughton's (2002, [134]) proof of the uniqueness of stress and strain states and the stability of plastic flow for non-associated plasticity models is limited to quadratic flow potentials.

The macroscopic and matrix behaviors are coupled through the rate of plastic work equivalence

$$\boldsymbol{\sigma}: \dot{\boldsymbol{\varepsilon}}^{\boldsymbol{p}} = (1-f)k\dot{\varepsilon}_M \tag{5-15}$$

while the strain hardening behavior of the matrix material is modeled by a modified Swift law

$$k = K(\varepsilon_M + \varepsilon_0)^n \tag{5-16}$$

with the three material parameters K, ε_0 and n.

In the original GTN-model, the first term of the differential equation describing the evolution of the void volume fraction,

$$\dot{f} = (1-f)\dot{\boldsymbol{\varepsilon}}^p: \mathbf{1} + \mathcal{D}\dot{\varepsilon}_M \tag{5-17}$$

is obtained from micromechanical analysis; it accounts for the growth of voids due to hydrostatic stress. The second term accounts for the nucleation of voids. Assuming that only plastic strain controlled void nucleation takes place, the nucleation coefficient $\mathcal{D}$ is given by (Chu & Needleman, 1980, [38])

$$\mathcal{D} = \begin{cases} \dfrac{f_N}{s_N\sqrt{2\pi}} \exp\left\{-\dfrac{1}{2}\left(\dfrac{\varepsilon_M - \varepsilon_N}{s_N}\right)^2\right\} & \text{for} \quad \sigma_m \geq 0 \\ 0 & \text{for} \quad \sigma_m < 0 \end{cases} \tag{5-18}$$

where f_N represents the total amount of voids to be nucleated per unit volume, ϵ_N is the average nucleation strain and s_N denotes the standard deviation of the assumed Gaussian void nucleation strain distribution. Voids nucleate only under positive stress triaxialities. The shear modified GTN-model considered in this study reads

$$\dot{f} = (1-f)\dot{\boldsymbol{\varepsilon}}^p: \mathbf{1} + \mathcal{D}\dot{\varepsilon}_M + k_\omega f \omega_0(\boldsymbol{\sigma}) \frac{\boldsymbol{s}: \dot{\boldsymbol{\varepsilon}}^p}{\sigma_{VM}} \tag{5-19}$$

with the parameter k_ω and the stress-state dependent weighting function $w(\boldsymbol{\sigma})$. The special case of $\omega_0(\boldsymbol{\sigma}) = \omega(\xi)$ corresponds to the extension proposed by Nahshon and Hutchinson (2008, [112]). Nielsen and Tvergaard (2010, [118]) propose a slightly different weighting function for the third term,

$$\omega_0(\boldsymbol{\sigma}) = \omega(\xi)\Omega(\eta) \quad \text{where} \quad \Omega(\eta) = \begin{cases} 1 & \text{for} \quad \eta < \eta_1 \\ \dfrac{(\eta - \eta_2)}{(\eta_1 - \eta_2)} & \text{for} \quad \eta_1 \leq \eta \leq \eta_2 \\ 0 & \text{for} \quad \eta > \eta_2 \end{cases} \tag{5-20}$$

The weighing factor $\Omega(\eta)$ makes the shear correction term only active for stress triaxialities smaller than η_2 . Note that when imposing $k_\omega = 0$ in (5-19), or $\eta_1 = \eta_2 = -\infty$ in (5-20), the Nielsen-Tvergaard model reduces to the well-known Gurson-Tvergaard-Needleman (GTN) model (Tvergaard and Needleman, 1984, [148]). Similarly, when setting $\eta_1 = \eta_2 = +\infty$ in (5-20), the Nahshon-Hutchinson model (2008, [112]) is obtained.

It is emphasized that the original physical meaning of *f* is lost due to the addition of the empirical third term in (5-19). In other words, f can no longer be seen as the void volume fraction and is interpreted as an empirical damage parameter. Furthermore, the assumption of the original GTN-model of equal plastic dissipation at the macroscopic level and within the matrix material breaks down in the case of the shear modified Gurson models by Nahshon and Hutchinson (2008, [112]) and Nielsen and Tvergaard (2010[118]).

5.4.2 Calibration

The shear-modified Gurson model is implemented into the finite element software Abaqus/explicit using a standard elastic predictor / return mapping algorithm (e.g. Simo and Hughes, 1998, [132]). The loss of the stress carrying capacity with increasing f can lead to numerical instabilities (in particular as $f \to f_f$). To avoid this problem, the damage accumulation is stopped when the damage parameter reaches $f = 0.9 f_f$ (as suggested in Nielsen and Tvergaard (2010, [118])). Fourteen material parameters need to be calibrated:

- the matrix strain hardening parameters *K*, ε_0 and *n*
- the macroscopic yield function coefficients q_1 and q_2
- the initial void volume fraction f_0 , the void volume fractions at the onset of void coalescence f_c and at fracture f_f
- the void nucleation parameters f_N, ε_N and s_N

- the shear damage parameters k_ω, η_1 and η_2

The model parameters are determined from four experiments: (1) uniaxial tension, (2) punch experiment: (3) notched tension with $R = 20mm$, and (4) shear-dominated butterfly experiment ($\beta = 0°$). A Monte-Carlo based inverse method is used to identify most model parameters. Details on the calibration procedure along with examples of the effect various parameters are given in the next subsections.

5.4.2.1 Initial void volume fraction f_0

Uthaisangsuk et al. (2009, [149]) measured an initial porosity of $f_0 = 6 \times 10^{-5}$ for a TRIP600 steel by means of Scanning Electron Micrography and X-ray Spectroscopy. For initially non-porous materials such as the TRIP780 steel considered here, the initial void volume fraction f_0 is orders of magnitude smaller than the nucleated void volume fraction f_N and has no significant impact on the model predictions. The result of Uthaisangsuk et al. (2009, [149]) will therefore be used here.

5.4.2.2 Strain hardening of the matrix material

The matrix strain hardening parameters $K = 1460MPa$, $\varepsilon_0 = 1.63\,10^{-3}$ and $n = 0.204$ are directly obtained from a fit of the macroscopic stress-strain curve for uniaxial tension up to the point of necking. Note that the initial porosity is very small and thus, the tensile behavior of the TRIP steel remains almost unaffected by the growth of voids for strains lower than the nucleation strain ε_N.

Table 5-5: Parameters of the shear modified Gurson model.

q_1 [-]	q_2 [-]	f_c [-]	f_f [-]	k_ω [-]	η_1 [-]	η_2 [-]
1.0	0.7	6.7 x 10^{-2}	8.0 x 10^{-2}	2.4	0.35	0.7
f_N [-]	ε_N [-]	s_N [-]	f_0 [-]			
4.5 x 10^{-2}	0.25	0.1	6 x 10^{-5}			

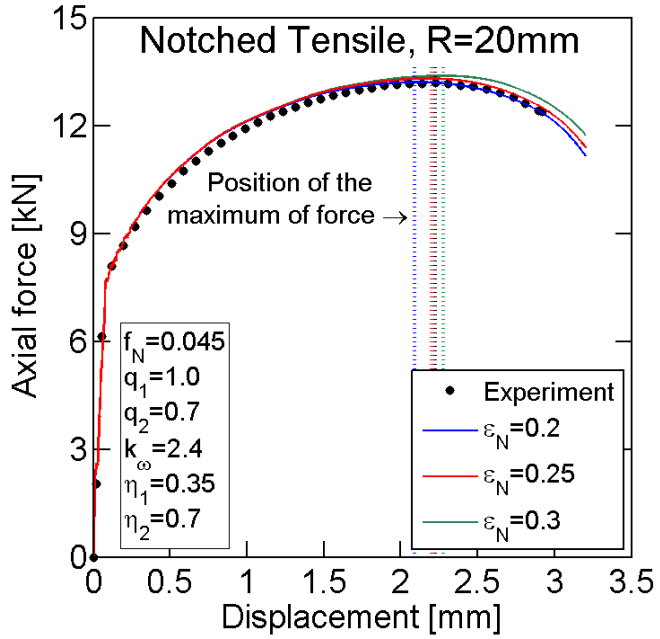

(a)

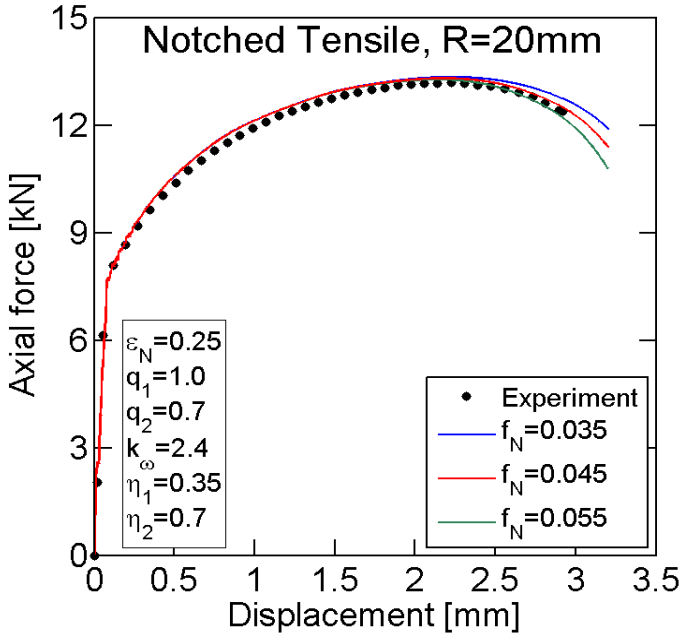

(b)

Figure 5-5: Influence of (a) the nucleation strain ε_N and (b) the nucleated void volume fraction f_N on the predicted force displacement curve of the 20mm notched tensile test. Experimental results are shown with black points.

5.4.2.3 Void nucleation law

The nucleation strain ε_N and the nucleated void volume fraction f_N are chosen such that the model predicts correctly the maximum force and subsequent decrease of the load carrying capacity of the notched tensile specimen with $R = 20mm$. Figure 5-5a depicts the influence of the nucleation strain ε_N on the force maximum (shown by vertical dashed lines): the larger ε_N, the later the force reaches its maximum. A nucleation strain of $\varepsilon_N = 0.25$ (in red) yields a good agreement with the experimental results (in black). In a similar manner, the nucleated void volume fraction f_N influences the loss of load carrying capacity of the notched specimen beyond the force maximum (Fig. 5-5b). The simulation agrees well with the experimental force-displacement curve (in black) for $f_N = 0.045$ (red curve). The predicted loss of load carrying capacity is too small with a smaller nucleated void volume fraction $f_N = 0.035$ (in blue), while it is too high with a larger nucleated void volume fraction $f_N = 0.055$ (in green). A standard deviation $s_N = 0.1$ is chosen for the nucleation law.

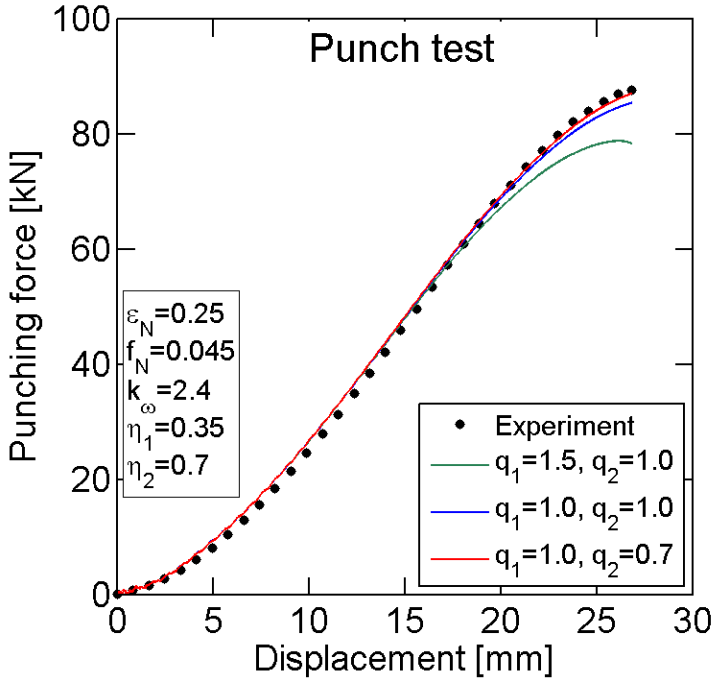

Figure 5-6: Influence of the parameters q_1 and q_2 on the predicted force displacement curve of the punch experiment. Black points depict experimental results.

5.4.2.4 Yield function coefficients q_1 and q_2

Those two fitting coefficients are chosen such that the model predicts correctly the force-displacement curve measured during the punch test. Figure 5-6 compares the experimental force-displacement curve (in black) to the simulation results for the following three sets of parameters: q_1=1.5 and q_2=1.0 (in green), q_1=1.0 and q_2=1.0 (in blue), q_1=1.0 and q_2=0.7 (in red). Observe that the punch force at the onset of fracture is correctly predicted when using the set of parameters q_1=1.0 and q_2=0.7.

5.4.2.5 Critical void volume fractions f_c and f_f

These parameters are chosen such that the fracture displacement in the punch experiment is predicted correctly. When a numerical simulation is run up to the experimental fracture displacement with the coalescence mechanism turned off ($f^* = f$ in

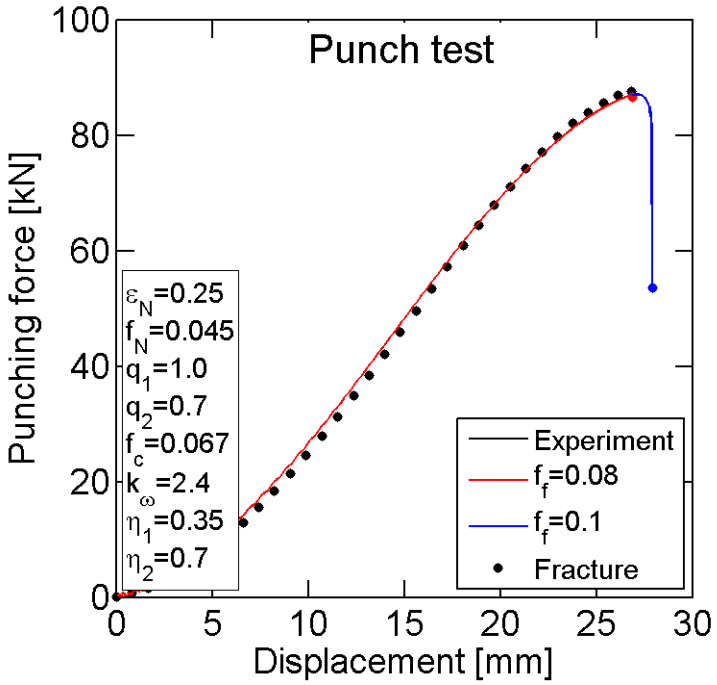

Figure 5-7: Influence of the fracture void volume fraction f_f on the predicted force displacement curve of the punch experiment. Colored points depict the simulated onset of fracture. Experimental results are shown with black points.

Eq. (5-12)), the maximum final void volume fraction is $f_{max} = 6.84 \times 10^{-2}$. Note that f_{max} is independent from the parameter k_ω since $\omega = 0$ in a punch experiment where $\xi = -1$. The introduction of void causes a loss of load carrying in the range $f_c < f < f_f$. Figure 5-7 shows the evolution of the punch force for $f_c = 6.7\text{x}10^{-2}$ and different values of f_f. When f_f is significantly higher than f_c (e.g. $f_f = 0.1$), punch force drops by about 40% before fracture (blue curve in Fig. 5-7). With f_f closer to f_c, the loss of load carrying capacity becomes unnoticeable: for example, it is only 0.2% for $f_f = 0.08$ (red curve in Fig. 5-7). For the present material, the experimental force-displacement curve (in black in Fig. 5-7) does not show any loss in load carrying capacity before fracture. Therefore, we chose $f_c = 6.7\text{x}10^{-2}$ and $f_f = 0.08$ for our subsequent simulations.

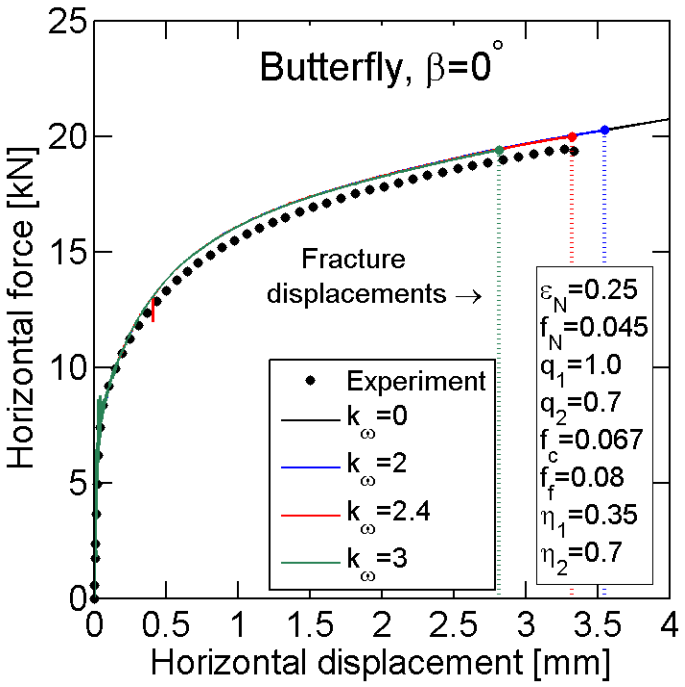

Figure 5-8: Influence of the shear damage parameter k_ω on the predicted force displacement curve and displacement to fracture of the $\beta = 0°$ butterfly experiment. Vertical dashed lines depict fracture displacements. Experimental results are shown with black points.

5.4.2.6 Shear damage parameter k_ω

The shear damage parameter k_ω is calibrated against the experimental result for a butterfly experiment at $\beta = 0°$. Figure 5-8 depicts the force-displacement curves for different values of k_ω. The corresponding fracture displacements are shown with vertical dashed lines. The predicted force-displacement curves are not affected by the choice of k_ω. As expected, no fracture is predicted for the limiting case of $k_\omega = 0$ (black line in Fig. 5-8). Among the simulations with non-zero values for k_ω, the best agreement with the experiment is observed for $k_\omega = 2.4$ (red curve in Fig. 5-8).

5.4.2.7 Weighting coefficients η_1 and η_2 of the shear damage accumulation

The result for the tensile experiment on a specimen with a large notch radius (R=20mm) is used to identify the coefficients η_1 and η_2 that control the activation of the shear-damage accumulation term in Eq. (5-19). Figure 5-9 depicts the predicted force displacement curves for different values of η_1 and η_2. The corresponding fracture displacements are shown with vertical dashed lines. Without the shear damage modification ($\eta_1 = \eta_2 = 0$, in blue in Fig. 5-9), the GTN model underestimates damage accumulation; observe that the fracture displacement is overestimated by about 8%. Conversely, the fracture displacement is underestimated by 5.6% when the shear damage term is fully active ($\eta_1 = \eta_2 = \infty$, see green curves in Fig. 5-9); note that this case corresponds to the Nahshon-Hutchinson model. With $\eta_1 = 0.35$ and $\eta_2 = 0.7$ (in red in Fig. 5-9), the experimental fracture displacement is predicted accurately. Note that the notched tension experiment for $R = 20mm$ is particularly suitable for the calibration η_1 and η_2: the stress triaxiality increases continuously from $\eta_{ini} = 0.4$ to $\eta_{fract} = 0.6$ because of the development of a localized neck (as discussed in Section 5.2.3); the damage accumulation therefore occurs within the range of stress triaxialities where the shear damage term becomes progressively inactive.

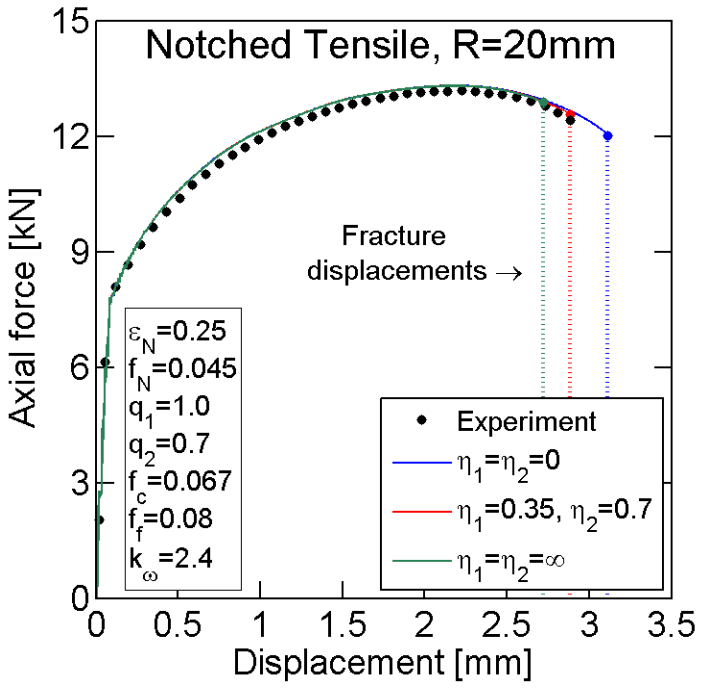

Figure 5-9: Influence of the shear damage weighting coefficients η_1 and η_2 on the predicted force displacement curve and displacement to fracture of the 20mm notched tensile experiment. Vertical dashed lines depict predicted fracture displacements. Experimental results are shown with black points.

5.4.2.8 Remarks

It is worth noting that the nucleation law coefficients and the yield function coefficients q_1 and q_2 have a similar influence on predicted force-displacement curve (Figs. 5-5 and 5-6): they control the specimen's load carrying capacity before failure. Therefore it is necessary to use different experiments to calibrate each set of parameters. Also, each calibration step is not independent from all subsequent steps. For example, results from simulation results depicted in Fig. 5-5 depend on the values of the parameters q_1, q_2, k_ω, $\eta_1$and η_2, The calibration procedure was repeated iteratively until satisfactory results were achieved.

Finite Element simulations using Gurson type models can be affected by spurious mesh sensitivity due to a possible true strain softening induced by void growth. However, with the present material model parameters, a converged solution of the computational problem seems to exist as the repetition of selected simulations with much finer meshes yielded the almost the same results in terms of force-displacement curves and displacement to fracture (less than 0.5% difference).

5.5 Comparison of model predictions and experiments

The fracture models are evaluated by comparing the predicted and experimentally-measured displacements to fracture for nine distinct experiments. FE simulations are run of all experiments with the measured displacements imposed as boundary conditions. The predicted displacement to fracture corresponds to the applied displacement at the instant when $D = 1$ for the MMC model and $f = 0.9f_f$ for the modified Gurson model. If this condition is not met before the experimental fracture displacement is reached, the simulation is continued with the same loading velocity. Since we are only interested in predicting the onset of fracture, the simulations are stopped as soon as one integration point fails. No attempt is made to model the propagation of cracks.

5.5.1 Modified Mohr-Coulomb Model

Figure 5-10 depicts the ratios of the predicted and measured displacements to fracture for all nine experiments. Error bars are included to represent the experimental scatter on the measured fracture displacements (when applicable). Figure 5-10 presents results from both the four-parameter MMC model (MMC4) and its simplified three parameter version (MMC3). Recall that only four experiments (three butterfly fracture experiments and the punch test) have been used to identify the parameters of the MMC4 model, while the simplified MMC3 has been calibrated through an optimization for all nine experiments.

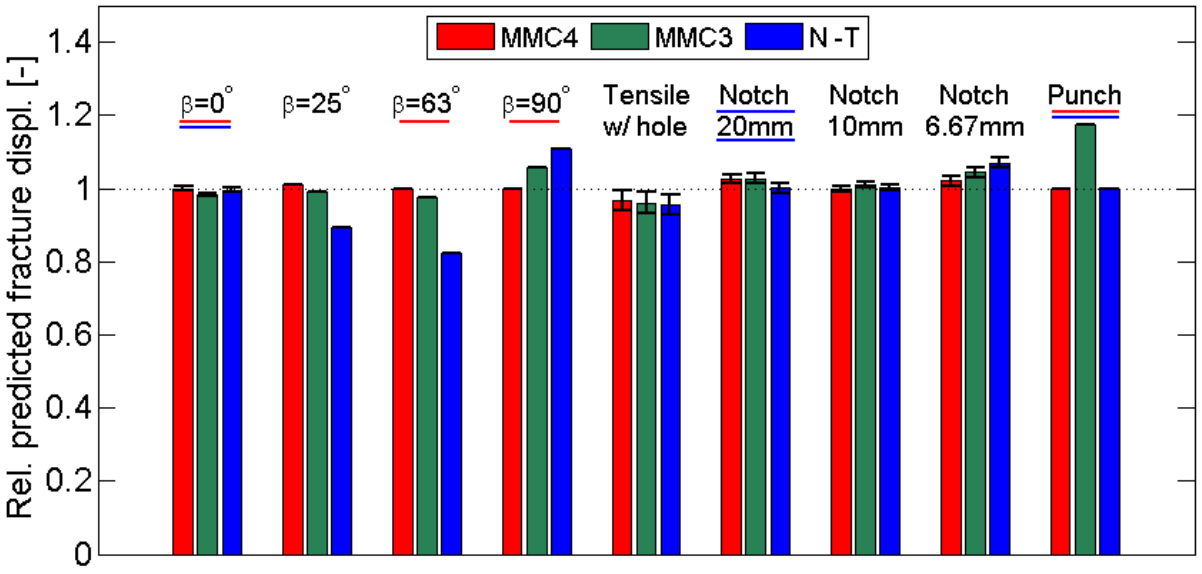

Figure 5-10: Ratio of predicted to experimental fracture displacement for all 9 experiments. Results from the 4-parameter MMC model are in red, from the 3-parameter MMC model are in green, and from the Nielsen-Tvergaard model are in blue. Experiments used for calibration have their name underlined. Error bars depict the experimental scatter, when applicable.

It is found that the MMC4 model predicts the displacements to fracture with great accuracy for all experiments. The relative error is smaller than 2% for eight of nine experiments. The largest relative error of 3.2% is observed for the tensile specimen with a central hole. Even though the MMC3 model has been calibrated for all nine experiments, it is less accurate that the MMC4 model for every experiment. In particular, the MMC3 model is not able to predict correctly the onset of fracture under equi-biaxial tension where a relative error of 17% is observed in the punch displacement to fracture. For all other experiments, the error is in the MMC3 model predictions is smaller than 5%.

5.5.2 Shear modified Gurson model

All nine experiments are simulated with the shear modified Gurson model by Nielsen and Tvergaard (2010, [118]) to evaluate its predictive capabilities. Recall that this model has been calibrated based on uniaxial tension, notched tension (with $R = 20mm$), one butterfly experiment (with $\beta = 0°$) and the punch test. Figures 5-1, 5-2 and 5-3 depict the force-displacement curves of all experiments (black dots) along with the predictions of the Nielsen-Tvergaard model (blue solid lines). The experimental and predicted curves lie almost perfectly on top of each other for the first two calibration experiments (notched tension (Fig. 5-1a) and the punch experiment (Fig. 5-2)). For the third calibration test (shear butterfly experiment, Fig. 5-3b), the predicted horizontal force is about 2.5% higher than the one measured experimentally, but the fracture displacement is predicted correctly.

The agreement of the predicted force-displacement curves with the experimental results is also very good for the two other notched tensile tests ($R = 10mm$ in Fig. 5-1b, and $R = 6.67mm$ in Fig. 5-1c). The difference between the simulation and the experimental results is less than 1% in both cases. For the specimen with a central hole (Fig. 5-1d), the predicted displacement at the force maximum is about 9% too low as compared to the experiment. As a result, the predicted force drops before fracture is too large. Butterfly experiments (Fig. 5-3) reveal more pronounced differences between the predicted and experimental results. In the simulation of the butterfly experiment for transverse plane strain tension ($\beta = 90°$, depicted in Fig. 5-3a), the force peak associated with the onset of localized necking is delayed by about 13%, resulting in a predicted force at fracture which is about 6.7% higher than that in the experiment. In the tension dominated experiment ($\beta = 63°$, Fig. 5-3c-d), both the horizontal and vertical force are predicted with 5% error. In addition, the Nielsen-Tvergaard model predicts fracture at only 82.3% of the experimental displacement to fracture which is even before the experimentally-measured force reaches its maximum.

The predicted displacements to fracture for all nine experiments are summarized in Fig. 5-10 (blue bars). For the three experiments used for calibration, the fracture displacements are predicted with less than 0.5% error. The fracture displacement of the

10mm notched specimen is very accurately predicted, with a relative error of 0.2% which is less than the experimental scatter. For the two other full thickness tensile experiments (6.67mm notch and specimen with a central hole), the relative error affecting the predicted displacement to fracture is less than 10% (respectively 6.9% and 4.5%). However, the shear-modified Gurson model is clearly inaccurate for three butterfly experiments (more than 10% error): it underestimates the displacement to fracture by 11% for the shear-dominated combined loading ($\beta = 25°$) and by 17.7% for tension-dominated combined loading ($\beta = 63°$); conversely, the fracture displacement is overestimated by 10.6% for the transverse plane strain tension experiment ($\beta = 90°$). It is worth noting that the present results have been obtained after calibrating the model for a particular choice of experiments. A different choice of calibration experiments may change the results for the shear-modified Gurson model. However, due to the diversity of our selection (in terms of stress states), it is expected that the present results allow for a representative assessment of the model performance.

5.6 Discussion

5.6.1 Modeling of the elasto-plastic response

The accumulation of damage affects the elasto-plastic material response prior to fracture when using the Gurson model. Conversely, the predictions of the standard plasticity model which is used in conjunction with the MMC model remain unaffected by the damage accumulation. The comparison of the force-displacement curves predicted by the standard plasticity model and the Nielsen-Tvergaard model (respectively in red and blue lines in Figs. 5-1, 5-2 and 5-3) show that in eight out of nine cases, both models predict the same global response of the specimens at the early stages of loading. Before nucleation occurs, material damage is negligible and the Gurson yield function, given in Eq. (5-12), reduces to a standard Hill'48 yield function (Eq. 5-3). The predicted force-displacement curves differ only when material damage becomes significant. This observation also implies that

differences due to the use of associated and non-associated flow rules are very small, which is consistent with the results reported in Chapter 2. It is interesting to see that the Nielsen-Tvergaard model does not always predict the force prior to fracture with greater accuracy; for tension with a central hole (Fig. 5-1d) and the butterfly experiment at $\beta = 0°$ (Fig. 5-3b), the uncoupled plasticity model predicts the force-displacement curves more accurately than the Gurson model.

The butterfly experiment at $\beta = 63°$ is the only experiment for which the predicted force-displacement curves (depicted in Fig. 5-3c-d) are significantly different. The Nielsen-Tvergaard model overestimates the vertical force by about 3% and underestimates the horizontal force by about 5%. It is speculated that this difference is due to the choice of the flow rule. Numerical predictions of the shear-dominated butterfly experiment ($\beta = 25°$) from the standard plasticity model show an abrupt drop of the predicted horizontal force (Fig. 5-3e) and a substantial increase of the predicted vertical force (Fig. 5-3f) prior to fracture; these sudden changes are associated with the development of a narrow band of strain localization in the numerical simulation (see also discussion in Section 4.5). The corresponding predictions of the Nielsen-Tvergaard model cannot be evaluated for this loading condition as the model predicts failure before the point of severe strain localization. However, when delaying void coalescence and fracture in the simulation (by increasing the values of f_c and f_f), the Nielsen-Tvergaard model also predicts a sudden increase of vertical force and drop of horizontal force before reaching the experimental displacement to fracture. Based on the above observations, it is tentatively concluded that the modeling of the effect of damage on the elasto-plastic behavior does not yield any improvement of the accuracy of force-displacement curve predictions.

5.6.2 Modeling of shear-induced material deterioration

As detailed in Section 5.4.1, the damage evolution equation of the GTN fracture model is modified to account for material deterioration under shear loading conditions. Nahshon and Hutchinson (2008, [112]) modified the model such as to satisfy the following hypotheses:

1. The shear damage rate is proportional to f, under the assumption that the effective void volume fraction is small;
2. The shear damage rate is the highest for generalized shear stress states ($\xi = 0$);
3. The shear damage rate is zero for axisymmetric loadings ($\xi = \pm 1$);
4. For pure shear, the shear damage increase rate scales as $\dot{f}_{shear} \sim k_\omega f \dot{\gamma}^p$, where $\dot{\gamma}^p$ is the plastic shear strain increment.

One simple form that satisfies these requirements is the assumption of a quadratic dependence of the rate of shear damage on the third stress invariant (Eq. 1-17). The results from shear-dominated butterfly experiments ($\beta = 0°$ and $\beta = 25°$) can be used to assess the validity of this choice. In those experiments, fracture occurs at stress triaxialities close to zero, while the corresponding third stress invariants are significantly different (Fig. 5-4). Before the onset of void coalescence ($f < f_c$), the ratio of the rates of void growth-induced damage, $\dot{f}_{growth}$, and shear-induced damage, $\dot{f}_{shear}$, can be simplified as:

$$\frac{\dot{f}_{growth}}{\dot{f}_{shear}} = \frac{(1-f)\dot{\boldsymbol{\varepsilon}}^{\boldsymbol{p}}\colon \mathbf{1}}{k_\omega f \omega_0(\boldsymbol{\sigma}) \dfrac{\boldsymbol{s}\colon \dot{\boldsymbol{\varepsilon}}^{\boldsymbol{p}}}{\sigma_{VM}}} \approx \frac{9}{4} \frac{q_1 q_2^2}{k_\omega \omega_0(\boldsymbol{\sigma})} \eta \tag{5-21}$$

This ratio is smaller than 11×10^{-2} in both experiments, and hence the predicted displacement to fracture is mostly controlled by the shear damage term. In the above calibration procedure, the experiment for $\beta = 0°$ has been used to calibrate the material parameter k_ω. The inability of the Nielsen-Tvergaard model to predict the fracture displacement for $\beta = 25°$ suggests that the empirical choice of the quadratic relationship between $\dot{f}_{shear}$ and ξ needs to be revisited.

5.6.3 Fracture locus for proportional loading conditions.

Proportional loadings are characterized by constant stress triaxiality η and normalized third invariant ξ throughout loading. In this specific case, the equivalent plastic strain to fracture, or fracture strain $\bar{\varepsilon}_f$, can be represented as a function of η and ξ to create the so-called fracture locus in the $(\eta, \xi, \bar{\varepsilon}^p)$ space. The MMC fracture locus is defined by Eq. 5-9.

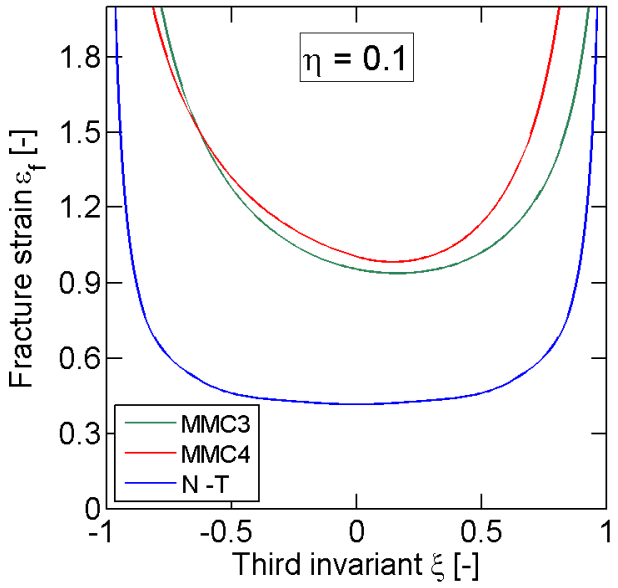
η = 0.1
Fracture strain ε_f [-]
Third invariant ξ [-]
MMC3
MMC4
N -T

(a)

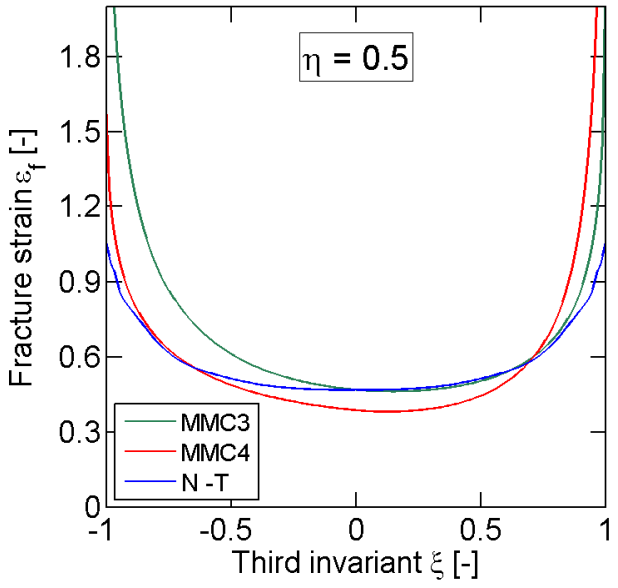
η = 0.5
Fracture strain ε_f [-]
Third invariant ξ [-]
MMC3
MMC4
N -T

(b)

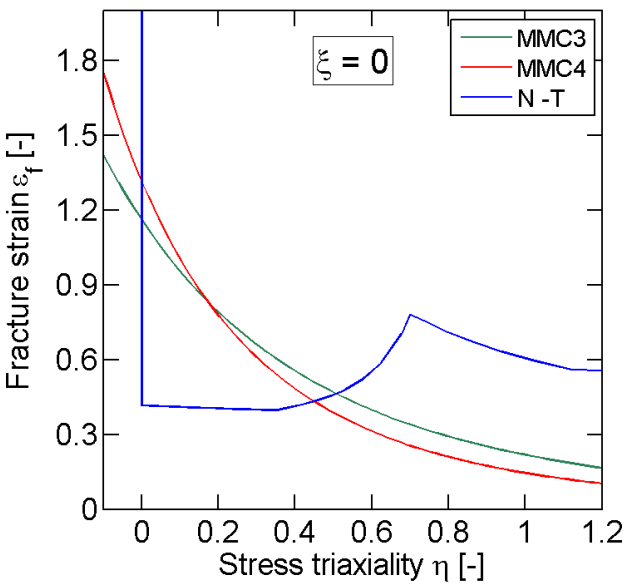
ξ = 0
Fracture strain ε_f [-]
Stress triaxiality η [-]
MMC3
MMC4
N -T

(d)

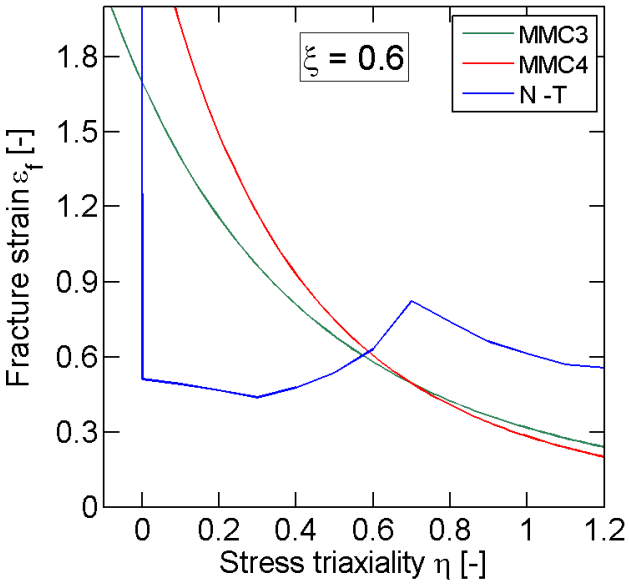
ξ = 0.6
Fracture strain ε_f [-]
Stress triaxiality η [-]
MMC3
MMC4
N -T

(e)

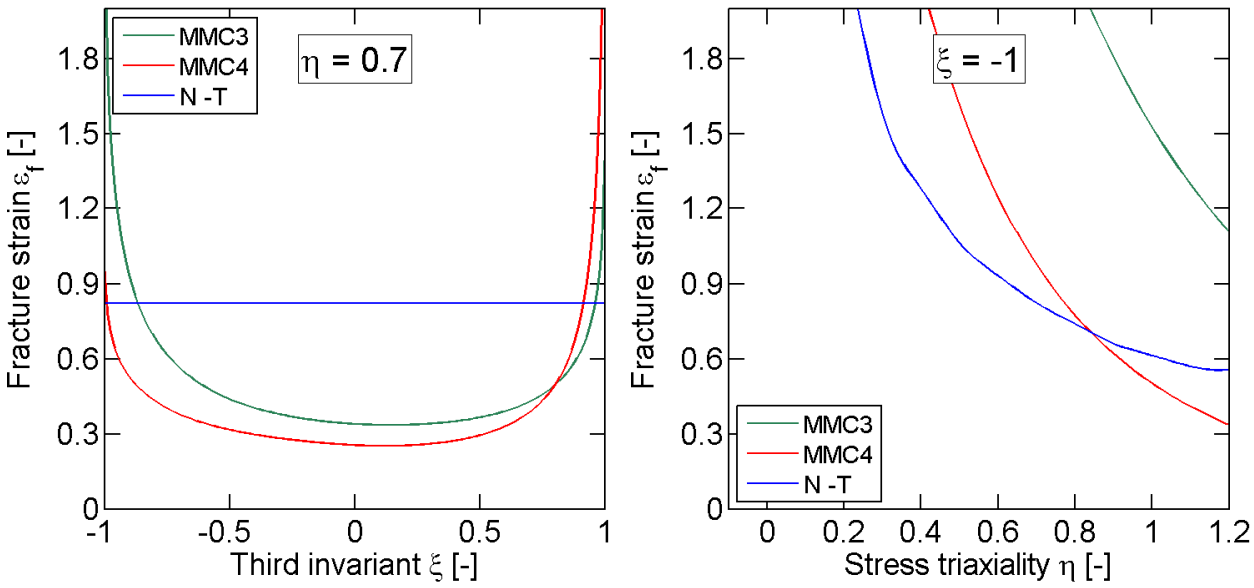

Figure 5-11: Fracture loci for proportional loading conditions in the $(\eta, \xi, \bar{\varepsilon}^p)$ plane of the MMC3 fracture criterion (in green), MMC4 fracture criterion (in red) and Nieslen-Tvergaard model (in blue). Cross sections at constant stress triaxiality: (a) $\eta = 0.1$, (b) $\eta = 0.5$, (c) $\eta = 0.7$; and constant third invariants: (d) $\xi = 0$, (e) $\xi = 0.6$ and (f) $\xi = -1$.

The Nielsen-Tvergaard fracture locus for proportional loading is constructed by applying various combinations of normal stresses to a single solid element, covering a wide range of stress triaxialities and third invariants. For each set of prescribed stress ratios, the calculations are run to determine the corresponding fracture strain for proportional loading.

Cross sections of the three fracture loci are depicted in Fig 5-11 (the MMC3 fracture locus is shown in green, the MMC4 locus in red and the Nielsen-Tvergaard locus in blue). Figures 5-11a to 5-11c depict the fracture strains for proportional loading as a function of the third stress invariant, at a fixed stress triaxiality ($\eta = 0.1$ in Fig. 5-11a, $\eta = 0.5$ in Fig. 5-11b, $\eta = 0.7$ in Fig. 5-11c), while Figs. 5-11d to 5-11f depict the fracture strains for proportional loading as a function of the stress triaxiality, at fixed third invariants ($\xi = 0$ in Fig. 5-11d, $\xi = 0.6$ in Fig. 5-11e, $\xi = -1$ in Fig. 5-11f).

The MMC fracture strain decreases in stress triaxiality and exhibits a U-shaped dependence on the third invariant, resulting in a continuous fracture locus shaped as a half-tube in the $(\eta, \xi, \bar{\varepsilon}^p)$ space (Bai and Wierzbicki, 2010, [5]). Note that both MMC3 and MMC4 fracture loci are asymmetric with respect to $\xi = 0$ and that, at a fixed stress triaxiality, the minimum ductility does not correspond to the generalized shear stress state (characterized by $\xi = 0$). The Nielsen-Tvergaard fracture locus shows a more complex dependence on the stress state. For low stress triaxialities ($0 < \eta < \eta_1$), the fracture locus is a U-shaped function of the third invariant. The fracture strain is smallest for generalized shear stress states ($\xi = 0$). For axisymmetric loading states ($\xi = \pm 1$), there is no shear-induced damage and the fracture strain increases asymptotically as the stress triaxiality decreases to 0. For intermediate stress triaxialities ($\eta_1 < \eta < \eta_2$), the fracture strain increases in stress triaxiality for loadings states with third invariants close to 0, as the shear-induced damage slows down. For high stress triaxialities ($\eta > \eta_2$), the shear damage term in Eq. 5-20 is inactive: the fracture strain decays almost exponentially in stress triaxiality and is independent of the third invariant. Note that the Nielsen-Tvergaard fracture locus is symmetric with respect to $\xi = 0$ and presents a discontinuity at $\eta = 0$, because of the discontinuous nucleation behavior (Eq. 5-18).

The MMC3 and MMC4 fracture loci are similar, except for stress states with third invariants close to $\xi = \pm 1$. In the specific case of $\xi = -1$ shown in Fig. 5-11f, the MMC3 fracure strain is higher by about 0.8. As a result, fracture predictions of both models differ the most for the punch test, which is characterized by $\xi = -1$. The calibrated MMC4 and Nielsen-Tvergaard fracture loci are remarkably different over the entire range of stress states considered, except within the vicinity of the experimental data that have been used to calibrate the Nielsen-Tvergaard model: for $\eta \cong 0.5$ and $\xi \cong 0.7$ (average stress state in the 20mm notch tensile experiment) and for $\eta \cong 0.7$ and $\xi \cong -1$ (average stress state in the punch experiment), the two fracture loci intersect (see Fig. 5-11b-c).

5.7 Concluding remarks

The ductile fracture of metals has been studied extensively over the past five decades. However, despite strenuous efforts in the area of micromechanical analysis, most state-of-the-art models are only physics-inspired with a strong empirical component. The MMC model has been developed with a stress-based fracture criterion in mind, but very strong empirical assumptions are made regarding the damage accumulation under non-proportional loading. The Nielsen-Tvergaard model is based on the rigorous micromechanical analysis of void growth, but strong empirical assumptions are made regarding the effect of void nucleation, void coalescence and the effect of shear. As a result of these empirical assumptions, the physical meaning of most material model parameters is lost; consequently, our comparative study is mostly concerned with the calibration of the respective mathematical models. The results from an extensive experimental program on a TRIP780 steel, including nine experiments with loading conditions ranging from pure shear to equibiaxial tension, are used as a basis for the calibration and validation of the models.

The 3-parameter version of the MMC fracture model cannot predict the onset of fracture over the complete range of stress states considered. Its accuracy is good for loading conditions ranging from pure shear to transverse plane strain tension which are characterized by positive third stress invariants. A fourth parameter controlling the asymmetry of the fracture criterion with respect to $\xi = 0$ is required to improve the model accuracy. With this additional parameter, the onset of fracture in all nine experiments carried out is predicted correctly by the MMC fracture model. The predictions of the shear-modified Gurson model are found to be less accurate. It is shown that the Lode angle dependence of the shear-induced damage mechanism needs to be modified further to improve the accuracy of the Nielsen-Tvergaard model.

Aside from the small differences in the prediction accuracies, it is surprising to see that two fundamentally different fracture models (stress-based criterion versus void growth model) are both able to predict the fracture displacement over a wide range of stress states. This observation suggests that the underlying physical assumptions are less important than the models' mathematical flexibility to be fitted to a wide range of experimental data.

Another key fundamental difference between the MMC model and the Nielsen-Tvergaard model lies in the coupling of plasticity and damage. The MMC model makes use of a damage indicator function which has no effect on the elasto-plastic behavior, while damage reduces the load carrying capacity and changes the shape of the yield surface in the case of the shear-modified Gurson model. However for the TRIP780 material, both models show equally good predictions of the force-displacement curves. The MMC model is recommended for practical applications because of the greater computational stability of uncoupled damage models, the smaller number of parameters to be identified and the ease of their identification based on experiments. However, it is important to identify the MMC model parameters based on experiments that cover a wide range of stress states.

Chapter 6

Modeling of plastic flow localization at intermediate stress triaxialities

Contents

[5] This Chapter is reproduced from: Dunand, M. and D. Mohr (2013). "Effect of Lode parameter on plastic flow localization at low stress triaxialities", *Submitted for publication*.

6.1 Introduction

The effect of the stress state on the localization of plastic flow in a Levy-von Mises material is investigated numerically. The particular focus is on the effect of the Lode parameter on the localization of plastic flow in void containing solids at intermediate stress triaxialities (from 0 to 1). A unit cell model is built with a spherical central void that acts as a defect triggering the onset of flow localization along a narrow band. Periodic boundary conditions are defined along all boundaries of the unit cell. Shear and normal loading is applied such that the macroscopic stress triaxiality and Lode parameter remain constant throughout the entire loading history. Due to the initially orthogonal symmetry of the unit cell model the deformation-induced anisotropy associated with void shape changes, both co-rotational and radial loading paths are considered. The simulation results demonstrate that the macroscopic equivalent plastic strain at the onset of localization decreases in stress triaxiality and is a convex, non-symmetric function of the Lode parameter. In addition to predicting the onset of localization through unit cell analysis, an analytical criterion is proposed which defines an open convex envelope in terms of the shear and normal stresses acting on the plane of localization.

6.2 Micromechanical model

A unit cell model with an initial spherical void is built and used to obtain a relationship between the macroscopic equivalent plastic strain to plastic localization and the stress state. The underlying motivation is the hypothesis that the localization of plastic deformation in a band indicates that the onset of fracture is imminent (Rice, 1977, [127]). Even though the overall elasto-plastic response of many metals can be described accurately up to very large strains without considering the nucleation and growth of voids, a low porosity is needed as imperfection triggering the localization of plastic deformation.

6.2.1 Matrix material

The matrix material is modeled as a rate-independent isotropic elastic-plastic Levy-von Mises solid. Only isotropic strain hardening is considered by a saturation hardening law that describes the relationship between the von Mises equivalent plastic strain λ and the flow resistance $k = k(\lambda)$. In differential form, the saturation law reads

$$\begin{cases} k(0) = k_0 \\ \dfrac{dk}{d\lambda} = H_0 \left(1 - \dfrac{k}{k_\infty}\right)^r \end{cases} \tag{6-1}$$

with the initial flow resistance k_0 and the saturation value k_∞. The strain hardening parameters $\{k_0, k_\infty, H_0, r\}$ and the elastic constants used in the calculations (Table 6-1) correspond approximately to the hardening behavior of the TRIP material.

Table 6-1: Matrix material model parameters

Elastic constants		Strain hardening constants			
E [MPa]	ν [-]	k_0 [MPa]	k_∞ [MPa]	H_0 [MPa]	r [-]
185,000	0.3	450	1,200	20,000	2.0

6.2.2 Unit cell geometry and kinematic boundary conditions

The undeformed unit cell consists of a rectangular cuboid of matrix material containing a spherical void at its center. We introduce the fixed Cartesian frame $[\boldsymbol{e_1}, \boldsymbol{e_2}, \boldsymbol{e_3}]$ corresponding to the normals to the cell's outer surfaces in the initial (undeformed) configuration. We limit our attention to a unit cell with the initial edge lengths $L_1 = L_2 = L$ and $L_3 = 2L$ (Fig. 6-1); the height-to-width ratio of $L_3 / L_1 = 2$ is chosen to facilitate the

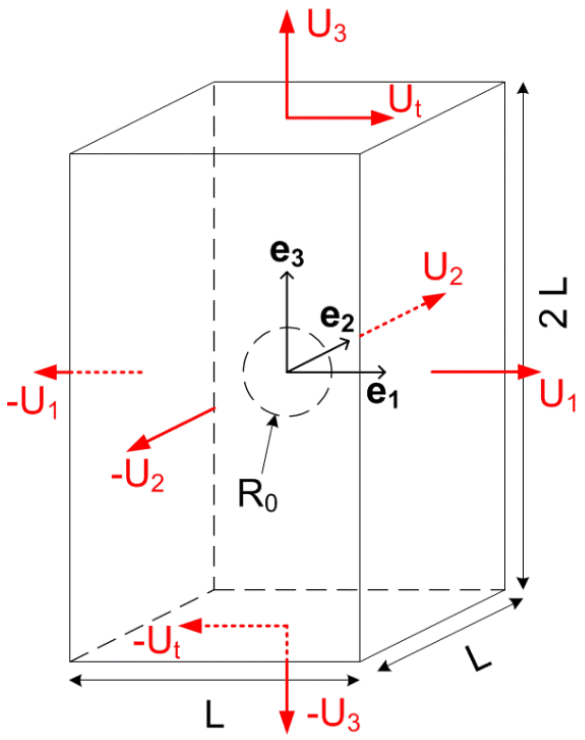

Figure 6-1: Initial geometry of the unit cell ; the displacements U_1, U_2, U_3 and U_t imposed to the unit cell boundaries are depicted in red.

detection of localization using a purely kinematic criterion. The cell features a central spherical void of radius $R = 0.15L$ which corresponds to an initial porosity of $f_0 \cong 0.7\%$.

Defining the macroscopic deformation gradient $\boldsymbol{F}$ as the spatial average of the local deformation gradient over the unit cell volume, the boundary conditions are chosen such that a gradient of the form

$$\boldsymbol{F} = F_{11}\boldsymbol{e}_1\otimes\boldsymbol{e}_1 + F_{22}\boldsymbol{e}_2\otimes\boldsymbol{e}_2 + F_{33}\boldsymbol{e}_3\otimes\boldsymbol{e}_3 + F_{13}\boldsymbol{e}_1\otimes\boldsymbol{e}_3 \tag{6-2}$$

can be applied to the unit cell. In other words, the unit cell is subject to normal loading along all its boundaries and shear loading in the $\boldsymbol{e}_1$-$\boldsymbol{e}_3$-plane. Denoting the average normal displacement along a boundary of normal $\pm\boldsymbol{e}_i$ as $\pm U_i$, and the average tangential displacements along the direction $\pm\boldsymbol{e_1}$ on the boundaries of normal the surfaces of normal $\pm\boldsymbol{e_3}$ as $\pm U_t$, the macroscopic deformation gradient reads

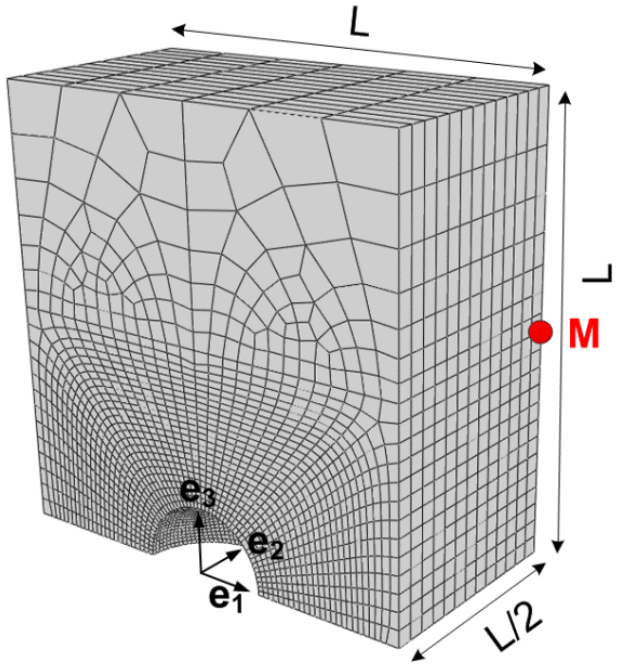

Figure 6-2: Finite element model of the unit cell.

$$\boldsymbol{F} = \begin{bmatrix} 1 + \dfrac{2U_1}{L} & 0 & \dfrac{U_t}{L} \\ 0 & 1 + \dfrac{2U_2}{L} & 0 \\ 0 & 0 & 1 + \dfrac{U_3}{L} \end{bmatrix} \tag{6-3}$$

For the isotopic matrix material, the associated mechanical problem is symmetric with respect to the $(\boldsymbol{e}_1, \boldsymbol{e}_3)$ plane, and antisymmetric with respect to the $(\boldsymbol{e}_1, \boldsymbol{e}_2)$ plane. Thus, only one quarter of the cell $(-L/2 \leq X_1 \leq L/2,\ 0 \leq X_2 \leq L/2$ and $0 \leq X_3 \leq L)$ is considered for finite element analysis (Fig. 6-2).

Symmetry conditions are imposed to the boundaries of the quarter model with the normal vectors $\pm\boldsymbol{e}_2$,

$$\begin{cases} u_2(X_1, 0, \mathrm{X}_3) = 0 \\ u_2(X_1, \mathrm{L}/2, \mathrm{X}_3) = U_2 \end{cases} \tag{6-4}$$

while anti-symmetry conditions (with respect to the $(\boldsymbol{e}_1, \boldsymbol{e}_2)$-plane) plane are imposed to the boundary of normal vector $-\boldsymbol{e}_3$,

$$\begin{cases} u_1(X_1, X_2, 0) + u_1(-X_1, X_2, 0) = 0 \\ u_2(X_1, X_2, 0) - u_2(-X_1, X_2, 0) = 0 \\ u_3(X_1, X_2, 0) + u_3(-X_1, X_2, 0) = 0 \end{cases} \tag{6-5}$$

Both tangential and normal displacements are applied to the boundary of normal vector $+\boldsymbol{e}_3$, i.e.

$$\begin{cases} u_1(X_1, X_2, L) + u_1(-X_1, X_2, L) = 2U_T \\ u_2(X_1, X_2, L) - u_2(-X_1, X_2, L) = 0 \\ u_3(X_1, X_2, L) + u_3(-X_1, X_2, L) = 2U_3 \end{cases} \tag{6-6}$$

The periodicity conditions for the boundaries of normal vectors $\pm\boldsymbol{e}_1$ read

$$\begin{cases} u_1(L/2, X_2, X_3) - u_1(-L/2, X_2, X_3) = 2U_1 \\ u_2(L/2, X_2, X_3) - u_2(-L/2, X_2, X_3) = 0 \\ u_3(L/2, X_2, X_3) - u_3(-L/2, X_2, X_3) = 0 \end{cases} \tag{6-7}$$

Note that the periodicity boundary conditions impose a strong kinematic restriction on the possible formation of a planar band of localized plastic deformation. It can only take the vector $\boldsymbol{e}_3$ as normal vector in order to be kinematically admissible.

6.2.3 Macroscopic rate of deformation

According to the above boundary conditions, the four displacement degrees of freedom,

$$\boldsymbol{u}(t) = \{U_1, , U_2, U_3, U_T\}^T \tag{6-8}$$

control the average deformation gradient in the unit cell. Introducing the velocity vector $\dot{\boldsymbol{u}}(t)$, the macroscopic rate of deformation tensor can also be expressed as a function of these four degrees of freedom,

$$\begin{aligned}\boldsymbol{D} = &\frac{2\dot{U}_1}{L+2U_1}\boldsymbol{e}_1\otimes\boldsymbol{e}_1 + \frac{2\dot{U}_2}{L+2U_2}\boldsymbol{e}_2\otimes\boldsymbol{e}_2 + \frac{\dot{U}_3}{L+U_3}\boldsymbol{e}_3\otimes\boldsymbol{e}_3 \\ &+\frac{1}{2(L+U_3)}\left(\dot{U}_t - 2\dot{U}_1\frac{U_t}{L+2U_1}\right)(\boldsymbol{e}_1\otimes\boldsymbol{e}_3 + \boldsymbol{e}_3\otimes\boldsymbol{e}_1)\end{aligned} \tag{6-9}$$

This symmetric tensor features only four non-zero components which are summarized in a rate of deformation vector

$$\vec{\boldsymbol{D}} = \{D_{11}, D_{22}, D_{33}, 2D_{13}\}^T \tag{6-10}$$

The linear relationship (6-9) between the rate of deformation tensor and the current macroscopic velocities, can thus be conveniently rewritten as

$$\vec{\boldsymbol{D}} = \boldsymbol{Q}\dot{\boldsymbol{u}} \tag{6-11}$$

with the time-dependent linear transformation

$$\boldsymbol{Q}(t) = \begin{bmatrix} \frac{2}{L+2U_1} & 0 & 0 & 0 \\ 0 & \frac{2}{L+2U_2} & 0 & 0 \\ 0 & 0 & \frac{1}{L+U_3} & 0 \\ \frac{-1}{L+U_3}\frac{2U_t}{L+2U_1} & 0 & 0 & \frac{1}{L+U_3} \end{bmatrix} \tag{6-12}$$

6.2.4 Control of the loading path in macroscopic stress space

The macroscopic stress tensor $\boldsymbol{\sigma}(t)$ is defined as the spatial average of the local Cauchy stress field over the current volume $V(t)$ of the unit cell. However, without explicitly calculating the macroscopic stress tensor, the stress state and the directions of the principal stresses are controlled throughout the simulations through a time-dependent kinematic constraint on the applied macroscopic velocities $\dot{\boldsymbol{u}}(t)$.

Consider first the rate of mechanical work for the unit cell at time t. It may be written as

$$\dot{\varphi} = V\boldsymbol{\sigma}:\boldsymbol{D} = V\vec{\boldsymbol{\sigma}} \cdot \vec{\boldsymbol{D}} = \boldsymbol{f} \cdot \dot{\boldsymbol{u}} \tag{6-13}$$

In (6-13), $\boldsymbol{f}$ denotes the vector of the work conjugate forces to the macroscopic translational degrees of freedom, while the vector $\vec{\boldsymbol{\sigma}}$ is work conjugate to $\vec{\boldsymbol{D}}$. The vector $\vec{\boldsymbol{\sigma}}$ summarizes four of the six independent components of the symmetric macroscopic Cauchy stress tensor,

$$\vec{\boldsymbol{\sigma}} = \{\sigma_{11}, \sigma_{22}, \sigma_{33}, \sigma_{13}\}^{\mathrm{T}} \tag{6-14}$$

It is assumed that the shear components σ_{12} and σ_{23} (which may become non-zero due to the deformation induced anisotropy) remain always small as compared to the other stress components and may be neglected when computing the stress triaxiality and/or the Lode angle parameter.

The stress vector may be written as

$$\vec{\boldsymbol{\sigma}} = \sigma_I(t)\tilde{\boldsymbol{a}}(t) = \sigma_I(t)\|\tilde{\boldsymbol{a}}\|\boldsymbol{a}(t) \tag{6-15}$$

with $\sigma_I(t)\|\tilde{\boldsymbol{a}}\| \geq 0$ denoting the amplitude and the unit vector $\boldsymbol{a} \in \mathbb{R}^4$ denoting the direction of the loading path in the reduced stress space. As will be shown below, the latter is a function of the orientation of the principal stresses and the stress state (i.e. the principal stress ratios).

Instead of specifying four non-homogeneous boundary conditions on the components of $\boldsymbol{f}$, a new set of velocity degrees of freedom $\dot{\boldsymbol{v}}$ is created through a linear transformation of $\dot{\boldsymbol{u}}$,

$$\dot{\boldsymbol{v}} = \boldsymbol{A}\dot{\boldsymbol{u}} \tag{6-16}$$

Based on the rate of work,

$$\tilde{\boldsymbol{f}} \cdot \dot{\boldsymbol{v}} = \boldsymbol{f} \cdot \dot{\boldsymbol{u}} \tag{6-17}$$

we define the work-conjugate force vector

$$\tilde{\boldsymbol{f}} = \boldsymbol{A}^{-T}\boldsymbol{f} \tag{6-18}$$

The time-dependent transformation $\boldsymbol{A}(t)$ is then chosen such that (6-15) is readily satisfied by specifying homogeneous boundary conditions on all but one component of the force vector $\tilde{\boldsymbol{f}}$. In other words, $\tilde{\boldsymbol{f}}$ takes the simple form

$$\tilde{\boldsymbol{f}} = f(t)\boldsymbol{e}_i \tag{6-19}$$

with $\boldsymbol{e}_i$ denoting one of the four orthogonal basis vectors of $\mathbb{R}^4$. Rewriting the rate of work, we have

$$\tilde{\boldsymbol{f}} \cdot \dot{\boldsymbol{v}} = V\vec{\boldsymbol{\sigma}} \cdot \boldsymbol{Q}\dot{\boldsymbol{u}} = V\vec{\boldsymbol{\sigma}} \cdot \boldsymbol{Q}\boldsymbol{A}^{-1}\dot{\boldsymbol{v}} = V(\boldsymbol{Q}\boldsymbol{A}^{-1})^T\vec{\boldsymbol{\sigma}} \cdot \dot{\boldsymbol{v}} \tag{6-20}$$

In the weak formulation of the unit cell problem, Eq. (6-20) must be fulfilled for any $\dot{\boldsymbol{v}}$ and hence

$$\tilde{\boldsymbol{f}} = V(\boldsymbol{Q}\boldsymbol{A}^{-1})^T\vec{\boldsymbol{\sigma}} \tag{6-21}$$

Satisfaction of the boundary condition $\tilde{\boldsymbol{f}} = f(t)\boldsymbol{e}_i$ implies $\boldsymbol{\sigma} = \sigma_I(t)\widetilde{\boldsymbol{a}}$ if the transformation matrix $\boldsymbol{A}$ satisfies the identity

$$V\sigma_I\|\widetilde{\boldsymbol{a}}\|(\boldsymbol{Q}\boldsymbol{A}^{-1})^T\boldsymbol{a} = f\boldsymbol{e}_i \tag{6-22}$$

Among all invertible transformation matrices that satisfy (6-22), we chose $\boldsymbol{A}$ such that $\boldsymbol{Q}\boldsymbol{A}^{-1}$ becomes a rotation matrix,

$$\boldsymbol{Q}\boldsymbol{A}^{-1} = \boldsymbol{a} \otimes \boldsymbol{e}_1 + \boldsymbol{b} \otimes \boldsymbol{e}_2 + \boldsymbol{c} \otimes \boldsymbol{e}_3 + \boldsymbol{d} \otimes \boldsymbol{e}_4 \tag{6-23}$$

with the unit vectors $\boldsymbol{a}$, $\boldsymbol{b}$, $\boldsymbol{c}$ and $\boldsymbol{d}$ forming an orthogonal basis of $\mathbb{R}^4$. Note that we also randomly chose the first component of $\tilde{\boldsymbol{f}}$ as the only non-zero force component, while a zero force boundary condition is imposed on the remaining three degrees of freedom.

By updating the coordinate transformation at each time step, we can control the loading path in stress space. Note that instead of prescribing the time history of the first component of $\tilde{\boldsymbol{f}}$, the work-conjugate velocity (first component of $\dot{\boldsymbol{v}}$) is applied.

6.2.5 Loading scenarios

In the above control scheme, linear and non-linear loading paths can be prescribed by specifying $\tilde{\boldsymbol{\alpha}}(t)$. The corresponding macroscopic Cauchy stress tensor in 3D reads

$$\boldsymbol{\sigma}(\mathrm{t}) = \sigma_I(t)[\tilde{a}_1 \boldsymbol{e}_1 \otimes \boldsymbol{e}_1 + \tilde{a}_2 \boldsymbol{e}_2 \otimes \boldsymbol{e}_2 + \tilde{a}_3 \boldsymbol{e}_3 \otimes \boldsymbol{e}_3 + \tilde{a}_4(\boldsymbol{e}_1 \otimes \boldsymbol{e}_3 + \boldsymbol{e}_3 \otimes \boldsymbol{e}_1)] \tag{6-24}$$

In terms of the principal stresses $\sigma_I \geq \sigma_{II} \geq \sigma_{III}$, the same stress tensor may be written as

$$\begin{aligned} \boldsymbol{\sigma}(\mathrm{t}) &= \sum_{i=I,II,III} \sigma_i(t) \boldsymbol{p_i}(t) \otimes \boldsymbol{p_i}(t) \\ &= \sigma_I(\boldsymbol{p}_I \otimes \boldsymbol{p}_I + \psi_{II} \boldsymbol{p}_{II} \otimes \boldsymbol{p}_{II} + \psi_{III} \boldsymbol{p}_{III} \otimes \boldsymbol{p}_{III}) \end{aligned} \tag{6-25}$$

with the unit vectors $\boldsymbol{p_i}(t) \in \mathbb{R}^3$ denoting the principal stress directions. Note that the stress state $\{\eta, \bar{\theta}\}$ is a function of the principal stress ratios $\psi_{II} = \sigma_{II}/\sigma_I$ and $\psi_{III} = \sigma_{III}/\sigma_I$ only,

$$\eta = \frac{\sqrt{2}}{3} \frac{1 + \psi_{II} + \psi_{III}}{\sqrt{(1 - \psi_{II})^2 + (1 - \psi_{III})^2 + (\psi_{II} - \psi_{III})^2}} \tag{6-26}$$

$$\bar{\theta} = 1 - \frac{2}{\pi} arccos\left(\frac{1}{2} \frac{(2 - \psi_{II} - \psi_{III})(1 - 2\psi_{II} + \psi_{III})(1 + \psi_{II} - 2\psi_{III})}{(1 + \psi_{II}^2 + \psi_{III}^2 - \psi_{II} - \psi_{III} - \psi_{II}\psi_{III})^3}\right) \tag{6-27}$$

The directions of the principal stresses can thus be chosen independently from the stress state. Recall that

(a) according to the periodic boundary conditions, the $(\boldsymbol{e}_1, \boldsymbol{e}_2)$-plane is the only possible plane of localization.

(b) according to Rudnicki and Rice (1975, [129]), the direction of the second principal stress is always parallel to the plane of localization.

For computational convenience, we impose

$$\boldsymbol{p_{II}} = \boldsymbol{e}_2 \tag{6-28}$$

in all simulations which is consistent with (a) and (b). The other two principal stress directions can then be expressed as a function of the angle $\alpha(t)$ between the first principal stress and the normal $\boldsymbol{n} = \boldsymbol{e}_3$ to the plane of localization,

$$\boldsymbol{p_I} = \begin{Bmatrix} \sin\alpha \\ 0 \\ \cos\alpha \end{Bmatrix} \quad \text{and} \quad \boldsymbol{p_{III}} = \begin{Bmatrix} -\cos\alpha \\ 0 \\ \sin\alpha \end{Bmatrix} \tag{6-29}$$

Using (6-28) and (6-29) in (6-25) allows us to express the loading path direction $\widetilde{\boldsymbol{\alpha}}$ as a function of the stress state $\{\eta, \bar{\theta}\} = f(\psi_{II}, \psi_{III})$ and the orientation α of the principal stresses,

$$\widetilde{\boldsymbol{\alpha}} = \begin{Bmatrix} \sin^2\alpha + \psi_{III}\cos^2\alpha \\ \psi_{II} \\ \cos^2\alpha + \psi_{III}\sin^2\alpha \\ (1-\psi_{III})\cos\alpha\sin\alpha \end{Bmatrix} \tag{6-30}$$

Since the planar band of localization can only form with its normal in the $\boldsymbol{e}_3$-direction, it is important to perform the unit cell analysis for all possible principal stress orientations to determine the lowest estimate of the strain to failure for a given stress state.

When specifying the loading path, there are also two sources of anisotropy which are worth considering:

1. *Topological anisotropy* associated with the spatial distribution of voids: According to the periodic boundary conditions, the determined effective behavior corresponds to a porous solid with voids positioned at the vertices of an orthorhombic lattice. The microstructure therefore features three orthogonal planes of symmetry which results in an orthotropic effective mechanical response.
2. *Morphological anisotropy* due to deformation-induced void shape changes: The initially spherical void changes into an ellipsoidal-like void. Even in the hypothetical case of an isotropic spatial void distribution (topological isotropy), the effective behavior would become anisotropic due to the evolution of the void

shape. In the special case of rotation free loading, the void shapes are expected to remain symmetric with respect to the directions of the principal stress.

The rotation $\boldsymbol{R}$ of the macroscopic material coordinate frame (Fig. 6-3a) is defined through the decomposition

$$\boldsymbol{F} = \boldsymbol{V}\boldsymbol{R} = \boldsymbol{U}\boldsymbol{R} \tag{6-31}$$

with $\boldsymbol{V} = \boldsymbol{V}^{\boldsymbol{T}}$ and $\boldsymbol{U} = \boldsymbol{U}^{T}$ denoting the left and right stretch tensors, respectively. Due to the two sources of anisotropy, material rotation may affect the results of the localization analysis. In particular, since the orientation of the possible band of localization is fixed in space, the directions of loading must be rotated (i.e. $U_T \neq 0$) to simulate different band orientations.

To shed some light on the effect of material rotation due to the (undesired, but unavoidable) anisotropy of the unit cell model on the predicted macroscopic strain to localization, we consider two scenarios for the evolution of the principal stress directions:

- Co-rotational loading: The evolution of the principal stress directions is coupled with the rotation of the material,

$$\boldsymbol{p_i}(t) = \boldsymbol{R}(t)\boldsymbol{p}_i^0 \tag{6-32}$$

  As illustrated in Fig. 6-3b, the angle between the principal stress directions and the directions of the orthogonal coordinate frame attached to the material remains constant throughout loading.

- Radial loading: The principal stress directions are kept constant throughout loading, i.e.

$$\boldsymbol{p_i}(t) = \boldsymbol{p}_i^0 \tag{6-33}$$

  In this case, the material rotates with respect to the loading, i.e. the angle between the principal stresses and the material changes as illustrated in Fig. 6-3c.

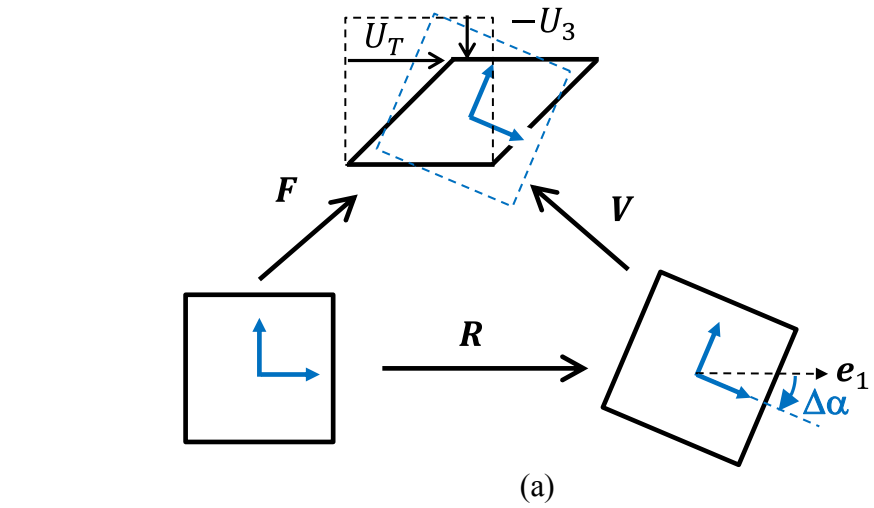

(a)

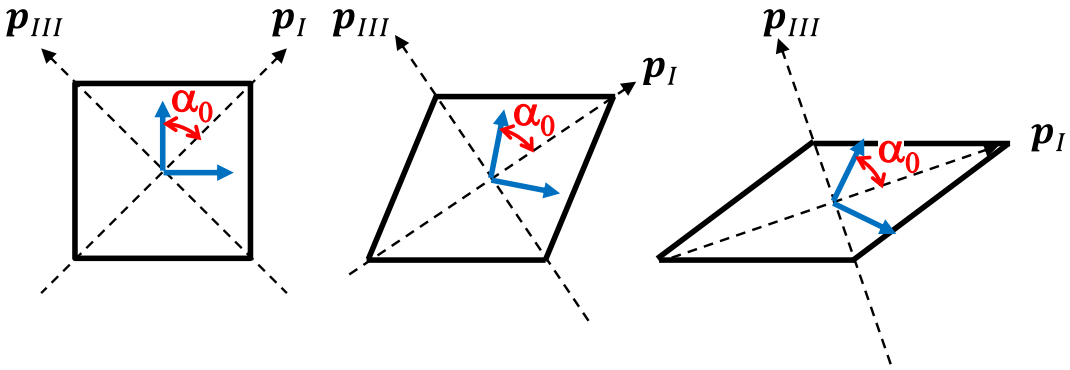

(b) Co-rotational loading

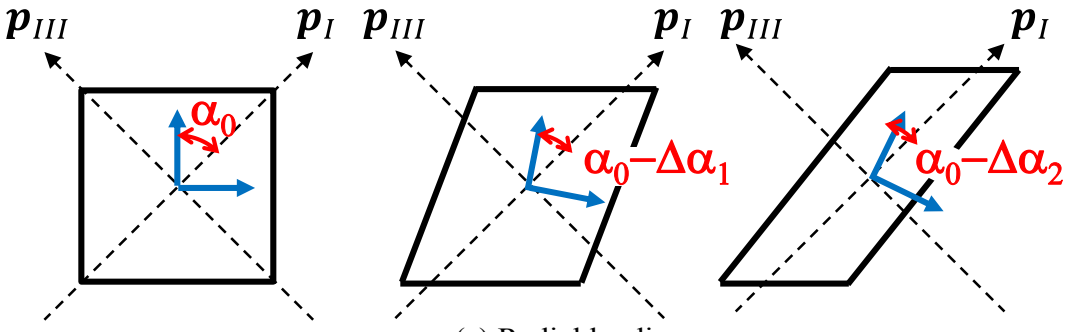

(c) Radial loading

Figure 6-3: Loading scénarii. (a) Rotation of the material coordinate system (blue) of an orthotropic solid; (b) simultaneous rotation of the material coordinate system (blue) and the principal stress directions.(c) Rotation of the material coordinate system (blue) with respect to the principal stress directions.

In both cases, the computations are performed over a wide range of initial principal stress orientations α_0. While α is kept constant throughout radial loading, the angle α evolves throughout co-rotational loading. After expressing $\boldsymbol{R}$ as a rotation by the angle $\Delta\alpha$ around the $\boldsymbol{e}_2$-axis (Fig. 6-3a),

$$\mathbf{R} = \begin{bmatrix} \cos(\Delta\alpha) & 0 & \sin(\Delta\alpha) \\ 0 & 1 & 0 \\ -\sin(\Delta\alpha) & 0 & \cos(\Delta\alpha) \end{bmatrix} \tag{6-34}$$

and decomposing the deformation gradient according to (6-31), the evolution of the principal stress directions (with respect to the stationary $\boldsymbol{e}_3$-axis) for co-rotational loading reads

$$\alpha(\mathrm{t}) = \alpha_0 + \Delta\alpha \tag{6-35}$$

with

$$\tan(\Delta\alpha) = \frac{F_{13}}{F_{11} + F_{33}} \tag{6-36}$$

6.2.6 Definition of the strain to failure

The definition of the "strain to failure" requires the definition of the instant of failure as well as that of a suitable macroscopic strain measure. Here, the onset of failure corresponds to the onset of localization of plastic flow. After the onset of localization, all additional plastic deformation is expected to accumulate within a narrow band of width w and of normal vector $\boldsymbol{e}_3$ in the vicinity of $X_3 = 0$. At the same time, the matrix material outside this band ($|X_3| > w/2$) should experience partial elastic unloading. Let $\boldsymbol{F_U}$ be the volume average of the deformation gradient of the upper part of the unit cell delimited by $L/2 \leq X_3 \leq L$, in which the deformation is expected to be approximately homogeneous (since $w \ll L$). Knowing the displacements u_1^M and u_3^M of a point M located at $(X_1, X_2, X_3) = (L/2\,, L/2\,, L/2)$ (Fig. 6-2), $\boldsymbol{F_U}$ can then be estimated as

$$\boldsymbol{F_U} \simeq \begin{bmatrix} F_{11} & 0 & \dfrac{U_t - (u_1^M - U_1)}{L/2} \\ 0 & F_{22} & 0 \\ 0 & 0 & 1 + \dfrac{U_3 - u_3^M}{L/2} \end{bmatrix} \tag{6-37}$$

Following Needleman and Tvergaard (1992, [115]), the localization of deformation into a narrow planar band is then assumed to occur when

$$\xi \equiv \frac{\|\dot{\boldsymbol{F}}\|}{\|\dot{\boldsymbol{F}}_{\boldsymbol{U}}\|} \gg 1 \tag{6-38}$$

where the tensorial norm $\|\cdot\|$ is defined as $\|\boldsymbol{X}\| = \sqrt{\boldsymbol{X}:\boldsymbol{X}}$. In all our computations, the instant of onset of failure, t_f, is defined as the instant when $\xi = 5$.

The macroscopic equivalent strain $\bar{\varepsilon}_p$ is defined based on the integral of the plastic work over the entire unit cell, φ, using the stress-strain relationship for the matrix material,

$$\int_0^{\bar{\varepsilon}_p} k(\lambda) d\lambda = \frac{\varphi}{V} \tag{6-39}$$

This definition is identical to defining the macroscopic equivalent plastic strain as work-conjugate to the macroscopic von Mises equivalent stress $\bar{\sigma}$,

$$\bar{\sigma} d\bar{\varepsilon}_p = \frac{d\varphi}{V} \tag{6-40}$$

provided that the deformation within the unit cell is uniform (i.e. approximately homogeneous local deformation field). We evaluated both definitions for selected computations and found almost identical results. However, definition (6-39) turned out to be more convenient from a computational point of view (no need to compute $\bar{\sigma}$).

With the definitions of the instant of failure and the equivalent plastic strain at hand, the macroscopic strain to failure $\bar{\varepsilon}_f$ for a given stress state is then defined as the minimum of the macroscopic equivalent plastic strain at the instant of failure over all possible angles α_0,

$$\bar{\varepsilon}_f(\eta,\bar{\theta}) := \min_{\alpha_0} \bar{\varepsilon}_p\left(\eta,\bar{\theta},t_f,\alpha_0\right) \tag{6-41}$$

Note that due to the strictly monotonic relationship between the equivalent plastic strain and the plastic work, the critical angle α_0 can also directly determined from the minimization of the total plastic work.

6.2.7 Computational aspects

The implicit solver of the commercial Finite Element package Abaqus is used. The unit cell is discretized by 23,338 fully integrated first-order solid elements (element C3D8 of the Abaqus/Standard library), as shown in Fig. 6-2. The boundary conditions described by Eqs. (6-4) to (6-7) are then enforced by imposing the corresponding kinematic constrains to the nodes located on the cell boundaries. The non-linear loading path control is achieved through a user defined subroutine (time-dependent multi-point constraint). For low triaxiality loadings, initially spherical voids tend to collapse into penny-shaped cracks (Tvergaard, 2008, [145]). Here the kinematic self-contact formulation of Abaqus/Standard is used to prevent interpenetration of the void walls. The contact is modeled as frictionless ($\mu = 0$), therefore transmitting only normal forces at the interface. The reader is referred to Dahl et al. (2012, [43]) for more details on the effect of friction.

6.3 Results

Simulations are performed for a dense grid of stress states within the range

$$0 \leq \eta \leq 1 \quad \text{and} \quad -1 \leq \bar{\theta} \leq 1 \tag{6-42}$$

Given the high computational costs, we performed the complete analysis for co-rotational loading only. Our discussion therefore makes reference to results for co-rotational loading. The only exception is Subsection 6.3.3, where results for radial loading are discussed and compared with those for co-rotational loading. Before showing the results for all stress states in Subsection 6.3.2, selected examples are discussed in detail in Subsection 6.3.1 showing

the evolution of the localization indicator, the effect of the shear band orientation and the captured deformation mechanisms at the unit cell level.

6.3.1 Demonstration of the analysis procedure

6.3.1.1 Evolution of the localization indicator

Figure 6-4a shows the evolution of the localization indicator as a function of the macroscopic effective plastic strain for three different stress states. The corresponding macroscopic equivalent stress-strain curves are depicted in Fig. 6-4b.

- The black curve ($\eta = 0.5,\ \bar{\theta} = 0$) is representative for simulations in which localization occurred: The localization indicator initially remains close to 1 followed by a moderate increase, before diverging to infinity. The divergence of the localization indicator is usually associated with a maximum of the macroscopic effective stress-strain curve. With the onset of localization (i.e. $\xi > 5$), the effective load carrying capacity drops. At this stage, most of the cell matrix material experiences elastic unloading, while increases in plastic deformation are limited to the material within the band of localization (grey area in Fig. 6-4c).
- The red curve ($\eta = 0.33, \bar{\theta} = 1$) shows an example where no localization occurred. The localization indicator remains more or less constant ($\xi \cong 1$) and the effective stress-strain curve continues to follow the solution for a homogeneous deformation field inside the unit cell.
- The blue curve ($\eta = 0, \bar{\theta} = 0$) depicts another example with no localization. However, in this case, the localization indicator evolution shows the signs of some pronounced non-uniform deformation at a strain of 0.6, but the unit cell remains stable and continues to deform in a uniform manner after an isolated peak in the localization indicator history.

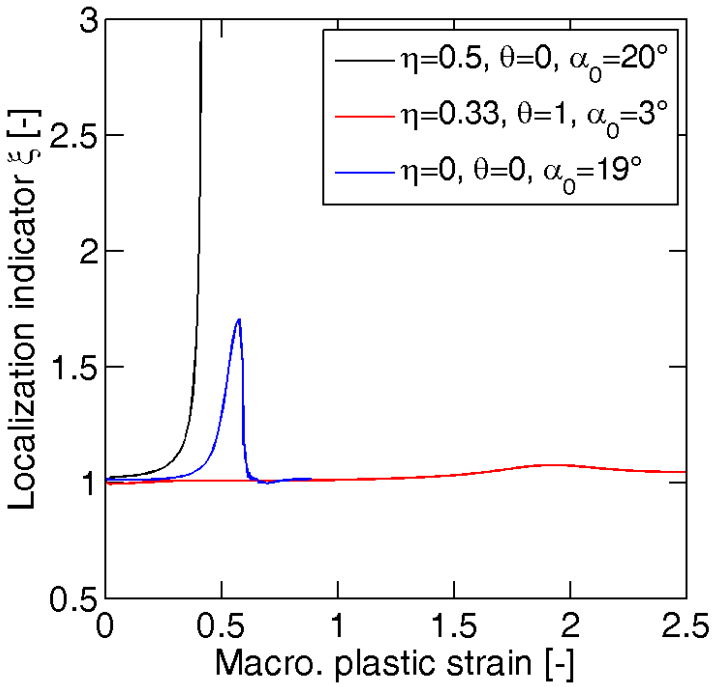
Localization indicator ξ [-]
Macro. plastic strain [-]
η=0.5, θ=0, α0=20°
η=0.33, θ=1, α0=3°
η=0, θ=0, α0=19°
3
2.5
2
1.5
1
0.5
0
0.5
1
1.5
2
2.5

(a)

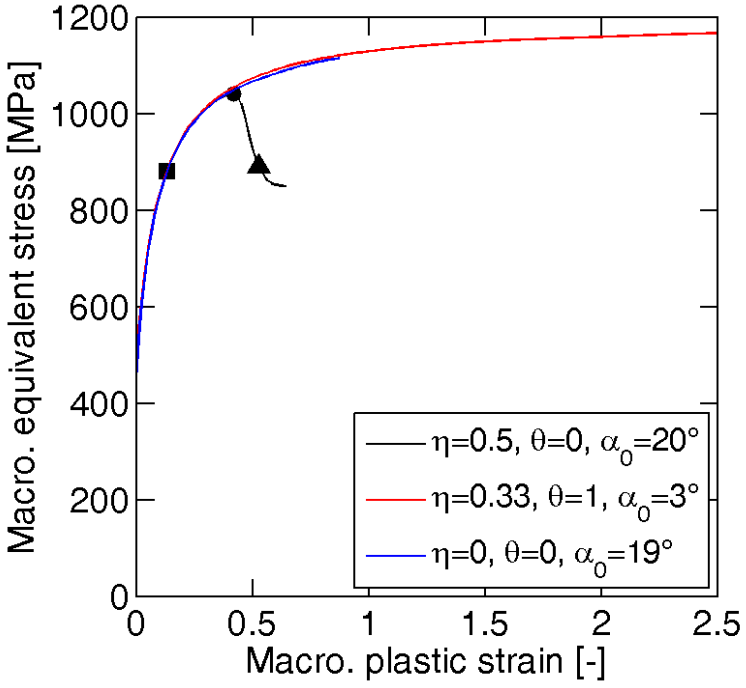
Macro. equivalent stress [MPa]
Macro. plastic strain [-]
η=0.5, θ=0, α0=20°
η=0.33, θ=1, α0=3°
η=0, θ=0, α0=19°
1200
1000
800
600
400
200
0
0
0.5
1
1.5
2
2.5

(b)

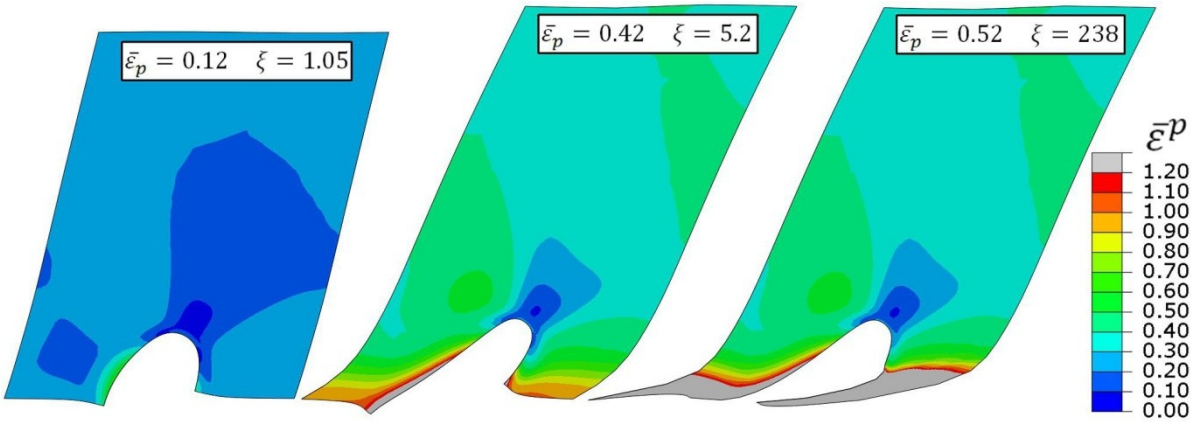

(c)

Figure 6-4: Influence of the stress state on the onset of localization : (a) Evolution of the localization indicator, and (b) macroscopic equivalent stress-strain curves for uniaxial tension $(\eta = 0.33, \bar{\theta} = 1)$, pure shear $(\eta = 0, \bar{\theta} = 0)$ and a triaxial state of stress $(\eta = 0.5, \bar{\theta} = 0)$. (c) Pre- and post-localization response observed at the microscale. The three contour plots correspond to the instants highlighted by dark dots in (b).

Choosing a rather large critical value of the localization indicator ($\xi = 5$) increased the reliability of the localization detections. Note that changes in the effective equivalent plastic strain are almost insignificant when the localization indicator increases from 2 to 5. In other words, the uncertainty in the reported strain to failure due to the choice of the critical value of the localization indicator is small.

6.3.1.2 Orientation of the localization band

For each stress state $\{\eta, \bar{\theta}\}$, the localization analysis is repeated for different band orientations. In our model, the band orientation is indirectly varied by changing the initial angle α_0 of the maximum principal stress. Figure 6-5 presents simulation results for a stress state of $\eta = 0.5$ and $\bar{\theta} = 0$, and three distinct initial orientations: $\alpha_0 = 20°$ (black curves), $\alpha_0 = 26.2°$ (red curves) and $\alpha_0 = 29.5°$ (blue curves). The computed macroscopic equivalent stress-strain curves (Fig. 6-5a) lie on top of each other prior to the onset of

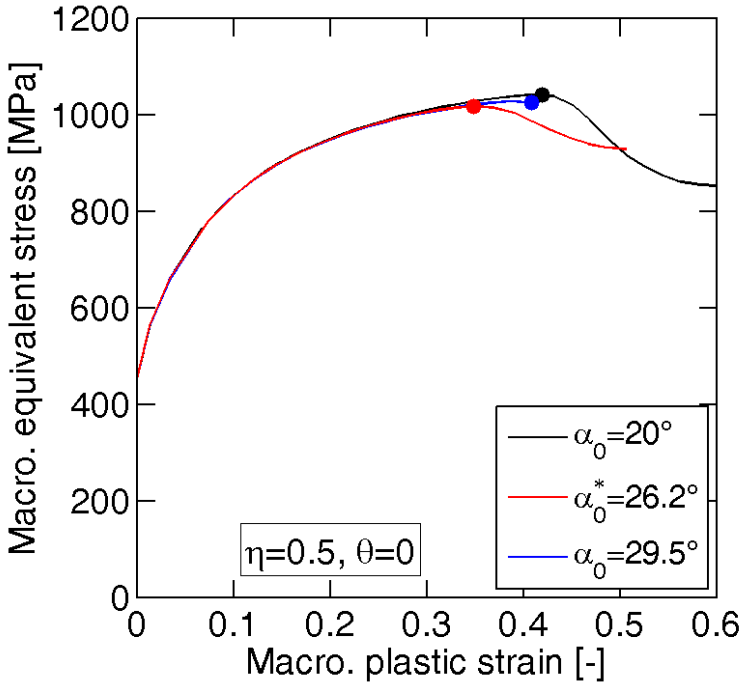
Macro. equivalent stress [MPa]
Macro. plastic strain [-]
η=0.5, θ=0
α0=20°
α0*=26.2°
α0=29.5°

(a)

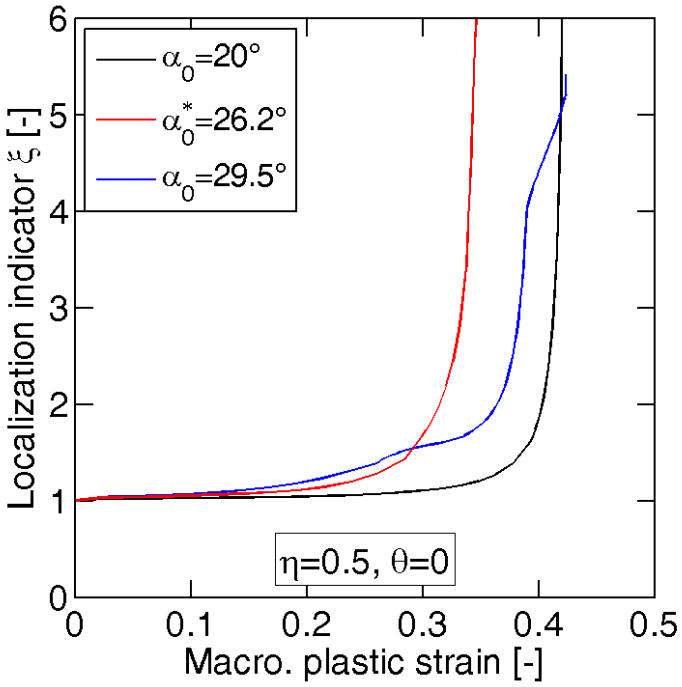
Localization indicator ξ [-]
Macro. plastic strain [-]
η=0.5, θ=0
α0=20°
α0*=26.2°
α0=29.5°

(b)

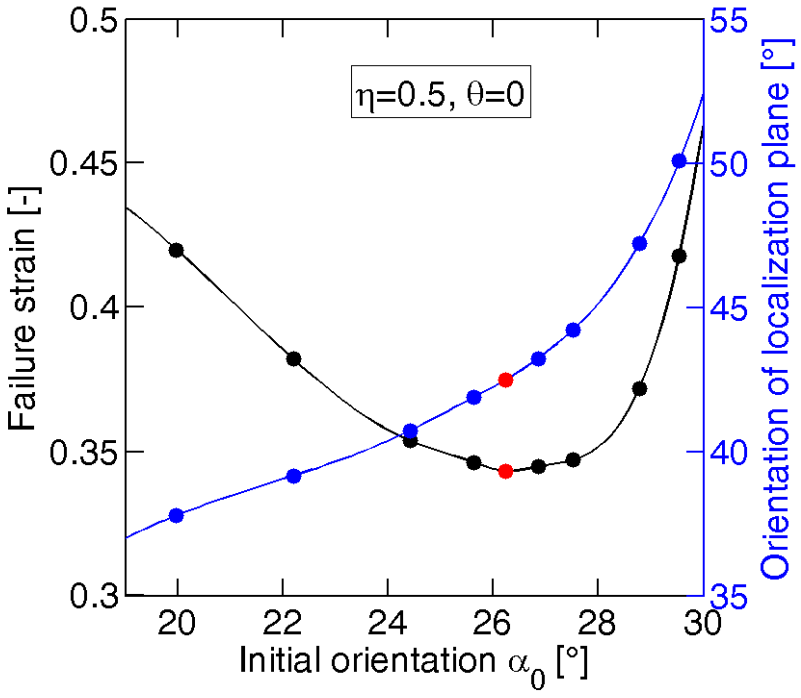

(c)

Figure 6-5: Effect of the initial orientation of the cell on localization behavior. (a) Macroscopic equivalent stress-strain curves, (b) evolution of the localization indicator for different initial orientations, and (c) predicted failure strain (in black) and orientation of the plane of localization α (in blue) as a function of the initial orientation α_0. Solid dots depict the onset of localization in (a) while each dot corresponds to a cell calculation in (c). The most favorable initial orientation α_0^* is shown in red.

localization, but the evolution of the localization indicator ξ clearly depends on α_0 (Fig. 6-5b).

The macroscopic plastic strain at which localization occurs for $\alpha_0 = 26.2°$ is about 20% lower than that for $\alpha_0 = 20°$ and $\alpha_0 = 29.5°$. Figure 6-5c depicts the dependency of $\bar{\varepsilon}(\eta, \bar{\theta}, t_f)$ – in black – and $\alpha(\eta, \bar{\theta}, t_f)$ – in blue – on α_0 over the interval $20° \leq \alpha_0 \leq 30°$. Each solid dot in Fig. 4c is the outcome of a unit cell analysis. A minimum of strain to localization is reached for $\alpha_0 = 26.2°$ (red dot in Fig. 6-5c), which therefore corresponds to the initial principal stress orientation which is most favorable for localization. We typically

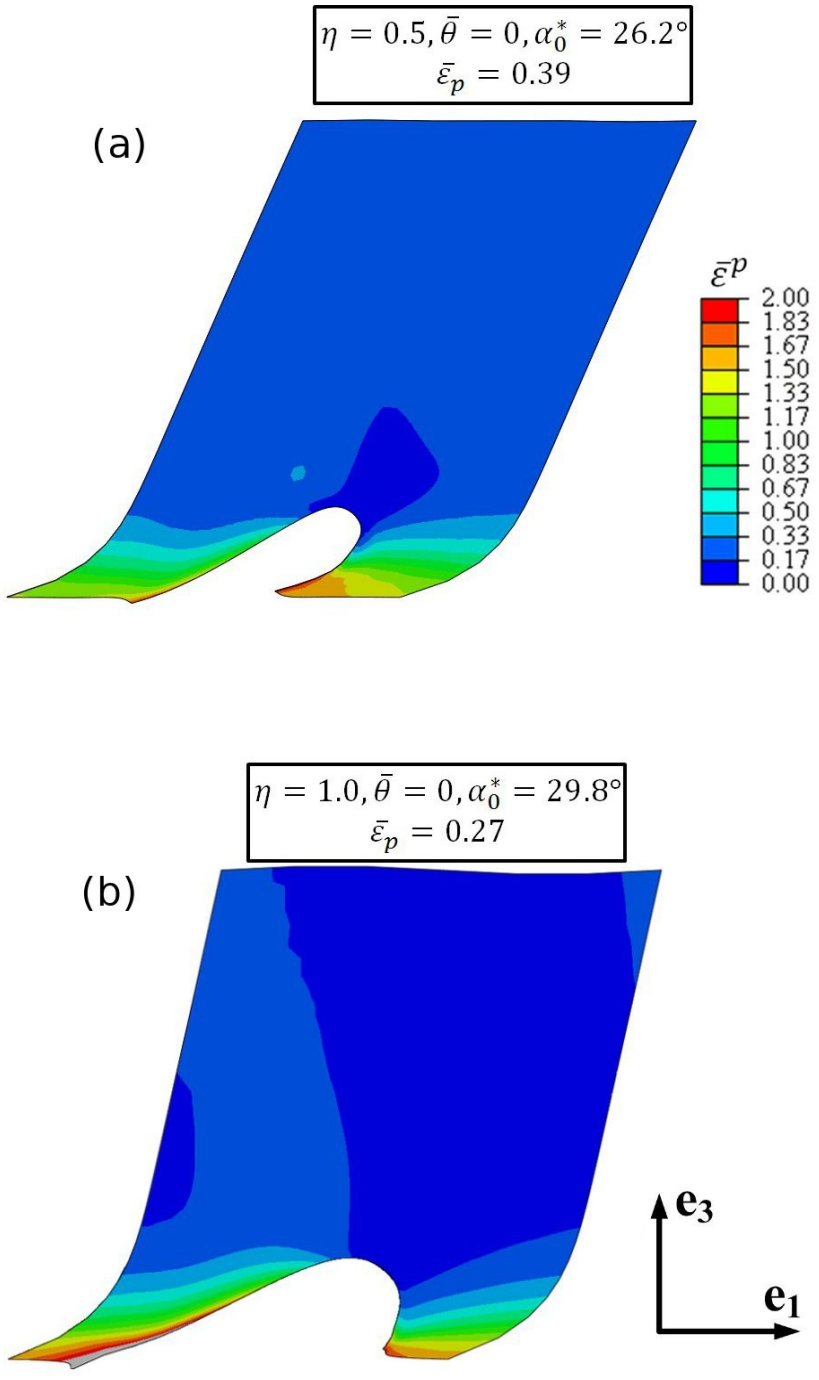
$\eta = 0.5, \bar{\theta} = 0, \alpha_0^* = 26.2°$
$\bar{\varepsilon}_p = 0.39$
(a)
$\bar{\varepsilon}^p$
2.00
1.83
1.67
1.50
1.33
1.17
1.00
0.83
0.67
0.50
0.33
0.17
0.00
$\eta = 1.0, \bar{\theta} = 0, \alpha_0^* = 29.8°$
$\bar{\varepsilon}_p = 0.27$
(b)
$\mathbf{e_3}$
$\mathbf{e_1}$

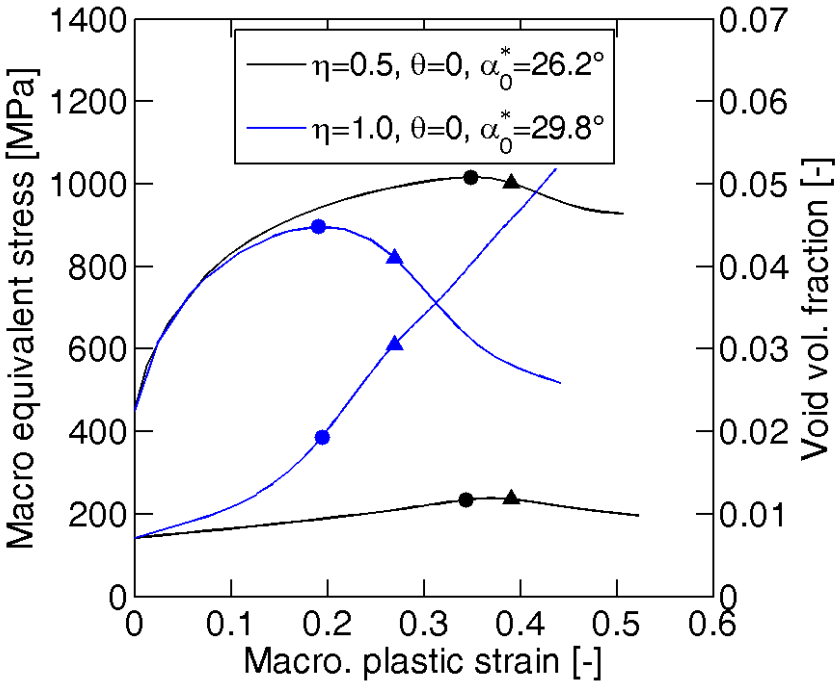

(c)

Figure 6-6: Captured failure mechanisms : (a) Shear failure ($\eta = 0.5,\ \bar{\theta} = 0, \bar{\varepsilon}_p = 0.39$) and (b) internal necking ($\eta = 1, \bar{\theta} = 0, \bar{\varepsilon}_p = 0.27$). The contour plots show the local plastic strain after the onset of localization ($\xi > 5$); (c) Evolution of the macroscopic equivalent stresses and void volume fractions as a function of the macroscopic plastic strain. Solid dots depict the onset of localization ($\xi = 5$), while the triangles indicate the instants at which the contour plots are extracted.

performed computations for ten initial orientations varying from 10° to 50°. In most cases, the plot of the dissipation $\varphi(t_f)$ as a function of α_0 showed a local minimum which is characterized with a relative precision of 3% on α_0. This local minimum is then assumed as the most critical orientation. Otherwise, the range of initial orientations is increased further until a minimum is found.

6.3.1.3 Captured failure mechanisms

It is noted that the localization criterion captures both inter-void ligament shear bands and internal necking. The cross-sectional cuts shown in Fig. 6-6 provide some insight into the post-localization behavior of the cell for an intermediate stress triaxiality loading ($\eta = 0.5,\ \bar{\theta} = 0$) and at high stress triaxiality loading ($\eta = 1,\ \bar{\theta} = 0$). The superposed contour plots show the local equivalent plastic strain distribution for a macroscopic equivalent strain of $\bar{\varepsilon}_p = 0.39$ and $\bar{\varepsilon}_p = 0.27$, respectively. The macroscopic equivalent stress-strain curves and the evolution of void volume fraction during deformation are also included in Fig. 6-6 (in black for $\eta = 0.5$, in blue for $\eta = 1$). It can be seen that

- at the intermediate stress triaxiality ($\eta = 0.5$), the overall shearing of the void is dominant and the void volume fraction remains approximately constant throughout loading.
- at the high stress triaxiality ($\eta = 1.0$), the volume change associated with the hydrostatic pressure is more significant and the void volume fraction increases from its initial value of 0.01 to about 0.04 at the onset of localization; the inter-void ligaments are therefore also being stretched in addition to shearing which introduces a neck into the sheared ligaments.

A detailed analysis of the deformation response at the unit cell level is omitted as the observed responses are in agreement with those reported in the literature. Readers interested in a comprehensive discussion of the failure mechanism under shear loading are referred to the literature (e.g. Tvergaard (2008, 2012, [145, 147])).

6.3.2 Strain to failure as function of stress state

The localization analysis has been executed for 178 different stress states within the domain specified in (6-42). For each stress state, at least 10 different possible shear band orientations have been considered. With an average computation time of about 3h per simulation (parallelized on 12 CPUs), it took about 30 weeks of calculation on a high performance work station to obtain the results. Summary plots showing the strain to failure

as a function of the Lode angle parameter and the stress triaxiality are presented in Fig. 6-7. Solid dots correspond to simulation results, while the solid lines correspond to cubic spline interpolations. Dashed lines correspond to spline extrapolations in a range where no localization was found in the calculations.

The failure strain $\bar{\varepsilon}_f$ exhibits a strong dependence on both the stress triaxiality η and the Lode parameter $\bar{\theta}$. In particular, it is observed that:

- The strain to failure is a monotonically decreasing function of the stress triaxiality. This can be clearly seen from Fig. 6-7a and 6-7b, where the strain to fracture is plotted as a function of the stress triaxiality for constant Lode angle parameters;
- The strain to fracture exhibits an asymptotic behavior at low stress triaxiality: there appears to exist a "cut-off value" of triaxiality $\tilde{\eta}_c$ below which no localization occurs. This can be seen from Figs. 6-7a and 6-7b and is elucidated further in Fig. 6-7d. The cut-off stress triaxiality η_c depends on the Lode parameter, and increases as the stress state departs from generalized shear ($\bar{\theta} = 0$) towards axisymmetric states of stress ($\bar{\theta} = \pm 1$): $\eta_c(\bar{\theta} = 0) \simeq 0.15$, while $\eta_c(\bar{\theta} = 1) \simeq 0.4$ and $\eta_c(\bar{\theta} = -1) \simeq 0.55$.
- It is worth noting that no localization occurs for pure shear ($\eta = 0$, $\bar{\theta} = 0$) and uniaxial tension ($\eta = 0.33$, $\bar{\theta} = 1$). For stress triaxialities greater than $\eta \geq 0.6$, localization occurs over the complete range of Lode parameters.
- The strain to failure is a non-symmetric convex function of the Lode angle parameter $\bar{\theta}$, exhibiting its minimum in the interior of its domain of definition (Fig. 6-7c). The minimum of the strain to failure does not exactly correspond to generalized shear loadings ($\bar{\theta} = 0$): for a triaxiality of $\eta = 1$, the minimum is at $\bar{\theta} = 0.3$; for $\eta = 0.2$, the minimum is at $\bar{\theta} = +0.05$.
- In the specific case of axisymmetric loadings, the failure strain $\bar{\varepsilon}_f$ is almost twice higher for $\bar{\theta} = -1$ than for $\bar{\theta} = +1$ at the same triaxiality η.

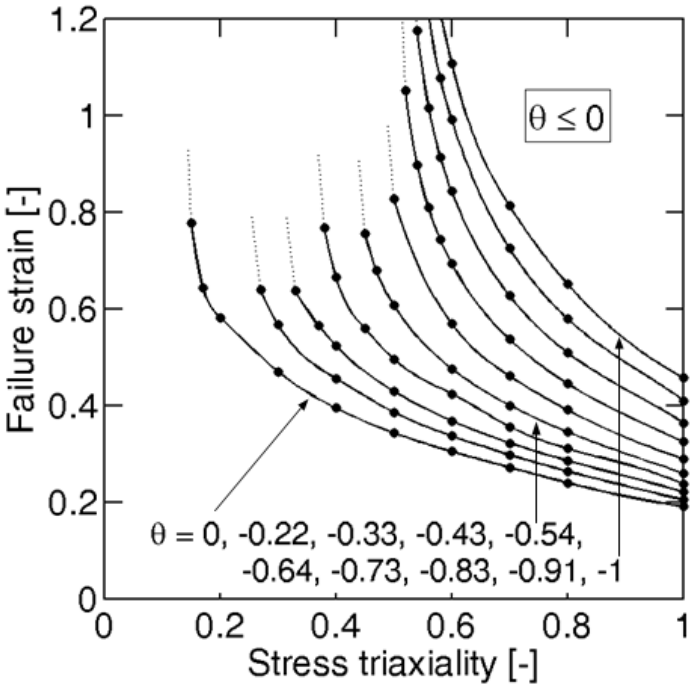

(a)

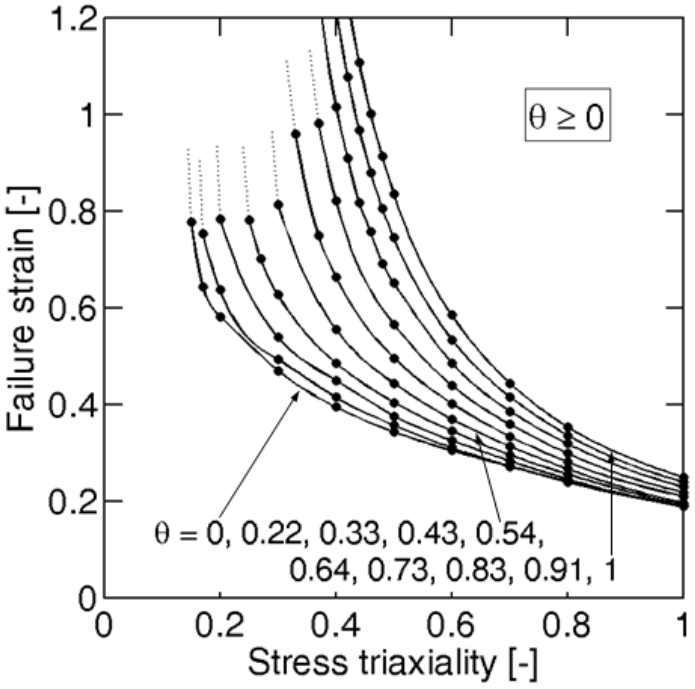

(b)

Figure 6-7: Failure strain as function of the stress triaxiality for (a) $\bar{\theta} \leq 0$, and (b) $\bar{\theta} \geq 0$; (c) representation of the same data as a function of the Lode parameter with stress triaxiality

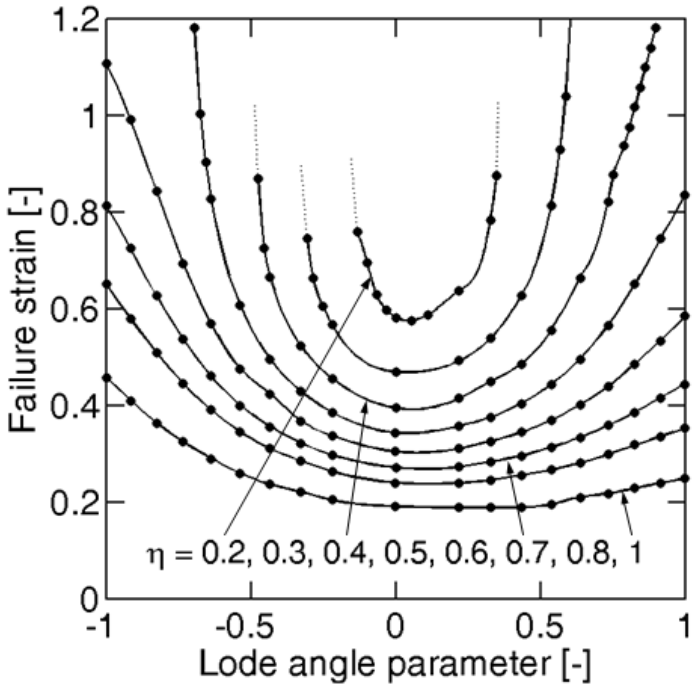

(c)

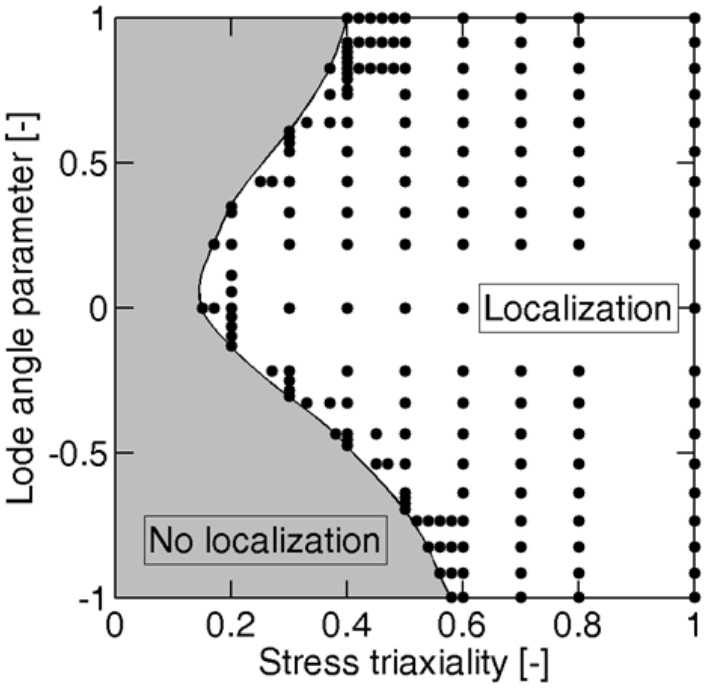

(d)

as curve parameter. (d) Projection on the $(\eta, \bar{\theta})$-plane showing the boundary of the domain of stress states with localization. Each solid dot corresponds to a unit cell analysis in which the onset of localization was reached.

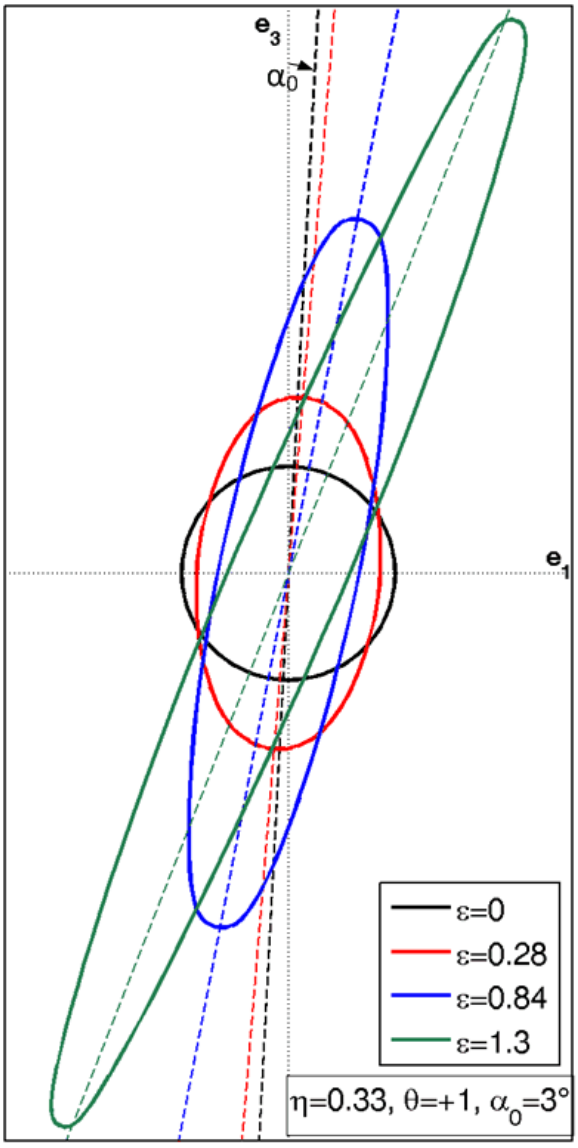

(a)

Figure 6-8: Computed void shape evolution (a) under uniaxial tension $(\eta = 0.33, \bar{\theta} = 1)$, (b) pure shear $(\eta = 0, \bar{\theta} = 0)$ and (c) triaxial loading $(\eta = 0.5, \bar{\theta} = 0)$. The solid lines depict the void contour in the $(\boldsymbol{e_1}, \boldsymbol{e_3})$-plane at different macroscopic equivalent plastic strain. The

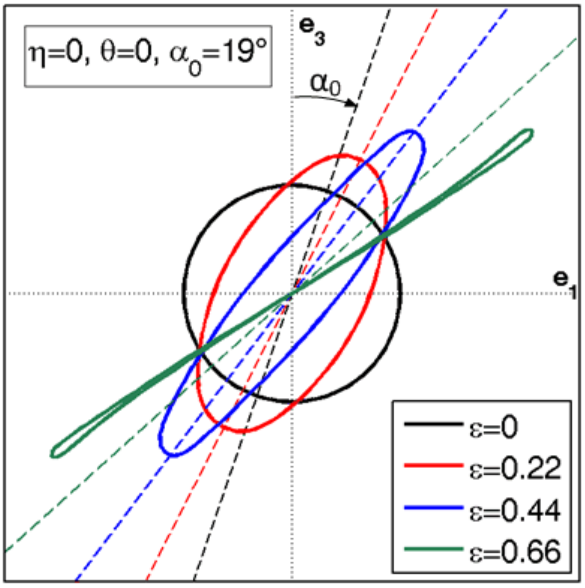

(b)

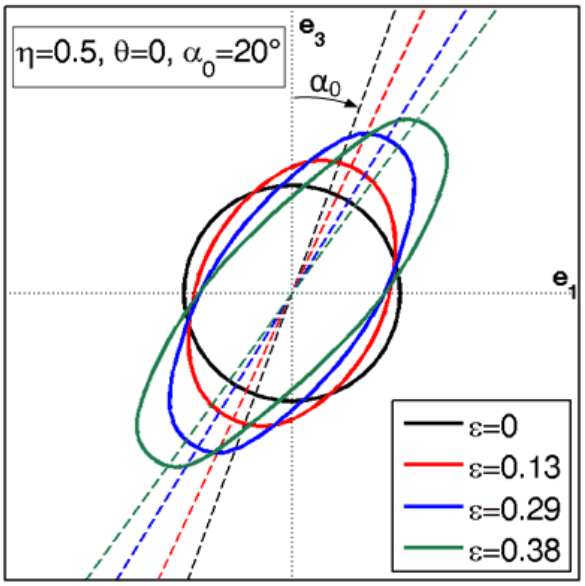

(c)

dashed lines indicate the current orientation of the first principal macroscopic stress. Note that the picture boundaries do not correspond to the boundaries of the unit cell.

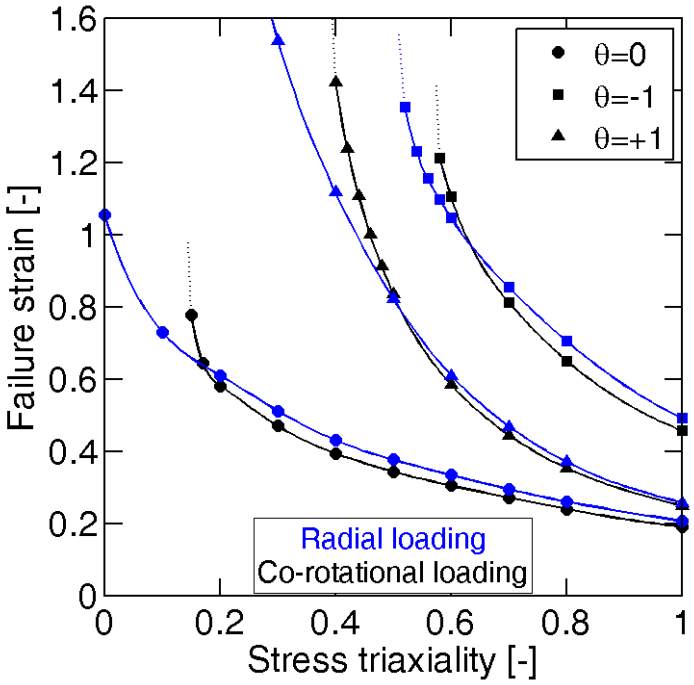

Figure 6-9: Comparison of the strain to failure for radial loading (blue curves) with that for co-rotational loading (black curves) for generalized shear ($\bar{\theta} = 0$), for axisymmetric tension ($\bar{\theta} = 1$) and for axisymmetric compression ($\bar{\theta} = -1$).

6.3.3 Effect of loading path

6.3.3.1 Void shape evolution under co-rotational loading

As detailed in Section 6.2.5, the principal macroscopic stress directions $\boldsymbol{p_I}$ and $\boldsymbol{p_{III}}$ evolve during the cell deformation, when a transverse displacement $U_t \neq 0$ is imposed (i.e. $\boldsymbol{R} \neq \boldsymbol{1}$). Figure 6-8 depicts the evolution of the void shape in the $(\boldsymbol{e_1}, \boldsymbol{e_3})$- cross-section (solid lines) along with the major principal macroscopic stress direction $\boldsymbol{p_I}$ (dashed lines) at different levels of deformation for the stress states considered under 6.3.1.1: (1) uniaxial tension (Fig. 6-8a), (2) pure shear (Fig. 6-8b) and (3) triaxial loading (Fig. 6-8c). In all three

cases, a transverse displacement is imposed to the cell boundaries (as $\alpha_0 \neq 0$), thereby inevitably shearing the unit cell.

During loading, the void evolves from an initially spherical shape to an elongated ellipsoidal-like shape. At low triaxiality loadings, the void eventually reduces to a penny-shaped crack (Fig. 6-8b). In addition to the evolution of its shape, the void also rotates with respect to the stationary unit cell frame $(\boldsymbol{e_1}, \boldsymbol{e_2}, \boldsymbol{e_3})$. Note that the major principal macroscopic stress direction $\boldsymbol{p_I}$ also rotates about the $\boldsymbol{e_2}$ axis (co-rotational loading), and remains approximately aligned with the major void axis throughout loading.

6.3.3.2 Co-rotational versus radial loading

The unit cell analysis is performed under radial loading for generalized shear ($\bar{\theta} = 0$), axisymmetric tension ($\bar{\theta} = 1$) and axisymmetric compression ($\bar{\theta} = -1$). As for co-rotational loading, the simulations for radial loading predict a monotonic decrease of the strain to failure as a function of the stress triaxiality (Fig. 6-9). Furthermore, the simulations for radial loading confirm that the microstructure is more prone to localization under axisymmetric tension than under axisymmetric compression. However, the quantitative comparison reveals lower cut-off stress triaxialities for radial loading (blue curves) as compared to co-rotional loading (black curves). In other words, the rotation of the orthotropy axes with respect to the directions of the principal stresses (radial loading) makes the unit cell more prone to localization at low stress triaxialities. This effect vanishes at higher stress triaxialities which is anticipated intuitively as the deformation-induced morphological anisotropy is expected to be less pronounced.

6.3.4 Effect of initial porosity

The central void acts as a defect that triggers the localization of the plastic deformation in the cell matrix. The computed failure strains are therefore expected to depend on the initial porosity. All results presented hereinbefore have been obtained for an initial void volume fraction of $f_0 = 0.71\%$. To shed more light on the dependence of the cell behavior

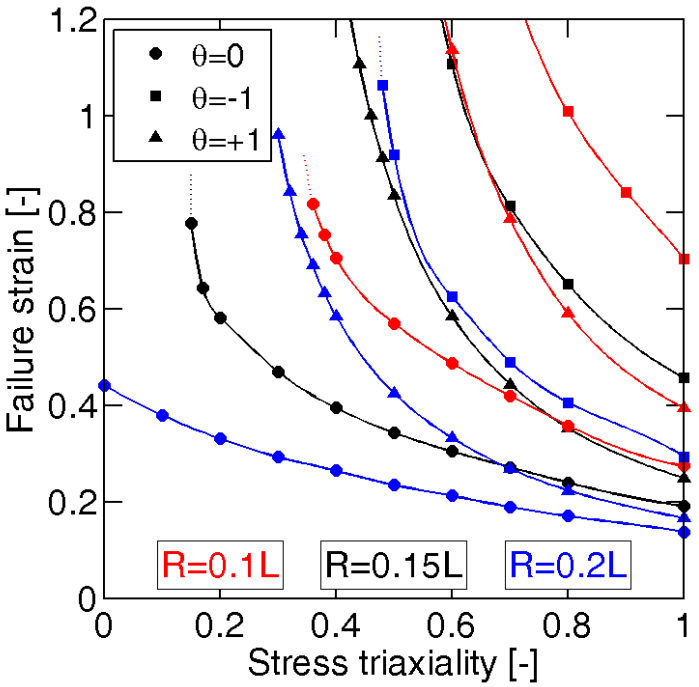

Figure 6-10: Effect of initial porosity on the predicted strain to failure for generalized shear ($\bar{\theta} = 0$), for axisymmetric tension ($\bar{\theta} = 1$) and for axisymmetric compression ($\bar{\theta} = -1$). The results are shown for $f_0 = 0.21\%$ (blue), $f_0 = 0.71\%$ (black) and $f_0 = 1.68\%$ (red).

on the initial porosity, additional simulations have been carried out on unit cells of lower porosity ($f_0 = 0.21\%$) and of higher porosity ($f_0 = 1.68\%$), respectively.

Figure 6-10 summarizes the simulation results for all three porosities ($f_0 = 0.21\%$=blue, $f_0 = 0.71\%$=black, $f_0 = 1.68\%$=red). It is observed that the initial volume fraction has two major effects on the onset of localization:

1. For a given stress state, the failure strain decreases as a function of the porosity. For example, for $\eta = 1$ and $\bar{\theta} = -1$, the strain to failure for the lowest porosity is 1.5 times higher than that for $f_0 = 0.71\%$, and 2.4 times higher than that for $f_0 = 1.68\%$.
2. The cut-off stress triaxiality below which no localization occurs decreases as the porosity increases. In case of a generalized shear stress state, the cut-off trixiality

is $\eta_c = 0.35$ for $f_0 = 0.21\%$, and $\eta_c = 0.15$ for $f_0 = 1.68\%$. For $f_0 = 1.68\%$, we have $\eta_c < 0$, i.e. localization occurs for all stress triaxialities considered in this study.

6.4 Macroscopic localization criterion

In view of developing ductile fracture models, we propose a macroscopic criterion to describe the strain to failure as a function of the stress state. Starting point is the formulation of a criterion in stress space, followed by a transformation into the mixed stress-strain space $\{\eta, \bar{\theta}, \bar{\varepsilon}_f\}$.

6.4.1 Criterion in terms of the normal and shear stress on the plane of localization

An attempt is made to find a relationship between the shear and normal stresses on the plane of localization. According to our coordinate definitions, the vector normal to the plane of localization reads

$$\boldsymbol{n} = \boldsymbol{e}_3 = \cos(\alpha)\,\boldsymbol{p}_I + \sin(\alpha)\boldsymbol{p}_{III} \tag{6-43}$$

Recall that the direction of the second principal stress is always parallel to the plane of localization. As a consequence, the normal and shear stress acting on that plane are independent of the second principal stress. Denoting the normal and shear stress acting on the plane of maximum shear ($\alpha = 45°$) as

$$\sigma_{ms} = \frac{\sigma_I + \sigma_{III}}{2} \tag{6-44}$$

$$\tau_{ms} = \frac{\sigma_I - \sigma_{III}}{2} \tag{6-45}$$

we have

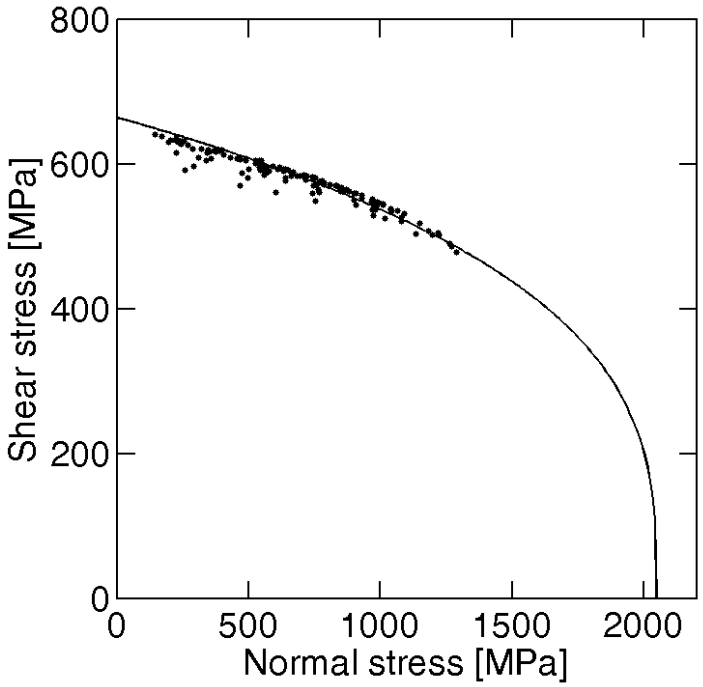

Figure 6-11: Shear stress versus the normal stress on the plane of localization. The solid dots represent the results from unit cell analyses, while the solid line represents the localization criterion defined by Eq. (6-48).

$$\sigma_n = \cos(2\alpha)\tau_{ms} + \sigma_{ms} \tag{6-46}$$

$$\tau = \sin(2\alpha)\tau_{ms} \tag{6-47}$$

The black dots in Figure 6-11 show the shear stress τ as a function of the normal stress σ_n at the onset of localization. Note that each data point $\{\sigma_n, \tau\}$ represents the result from a unit cell analysis for a specific stress state. The striking outcome is that all data points seem to lie on a smooth curve in that space. In particular, the plot is reminiscent of the criterion sketched by Mohr (1900, [110]). Here, we propose an open convex envelope as criterion for the onset of shear localization,

$$\frac{|\tau|}{\tau_0} = \left[1 - \frac{\sigma_n}{\sigma_0}\right]^n \tag{6-48}$$

with $0 < n \leq 1$; τ_0 and σ_0 denote the respective limiting shear and normal stresses on the plane of localization. The black curve in Fig. 6-11 corresponds to a fit with $\tau_0 = 664MPa$, $\sigma_0 = 2048MPa$ and $n = 0.32$.

Aside from the good agreement with the simulation results in terms of stresses, it is worth noting that the above shear localization criterion also provides a relationship between the orientation of the plane of localization and the stress state. For a given stress state $\{\eta, \bar{\theta}\}$, the mathematical problem determining the orientation α of the localization plane reads

$$\alpha(\eta, \bar{\theta}) = \underset{\alpha}{\operatorname{argmin}}\{\bar{\sigma}(\alpha, \eta, \bar{\theta})\} \tag{6-49}$$

where $\bar{\sigma}(\alpha, \eta, \bar{\theta})$ is given through the implicit equation

$$\bar{\sigma}\tau^* - [1 - \bar{\sigma}\sigma^*]^n = 0 \tag{6-50}$$

With

$$\sigma^*(\alpha, \eta, \bar{\theta}) = \cos(2\alpha)\frac{f_I(\bar{\theta}) - f_{III}(\bar{\theta})}{2\sigma_0} + \frac{2\eta + f_I(\bar{\theta}) + f_{III}(\bar{\theta})}{2\sigma_0} \tag{6-51}$$

And

$$\tau^*(\alpha, \eta, \bar{\theta}) = \sin(2\alpha)\frac{f_I(\bar{\theta}) - f_{III}(\bar{\theta})}{2\tau_0} \tag{6-52}$$

Figure 6-12a shows the predicted angle α as a function of the stress triaxiality and the Lode angle parameter. Apart from the immediate vicinity of the cut-off stress triaxiality, the model provides a reasonable approximation of the simulation results (Fig. 6-12b): the angle α decreases as a function of the stress triaxiality and the Lode angle parameter, with values in the vicinity of $\alpha = 45°$ (i.e. close to the plane of maximum shear).

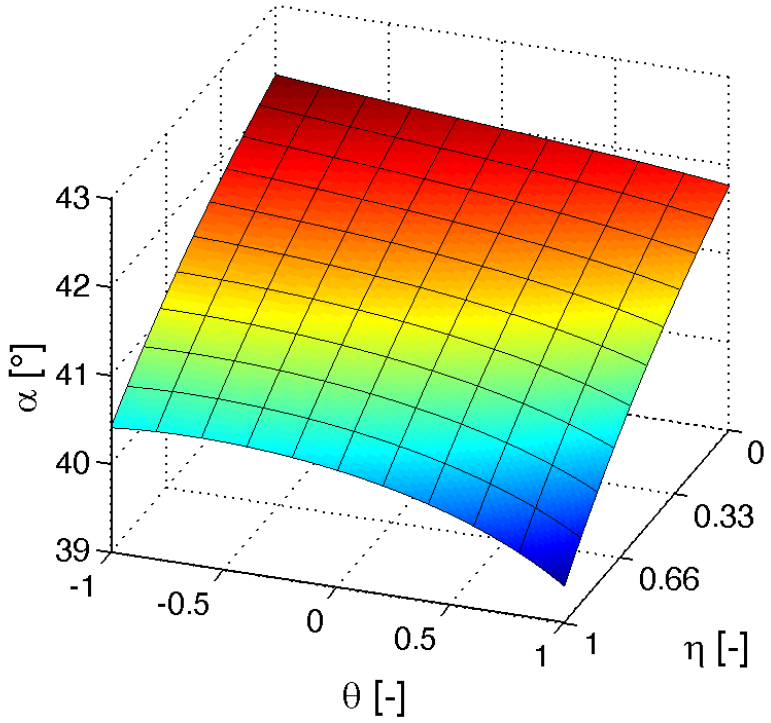

(a)

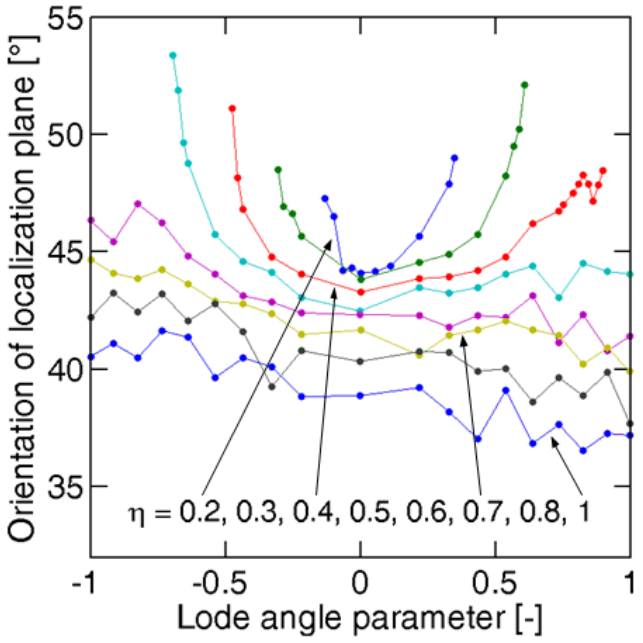

(b)

Figure 6-12: Orientation of the plane of localization (a) according to the analytical model, and (b) according to the unit cell analyses.

6.4.2 Criterion in mixed stress-strain space

In the general framework provided by Mohr and Marcadet (2012, [108]), the solution

$$\bar{\sigma}_f(\eta, \bar{\theta}) = \min\{\bar{\sigma}(\alpha, \eta, \bar{\theta})\} \tag{6-53}$$

of Eq. (6-49) corresponds to a conversion of the localization criterion from the two-dimensional stress space $\{\sigma_n, \tau\}$ to the three-dimensional modified Haigh-Westergaard space $\{\eta, \bar{\theta}, \bar{\sigma}\}$. Using the isotropic hardening law, the localization criterion can then also be converted into the mixed stress-strain space $\{\eta, \bar{\theta}, \bar{\varepsilon}_p\}$,

$$\bar{\varepsilon}_f = k^{-1}[\bar{\sigma}_f(\eta, \bar{\theta})] \tag{6-54}$$

with k^{-1} denoting the inverse of the hardening function given by (6-1). The corresponding plot of the computed strain to failure as a function of stress triaxiality and the Lode angle parameter is shown in Fig. 6-13a. It agrees well with that obtained from localization analysis (Fig. 6-13b) which is another confirmation of the applicability of criterion (6-48) for predicting the onset of shear localization.

6.4.3 Discussion

One of the key features of the proposed localization criterion is its independence of the intermediate principal stress. It can thus be written in terms of two stress quantities only. However, the right pair of stress measures must be chosen, e.g. σ_I and σ_{III}, or σ_n and τ. Attempts were made in the past to formulate phenomenological ductile fracture criteria in terms of $\bar{\varepsilon}_p$ and η (e.g. Johnson and Cook, 1985, [76]). For isotropic hardening Levy-von Mises materials, this corresponds to a criterion in terms of $\bar{\sigma}$ and σ_m in stress space. The poor agreement of such criteria with experimental data for non-axisymmetric stress states led to the introduction of the Lode (angle) parameter. Based on the above findings (and the assumption that ductile fracture is imminent with the onset of localization), the introduction of a third stress measure into ductile fracture criteria is only needed because the equivalent von Mises stress (and hence also the equivalent plastic strain) is not orthogonal to the second

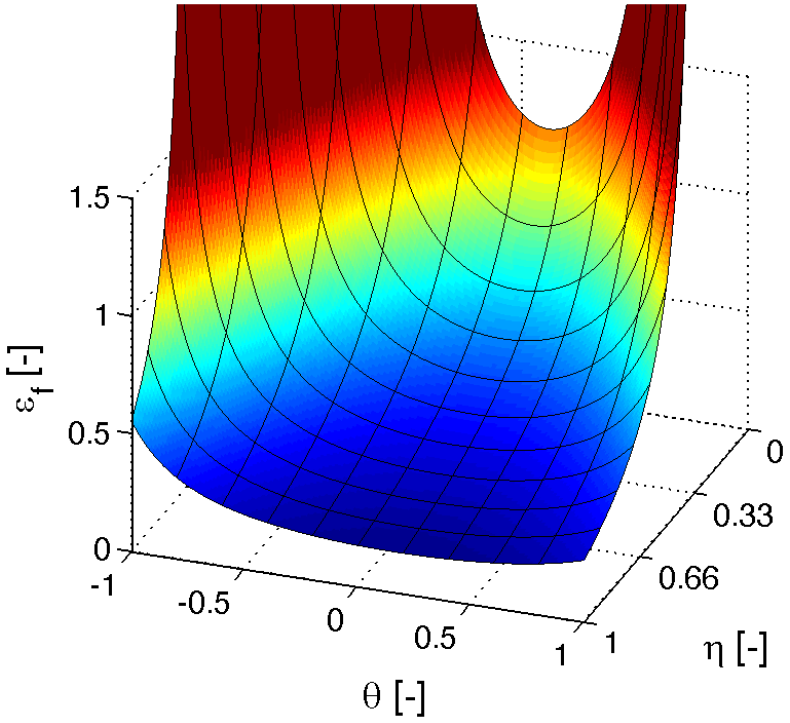

(a)

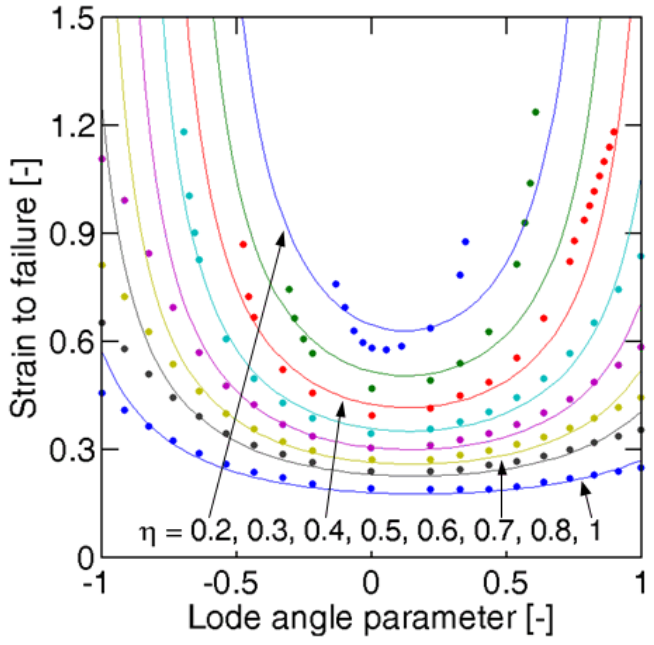

(b)

Figure 6-13: Visualization in the mixed stress-strain space: (a) strain to failure according to the localization criterion as a function of the stress triaxiality and the Lode angle parameter, (b) Comparison of the analytical model (dark curves) with the simulation results (dark dots).

principal stress.

It is worth noting that unlike the von Mises stress, the Tresca stress τ_{ms} is orthogonal to the second principal stress and could be used in conjunction with the normal stress σ_{ms} acting on the plane of maximum shear to formulate a fracture criterion. As compared to using the normal and shear stresses on the plane of localization, the latter criterion would not require the identification of the critical plane. Preliminary computations actually showed that (6-48) also yields good results when using the $\{\sigma_{ms}, \tau_{ms}\}$ instead of $\{\sigma_n, \tau\}$.

6.5 Concluding remarks

Motivated by the assumption that ductile fracture is imminent with the onset of localization, a fully three-dimensional unit cell model with a spherical void defect is built to investigate the effect of the stress state on the onset of localization in a Levy-von Mises solid. The particular feature of the present analysis is that it covers a rather dense grid of stress states, with stress triaxialities ranging from 0 to 1 and the full range of Lode parameters. The periodic boundary conditions are formulated such that the macroscopic stress triaxiality and Lode parameter are kept constant up to the onset of localization. The simulations are performed for co-rotational loading to compensate for the effect of unavoidable material rotation due to the tangential loading along the unit cell boundaries.

The simulation results reveal that the macroscopic failure strain is a monotonically decreasing smooth function of the stress triaxiality, and a non-symmetric convex function of the Lode parameter. This observation is in qualitative agreement with the simulations of Nahshon and Hutchinson (2008, [112]) who carried out a localization analysis (based on the theoretical framework proposed by Rice (1977, [127])) using an isotropic shear-modified Gurson model (Fig. 6-14). A plot of the shear stress as a function of the normal stress acting on the plane of localization for all simulations suggests a simple open convex envelope as a criterion for predicting the onset of localization. The transformation of this criterion into the mixed stress-strain space of stress triaxiality, Lode angle parameter and equivalent plastic strain leads to an accurate analytical description of all simulation results. It is worth noting

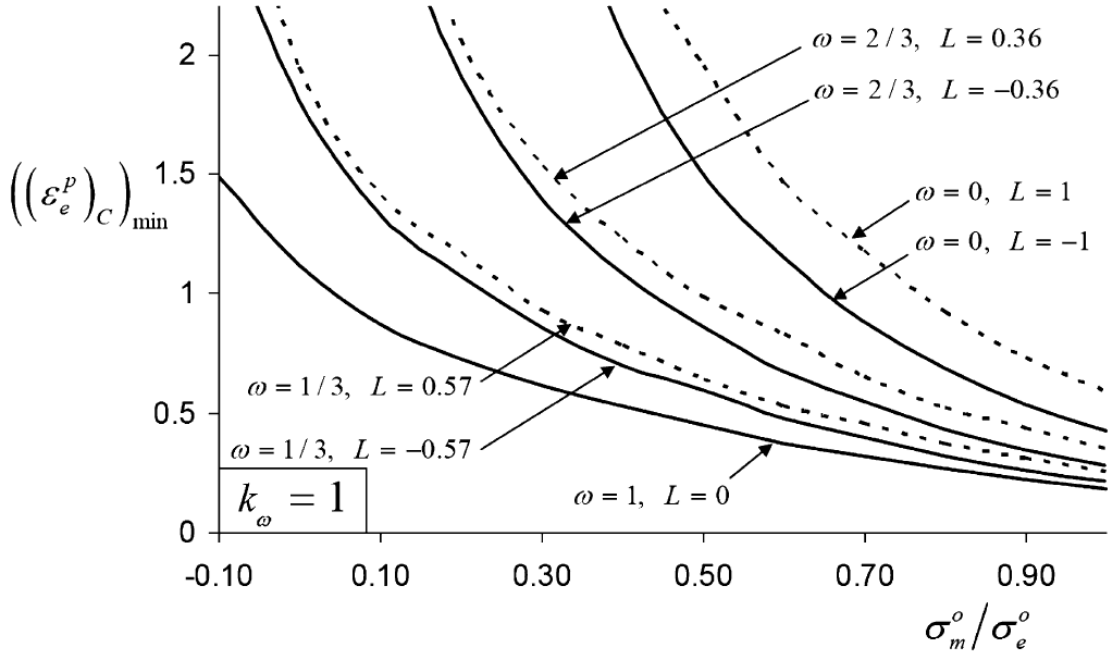

Figure 6-14: Minimum effective plastic strain at localization for constant values of ω as predicted by the shear-modified Gurson model. From Nahshon and Hutchinson (2008, [112])

that the proposed criterion can be found as a sketch in the early work of Mohr (1900, [110]), with the well-known Mohr-Coulomb model corresponding to a linear approximation of the proposed localization criterion. The present micromechanical analysis therefore provides strong support for phenomenological ductile fracture models that postulate the existence of a Mohr-Coulomb type of failure surface in stress space for proportional loading (e.g. Bai and Wierzbicki, 2010, [5]; Mohr and Marcadet, 2012, [108]).

Chapter 7

Conclusion

Contents

7.1 Summary of the contributions

7.1.1 Constitutive modeling of AHSS

An extensive experimental program has been carried out to investigate the inelastic behavior of TRIP780 and DP590 materials under large deformations. Almost the same stress-strain curve has been determined from uniaxial tensile tests performed for seven different specimen orientations. However, the plastic flow (as characterized by Lankford's r-ratios) is direction dependent and its modeling requires the use of an anisotropic quadratic flow potential function. Here, a constitutive model with a planar isotropic quadratic yield function and a non-associated anisotropic flow rule is employed. Biaxial plasticity

experiments have demonstrated that this constitutive model yields accurate predictions of the mechanical response under multi-axial loading.

7.1.2 Fracture experiments for sheet materials

Two series of fracture experiments for sheet materials were developed and analyzed in detail. A first series, consisting of full thickness specimens with different geometries, permits to reach stress states ranging from uniaxial to equi-biaxial tension. A second series makes use of a butterfly-shaped reduced thickness specimen. Used in conjunction with a dual-actuator system, any stress state from pure shear to transverse plane strain tension can be achieved. The butterfly specimen is optimized more specifically for shear-dominated conditions. The shape of the specimen gage section is design such that fracture initiates away from the specimen boundaries and that the strain field is approximately uniform at the specimen center. It features clothoidal shaped boundaries for that purpose. However, experimental results showed that despite this optimization effort, the location of fracture initiation under shear loading is not completely controlled.

7.1.3 Characterization of the effect of stress state on ductile fracture of AHSS

An extensive experimental program covering stress states from pure shear to equi-biaxial tension was carried on TRIP780 sheet specimens. Overall nine different loading conditions were investigated. Surface strains fields and displacement of specimen boundaries were measured using planar or stereo Digital Image Correlation, while detailed finite element simulations were performed of all experiments to determine the evolution of local stress and strain fields inside the specimens and the material state at the onset of fracture. Possible experimental and numerical sources of inaccuracy in the resulting loading paths to fracture were analyzed and minimized. Results of this hybrid experimental-numerical method showed a strong dependence of ductility to stress state. Furthermore, strain to failure could not be considered as a function of the stress triaxiality only. For the

present TRIP780 sheet material, a minimum of ductility is observed for transverse plane strain tension loading.

7.1.4 Plastic localization analysis

A numerical model was developed to investigate the effect of the stress state on the onset of plastic localization in a void containing material. It is based on a cubic three-dimensional unit cell containing an initially spherical cavity, deformed under a combination of normal and tangential displacements. Fully periodic boundary conditions are applied, while specific kinematic constraints are imposed to the cell degrees of freedom in order to control the macroscopic stress state as well as the macroscopic principal stress directions during deformation. The onset of plastic localization is defined by a kinematic criterion comparing the rates of deformation gradients inside and outside the band of localization. The complete range of intermediate stress triaxialities (from 0 to 1) is investigated, with Lode angle parameters varying from -1 to 1. To account for topological and morphological anisotropy, both radial and co-rotational loading paths are considered.

Results of the localization analysis show that the macroscopic failure strain is a monotonically decreasing smooth function of the stress triaxiality, and a non-symmetric convex function of the Lode angle parameter. Furthermore it was found that no localization occurs in the vicinity of axisymmetric stress states at low stress triaxiality. An analysis of the shear and normal stresses acting on the plane of localization for all simulations suggests a simple open convex envelope as a criterion for predicting the onset of localization in the stress space. It is shown that this envelop can be approximated by a Mohr-Coulomb criterion.

7.1.5 Modeling the onset of ductile fracture in AHSS

The extensive experimental program carried out on the TRIP780 material is used to calibrate and evaluate the predictive capabilities of two fracture models: a Shear-modified Gurson model and the Modified Mohr-Coulomb (MMC) fracture model. The MMC model

is based on the assumption that the initiation of fracture is determined by a critical stress state, while the shear-modified Gurson model assumes fracture initiates when a critical void volume fraction is reached. In addition, the Gurson model explicitly includes damage in the constitutive equations, while the MMC model is based on an uncoupled approach where fracture model does not influence the plasticity model.

Considering the very low level of void volume fraction reached at the onset of fracture in the present TRIP material, it is found that embedding damage in the constitutive model does not noticeably improve predictions of the macroscopic behavior of the material. Furthermore, the MMC model can predict the onset of fracture with a higher accuracy while featuring less parameters. Results of the unit cell localization analysis also strongly support the choice of a Mohr-Coulomb type fracture criterion in the range of intermediate stress triaxialities.

7.2 Future research

7.2.1 Non-linear loading paths

All the experiments presented in this work have been carried out under proportional loading conditions. As a result loading trajectories that have been investigated are close to linear (proportional) in the stress space. Small deviations from linear loading paths observed in fracture experiments described in Chapter 3 and Chapter 4 are due to localized necking and/or geometry effects caused by the large deformation of specimens. Note that because those necking and/or large deformation effects, strictly linear loading paths are highly difficult to achieve.

However, in most industrial applications where an accurate prediction of the onset of ductile fracture in thin-walled structures is of interest (sheet metal forming, crash simulations…), loading paths are often highly non-linear in the stress space. An extension of the hybrid experimental-numerical method presented in Chapter 3 would be required to characterize the onset of ductile fracture under such non-proportional loadings. Note that the

biaxial tension-shear experimental procedure developed in Chapter 4 may be used to carry out non-proportional loading conditions. In addition, tension-compression experiments, using an appropriate anti-buckling device (Mohr and Mansour, 2009, [107]), can also be used for that purpose. Note that the plasticity model detailed in Chapter 2 was developed in view of proportional loading conditions only, as it can only describe isotropic hardening. An extension accounting for kinematic hardening would be needed in order to extend the hybrid experimental-numerical method to non-linear loading paths.

7.2.2 Damage accumulation rule

The uncoupled framework for phenomenological fracture models presented in Chapter 5 is based on the definition of a reference fracture strain for proportional loading conditions. Application of this approach to non-linear loading paths requires introducing a damage indicator incrementally defined by a damage accumulation rule (Eq. 1-1). Here a linear accumulation rule is chosen, where the increment of damage is proportional to the increment of equivalent plastic strain. Note that the MMC fracture model is applied to almost proportional loading paths in Chapter 5, which therefore do not permit to assess the validity of a linear accumulation of damage. In addition, experimental evidence or theoretical justifications for a linear accumulation of damage are scarce in the open literature.

Recent experimental investigations on butterfly-shaped specimens submitted to shear followed by traction indicate that a linear accumulation of damage is not appropriate for highly non-linear loading paths (Marcadet, 2013, [99]). Additional research is needed to develop and validate a damage accumulation rule applicable to non-linear loading conditions.

7.2.3 Unit cell calculations

The unit cell model developed in Chapter 6 is subject to undesired topological anisotropy. The topological anisotropy may by suppressed by replacing the single-cavity cubic unit cell by a Representative Volume Element (RVE) containing multiple cavities

such that the resulting periodic material be isotropic. Significant challenges are associated with the choice of an isotropic distribution of cavities, as well as with simulation of the deformation of the RVE, due to large meshes involved.

The physical scale representative of the unit cell model is the grain scale. Cavities observed in the deformed TRIP material have a diameter of 1 to 3 μm. At this scale the matrix material does not behave as a continuum but as a crystal aggregate. The maximum grain size is about 5 μm. Therefore a more representative model for the detection of plastic localization at the grain scale may be obtained by replacing the isotropic matrix material by a polycrystalline RVE whose deformation is governed by crystal plasticity.

Appendix A

Publications & Presentations

A.1 Refereed journal publications

[1] M. Dunand & D. Mohr (2010). "Hybrid Experimental-numerical Analysis of Basic Ductile Fracture Experiments for sheet metals", International Journal of Solids and Structures **47** (9), 1130-1143.

[2] D. Mohr, M. Dunand and H.W. Kim (2010). "Evaluation of Associated and Non-Associated Quadratic Plasticity Models for Advanced High Strength Steel Sheets under Multi-axial Loading", International Journal of Plasticity **26** (7), 939-956.

[3] M. Dunand & D. Mohr (2011). "On the Predictive Capabilities of the Shear Modified Gurson and the Modified Mohr-Coulomb Fracture Models over a Wide Range of Stress Triaxialities and Lode Angles", Journal of the Mechanics and Physics of Solids **59** (7), 1374-1394.

[4] M. Dunand & D. Mohr (2011). "Optimized Specimen for the Fracture Testing of Advanced High Strength Steels under Combined Normal and Shear Loading", Engineering Fracture Mechanics **78** (17), 2919-2934.

[5] M. Dunand, A. Maertens, M. Luo & D. Mohr (2012). "Experiments and Modeling of Anisotropic Aluminum Extrusions under Multi-axial Loading – Part I: Plasticity", International Journal of Plasticity **36**, 35-49.

[6] M. Luo, M. Dunand & D. Mohr (2012). "Experiments and Modeling of Anisotropic Aluminum Extrusions under Multi-axial Loading – Part II: Ductile Fracture", International Journal of Plasticity **32-33**, 36-58.

[7] M. Dunand, G. Gary & D. Mohr (2013). "Load-inversion Device for the High Strain Rate Tensile Testing of Sheet Materials with Hopkinson Pressure Bars", Experimental Mechanics *(In Press)*.

[8] M. Dunand & D. Mohr, "Effect of Lode parameter on plastic flow localization at low stress triaxialities", *Submitted for publication*.

[9] M. Dunand & D. Mohr, "Rate-dependent behavior of Advanced High Strength steels under multi-axial loading: characterization and modeling at large strains", *In preparation*.

[10] M. Dunand, D. Mohr & K. Ravi-Chandar, "Shear Fracture of Advanced High Strength Steel: Fractography and Micromechanical modeling", *In preparation*.

A.2 Conference proceedings

[1] M. Dunand & D. Mohr, "Plasticity of Aluminum Extrusions under Combined Normal and Shear Loading", Proc. 15th International Symposium on Plasticity in St Thomas, USVI, edited by A.S. Khan, 2009.

[2] D. Mohr, F. Ebnoether and M. Dunand, "Plasticity and Fracture of Advanced High Strength Steel Sheets under Combined Tensile and Shear Loading", in Dynamic Behavior of Materials, edited by A. Rusinek and P. Chevrier, pp. 147-154.

[3] M. Dunand & D. Mohr, "Ductile fracture of TRIP780 sheets under multi-axial loading", AIP Conference Proceedings Vol. 1252, 1295-1302, 2010 (Proceedings of the 10th Int. Conf. on Numerical Methods in Industrial Forming Processes Dedicated to Pr. O.C. Zienkiewicz in Pohang, Republic of Korea, edited by F. Barlat, Y.H. Moon and M.G. Lee).

[4] M. Dunand & D. Mohr, "On the limitations of Shear-modified Gurson models: Comparison of numerical predictions with experimental results for ductile fracture

under combined tension and shear loading", Proc. 17th International Symposium on Plasticity in Puerto Vallarta, Mexico, edited by A.S. Khan, 2011.

[5] M. Dunand & D. Mohr, "Ductile fracture of AHSS sheets under multi-axial loading: experiments and modeling", AIP Conference Proceedings Vol. 1383, 484-491, 2011 (Proceedings of the 8th Int. Conf. on Numerical Simulation of 3D sheet metal forming processes in Seoul, Republic of Korea, edited by K. Chung).

[6] M. Dunand & D. Mohr, "On the modeling of damage and ductile fracture in advanced high strength steel sheets using void cell calculations", Proceedings of the 23rd International Congress of Theoretical and Applied Mechanics in Beijing, China, August 19-24, 2012.

[7] M. Dunand & D. Mohr, "High strain rate tensile testing of sheet materials using three Hopkinson pressure bars", Proceedings of the 10th International DYMAT Conference in Freiburg, Germany, September 2nd-7th, 2012.

[8] M. Dunand & D. Mohr, "Effect of Strain Rate and Stress State on the Ductile Fracture of AHSS Sheets: a Micromechanical Analysis", Proceedings of the International Deep Drawing Research Group 12' Conference in Mumbai, India, November 25-29, 2012.

[9] M. Dunand & A. Kamoulakos, "Application of shell-to-solid re-meshing to accurate ductile fracture predictions in Advanced High Strength steel sheets", Proceedings of the 3rd International Conference on Engineering against Failure in Kos, Greece, June, 2013

A.3 Presentations

[1] M. Dunand & D. Mohr, "Plasticity of Aluminum extrusions under combined and shear loading", 15th International Symposium on Plasticity in St Thomas, USVI, January 3rd-6th, 2009.

[2] M. Dunand & D. Mohr, “Determination of ductile fracture properties of TRIP steel using notched tensile specimens”, 5th MIT Workshop on Experimental and Computational Fracture Mechanics in Cambridge, USA, April 2009.

[3] D. Mohr & M. Dunand, “Onset of Fracture in Advanced High Strength Steels Under Multi-axial Loading”, ASME Exposition and Congress, Lake Buena Vista, USA, November 17th, 2009.

[4] M. Dunand & D. Mohr, “Assessment of the accuracy of selected fracture experiments”, 6th MIT Workshop on Experimental and Computational Fracture Mechanics in Cambridge, USA, November 19th, 2009.

[5] M. Dunand & D. Mohr, “Standardized fracture model identification procedure based on butterfly experiments”, 6th MIT Workshop on Experimental and Computational Fracture Mechanics in Cambridge, USA, November 19th, 2009.

[6] M. Dunand & D. Mohr, “Ductile fracture of TRIP780 steel under multi-axial loading”, 10th Int. Conf. on Numerical Methods in Industrial Forming Processes in Pohang, South Korea, June 7th, 2010.

[7] M. Dunand & D. Mohr, “Comparison of the performances of the MMC fracture model with shear modified Gurson models”, 7th MIT Workshop on Experimental and Computational Fracture Mechanics in Cambridge, USA, October 7th, 2010.

[8] M. Dunand & D. Mohr, “Ductile fracture under multi-axial loadings: Comparison of numerical predictions with experimental results”, 17th International Symposium on Plasticity in Puerto Vallarta, Mexico, January 5th, 2011.

[9] M. Dunand & D. Mohr, “Ductile fracture of AHSS sheets under multi-axial loadings: Experiments and modeling”, 8th International Conference on Numerical Simulation of 3D sheet metal forming processes in Seoul, South Korea, August 24th, 2011.

[10] M. Dunand, G. Gary & D. Mohr, “A Hybrid Experimental-numerical Method to Characterize the Effect of Strain Rate on Sheet Metal Fracture”, 8th International

Conference on Numerical Simulation of 3D sheet metal forming processes in Seoul, South Korea, August 24th, 2011.

[11] M. Dunand, G. Gary & D. Mohr, "A new SHPB technique to study strain rate dependent fracture", 8th MIT Workshop on Experimental and Computational Fracture Mechanics in Cambridge, USA, October 6th, 2011.

[12] M. Dunand & D. Mohr, "Microscopic Analysis of the fracture mechanisms of AHSS", Interim meeting of the MIT/Industry Fracture Consortium in Paris, France, March 23rd, 2012.

[13] M. Dunand & D. Mohr, "Reliable procedure for high strain rate tensile testing of sheet materials", Interim meeting of the MIT/Industry Fracture Consortium in Paris, France, March 23rd, 2012.

[14] M. Dunand & D. Mohr, "Ductile fracture mechanisms: micro-analysis and modeling", 5th Forming Technology Forum in ETH Zurich, Swiss, June 4th, 2012.

[15] M. Dunand & D. Mohr, "Microscopic analysis of the fracture mechanisms of Advanced High Strength Steel sheets", Jean Mandel Symposium on Damage and Rupture in Palaiseau, France, June 7th, 2012.

[16] M. Dunand & D. Mohr, "Experimental and numerical investigations of the damage and ductile fracture mechanisms in TRIP steel sheets", 8th European Solid Mechanics Conference in Graz, Austria, July 12th, 2012.

[17] M. Dunand & D. Mohr, "On the modeling of damage and ductile fracture in Advanced High Strength Steel sheets using void cell caclulations", 23rd International Congress of Theoretical and Applied Mechanics in Beijing, China, August 23rd, 2012.

[18] M. Dunand, G. Gary and D. Mohr, "High strain rate tensile testing of sheet materials using split Hopkinson Pressure bars", 10th International DYMAT Conference in Freiburg, Germany, September 6th, 2012.

[19] M. Dunand & A. Kamoulakos, "Application of shell-to-solid re-meshing to accurate ductile fracture predictions in AHSS sheets", 9th MIT Workshop on Experimental and Computational Fracture Mechanics in Cambridge, USA, October 8th, 2012.

[20] M. Dunand & D. Mohr, "Rate-dependent plasticity of AHSS: model formulation and experimental validation", 9th MIT Workshop on Experimental and Computational Fracture Mechanics in Cambridge, USA, October 8th, 2012.

[21] C. Roth & M. Dunand, "Effect of strain rate on the fracture of DP590", 9th MIT Workshop on Experimental and Computational Fracture Mechanics in Cambridge, USA, October 8th, 2012.

[22] M. Dunand, G. Gary & D. Mohr, "Hybrid experimental-numerical characterization of the effect of strain rate on the ductile fracture properties of AHSS sheets", Journée des Doctorants – LMS, Palaiseau, France, October 16th, 2012.

[23] M. Dunand & D. Mohr, "Effect of stress state and strain rate on the ductile fracture of AHSS sheets", International Deep Drawing Research Group 12' Conference in Mumbai, India, November 26th, 2012.

[24] M. Dunand & D. Mohr, "Prediction of shear localization in AHSS", Interim meeting of the MIT/Industry Fracture Consortium in Paris, France, April 5th, 2013.

[25] M. Dunand & D. Mohr, "Coupled rate and temperature dependent plasticity model for AHSS", Interim meeting of the MIT/Industry Fracture Consortium in Paris, France, April 5th, 2013.

Bibliography

1. Abaqus (2011). "Reference manual v6.11". Abaqus Inc.

2. Angel, T. (1954). "Formation of martensite in austenitic stainless steels, effect of deformation, temperature and composition". *Journal of the Iron and Steel Institute*: p. 165.

3. ASTM-E8M-04, *Standard Test Methods for Tension Testing of Metallic Materials*, 2004.

4. Bai, Y.L. (2008). "Effect of Loading History on Necking and Fracture". Ph.D., Department of Mechanical Engineering, Massachusetts Institute of Technology, Cambridge, MA.

5. Bai, Y.L. and T. Wierzbicki (2010). "Application of extended Mohr-Coulomb criterion to ductile fracture". *International Journal of Fracture* **161**(1): p. 1-20.

6. Banabic, D., H.J. Bunge, K. Pöhlandt, and A. Tekkaya (2000). "Formability of Metallic Materials". Berlin: Springer.

7. Banu, M., M. Takamura, T. Hama, O. Naidim, C. Teodosiu, and A. Makinouchi (2006). "Simulation of springback and wrinkling in stamping of a dual phase steel rail-shaped part". *Journal of Materials Processing Technology* **173**(2): p. 178-184.

8. Bao, Y. (2003). "Prediction of Ductile Crack Formation in Uncracked Bodies". Ph.D. Thesis, Ocean Engineering, Massachusetts Institute of Technology, Cambridge, USA.

9. Bao, Y. and T. Wierzbicki (2004). "A Comparative Study on Various Ductile Crack Formation Criteria". *Journal of Engineering Materials and Technology* **126**(3): p. 314-324.

10. Barlat, F., J.C. Brem, J.W. Yoon, K. Chung, R.E. Dick, D.J. Lege, F. Pourgoghrat, S.H. Choi, and E. Chu (2003). "Plane stress yield function for aluminum alloy sheets - part 1: theory". *International Journal of Plasticity* **19**(9): p. 1297-1319.

11. Barlat, F., J.M.F. Duarte, J.J. Gracio, A.B. Lopes, and E.F. Rauch (2003). "Plastic flow for non-monotonic loading conditions of an aluminum alloy sheet sample". *International Journal of Plasticity* **19**(8): p. 1215-1244.

12. Barranger, Y., P. Doumalin, J.-C. Dupre, A. Germaneau, S. Hedan, and V. Valle (2009). "Evaluation of three-dimensional and two-dimensional full displacement fields of a single edge notch fracture mechanics specimen, in light of experimental data using X-ray tomography". *Engineering Fracture Mechanics* **76**(15): p. 2371-2383.

13. Barsoum, I. and J. Faleskog (2007). "Rupture mechanisms in combined tension and shear—Micromechanics". *International Journal of Solids and Structures* **44**(17): p. 5481-5498.

14. Barsoum, I. and J. Faleskog (2007). "Rupture mechanisms in combined tension and shear - Experiments". *International Journal of Solids and Structures* **44**(6): p. 1768-1786.

15. Barsoum, I. and J. Faleskog (2011). "Micromechanical analysis on the influence of the Lode parameter on void growth and coalescence". *International Journal of Solids and Structures* **48**(6): p. 925-938.

16. Bathe, K.J. (1996). "Finite Element Procedures". Upper Saddle River: Prentice-Hall Inc.

17. Beese, A.M., M. Luo, Y.N. Li, Y.L. Bai, and T. Wierzbicki (2010). "Partially coupled anisotropic fracture model for aluminum sheets". *Engineering Fracture Mechanics* **77**(7): p. 1128-1152.

18. Benzerga, A.A. (2002). "Micromechanics of coalescence in ductile fracture". *Journal of the Mechanics and Physics of Solids* **50**(6): p. 1331-1362.

19. Benzerga, A.A. and J. Besson (2001). "Plastic potentials for anisotropic porous solids". *European Journal of Mechanics a-Solids* **20**(3): p. 397-434.

20. Benzerga, A.A., J. Besson, and A. Pineau (2004). "Anisotropic ductile fracture Part II: theory". *Acta Materialia* **52**(15): p. 4639-4650.

21. Benzerga, A.A. and J.B. Leblond (2010). "Ductile Fracture by Void Growth to Coalescence". *Advances in Applied Mechanics, Vol 44* **44**: p. 169-305.

22. Bishop, J.F.W. and R. Hill (1951). "A theory of the plastic distortion of a polycrystalline aggregate under combined stresses". *Philos. Mag*: p. 42.

23. Boehler, J.P., S. Demmerle, and S. Koss (1994). "A new direct biaxial testing machine for anisotropic materials". *Experimental Mechanics* **34**(1): p. 1-9.

24. Brocks, W., D.Z. Sun, and A. Honig (1995). "Verification of the transferability of micromechanical parameters by cell model calculations with visco-plastic materials". *International Journal of Plasticity* **11**(8): p. 971-989.

25. Broggiato, G.B., F. Campana, and L. Cortese (2008). "The Chaboche nonlinear kinematic hardening model: calibration methodology and validation". *Meccanica* **43**(2): p. 115-124.

26. Brown, L.M. and J.D. Embury (1973). "The initiation and growth of voids at second phase particles". In: *Proceedings of the Third International Conference on Strength of Metals and Alloys. ICSMA 3*, p. 164–169.

27. Brozzo, P., B. Deluca, and R. Rendina (1972). "A New Method for Prediction of Formability in Metal Sheets". In: *7th biennial Conference of the IDDRG*,

28. Brunig, M. (1999). "Numerical simulation of the large elastic-plastic deformation behavior of hydrostatic stress-sensitive solids". *International Journal of Plasticity* **15**(11): p. 1237-1264.

29. Brunig, M., O. Chyra, D. Albrecht, L. Driemeier, and M. Alves (2008). "A ductile damage criterion at various stress triaxialities". *International Journal of Plasticity* **24**(10): p. 1731-1755.

30. Brunig, M. and H. Obrecht (1998). "Finite elastic-plastic deformation behaviour of crystalline solids based on a non-associated macroscopic flow rule". *International Journal of Plasticity* **14**(12): p. 1189-1208.

31. Burford, D., K. Narasimhan, and R. Wagoner (1991). "A theoretical sensitivity analysis for full- dome formability tests: parameter study for<i>n, m, r,</i> and μ". *Metallurgical and Materials Transactions A* **22**(8): p. 1775-1788.

32. Cao, J., W. Lee, H.S. Cheng, M. Seniw, H.P. Wang, and K. Chung (2009). "Experimental and numerical investigation of combined isotropic-kinematic hardening behavior of sheet metals". *International Journal of Plasticity* **25**(5): p. 942-972.

33. Casey, J. and T.D. Sullivan (1985). "Pressure dependency, strength-differential effect, and plastic volume expansion in metals". *International Journal of Plasticity* **1**: p. 39-61.

34. Chaboche, J.L. (1988). "Continuum damage mechanics. 1. General concepts". *Journal of Applied Mechanics-Transactions of the Asme* **55**(1): p. 59-64.

35. Chaboche, J.L. (1988). "Continuum damage mechanics: part ii—damage growth, crack initiation and crack growth". *Journal of Applied Mechanics-Transactions of the Asme* **55**(1): p. 65-72.

36. Chaboche, J.L. (2008). "A review of some plasticity and viscoplasticity constitutive theories". *International Journal of Plasticity* **24**(10): p. 1642-1693.

37. Chen, P. and M. Koc (2007). "Simulation of springback variation in forming of advanced high strength steels". *Journal of Materials Processing Technology* **190**(1-3): p. 189-198.

38. Chu, C.C. and A. Needleman (1980). "Void nucleation effects in biaxially stretched sheets". *J. Eng. Mater. Technol.* **102**(3): p. 240-256.

39. Clausing, D.P. (1970). "Effect of plastic strain rate on ductility and toughness". *International Journal of Fracture Mechanics* **6**(1): p. 71-85.

40. Clift, S.E., P. Hartley, C.E.N. Sturgess, and G.W. Rowe (1990). "Fracture prediction in plastic deformation processes". *International Journal of Mechanical Sciences* **32**(1): p. 1-17.

41. Cockcrof, M.G. and D.J. Latham (1968). "Ductility and the workability of metals". *Journal of the Institute of Metals* **96**: p. 33-39.

42. Cvitanic, V., F. Vlak, and Z. Lozina (2008). "A finite element formulation based on non-associated plasticity for sheet metal forming". *International Journal of Plasticity* **24**(4): p. 646-687.

43. Dahl, J., K.L. Nielsen, and V. Tvergaard (2012). "Effect of Contact Conditions on Void Coalescence at Low Stress Triaxiality Shearing". *Journal of Applied Mechanics* **79**(2): p. 021003-7.

44. Danas, K. and P.P. Castaneda (2009). "A finite-strain model for anisotropic viscoplastic porous media: II - Applications". *European Journal of Mechanics a-Solids* **28**(3): p. 402-416.

45. Danas, K. and P.P. Castaneda (2012). "Influence of the Lode parameter and the stress triaxiality on the failure of elasto-plastic porous materials". *International Journal of Solids and Structures* **49**(11-12): p. 1325-1342.

46. Danas, K. and P. Ponte Castaneda (2009). "A finite-strain model for anisotropic viscoplastic porous media: I – Theory". *European Journal of Mechanics a-Solids* **28**(3): p. 402-416.

47. Delannay, L., I. Doghri, and O. Pierard (2007). "Prediction of tension-compression cycles in multiphase steel using a modified incremental mean-field model". *International Journal of Solids and Structures* **44**(22-23): p. 7291-7306.

48. Delannay, L., P. Jacques, and T. Pardoen (2008). "Modelling of the plastic flow of trip-aided multiphase steel based on an incremental mean-field approach". *International Journal of Solids and Structures* **45**(6): p. 1825-1843.

49. Dunand, M., D. Mohr, and K. Ravi-Chandar (2013). "Shear Fracture of Advanced High Strength Steel: Fractography and Micromechanical modeling". *In preparation*.

50. Durrenberger, L., J.R. Klepaczko, and A. Rusinek (2007). "Constitutive modeling of metals based on the evolution of the strain-hardening rate". *Journal of Engineering Materials and Technology-Transactions of the Asme* **129**(4): p. 550-558.

51. Durrenberger, L., A. Molinari, and A. Rusinek (2008). "Internal variable modeling of the high strain-rate behavior of metals with applications to multiphase steels". *Materials Science and Engineering a-Structural Materials Properties Microstructure and Processing* **478**(1-2): p. 297-304.

52. Duszek, M.K. and P. Perzyna (1991). "The localization of plastic deformation in thermoplastic solids". *International Journal of Solids and Structures* **27**(11): p. 1419-1443.

53. Embury, J.D. and G.H. Leroy (1977). "Failure maps applied to metal deformation processes". In: *ICF-4*, p. 15-42.

54. Fagerholt, E., C. Dorum, T. Borvik, H.I. Laukli, and O.S. Hopperstad (2010). "Experimental and numerical investigation of fracture in a cast aluminium alloy". *International Journal of Solids and Structures* **47**(24): p. 3352-3365.

55. Fischer, F.D., O. Kolednik, G.X. Shan, and F.G. Rammerstorfer (1995). "A note on calibration of ductile failure damage indicators". *International Journal of Fracture* **73**(4): p. 345-357.

56. Gao, X. and J. Kim (2006). "Modeling of ductile fracture: Significance of void coalescence". *International Journal of Solids and Structures* **43**(20): p. 6277-6293.

57. Gao, X.S., G.H. Zhang, and C. Roe (2010). "A Study on the Effect of the Stress State on Ductile Fracture". *International Journal of Damage Mechanics* **19**(1): p. 75-94.

58. Gao, X.S., T.T. Zhang, J. Zhou, S.M. Graham, M. Hayden, and C. Roe (2011). "On stress-state dependent plasticity modeling: Significance of the hydrostatic stress, the third invariant of stress deviator and the non-associated flow rule". *International Journal of Plasticity* **27**(2): p. 217-231.

59. Garajeu, M., J.C. Michel, and P. Suquet (2000). "A micromechanical approach of damage in viscoplastic materials by evolution in size, shape and distribution of voids". *Computer Methods in Applied Mechanics and Engineering* **183**(3-4): p. 223-246.

60. Gologanu, M., J.B. Leblond, and J. Devaux (1993). "Approximate models for ductile metals containing nonspherical voids—case of axisymmetrical prolate ellipsoidal cavities". *Journal of the Mechanics and Physics of Solids* **41**(11): p. 1723-1754.

61. Gologanu, M., J.B. Leblond, and J. Devaux (1994). "Approximate models for ductile metals containing nonspherical voids—case of axisymmetrical oblate ellipsoidal cavities". *Journal of Engineering Materials and Technology-Transactions of the Asme* **116**(3): p. 290-297.

62. Graf, A. and W. Hosford (1994). "The influence of strain-path changes on forming limit diagrams of Al6111 T4". *International Journal of Mechanical Sciences* **36**(10): p. 897-910.

63. Grange, M., J. Besson, and E. Andrieu (2000). "An anisotropic Gurson type model to represent the ductile rupture of hydrided Zircaloy-4 sheets". *International Journal of Fracture* **105**(3): p. 273-293.

64. Green, D.E., K.W. Neale, S.R. MacEwen, A. Makinde, and R. Perrin (2004). "Experimental investigation of the biaxial behaviour of an aluminum sheet". *International Journal of Plasticity* **20**(8-9): p. 1677-1706.

65. Greenwood, G.W. and R.H. Johnson (1965). "The deformation of metals under small stresses during phase transformation". *Proceedings of the Royal Society of London Series a-Mathematical and Physical Sciences* **283**(1394): p. 403.

66. Gurson, A.L. (1977). "Continuum theory of ductile rupture by void nucleation and growth: part i yield criteria and flow rules for porous ductile media". *Journal of Engineering Materials and Technology-Transactions of the Asme* **99**(1): p. 2-15.

67. Gurtin, M.E. and L. Anand (2005). "A theory of strain-gradient plasticity for isotropic, plastically irrotational materials. Part II: Finite deformations". *International Journal of Plasticity* **21**(12): p. 2297-2318.

68. Haltom, S.S., S. Kyriakides, and K. Ravi-Chandar (2013). "Ductile Failure Under Combined Shear and Tension". *International Journal of Solids and Structures*(To appear).

69. Hancock, J.W. and D.K. Brown (1983). "On the role of strain and stress state in ductile failure". *Journal of the Mechanics and Physics of Solids* **31**(1): p. 1-24.

70. Hancock, J.W. and A.C. Mackenzie (1976). "On the mechanisms of ductile failure in high-strength steels subjected to multi-axial stress states". *Journal of the Mechanics and Physics of Solids* **24**(2-3): p. 147-160.

71. Hasek, V. (1978). "Untersuchung and Theoretische Beschribung wichtiger Einflussgroessen auf das Grenzformaenderungsschaubild". *Bleche Rohre Profile* **25**.

72. Hershey, A.V. (1954). "Plasticity of isotropic aggregate of anisotropic facecentered cubic crystals". *Journal of Applied Mechanics-Transactions of the Asme* **21**(3): p. 241-249.

73. Hill, R. (1948). "A theory of the yielding and plastic flow of anisotropic metals". *Proceedings of the Royal Society of London Series a-Mathematical and Physical Sciences* **193**(1033): p. 281-297.

74. Huh, H., S.B. Kim, J.H. Song, and J.H. Lim (2008). "Dynamic tensile characteristics of TRIP-type and DP-type steel sheets for an auto-body". *International Journal of Mechanical Sciences* **50**(5): p. 918-931.

75. Jacques, P., Q. Furnemont, A. Mertens, and F. Delannay (2001). "On the sources of work hardening in multiphase steels assisted by transformation-induced plasticity". *Philosophical Magazine a-Physics of Condensed Matter Structure Defects and Mechanical Properties* **81**(7): p. 1789-1812.

76. Johnson, G.R. and W.H. Cook (1985). "Fracture characteristics of three metals subjected to various strains, strain rate, temperatures and pressures". *Engineering Fracture Mechanics* **21**(1): p. 31-48.

77. Keeler, S.P. and W.A. Backhofen (1964). "Plastic Instability and Fracture in Sheet Stretched over Rigid Punches". *ASM Trans. Quart.* **56**: p. 25-48.

78. Koplik, J. and A. Needleman (1988). "Void growth and coalescence in porous plastic solids". *International Journal of Solids and Structures* **24**(8): p. 835-853.

79. Kuwabara, T. (2007). "Advances in experiments on metal sheets and tubes in support of constitutive modeling and forming simulations". *International Journal of Plasticity* **23**(3): p. 385-419.

80. Kuwabara, T., S. Ikeda, and K. Kuroda (1998). "Measurement and analysis of differential work hardening in cold-rolled steel sheet under biaxial tension". *Journal of Materials Processing Technology* **80-1**: p. 517-523.

81. Lademo, O.G., O.S. Hopperstad, and M. Langseth (1999). "An evaluation of yield criteria and flow rules for aluminium alloys". *International Journal of Plasticity* **15**(2): p. 191-208.

82. Lassance, D., D. Fabregue, F. Delannay, and T. Pardoen (2007). "Micromechanics of room and high temperature fracture in 6xxx Al alloys". *Progress in Materials Science* **52**(1): p. 62-129.

83. Laukonis, J.V. and A.K. Ghosh (1978). "Effects of strain pah changes on the formability of sheet metals". *Metallurgical Transactions a-Physical Metallurgy and Materials Science* **9**(12): p. 1849-1856.

84. Leblond, J.B. and M. Gologanu (2008). "External estimate of the yield surface of an arbitrary ellipsoid containing a confocal void". *Comptes Rendus Mécaniques* **336**(11-12): p. 813-819.

85. Leblond, J.B., G. Perrin, and J. Devaux (1995). "An improved Gurson-type model for hardenable ductile metals". *European Journal of Mechanics a-Solids* **14**(4): p. 499-527.

86. Lecroise, F. and A. Pineau (1972). "Martensitic transformations induced by plastic deformation in the Fe–Ni–Cr–C system". *Metallurgical Transactions* **3**(2): p. 387-&.

87. Lee, K.L., A.F. Whitehouse, P.J. Withers, and M.R. Daymond (2003). "Neutron diffraction study of the deformation behaviour of deformation processed copper-chromium composites". *Materials Science and Engineering a-Structural Materials Properties Microstructure and Processing* **348**(1-2): p. 208-216.

88. Lee, M.G., D. Kim, C. Kim, M.L. Wenner, R.H. Wagoner, and K.S. Chung (2007). "A practical two-surface plasticity model and its application to spring-back prediction". *International Journal of Plasticity* **23**(7): p. 1189-1212.

89. Lee, M.G., D. Kim, C.M. Kim, M.L. Wenner, R.H. Wagoner, and K. Chung (2005). "Spring-back evaluation of automotive sheets based on isotropic-kinematic hardening laws and non-quadratic anisotropic yield functions - Part II: characterization of material properties". *International Journal of Plasticity* **21**(5): p. 883-914.

90. Lee, W., K.H. Chung, D. Kim, J. Kim, C. Kim, K. Okamoto, R.H. Wagoner, and K. Chung (2009). "Experimental and numerical study on formability of friction stir welded TWB sheets based on hemispherical dome stretch tests". *International Journal of Plasticity* **25**(9): p. 1626-1654.

91. Lemaitre, J. (1985). "A continuum damage mechanics model for ductile fracture". *Journal of Engineering Materials and Technology-Transactions of the Asme* **107**(1): p. 83-89.

92. Leroy, G., J.D. Embury, G. Edward, and M.F. Ashby (1981). "A model of ductile fracture based on the nucleation and growth of voids". *Acta Metallurgica* **29**(8): p. 1509-1522.

93. Lin, S.B. and J.L. Ding (1995). "Experimental study of the plastic yielding of rolled sheet metals with the cruciform plate specimen". *International Journal of Plasticity* **11**(5): p. 583-604.

94. Lloyd, D. and H. Sang (1979). "The influence of strain path on subsequent mechanical properties—Orthogonal tensile paths". *Metallurgical and Materials Transactions A* **10**(11): p. 1767-1772.

95. Lode, W. (1925). "Versuche über den einflub der mittleren hauptspannug auf die fliebgrenze". *Zeitschrift für angewandte mathematik und mechanik* **5**(2): p. 142-144.

96. Logan, R.W. and W.F. Hosford (1980). "Upper bound anisotropic yield locus calculations assuming <1 1 1>-pencil glide". *International Journal of Mechanical Sciences* **22**(7): p. 419-430.

97. Luo, M. and T. Wierzbicki (2010). "Numerical failure analysis of a stretch-bending test on dual-phase steel sheets using a phenomenological fracture model". *International Journal of Solids and Structures* **47**(22-23): p. 3084-3102.

98. Makinde, A., L. Thibodeau, and K.W. Neale (1992). "Development of an apparatus for biaxial testing using cruciform specimens". *Experimental Mechanics* **32**(2): p. 138-144.

99. Marcadet, S. (2013). "Experimental investigation of the effect of loading history on fracture: shear followed by tension". In: *Industrial Fracture Consortium Interim Meeting, April 5th 2013, Paris*,

100. Marciniak, Z. and K. Kuczinski (1967). "Limit strains in the processes of stretch-forming sheet metal". *International Journal of Mechanical Sciences* **9**: p. 609-620.

101. McClintock, F. (1968). "A criterion of ductile fracture by growth of holes". *Journal of Applied Mechanics* **35**(2): p. 363-&.

102. Mear, M.E. and J.W. Hutchinson (1985). "Influence of yield surface curvature on flow localization in dilatant plasticity". *Mechanics of Materials* **4**(3-4): p. 395-407.

103. Michel, J.C., O. Lopez-Pamies, P.P. Castaneda, and N. Triantafyllidis (2007). "Microscopic and macroscopic instabilities in finitely strained porous elastomers". *Journal of the Mechanics and Physics of Solids* **55**(5): p. 900-938.

104. Mohr, D. and F. Ebnoether (2009). "Plasticity and fracture of martensitic boron steel under plane stress conditions". *International Journal of Solids and Structures* **46**(20): p. 3535-3547.

105. Mohr, D. and S. Henn (2007). "Calibration of stress-triaxiality dependent crack formation criteria: A new hybrid experimental-numerical method". *Experimental Mechanics* **47**(6): p. 805-820.

106. Mohr, D. and J. Jacquemin (2008). "Large deformation of anisotropic austenitic stainless steel sheets at room temperature: Multi-axial experiments and phenomenological modeling". *Journal of the Mechanics and Physics of Solids* **56**(10): p. 2935-2956.

107. Mohr, D. and P. Mansour (2009). "Cyclic Large Deformation Tests on TKS TRIP690", Massachusetts Institute of Technology, Impact and Crashworthiness Lab, Technical report 202.

108. Mohr, D. and S. Marcadet (2012). "Extended Mohr-Coulomb (EMC) model: theory and application to DP590, DP780 and TRIP780 steel", Massachusetts Institute of Technology, Impact and Crashworthiness Laboratory, Technical report 242.

109. Mohr, D. and M. Oswald (2008). "A new experimental technique for the multi-axial testing of advanced high strength steel sheets". *Experimental Mechanics* **48**(1): p. 65-77.

110. Mohr, O. (1900). "Welche Umstande bedingen die Elastizitatsgrenze und den Bruch eines Materials". *Zeitschrift des Vereins Deutscher Ingenieure Band* **44**: p. 1524–1530.

111. Muller, W. and K. Pohlandt (1996). "New experiments for determining yield loci of sheet metal". *Journal of Materials Processing Technology* **60**(1-4): p. 643-648.

112. Nahshon, K. and J.W. Hutchinson (2008). "Modification of the Gurson Model for shear failure". *European Journal of Mechanics a-Solids* **27**(1): p. 1-17.

113. Nahshon, K. and Z.Y. Xue (2009). "A modified Gurson model and its application to punch-out experiments". *Engineering Fracture Mechanics* **76**(8): p. 997-1009.

114. Nakazima, K., T. Kikuma, and K. Hasuka (1971). "Study on the formability of steel sheets", Yawat Tech Rep 284.

115. Needleman, A. and V. Tvergaard (1992). "Analyses of Plastic Flow Localization in Metals". *Applied Mechanics Reviews* **45**(3S): p. S3-S18.

116. Nielsen, K., J. Dahl, and V. Tvergaard (2012). "Collapse and coalescence of spherical voids subject to intense shearing: studied in full 3D". *International Journal of Fracture* **177**(2): p. 97-108.

117. Nielsen, K.L. and V. Tvergaard (2009). "Effect of a shear modified Gurson model on damage development in a FSW tensile specimen". *International Journal of Solids and Structures* **46**(3-4): p. 587-601.

118. Nielsen, K.L. and V. Tvergaard (2010). "Ductile shear failure or plug failure of spot welds modelled by modified Gurson model". *Engineering Fracture Mechanics* **77**(7): p. 1031-1047.

119. Oh, S.I., C.C. Chen, and S. Kobayashi (1979). "Ductile failure in axisymmetric extrusion and drawing, part 2, workability in extrusion and drawing". *Journal of Engineering for Industry-Transactions of the Asme* **101**(1): p. 36-44.

120. Olson, G. and M. Cohen (1975). "Kinetics of strain-induced martensitic nucleation". *Metallurgical and Materials Transactions A* **6**(4): p. 791-795.

121. Padmanabhan, R., A.J. Baptista, M.C. Oliveira, and L.F. Menezes (2007). "Effect of anisotropy on the deep-drawing of mild steel and dual-phase steel tailor-welded blanks". *Journal of Materials Processing Technology* **184**(1-3): p. 288-293.

122. Papatriantafillou, I., M. Agoras, N. Aravas, and G. Haidemenopoulos (2006). "Constitutive modeling and finite element methods for TRIP steels". *Computer Methods in Applied Mechanics and Engineering* **195**(37-40): p. 5094-5114.

123. Pardoen, T. and J.W. Hutchinson (2000). "An extended model for void growth and coalescence". *Journal of the Mechanics and Physics of Solids* **48**(12): p. 2467-2512.

124. Ponte Castaneda, P. (1992). "New variational principles in plasticity and their application to composite materials". *Journal of the Mechanics and Physics of Solids* **49**(1757-1788).

125. Rahman, M.A., C. Butcher, and Z.T. Chen (2012). "Void evolution and coalescence in porous ductile materials in simple shear". *International Journal of Fracture* **177**(2): p. 129-139.

126. Rees, D.W.A. (1995). "Instability limits to the forming of sheet metals". *Journal of Materials Processing Technology* **55**(3-4): p. 146-153.

127. Rice, J.R. (1976). "The localization of plastic deformation". In: *Theoretical and Applied Mechanics (Proceedings of the 14th International Congress on Theoretical and Applied Mechanics, Delft, ed. W.T. Koiter)*, p. 207-220.

128. Rice, J.R. and D.M. Tracey (1969). "On the ductile enlargement of voids in triaxial stress fields". *Journal of the Mechanics and Physics of Solids* **17**(3): p. 201-&.

129. Rudnicki, J.W. and J.R. Rice (1975). "Conditions for the localization of deformation in pressure-sensitive dilatant materials". *Journal of the Mechanics and Physics of Solids* **23**(6): p. 371-394.

130. Rusinek, A. and J.R. Klepaczko (2009). "Experiments on heat generated during plastic deformation and stored energy for TRIP steels". *Materials & Design* **30**(1): p. 35-48.

131. Scheyvaerts, F., P.R. Onck, C. Tekoglu, and T. Pardoen (2011). "The growth and coalescence of ellipsoidal voids in plane strain under combined shear and tension". *Journal of the Mechanics and Physics of Solids* **59**(2): p. 373-397.

132. Simo, J.C. and T.J.R. Hughes (1998). "Computational Inelasticity". Berlin: Springer.

133. Spitzig, W.A. and O. Richmond (1984). "The effect of pressure on the flow stress of metals". *Acta Metallurgica* **32**(3): p. 457-463.

134. Stoughton, T.B. (2002). "A non-associated flow rule for sheet metal forming". *International Journal of Plasticity* **18**(5-6): p. 687-714.

135. Stoughton, T.B. and J.W. Yoon (2004). "A pressure-sensitive yield criterion under a non-associated flow rule for sheet metal forming". *International Journal of Plasticity* **20**(4-5): p. 705-731.

136. Stoughton, T.B. and J.W. Yoon (2008). "On the existence of indeterminate solutions to the equations of motion under non-associated flow". *International Journal of Plasticity* **24**(4): p. 583-613.

137. Stringfellow, R.G., D.M. Parks, and G.B. Olson (1992). "A constitutive model for transformation plasticity accompanying strain-induced martensitic transformations in metastable austenitic steels". *Acta Metallurgica Et Materialia* **40**(7): p. 1703-1716.

138. Sutton, M., J.J. Orteu, and H. Schreier (2009). "Image Correlation for Shape, Motion and Deformation Measurements. Basic Concepts, Theory and Applications": Springer.

139. Swift, H.W. (1952). "Plastic instability under plane stress". *Journal of the Mechanics and Physics of Solids* **1**(1): p. 1-18.

140. Tarigopula, V., O.S. Hopperstad, M. Langseth, and A.H. Clausen (2008). "Elastic-plastic behaviour of dual-phase, high-strength steel under strain-path changes". *European Journal of Mechanics a-Solids* **27**(5): p. 764-782.

141. Tekoglu, C., J.B. Leblond, and T. Pardoen (2012). "A criterion for the onset of void coalescence under combined tension and shear". *Journal of the Mechanics and Physics of Solids* **60**(7): p. 1363-1381.

142. Thomason, P.F. (1985). "A 3-dimensional model for ductile fracture by the growth and coalescence of microvoids". *Acta Metallurgica* **33**(6): p. 1087-1095.

143. Turteltaub, S. and A.S.J. Suiker (2005). "Transformation-induced plasticity in ferrous alloys". *Journal of the Mechanics and Physics of Solids* **53**(8): p. 1747-1788.

144. Tvergaard, V. (1981). "Influence of voids on shear band instabilities under plane strain conditions". *International Journal of Fracture* **17**(4): p. 389-407.

145. Tvergaard, V. (2008). "Shear deformation of voids with contact modelled by internal pressure". *International Journal of Mechanical Sciences* **50**(10–11): p. 1459-1465.

146. Tvergaard, V. (2009). "Behaviour of voids in a shear field". *International Journal of Fracture* **158**(1): p. 41-49.

147. Tvergaard, V. (2012). "Effect of stress-state and spacing on voids in a shear-field". *International Journal of Solids and Structures* **49**(22): p. 3047-3054.

148. Tvergaard, V. and A. Needleman (1984). "Analysis of the cup-cone fracture in a round tensile bar". *Acta Metallurgica* **32**(1): p. 157-169.

149. Uthaisangsuk, V., U. Prahl, and W. Bleck (2009). "Characterisation of formability behaviour of multiphase steels by micromechanical modelling". *International Journal of Fracture* **157**(1-2): p. 55-69.

150. Walters, C.L. (2009). "Effect of Strain Rate on Fracture". Ph.D. Thesis, Department of Mechanical Engineering, Massachusetts Institute of Technology, Cambridge, USA.

151. Wang, J., V. Levkovitch, F. Reusch, B. Svendsen, J. Huetink, and M. van Riel (2008). "On the modeling of hardening in metals during non-proportional loading". *International Journal of Plasticity* **24**(6): p. 1039-1070.

152. Wei, X., R. Fu, and L. Li (2007). "Tensile deformation behavior of cold-rolled TRIP-aided steels over large range of strain rates". *Materials Science and Engineering: A* **465**(1-2): p. 260-266.

153. Wierzbicki, T. and L. Xue (2005). "On the Effect of the Third Invariant of the Stress Deviator on Ductile Fracture", Massachusetts Institute of Technology, Impact and Crashwortiness Laboratory, Technical report 136.

154. Wilkins, M.L., R.D. Streit, and J.E. Reaugh (1980). "Cumulative Strain-Damage Model of Ductile Fracture: Simulation and Prediction of Engineering Fracture Tests", Lawrence Livermore National Laboratory,

155. Xue, L. (2008). "Constitutive modeling of void shearing effect in ductile fracture of porous materials". *Engineering Fracture Mechanics* **75**(11): p. 3343-3366.

156. Yoshida, F., T. Uemori, and K. Fujiwara (2002). "Elastic-plastic behavior of steel sheets under in-plane cyclic tension-compression at large strain". *International Journal of Plasticity* **18**(5-6): p. 633-659.

157. Zhang, K.S., J.B. Bai, and D. Francois (2001). "Numerical analysis of the influence of the Lode parameter on void growth". *International Journal of Solids and Structures* **38**(32-33): p. 5847-5856.